Nanoscale Spherical-Supported Membranes as Novel Platforms for Improving the Phage Display Screening of Antibody Mimetics against Membrane Protein Targets

Vlad Vasilca

Submitted in accordance with the requirements for the degree of
Doctor of Philosophy

The University of Leeds

School of Biomedical Sciences

September 2016

The candidate confirms that the work submitted is his own and that appropriate credit has been given where reference has been made to the work of others.

ACKNOWLEDGEMENTS

First of all, I would like to extend my gratitude to my supervisors Dr. Lars Jeuken, Dr. Stephen Muench and Prof. Stephen Baldwin for their constant support and guidance throughout my PhD and for entrusting me with such a challenging and, ultimately, satisfying project to work on. It has been a genuine privilege to learn so much from them and gradually develop the SSBLM platform under their expert tutelage.

Further thanks go to all of the current and past members of the Jeuken research group that I have had the pleasure of meeting and working with, including Dr. Valentin Radu, Dr. Mengqiu Li, Dr. Khizar Sheikh, Dr. Ee Taek Hwang, Dr. George Heath, Dr. Duncan McMillan, Anna Wroblewska-Wolna, Theodoros Laftsoglou, Joseph Oram, Matthias Gantner, Anna Stikane, Honling Rong and Riitta Partanen. Their expertise and collegiality within the lab is equally matched by their camaraderie and goodwill without.

Several other research groups from the University of Leeds contributed to the success of this project and thus I must also thank Dr. Vincent Postis, Dr. Vincent Agboh and David Sharples for their help with target protein expression and purification, as well as DNA molecular biology. My gratitude also extends to Shaun Rawson for his aid in the cryo-EM imaging of the SSBLM particles and to Dr. Amin Sadeghpour from the School of Food Science and Nutrition for his invaluable help with the SAXS measurements.

Our collaborators from MedImmune Ltd – Dr. Trevor Wilkinson, Dr. David Bannister, Dr. Stacey Chin, Dr. Elizabeth England, Dr. Christine Rossant, Dr. Roger Dodd and the rest of the Protein Sciences Group – all deserve special thanks for not only sharing their expertise and facilities for the numerous DARPin selections and beyond, but also for their cordiality and interest in my project from my very first day on-site in Cambridge.

Equally, I must also extend my thanks to both the Biotechnology and Biological Sciences Research Council (BBSRC) and MedImmune Ltd for their generous funding of this project, as well as to my entire family for their unconditional support throughout these many years of hard work and lengthy separation.

Ultimately, my most heartfelt thanks go to my lovely fiancée for her unwavering commitment, support and understanding throughout all of the good and the bad that accompanied such a complex and demanding research project. I would not have grown into the man I am today without her always by my side.

Dedicated to **Prof. Stephen Allan Baldwin** (1952 – 2014), whose lifelong interest and expertise in the field of Membrane Biology helped bring this project to fruition.

“Ever onwards and upwards!”

ABSTRACT

Membrane proteins represent the majority of therapeutic targets for the antibody-based drugs available today. These are routinely identified via phage display screening, but traditional antigen presentation methods require membrane protein targets to be detergent-solubilised in order to preserve their native conformations post-purification. Unfortunately, detergent solubilisation can not only lead to gradual target denaturation over time, but the detergent micelles can also occlude important epitopes on the extramembranous loops and thus prevent the discovery of antibody binders.

The current thesis aimed to demonstrate that, by reconstituting purified membrane proteins into spherical-supported bilayer lipid membranes (SSBLMs) deposited on nanosized substrates, a versatile platform can be constructed for performing phage display screening against membrane protein targets, while not only presenting these within a native-like lipid environment, but also eliminating detergents from the screening phase altogether. For providing proof-of-concept, 100- and 200 nm silica nanoparticles were covered with POPC SSBLMs embedding the bacterial nucleoside transporter NupC. Full substrate coverage and the correct formation of the lipid bilayer components were established via spectrofluorometry, using fluorescent labelling and small-angle X-ray scattering (SAXS) respectively, while Western blotting and high-affinity antibody binding confirmed the presence of SSBLM-embedded NupC.

The platform was then used to screen designed ankyrin repeat proteins (DARPins) against a His_6-tagged construct of NupC across different screening formats so as to offer a comparison to the classic 96-well plate antigen presentation method. Following that, the DARPin binders showing the highest potential affinity for NupC were purified and subjected to further binding validation assays against two other constructs – detergent-solubilised double Strep-tagged NupC and SSBLM-embedded untagged/wild-type NupC – in order to identify any binders targeting extramembranous epitopes that would be accessible *in vivo* as well. Ultimately, the results presented throughout indicated that SSBLMs constitute a promising means of screening antibody binders against membrane protein targets embedded in a close-to-native format.

CONTENTS

List of Figures x

List of Tables xiii

Abbreviations and Constants xiv

Chapter 1 – Project Aim and Introduction 1

- 1.1. Background and Aim 1
  - 1.1.1. The present focus of the pharmaceutical industry 1
  - 1.1.2. The issues surrounding the study of membrane proteins 2
  - 1.1.3. The detergent solubilisation of membrane proteins 3
  - 1.1.4. The drawbacks of the membrane protein detergent solubilisation 6
  - 1.1.5. Improving antibody screening against membrane protein targets 7
- 1.2. Lipid Membrane Research 8
  - 1.2.1. An era of lipid membrane research 8
  - 1.2.2. The Davson-Danielli-Robertson cell membrane model 10
  - 1.2.3. The Benson-Green cell membrane model 12
  - 1.2.4. The fluid mosaic cell membrane model 15
- 1.3. Model Membranes 17
  - 1.3.1. Supported lipid membranes 17
  - 1.3.2. Inserting membrane protein targets into solid-supported membranes 19
  - 1.3.3. Current model membrane applications 23
- 1.4. Providing Proof-of-Concept 24
  - 1.4.1. The bacterial nucleoside transporter NupC 24
  - 1.4.2. Spherical-supported bilayer lipid membranes 25

Chapter 2 – Experimental Techniques 30

- 2.1. Quartz Crystal Microbalance with Dissipation Monitoring 30
  - 2.1.1. Introduction to QCM-D technology 30
  - 2.1.2. The QCM-D operating principle 31
  - 2.1.3. QCM-D sensor design and sample loading 32
  - 2.1.4. The Q-Sense E4 QCM-D setup 35

2.1.5. Monitoring lipid bilayer formation kinetics via QCM-D 36

2.1.6. The virtues and limitations of QCM-D technology 38

2.2. SURFE2R N1 Transport Activity Assay 41

2.2.1. Introduction to SSM-based electrophysiology 41

2.2.2. The SURFE2R operating principle 42

2.2.3. Successful applications of SURFE2R technology 44

2.2.4. The virtues and limitations of SURFE2R technology 45

2.3. Cryo-Electron Microscopy 46

2.3.1. Introduction to electron microscopy 46

2.3.2. The different types of electron microscopes 47

2.3.3. Cryofixation and the emergence of cryo-EM 48

2.3.4. Preparing samples for cryo-EM 49

2.3.5. The virtues and limitations of cryo-EM 52

2.4. Small-Angle X-Ray Scattering 53

2.4.1. Introduction to X-ray scattering 54

2.4.2. The SAXS experimental setup and operating principle 54

2.4.3. The virtues and limitations of SAXS 58

2.5. Phage Display Screening 60

2.5.1. Introduction to phage display screening 60

2.5.2. Types of phages used in the display of antibody binders 62

2.5.3. Phage versus phagemid library creation 64

2.5.4. The virtues and limitations of phage display screening 67

2.5.5. Immunoglobulins 68

2.5.6. Monoclonal antibodies 70

2.5.7. Designed ankyrin repeat proteins 72

Chapter 3 – Materials and Methods 80

3.1. Reiterating the Overall Experimental Plan 80

3.2. Materials 80

3.3. Buffers, Media and Solutions 84

3.4. Methods 90

3.4.1. General methods 90

3.4.2. Double Strep-tagged NupC expression and purification 94

3.4.3. His$_6$-tagged NupC expression and purification 97

3.4.4. Untagged NupC expression and *E. coli* inner membrane extraction 98

3.4.5. His$_6$-tagged PepTSo expression and purification 98

3.4.6. Measuring nucleoside transport activity via the SURFE2R N1 99

3.4.7. Traditional plate-based phage display screening 100

3.4.8. Plasmid DNA extraction 102

Chapter 4 – SSBLM Formation and Characterisation **103**

4.1. Target Protein Expression and Purification 103

4.1.1. Double Strep-tagged NupC expression and purification 103

4.1.2. His$_6$-tagged NupC expression and purification 104

4.1.3. Untagged NupC expression and *E. coli* inner membrane extraction 105

4.1.4. His$_6$-tagged PepTSo expression and purification 105

4.2. Assaying the Transport Activity of Purified NupC 106

4.3. Planar SSM Formation and Characterisation 108

4.3.1. Monitoring planar SSM formation via QCM-D 109

4.3.2. Planar SSM formation using NupC-embedding proteoliposomes 110

4.4. SSBLM Formation and Characterisation 113

4.4.1. Confirmation of substrate saturation via fluorescence spectroscopy 113

4.4.2. Characterisation of SSBLM formation via SAXS 115

4.5. Formation and Characterisation of SSBLMs Embedding NupC 117

4.5.1. Confirmation of SSBLM-embedded NupC via Western blotting 117

4.5.2. Confirmation of SSBLM-embedded NupC via peroxidase assay 118

4.5.3. Confirmation of SSBLM-embedded NupC via cryo-EM 123

Chapter 5 – SSBLM-Based Phage Display Screening **127**

5.1. Introduction to SSBLM-Based Screening against NupC 127

5.2. The Different DARPin Screening Formats Tested against NupC 128

5.2.1. Traditional plate-based screening against detergent-solubilised NupC 128

5.2.2. Novel SSBLM-based screening against detergent-free NupC 129

5.3. Identifying the Lead Candidate DARPin Binders 131
5.3.1. Aligning the amino acid sequences of the total selection output 131
5.4. Purifying the Lead Candidate DARPin Binders 134
5.4.1. Isolating the plasmid DNA encoding the lead candidate DARPins 134
5.4.2. Small-scale expression trial of the lead candidate DARPins 135
5.4.3. Full-scale expression and purification of the lead candidate DARPins .137
5.5. Characterising the Purified Lead Candidate Binders.....................................139
5.5.1. Re-screening against detergent-solubilised double Strep-tagged NupC 139
5.5.2. Re-screening against detergent-free untagged NupC.............................140
5.6. Evaluating the Outcome of the DARPin Selections 143
5.6.1. The phage display screening of antibodies against membrane proteins.143
5.6.2. Testing the SSBLM format on new membrane protein targets..............144

Chapter 6 – Discussion and Conclusions 148

6.1. Discussion...148
6.1.1. Presenting targets for screening in a close-to-native format 148
6.1.2. Current limitations of the SSBLM screening format 149
6.2. Future Directions 150
6.3. Conclusions...151

Bibliography 154

Appendix 177

LIST OF FIGURES

1.1.3.1. Models of D-octylglucoside monomers and micelles 3

1.1.3.2. Structures of common detergent monomers...5

1.1.3.3. Diagram of native membrane detergent solubilisation....................................6

1.1.4.1. Membrane protein epitope occlusion by detergent micelles 7

1.2.2.1. The Danielli-Davson cell membrane model..10

1.2.2.2. Electron micrograph of two Schwann cells 11

1.2.2.3. Diagram of J. D. Robertson’s “unit membrane” hypothesis 11

1.2.2.4. Electron micrographs of the discrete structure of the cell membrane 12

1.2.3.1. Electron micrographs of the discrete structure of plant chloroplasts 13

1.2.3.2. The fluid mosaic cell membrane model 14

1.2.4.1. The mattress cell membrane model..16

1.3.1.1. Lipid monolayer formation at the air-water interface in a Langmuir trough .17

1.3.1.2. Atomic-force micrograph of an SSM embedding reconstituted proteins.......18

1.3.1.3. Different types of SSMs embedding reconstituted membrane proteins.........19

1.3.2.1. Fluorescence microscopy images of GUVs..20

1.3.2.2. The oriented reconstitution of P2X2-Neon into a PEGylated SSM 22

1.3.3.1. High-resolution microscopy images of different lipid raft domains 23

1.4.2.1. Cryo-EM image of SSBLM-embedded OprM..27

1.4.2.2. Diagram of a “proteo-lipobead” 28

1.4.2.3. Workflow illustrating the overall project aims and experimental plan 29

2.1.1.1. Diagram of a QCM-D flow cell featuring a singular flow module 31

2.1.2.1. Diagram of the converse piezoelectric effect 31

2.1.4.1. The Q-Sense E4 QCM-D setup 36

2.1.5.1. The frequency and dissipation changes brought on by vesicle deposition.....37

2.1.5.2. The different pathways leading to lipid bilayer formation............................38

2.1.6.1. Diagram of an enhanced MQCM sensor design..40

2.2.1.1. Top and bottom views of a SURFE2R N1 sensor chip 42

2.2.2.1. Diagram of a capacitively-coupled vesicle-SSM complex............................42

2.2.2.2. Diagram of the SURFE2R operating principle...43

2.3.1.1. Digitally-enhanced photograph of the first electron microscope prototype ... 46
2.3.2.1. The FEI Tecnai – a modern TEM ... 47
2.3.2.2. TEM image of the plasma membrane phospholipid bilayer component ... 48
2.3.4.2. Different types of cryo-EM grids and their respective support films ... 50
2.3.5.1. Cryo-EM evidence of SSBLM formation around silica nanoparticles ... 53
2.4.2.1. Diagram of a pinhole-collimated SAXS instrument ... 55
2.4.2.2. Diagram of the SAXS operating principle ... 55
2.4.2.3. Normalised Kratky plot of different protein scattering profiles ... 58
2.5.1.1. Diagram of a typical filamentous bacteriophage displaying a binder ... 60
2.5.1.2. Schematic representation of the phage display screening process ... 62
2.5.2.1. Transmission electron micrographs of the T4 bacteriophage ... 63
2.5.2.2. The two possible bacteriophage life cycles ... 64
2.5.5.1. Structures of three human antibody classes: IgG, IgE and IgA ... 69
2.5.6.1. Schematic of a hybridoma cell line producing monoclonal antibodies ... 71
2.5.7.1. Diagram of DARPin library design ... 74
2.5.7.2. Functionalisation capabilities of therapeutic DARPins ... 76
2.5.7.3. Examples of DARPin-based drugs currently undergoing clinical trials ... 77
2.5.7.4. Diagram of transforming regular DARPins into LoopDARPins ... 79
4.1.1.1. SDS-PAGE and Western blot of double Strep-tagged NupC samples ... 103
4.1.2.1. SDS-PAGE and Western blot of His_6-tagged NupC samples ... 104
4.1.3.1. SDS-PAGE of untagged NupC samples ... 105
4.1.4.1. SDS-PAGE and Western blot of His_6-tagged PepTSo samples ... 106
4.2.1.1. SURFE2R trace of untagged NupC transport activity in IM LUVs ... 107
4.2.1.2. SURFE2R trace of untagged NupC transport activity in IM/PLE LUVs ... 107
4.2.1.3. Michaelis-Menten curve of transient inward current peak amplitudes ... 108
4.3.1.1. Planar lipid SSM formation kinetics monitored via QCM-D ... 109
4.3.2.1a. Negative control POPC SSM formation kinetics ... 111
4.3.2.1b. Double Strep-tagged NupC-embedding SSM formation kinetics ... 111
4.3.2.1c. His_6-tagged NupC-embedding SSM formation kinetics ... 112
4.3.2.1d. Untagged NupC-embedding SSM formation kinetics ... 113
4.4.1.1. The fluorescence emissions resulting from TR-labelled POPC SSBLMs ... 114

4.4.2.1. SAXS scattering profiles from stock and POPC-covered nanoparticles......116
4.4.2.2. Fitted scattering profiles from stock and POPC-covered nanoparticles.......116
4.5.1.1. Western blot of POPC SSBLMs embedding His_6-tagged NupC 118
4.5.2.1. SSBLM-embedded His_6-tagged NupC peroxidase assay............................120
4.5.2.2. Optimised SSBLM-embedded His_6-tagged NupC peroxidase assay 121
4.5.2.4. IM/POPC SSBLM-embedded His_6-tagged NupC peroxidase assay...........123
4.5.3.1. Initial cryo-EM imaging of His_6-tagged NupC-embedding SSBLMs.........124
4.5.3.2. Optimised cryo-EM imaging of His_6-tagged NupC-embedding SSBLMs ..125
4.5.3.3. Workflow summarising the experimental findings presented in Chapter 4 .126
5.3.1.1. The DARPin amino acid sequences with the highest number of repeats.....132
5.3.1.2. The phylogenetic tree of the most recurring DARPin sequences................133
5.4.1.1. TAE agarose gel of lead candidate DNA subcloned into pET-16b.............135
5.4.2.1. SDS-PAGE and Western blot of small-scale DARPin expression trial.......136
5.4.3.1. SDS-PAGE and Western blot of DARPin purification samples 138
5.5.1.1. DARPin ELISA against detergent-solubilised double Strep-tagged NupC .140
5.5.2.1. DARPin ELISA against detergent-free untagged NupC 142
5.6.2.1. Concept-validation ELISA against SSBLM-embedded mammalian FPR...146
5.6.2.2. Workflow summarising the experimental findings presented in Chapter 5 .147
A1. Map of the pBPT-0217-CS2T plasmid...177
A2. Map of the pLH13 plasmid..177
A3. Map of the pGJL16 plasmid 178
A4. Map of the pMPSIL0079A plasmid 178

LIST OF TABLES

2.1.3.2. Examples of QCM sensor surface chemistry interactions.............................33
3.3.1.1a. General buffers and solutions used throughout the entire project..................84
3.3.1.1b. Bacterial growth media used throughout the entire project............................85
3.3.1.1c. Double Strep-tagged NupC expression and purification buffers....................86
3.3.1.1d. $\mathrm{His_6}$-tagged NupC expression and purification buffers.................................86
3.3.1.1e. Untagged NupC expression and inner membrane extraction buffers.............86
3.3.1.1f. BCA assay solutions used throughout the entire project................................87
3.3.1.1g. SDS-PAGE buffers and solutions..87
3.3.1.1h. Western blotting buffers..88
3.3.1.1i. SURFE2R assay solutions..88
3.3.1.1j. Phage display screening buffers..88
3.3.1.1k. DARPin DNA molecular biology reaction mixtures.....................................89
3.3.1.1l. Lead candidate binder purification buffers..89
3.3.1.1m. Detergent-solubilised double Strep-tagged NupC ELISA buffers.................90
3.3.1.1n. Detergent-free, SSBLM-embedded untagged NupC ELISA buffers.............90
3.3.1.1o. SSBLM-embedded mammalian FPR ELISA buffers....................................90
4.5.2.3. Optimised SSBLM-embedded NupC peroxidase assay protocol................122
5.2.1.1. Outcomes of the DARPin selections against detergent-solubilised NupC...128
5.2.2.1. Outcomes of the DARPin selections against SSBLM-embedded NupC 131

ABBREVIATIONS AND CONSTANTS

Abbreviations

AC – alternating (electrical) current

ADHP – 10-Acetyl-3,7-dihydroxyphenoxazine

ADP – adenosine diphosphate

AFM – atomic-force microscopy

AP – atom probe

APH – aminoglycoside phosphotransferase

APS – ammonium persulfate

$A(s)$ – (X-ray) scattering amplitude (SAXS)

ATP – adenosine triphosphate

BBSRC – Biotechnology and Biological Sciences Research Council

BCA – bicinchoninic acid

BLM – black lipid membrane

BSA – bovine serum albumin

CA – 1,1’,2,2’-Tetraoleoyl cardiolipin

CCD – charged-coupled device (camera)

CD – circular dichroism

cDNA – circular deoxyribonucleic acid

CDR – (immunoglobulin) complementarity-determining region

Cfu – (bacterial) colony-forming unit

C_H – constant heavy (immunoglobulin) domain

Chol – cholesterol

C_L – constant light (immunoglobulin) domain

CMC – critical micellar concentration

CNT – concentrative nucleoside transporter

Cran – randomised (LoopDARPin) C-terminal cap

Cryo-EM – cryo-electron microscopy

CV – column volume

Cyt*c*O – cytochrome *c* oxidase

DARPin – designed ankyrin repeat protein

DDM – *n*-Dodecyl β-D-maltoside

DDR – Davson-Danielli-Robertson (cell membrane model)

DiPhyPC – 1,2-Diphytanoyl-*sn*-glycero-3-phosphocholine

D_{max} – maximum dimension of the sampled particles (SAXS)

DNA – deoxyribonucleic acid

DOPC – 1,2-Dioleoyl-*sn*-glycerophosphocholine

DOPE – 1,2-Dioleoyl-*sn*-glycerophosphoethanolamine

DOPG – 1,2-Dioleoyl-*sn*-glycero-3-[phospho-*rac*-(1-glycerol)]

DOPS – 1,2-Dioleoyl-*sn*-glycero-3-phospho-L-serine

DOTAP – 1,2-Dioleoyl-3-trimethylammonium-propane

DPI – dual polarisation interferometry

DPPC – 1,2-Dipalmitoyl-*sn*-glycero-3-phosphocholine

DTT – *threo*-1,4-Dimercapto-2,3-butanediol

E. coli – *Escherichia coli*

EDTA – ethylenediaminetetraacetic acid

EEF – electrophoretic-electroosmotic focusing

ELISA – enzyme-linked immunosorbent assay

EM – electron microscopy

EQCM – electrochemical quartz crystal microbalance

Fab – fragment-antigen binding (immunoglobulin region)

Fc – fragment-crystallisable (immunoglobulin region)

FCCP – carbonyl cyanide-*p*-trifluoromethoxyphenylhydrazone

FDA – (US) Food and Drug Administration

FIA – flow injection analysis

FM – flexural mode

Fos-Choline-12 – *n*-Dodecylphosphocholine

FPR – formyl peptide receptor

FSM – face shear mode

GPCR – G-protein coupled receptor

GUV – giant unilamellar vesicle

HEPES – N-(2-Hydroxyethyl)piperazine-N′-(2-ethanesulfonic acid)

HRP – horseradish peroxidase

I – internal (LoopDARPin) library module

$I(0)$ – (X-ray) forward scattering (SAXS)

IDP – intrinsically-disordered protein

IF – internal (LoopDARPin) library module following loop

Ig – immunoglobulin

IL – internal loop-containing (LoopDARPin) library module

IM – (bacterial) inner membrane

IPTG – isopropyl β-D-thiogalactoside

$I(s)$ – intensity of scattered X-rays (SAXS)

K_m – Michaelis constant

KOD – *Thermococcus kodakarensis*

LB – Luria-Bertani (bacterial growth medium)

LDAO – lauryldimethylamine N-oxide

LS – light scattering

LuSy – lumazine synthase

LUV – large unilamellar vesicle

MAB – monoclonal antibody

MBP – maltose binding protein

MD – molecular dynamics

MOPS – 3-(N-Morpholino)propanesulfonic acid

MQCM – monolithic quartz crystal microbalance

MRC – (UK) Medical Research Council

MRI – magnetic resonance imaging

mRNA – messenger ribonucleic acid

MWCO – molecular weight cut-off

Ni-NTA – nickel-nitrilotriacetic acid

NMR – nuclear magnetic resonance

Nran – randomised (LoopDARPin) N-terminal cap

NTA – nitrilotriacetic acid

OM – (bacterial) outer membrane

PAGE – polyacrylamide gel electrophoresis

PBS – phosphate-buffered saline

PC – phosphatidylcholine

PCR – polymerase chain reaction

PDB – (Research Collaboratory for Structural Bioinformatics) Protein Data Bank

PDMS – polydimethylsiloxane

PE – phosphatidylethanolamine

PEG – polyethylene glycol

PLE – (*E. coli*) polar lipid extract

POPC – 1-Palmitoyl-2-oleoyl-*sn*-glycero-3-phosphocholine

QCM – quartz crystal microbalance

QCM-D – quartz crystal microbalance with dissipation monitoring

R_g – radius of gyration (SAXS)

R_{sat} – maximal (lipid membrane) detergent saturation point

R_{sol} – maximal (lipid membrane) detergent solubilisation point

SAES – small-angle electron scattering

SAGS – small-angle gamma ray scattering

SANS – small-angle neutron scattering

SAXS – small-angle X-ray scattering

ScFv – single-chain variable (antibody) fragment

SDS – sodium dodecyl sulfate

SDS-PAGE – SDS-polyacrylamide gel electrophoresis

SLS – Scientific Laboratory Supplies

SMALP – styrene-maleic acid copolymer lipid particle

SPR – surface plasmon resonance

SRBC – sheep red blood cell

SSBLM – spherical-supported bilayer lipid membrane

SSM – solid-supported membrane

SUV – small unilamellar vesicle

TAE – Tris, acetic acid and EDTA (buffer)

TBS – Tris-buffered saline

TBS-T – Tris-buffered saline with Tween® 20

TEM – transmission electron microscope

TEMED – N,N,N’,N’-Tetramethylethylenediamine

TIRF – total internal reflection fluorescence (microscopy)

TMB – 3,3′,5,5′-Tetramethylbenzidine

TR – Texas Red® (1,2-Dihexadecanoyl-*sn*-glycero-3-phosphoethanolamine triethylammonium salt)

Tris – tris(hydroxymethyl)aminomethane

Triton X-100 – α-[4-(1,1,3,3-Tetramethylbutyl)phenyl]-w-hydroxy-poly(oxy-1,2-ethanediyl)

TSM – thickness shear mode

TY – tryptone-yeast extract (bacterial growth medium)

TYAG – tryptone-yeast extract (bacterial growth medium) supplemented with ampicillin and glucose

TYAK – tryptone-yeast extract (bacterial growth medium) supplemented with ampicillin and kanamycin

UCP1 – uncoupling protein 1

UV – ultraviolet (radiation)

VEGF – vascular endothelial growth factor

V_H – variable heavy (immunoglobulin) domain

V_L – variable light (immunoglobulin) domain

V_{max} – maximum reaction rate

WAXS – wide-angle X-ray scattering

Constants

AT-cut quartz crystal shear modulus (μ_q) – 2.947×10^{11} g cm^{-1} s^2

Quartz crystal density (ρ_q) – 2.648 g cm^{-3}

Room temperature – 293.15 K

CHAPTER 1

Project Aim and Introduction

1.1. Background and Aim

Membrane proteins represent a vital category of cellular membrane constituents responsible for facilitating a multitude of processes involved in homeostasis, including cell-to-cell interactions, nerve excitation and signal transduction, ion and nutrient transmembrane transport, cell respiration and photosynthesis, as well as the elimination of unwanted cellular by-products and waste (Patching et al., 2005). Members of this protein class include – but are not limited to – G-protein coupled receptors (GPCRs), ligand- and voltage-gated ion channels (Overington et al., 2006), protein kinases, phospholipases and biochemical receptors of all kinds (Johnson and Cornell, 1999). Regardless of whether they span the full thickness of the lipid bilayer (i.e. "integral") or are only attached to one side of their native membranes (i.e. "peripheral") (Cho and Stahelin, 2005), membrane proteins are encoded by approximately 30% of the genomes of archaea, eubacteria and eukaryotes – a proportion clearly underlining their indispensability towards sustaining life in its many different forms (Wallin and von Heijne, 1998).

1.1.1. The present focus of the pharmaceutical industry

Given that a large number of debilitating diseases such as Bartter syndrome, osteoporosis, myotonia congenita, cardiac arrhythmia, hypertension, congenital deafness and epilepsy (Hübner and Jentsch, 2002) or cystic fibrosis and polycystic kidney disease (Aperia, 2007) are caused by the incorrect function of specific classes of membrane-bound proteins, it is unsurprising that a majority of the therapeutics that are commercially-available today target membrane proteins exclusively (Hopkins and Groom, 2002). Of these, antibody-based drugs represent major drivers of the pharmaceutical industry, capable of binding virtually any biological target with high affinity and specificity, while also provoking less side-effects compared to small molecule therapeutics (Imai and Takaoka, 2006). In an attempt at discovering new therapeutic antibodies, the industry relies on the use of high-throughput *in vitro* techniques such as phage display screening in order to scan million-strong binder candidate libraries against the membrane protein targets of interest. However, the identification of highly-specific antibody binders demands a similarly high level of purity from the targets themselves and this is where the bottlenecks impeding membrane protein screening start to arise from.

1.1.2. The issues surrounding the study of membrane proteins

As opposed to cytoplasmic (i.e. soluble) proteins, only very few membrane proteins ever see high levels of expression within biological membranes (e.g. aquaporins (Zeuthen et al., 2013), rhodopsins (Schertler, 2015) or ATPases (Andersen et al., 2016)) and these have already been studied at length and have had their structures determined as a result. Since circular dichroism (CD), kinetic and ligand-binding characterisation, nuclear magnetic resonance (NMR) or X-ray crystallography studies cannot be performed directly on native membranes, information on classes of membrane proteins showing poor native expression is severely limited by not only the difficulties inherent to the production of enough recombinant protein, but also by their isolation with the high purity and conformational stability required for meeting the rigours of the above-mentioned research techniques (Seddon et al., 2004).

Whether this is due to various differences in the membrane protein biogenesis pathways (e.g. cellular chaperones, foldases, signal recognition and translocon components) or the xenobiotic toxicity levied onto the host expression system (Mancia and Love, 2010), the overproduction of specific classes of membrane proteins will almost always be very low (Bill et al., 2011). This is certainly the case with mammalian membrane proteins expressed in bacterial (e.g. *Escherichia coli*) systems (Tate, 2001), whose cellular membranes can only express limited amounts of recombinant protein even in the best scenarios (Rahman et al., 2007). Furthermore, membrane proteins are notoriously averse to standard purification techniques such as hydrophobic interaction chromatography and ion exchange (Mancia and Love, 2010), and even when employing high-affinity chromatography methods facilitated by the introduction of specialised (e.g. Strep- or polyhistidine) tags (Mohanty and Wiener, 2004), their purification to a high-enough standard to support rigorous subsequent studies is also met with considerable hurdles, including poor overall yields and post-purification denaturation (Yang et al., 2014). One important contributing factor to this latter impediment is undoubtedly represented by the traditional reliance on detergent solubilisation for counteracting the considerable hydrophobicity of membrane protein targets and their tendency to aggregate in solution once they are removed from their native lipid membrane environment (Bill et al., 2011).

1.1.3. The detergent solubilisation of membrane proteins

Owing to their particular structure, consisting of a polar (i.e. hydrophilic) head group attached to a non-polar (i.e. hydrophobic) alkyl chain or "tail" (Figure 1.1.3.1), detergents are amphipathic molecules that can spontaneously self-associate to form largely spherical micellar structures when introduced to aqueous solutions above their critical micellar concentration, or "CMC" for short (Garavito and Ferguson-Miller, 2001).

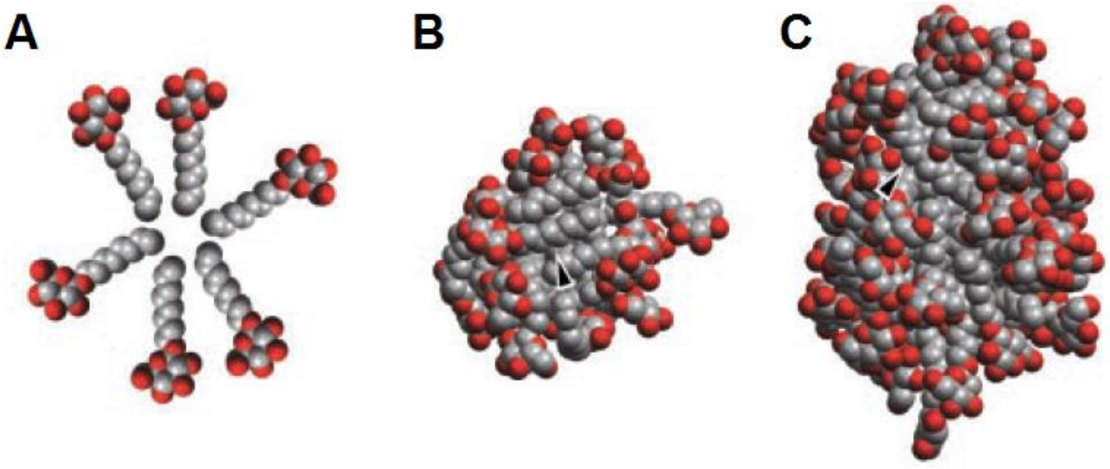

Figure 1.1.3.1. Models of D-octylglucoside monomers and micelles, depicting both their carbon (grey) and oxygen atoms (red): A) Individual detergent monomers; B) A 20-monomer micelle; C) A 50-monomer micelle. Detergent micelles are seldom perfectly spherical and instead assume non-uniform cluster-like shapes, as derived from molecular dynamics (MD) simulation data. Since in actuality the polar head groups of individual monomers do not effectively cover the entire micellar surface in an orderly fashion, some of the alkyl chains also become exposed to the solvent at certain times (black arrows) (adapted from Garavito and Ferguson-Miller, 2001).

The CMC represents the minimal concentration at which individual detergent monomers can self-assemble into micelles and fulfil their role as surfactants, lowering the surface tension between different interfaces (e.g. liquid-solid). A multitude of factors influence the CMC of a detergent, including the ionic strength, pH and temperature of the aqueous solution, along with the length of the alkyl chain (i.e. longer chains reduce the CMC) and the number of double bonds and branch points present in the monomer structure (i.e. higher double bond and branch point numbers increase the CMC) (Seddon et al., 2004). When used for the purification of membrane protein targets, detergents are generally present in the buffers used to equilibrate the high-affinity chromatography columns at concentrations 2-3× greater than their CMC, in order to ensure that free detergent micelles will always be available in sufficient numbers to prevent membrane proteins from becoming unstable upon delipidation (Kunji et al., 2008).

Detergents are regularly classified according to the chemistry of their head groups, either as ionic (i.e. anionic or cationic), non-ionic or zwitterionic (i.e. both anionic and cationic) (Garavito and Ferguson-Miller, 2001), and it is through their unique structural and functional properties that they are able to bind other hydrophobic surfaces (Seddon et al., 2004). Since lipids are essentially surfactants as well, detergents can also be used as lipid bilayer mimics when isolating membrane proteins from their native environment during purification.

Upon their solubilisation and the removal of surrounding membrane lipids, the hydrophobic areas of membrane proteins – which are normally shielded from the aqueous phase by the lipid bilayer – become enveloped in a protective detergent micelle which renders them soluble as protein-detergent complexes (Garavito and Ferguson-Miller, 2001). In an ideal scenario, detergent-mediated solubilisation would preserve not only the structural properties, but also the *in vivo* function of a membrane protein target. Unfortunately, this is by no means a simple process, as using an unsuitable detergent or even non-optimal amounts of a suitable detergent can both hinder membrane protein solubilisation (le Maire et al., 2000).

This is the reason why "milder" (i.e. less denaturing) detergents are better for certain membrane protein studies than other, "harsher" (i.e. more denaturing) ones. Two parameters that greatly influence the mildness or harshness of a detergent are the length of its alkyl chain (Kunji et al., 2008) and the chemistry of its head group (Tate, 2010) (Figure 1.1.3.2 overleaf). Whereas short-chain detergents (e.g. octylglucoside) can form micelles around membrane proteins while leaving a larger portion of their hydrophilic areas exposed (Kunji et al., 2008), long-chain detergents (e.g. *n*-Dodecyl β-D-maltoside (DDM)) are better suited for extracting membrane proteins while also preserving their *in vivo* functions as a consequence of their reduced denaturing effect (Tate, 2010).

Similarly, the "harsh" nature of ionic detergents (e.g. sodium dodecyl sulfate (SDS)) explains why they are commonly used in techniques involving denatured proteins, such as polyacrylamide gel electrophoresis (PAGE) (le Maire et al., 2000), despite their highly-efficient membrane solubilisation properties (Seddon et al., 2004). Conversely, "milder" non-ionic detergents (e.g. α-[4-(1,1,3,3-Tetramethylbutyl)phenyl]-*w*-hydroxy-poly(oxy-1,2-ethanediyl) (Triton X-100)) are preferred for more delicate membrane protein reconstitution work, due to their efficacy in solubilising lipid membranes without also denaturing the proteins present in solution (le Maire et al., 2000).

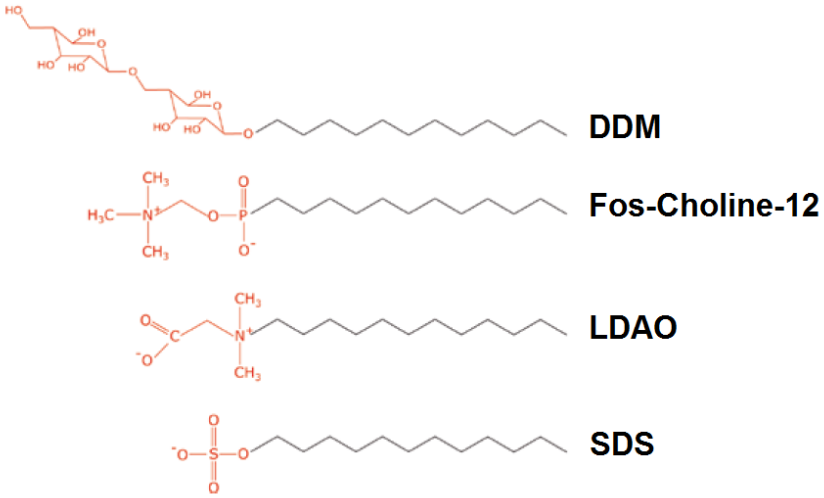

Figure 1.1.3.2. Structures of common detergent monomers, both mild and harsh (from top-to-bottom): *n*-Dodecyl β-D-maltoside (DDM), *n*-Dodecylphosphocholine (Fos-Choline-12), lauryldimethylamine N-oxide (LDAO) and sodium dodecyl sulfate (SDS). While all of these detergents feature similarly-long alkyl chains, their denaturing effects increase from top-to-bottom with the decreasing head group size and the emergence of charged moieties (adapted from Tate, 2010).

In an ideal solubilisation scenario (Figure 1.1.3.3 overleaf), the detergent is added to the native membrane solution and begins its interaction with the lipid phase in non-micellar form (le Maire et al., 2000). The onset of the solubilisation process increases the turbidity of the solution until a maximal detergent saturation point is reached (i.e. R_{sat}), beyond which lipid bilayers cannot preserve their shape (Knol et al., 1998). Following R_{sat}, the turbidity of the solution will steadily fall for the remainder of the process as increasing numbers of detergent monomers interact with the lipid bilayers and the detergent-detergent interactions cause the membrane structure to dissolve (Seddon et al., 2004). This leads to the formation of mixed detergent-lipid micelles and the exposure of the embedded membrane proteins to the detergent micelles that have already formed in solution (le Maire et al., 2000). In the final stage of the process (i.e. R_{sol}), both the lipid component of native membranes and the membrane proteins contained therein become completely solubilised (Knol et al., 1998) and any excess detergent will only serve to further dilute the phospholipids of individual micelles (Seddon et al., 2004). It is important to note, however, that in reality all of these transitions normally overlap and that the optimal destabilisation point of any native membrane depends not only on its constituent lipid species, but also on the solubilising properties of the detergent at hand (le Maire et al., 2000).

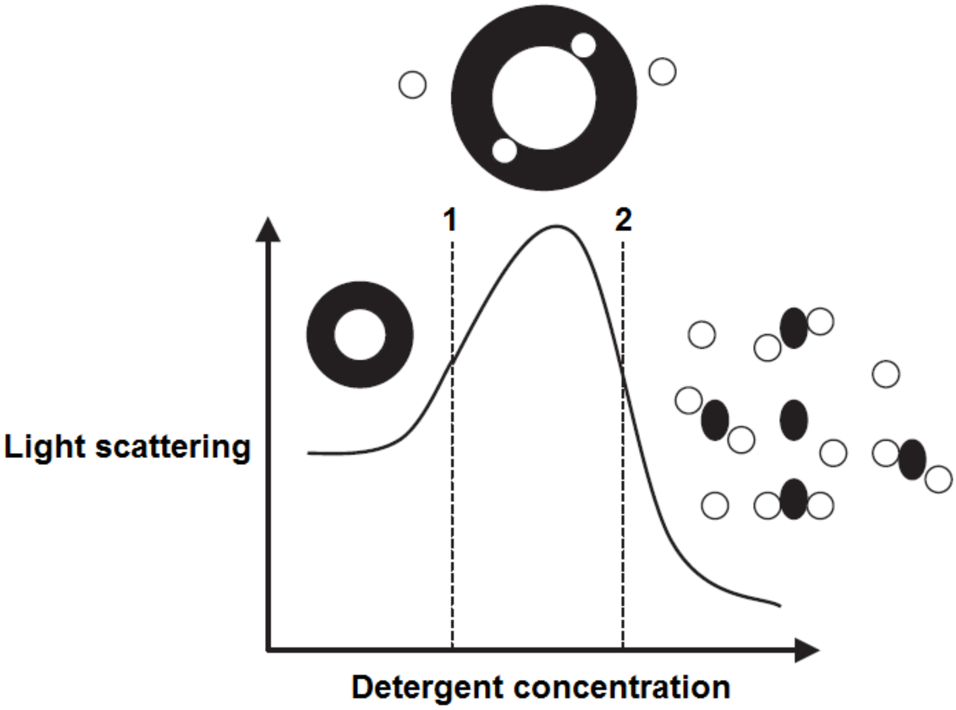

Figure 1.1.3.3. Diagram of native membrane detergent solubilisation (lipid vesicles in black and detergent monomers in white). Increasing the concentration of detergent monomers initially triggers the swelling of the vesicles as detergent molecules infiltrate the lipid bilayers. This is reflected by a linear increase in turbidity when measuring the light scattering of the solution. Beyond point 1, the vesicles steadily become saturated with detergent (R_{sat}), after which the lipid bilayers begin to fall apart into mixed detergent-lipid micelles (i.e. point 2) until all of the lipids have been completely solubilised by the detergent (R_{sol}) (adapted from Seddon et al., 2004).

1.1.4. The drawbacks of membrane protein detergent solubilisation

While detergents are often used in excess during membrane protein purification in order to always keep their concentration above their CMC, their presence in solution post-purification is seldom favourable to the subsequent experimental work (Yang et al., 2014). As such, purified membrane protein suspensions are generally dialysed against plain buffer in order to dilute the detergent below the CMC and cause the micelles to disintegrate into individual monomers, which can then be more easily removed via further dialysis, gel or ion-exchange chromatography or hydrophobic absorption (Seddon et al., 2004). The purified membrane proteins can then either be transferred into a less disruptive detergent solution or alternatively reconstituted into model membranes such as liposomes and thus be separated from detergents altogether. This latter method is actually preferred in most cases since, depending on the type of detergent being used, a significant number of membrane proteins – particularly those originating from higher eukaryotes – can rapidly denature upon their extraction from native membranes, rendering their high-quality purification almost impossible (Bill et al., 2011).

While detergent solubilisation does permit the study of protomeric and self-associated membrane proteins, as well as their interactions with other biomolecules such as ligands or inhibitors (le Maire et al., 2000), even the mildest detergents are ultimately rather poor mimics of native membranes and can still lead to the complete inactivation of the solubilised membrane proteins over long periods of time (Seddon et al., 2004). Furthermore, for the purposes of screening antibody binders against membrane protein targets, the presence of detergents can also result in the occlusion of potential epitopes (Figure 1.1.4.1) and thus ultimately impede the discovery of novel therapeutics (Kunji et al., 2008).

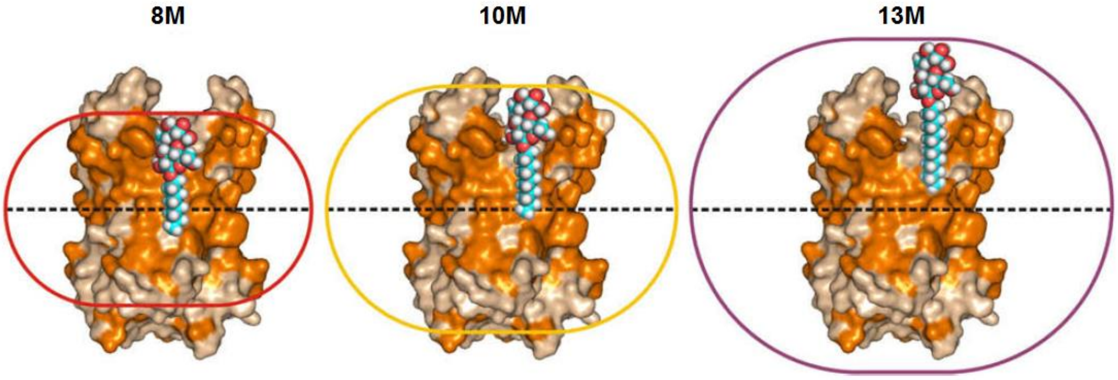

Figure 1.1.4.1. The mitochondrial inner membrane ADP/ATP translocator protein AAC1, solubilised in detergents with different alkyl chain lengths. As the size of the detergent monomers increases, so too can the resulting micelles block potential epitopes on the surface of the protein of interest and thus prevent the binding of antibody candidates (adapted from Kunji et al., 2008).

To this end, alternative methods for presenting membrane proteins towards antibody screening needed to be explored. As previously mentioned, membrane protein targets can alternatively be reconstituted into artificial model membranes post-purification in an attempt at minimising the negative effects of detergent solubilisation. Doing so will not only present them for study or screening in a closer-to-native format that shields their hydrophobic regions inside a lipid bilayer, but will also expose their extracellular loops to the external aqueous environment (and, consequently, to antibody binding) at the same time.

1.1.5. Improving antibody screening against membrane protein targets

The main objective of the current research project was to present membrane protein targets for phage display screening in a novel format that could forgo the presence of detergents during antibody binding. Through the use of solid-supported membrane (SSM) technology, purified membrane proteins were reconstituted into biomimetic model membranes providing a close-to-native environment that not only mimicked the original biological membranes from which the targets originated, but also completely eliminated the need for having detergent present during screening. The means through which this aim was achieved will be discussed throughout the thesis, starting with an overview of the significant progress reported in lipid membrane research throughout the ages.

1.2. Lipid Membrane Research

Cellular membranes represent bioarchitectural structures essential to the existence of all known forms of life (Gunning, 2012). Almost all homeostatic processes rely on the existence of lipid barriers to provide a clear demarcation between the extracellular and intracellular environments, as well as to offer cytoskeletal support, facilitate extracellular signalling, enable intracellular transport of electrolytes and regulate cytoplasmic pH, among many other functions. Due to their overwhelming complexity and the importance of their correct function towards supporting life, substantial research has been channelled over the last century into understanding the mechanisms behind their function and elucidating the means through which malfunctioning cellular membranes lead to pathogenesis. It is this scientific insight that has led to the creation of model lipid membranes – facile biomimetic constructs allowing the study of the multifaceted interactions occurring between different membrane components via their reconstitution into an artificial, yet exceptionally versatile research platform.

1.2.1. An era of lipid membrane research

Inquiries into the properties of lipid membranes began millennia ago with the simple observation of single molecule lipid film formation at the interface between air and a body of water. Films of oil floating on water were actually first described in cuneiform on Babylonian clay tablets as a form of divination. The practice was still popular by the time of the ancient Greeks, who termed it "lecanomancy" from *lekami*, meaning "bowl" and *manteia*, meaning "divination" (Tabor, 1980). Lecanomancy proved to be so widespread that even the Japanese were no strangers to the practice. In fact, the Nippon civilization was credited with the earliest technical application of lipid surface films through the old art of *sumiganashi* or "ink-float", where Japanese ink – *sumi*, harbouring a significant lipid content – was dropped into a bowl of water and then gently blown across its surface in order to create fantastical shapes of great mystical importance (Dynarowicz-Łątka et al., 2001).

CHAPTER 1 – PROJECT AIM AND INTRODUCTION

Since ancient times, fishermen, sailors, merchants and other seafarers have reported the calming effects oil spreads have on stormy seas and these have even been described in the works of great philosophers such as Plutarch, Aristotle and Plinius (Fulford, 1968). However, the scientific investigation of the mechanisms behind this favourable property of lipid films only began approximately two millennia later, when polymath and Founding Father of the United States, Benjamin Franklin, performed the Clapham pond experiment in 1774 so as to witness this curious phenomenon for himself. In his reports, Franklin noted that “the oil, though not more than a teaspoonful… spread amazingly… making all that quarter of the pond, perhaps half an acre, as smooth as a looking glass” (Gaines Jr., 1983). In the years since, Franklin’s experiment has been credited as the first quantitative observation of the effects lipid films have on water surface tension (Dynarowicz-Łątka et al., 2001).

The molecular study of oil film spreads began more than a century later, following the kitchen experiments of then 20-year-old Agnes Pockels. Throughout her career as a German Chemistry pioneer, she performed systematic studies on the relationship between oil layer compression and water surface tension by spreading oil films of varying thicknesses in water-filled troughs (Gaines Jr., 1983). Pockels observed that water surface tension dropped rapidly when the suspended oil film was compressed by a certain ratio (Pockels, 1891) and disseminated her observations in the now-famous correspondence with British physicist and Nobel laureate Lord Rayleigh, who proposed that the films were monomolecular in nature (Gaines Jr., 1983). Lord Rayleigh was also the first to quantitatively investigate water surface tension reduction following olive oil application and to provide a thickness estimate for the oil film itself, namely 16 Å (Dynarowicz-Łątka et al., 2001). Agnes Pockels’ observations led Lord Rayleigh to believe that, below a certain compression ratio, oil molecules were naturally pressed together and his hypothesis later on became the premise for the subject of monomolecular lipid film study.

The scientific evidence supporting Lord Rayleigh’s theory was only provided years later by the American chemist and physicist Irving Langmuir, who characterised the orientation of lipid molecules at the air-water interface and showed how monomolecular layers could be transferred onto solid substrates (Gaines Jr., 1983). Working alongside his fellow compatriot and physicist Katharine Burr Blodgett, Langmuir first demonstrated multilayer film formation via the sequential transfer of lipid monolayers onto a solid surface (Dynarowicz-Łątka et al., 2001). These structures have since been referred to as “Langmuir-Blodgett” films and were shortly thereafter used in a key experiment which gave birth to our contemporary structural vision of a biological membrane (Bagatolli et al., 2010).

The bilayer structure of biological membranes was actually established years later in 1925, when Dutch physicians Gorter and Grendel compared the total surface areas of lipid extracts obtained from human, rabbit, dog, guinea pig, sheep and goat erythrocyte cell membranes with the average surface areas of whole blood cells. Discovering that the former were curiously double the size of the latter, the two researchers concluded that the “layer of lipoids” surrounding blood “chromocytes” was in reality “two molecules thick” (Gorter and Grendel, 1925). However, even with all of these scientific findings accrued by the onset of the 20th century, the existence of proteins expressed in biological membranes still remained completely unknown (Bagatolli et al., 2010).

1.2.2. The Davson-Danielli-Robertson cell membrane model

It was only in 1935 that James Frederic Danielli and Hugh Davson, from the Department of Biochemistry at University College London, drew attention to the protein content of cellular membranes through their thermodynamic studies performed on plant, erythrocyte and marine egg cells. Judging from their findings, the two suggested a cell membrane model where globular proteins were attached to the surface of the membranes (Figure 1.2.2.1), forming a protein “film” which was capable of selectively allowing the passage of “non-lipoid” molecules of different sizes through an otherwise impermeable “lipoid” bilayer.

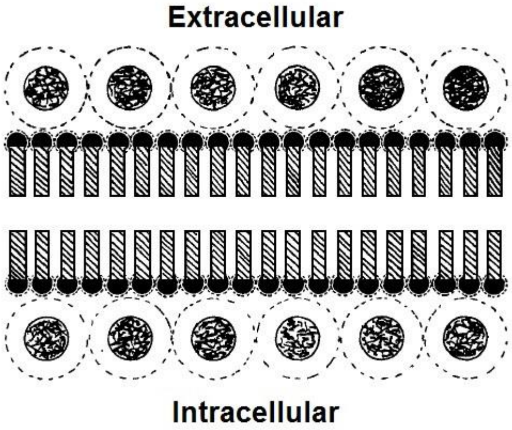

Figure 1.2.2.1. The Danielli-Davson cell membrane model, depicting a lipid bimolecular layer to which a film of globular proteins is attached on both the extra- and intracellular side of the cellular membrane (adapted from Danielli and Davson, 1935).

The two proponents of the eponymous cell membrane model also theorised that, unless the lipid content of other cell types was of a radically different composition, the presence and activity of their associated protein film would remain the same (Danielli and Davson, 1935). Twelve years later, David J. Robertson, from the Department of Anatomy at University College London, confirmed Danielli and Davson's assumptions through his research into the ultrastructure of frog peripheral nerve fibres (Robertson, 1957). Robertson's electron micrographs showed two individualised "dense lines" in frog Schwann cell and neuronal axon membranes instead of just the one suggested until then, each measuring less than 100 Å in thickness and being separated by a "light interzone" almost 150 Å wide (Figure 1.2.2.2).

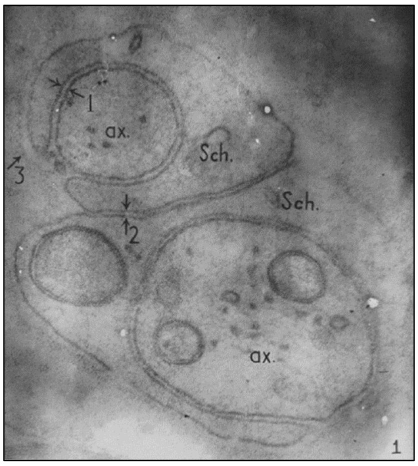

Figure 1.2.2.2. Electron micrograph of two Schwann cells (Sch.) enveloping two frog peripheral nerve axons (ax.). The arrows (1, 2) indicate the bilayer nature of the cell membranes (~75 Å in thickness), as well as the "interzones" (~145 Å in thickness) present at the axon-Schwann (1) and Schwann-Schwann (2) cellular interfaces (adapted from Robertson, 1957).

According to Robertson (1957), all cellular membranes featured a bimolecular lipid "leaflet" containing embedded "associated proteins" – a construct which he coined the "unit membrane" (Figure 1.2.2.3). Robertson's findings ultimately led to the emergence of the "Davson-Danielli-Robertson" (DDR) cell membrane model, which became widely-accepted in membrane research between the 1960s and 1970s (Stoeckenius, 1962).

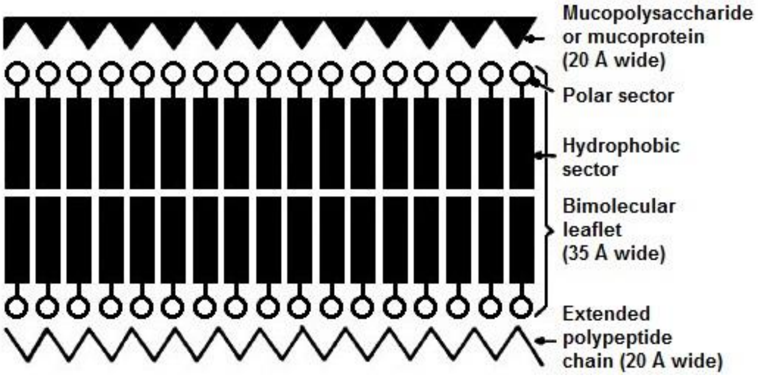

Figure 1.2.2.3. Diagrammatic representation of J. D. Robertson's "unit membrane" hypothesis (adapted from Green and Perdue, 1966).

The early 1960s provided researchers with another equally important discovery. In 1964, light was shed upon the nature of lipid bilayer formation through the work of Bangham and Horne, from the Agricultural Research Council Institute of Animal Physiology in Cambridge, UK, who reported the formation of "spherulites" (i.e. liposomes) comprised of "many hundreds" of concentric lecithin lamellae (Figure 1.2.2.4) while studying lipid phase structures under the electron microscope (Bangham and Horne, 1964).

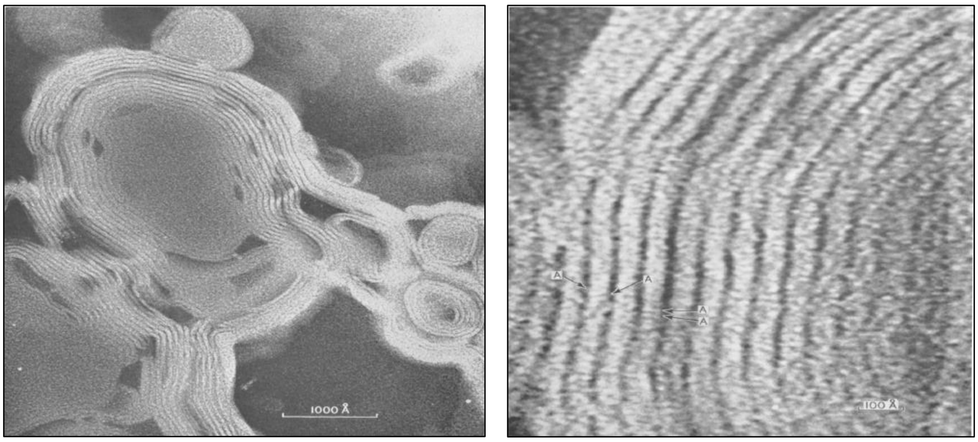

Figure 1.2.2.4. Bangham and Horne's electron micrographs of the discrete structure of the cell membrane. Left: a negatively-stained preparation of ovolecithin, treated by ultrasound and mixed with 2% (w/w) potassium phosphotungstate, depicting multi-lamellar lipid "spherulites" (i.e. liposomes). Right: enlargement of the lamellar section of a "spherulite" with arrows highlighting rod-shaped elements lying at right angles to the axis of the lamellae, presumed to be individual lipid molecules (adapted from Bangham and Horne, 1964).

Bangham and Horne used potassium phosphotungstate as a negative stain for their electron micrographs due to its low surface reactivity and its capability of preserving lipid structures in a rigid, electron-dense setting that allowed for very high resolution images of the discrete membrane structures to be taken.

1.2.3. The Benson-Green cell membrane model

Two years later, A. A. Benson, from the Department of Marine Biology at the University of California, USA, was one of the first to challenge the universal applicability of the DDR cell membrane model by studying plant chloroplasts instead of neuronal or glial cells (Benson, 1966). Benson employed the "freeze-etch" technique used previously in the study of osmium tetroxide (OsO_4)-stained chloroplast sections under the electron microscope (Bagatolli et al., 2010) and deduced that plant chloroplast membranes featured lamellae that could be clearly divided into individual lipoprotein subunits, or "quantasomes", containing four surfactant lipids arranged in a mosaic-like pattern (Figure 1.2.3.1 overleaf).

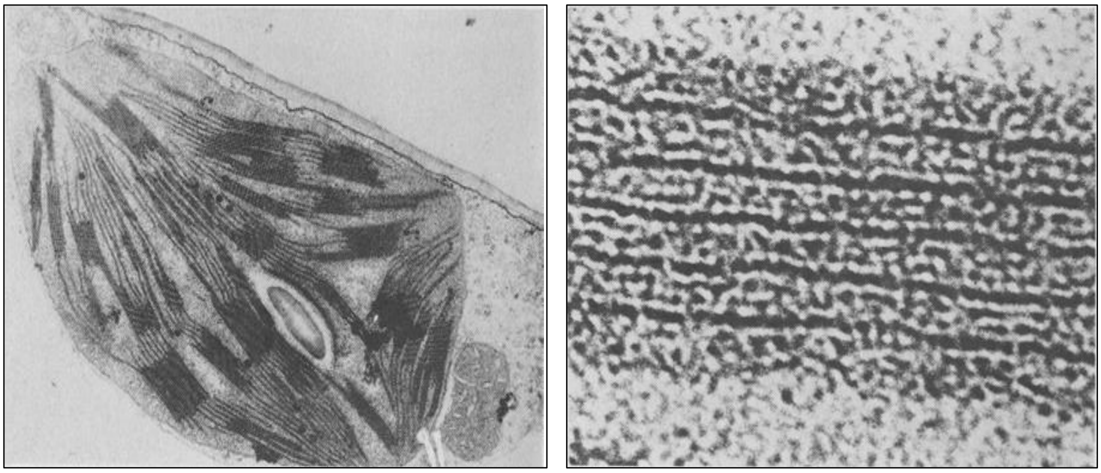

Figure 1.2.3.1. Benson's electron micrographs of the discrete structure of plant chloroplasts. Left: a bean leaf stained with osmium tetroxide (OsO_4), depicting chloroplasts with lamellar structures and bilayer cellular membranes. Right: enlarged chloroplast lamellae section, depicting multiple repeating lipoprotein subunits (adapted from Benson, 1966).

Two other researchers, David E. Green and James F. Perdue, contemporaries of Benson's from the Institute of Enzyme Research at the University of Wisconsin, USA, also commented on the limitations of the DDR cell membrane model – more specifically, the bond between the phospholipid bilayer and the attached protein film, which were until then believed to be held together primarily by electrostatic forces occurring between two types of molecules of essentially separate phases (Green and Perdue, 1966). Green and Perdue reviewed several membrane studies of their time, such as Green and Fleischer (1963) – on the mitochondrial energy coupling system and its oxidative phosphorylation pathways, Brown (1965) – on the membranes of the halophilic (i.e. "salt-loving") bacterium *Halobacterium halobium* and even Benson's earlier work on plant chloroplast membranes and their lipid molecule content (Benson, 1964), ultimately concluding that the predominant binding between the phospholipid and protein constituents was not electrostatic, but rather hydrophobic in nature, implying a strong connection between the hydrophobic regions of membrane proteins and the hydrocarbon residues of phospholipid molecules (Bagatolli et al., 2010).

Furthermore, Green and Perdue uncovered through the work of Fleischer et al. (1962) that this hydrophobic interaction was so strong that, upon using bile salts to disassociate the lipoprotein complexes of the mitochondrial electron transfer chain, the lipid-protein stoichiometry in the separated complexes was left undisturbed. Fleischer et al. (1962) also observed that the electron transfer complexes of the inner mitochondrial membrane lost their capacity for integrated electron transfer following their disassociation from the lipid bilayer, only to regain this property when the lipids were reintroduced. This finding helped underline the importance of lipid molecules towards the correct function of membrane proteins. Green and Perdue assumed this was due to the nature of the hydrophobic interactions occurring between the lipids and proteins, theorising that lipid molecules could influence the conformation of protein molecules to such an extent as to prevent their function upon their removal (Green and Perdue, 1966). Nevertheless, the reviewers agreed with Robertson's "paucimolecular" unit membrane, concluding that it was "highly probable" that all biological membranes consisted of smaller, repeating membrane units. Robertson's theory was ultimately confirmed through studies such as Green et al. (1967) – on the individual complexes of the mitochondrial electron transfer chain and the membrane structures of rat liver mitochondria, spinach chloroplasts, as well as bovine heart, photoreceptor and liver microsomal cells.

However, at the beginning of the 1970s, the DDR and Benson-Green cell membrane models came under new scrutiny when Walther Stoeckenius and Donald M. Engelman, from the Cardiovascular Research Institute at the University of California, USA, published a comprehensive review of all of the proposed biological membrane models available to that date, presenting each of their limitations in great detail and supporting their claims with exhaustive scientific evidence (i.e. approximately 300 individual literature sources). Stoeckenius and Engelman (1969) concluded that even though the lipid bilayer model provided the best approximation of the main structural principles of biological membranes, there was still no model in existence that could explain all of the experimental data determined from different types of biological membranes. At a time when no immediate consensus could be reached upon a more general representation of cellular membranes, the emergence of "the fluid mosaic model" (Figure 1.2.3.2) – published by S. J. Singer and Garth L. Nicolson in 1972 – was unanimously heralded as a "second wind" in biological membrane research (Singer and Nicolson, 1972).

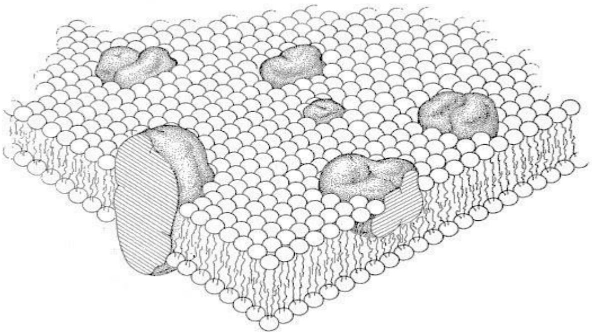

Figure 1.2.3.2. An integral and peripheral membrane protein mosaic embedded within a lipid matrix, or "the fluid mosaic model of the structure of cell membranes" (adapted from Singer and Nicolson, 1972).

1.2.4. The fluid mosaic cell membrane model

More than 40 years have passed since this model was proposed and it is still considered a central paradigm of biological membrane research even today (Bagatolli et al., 2010). The fluid mosaic representation was the first model that could be applied to a majority of biological membranes, be they "functional" (e.g. intracellular, mitochondrial, plasmalemmal or chloroplast membranes) or otherwise (e.g. myelin sheaths, animal virus membranes, etc.) (Singer and Nicolson, 1972). Not just that, but the model also respected many experimental observations, such as the limited transverse mobility of lipid molecules, the possibility of lateral diffusion for all membrane constituents, the permeability capacity of the membrane, as well as the differences between the various categories of membrane proteins (e.g. integral, α-helical, globular or peripheral) and those between discrete membrane phase transitions (Bagatolli et al., 2010). While the fluid mosaic model was at times dismissed as a generalised representation of proteins "floating as icebergs in a sea of lipids" (Luckey, 2008), lateral mobility in a pseudo-two-dimensional liquid is but one of the physical properties accounted for by this cell membrane model. The thermodynamics underlying the hydrophobic and hydrophilic interactions occurring between different molecules, the multiple types of non-covalent binding contributing to the macromolecular membrane structure (e.g. hydrogen bonding, electrostatic forces, dipole-dipole interactions), the predominance of protein molecules over other major classes of membrane constituents, such as oligosaccharides, as well as their role in sustaining a complex homeostatic and structural balance, are equally represented and respected by the fluid mosaic cell membrane model (Singer and Nicolson, 1972).

Throughout later years, multiple improvements to the fluid mosaic model were proposed, usually after new studies uncovered specialised features of specific membrane types (Bagatolli et al., 2010). Notable examples include the refinements brought by Marčelja (1976) and Israelachvili (1977), which took into account additional membrane properties such as folding, pore formation and variations in lipid bilayer thickness. These refinements contributed shortly thereafter to Mouritsen and Bloom's "mattress" cell membrane model (Mouritsen and Bloom, 1984), based on their deuterium NMR studies. The mattress model suggested that the interactions between membrane-bound lipid and protein molecules gave way to positive Gibbs energy due to localised variations existing in the hydrophobic regions of each molecule. This, in turn, caused interfacial tension and resulted in the capillary-force-mediated aggregation of specific types of lipids around protein molecules, forming mattress-like structures (Figure 1.2.4.1).

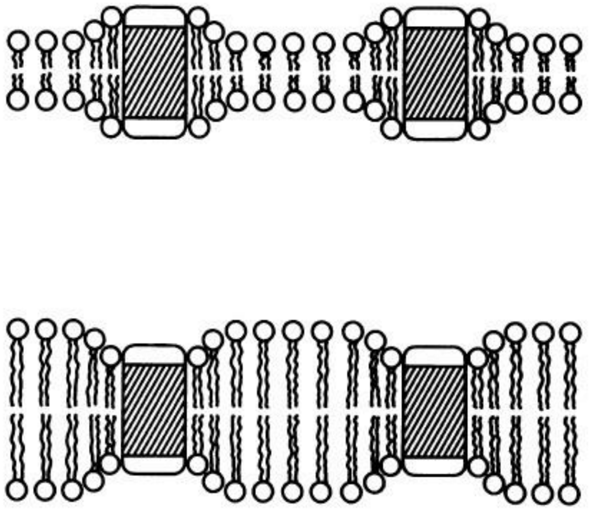

Figure 1.2.4.1. Examples of cell membranes embedding integral proteins that do not match the equilibrium thickness of the surrounding lipid bilayers and thus resemble the appearance of a mattress (adapted from Mouritsen and Bloom, 1984).

The mattress cell membrane model, together with Sackmann’s principle for trigger processes (Sackmann, 1995a) – implying that a majority of membrane processes are triggered by a local transient influx of Ca^{2+} ions, such as the one generated by the fusion of synaptic vesicles with the neuronal presynaptic membrane – highlighted the emerging importance of modelling membrane regions differently around integral membrane proteins (Mouritsen, 2011b). Sackmann also notably provided further refinements to the fluid mosaic model, which included the incorporation of the glycocalyx and the cytoskeleton, both of which attach to cell membranes and play important cytoarchitectural and homeostatic roles (Sackmann, 1995a). Together with several other lipid biophysicists, Sackmann anticipated the impact lipid-protein interactions occurring in separate membrane regions had towards membrane-mediated processes (Shimshick and McConnell, 1973), basing his assumption on the lateral segregation of lipids under specific temperatures and compositions giving rise to the formation of distinct lipid domains with discrete structural properties (Sackmann, 1995b). Even following lengthy discussions regarding alternative membrane models derived from novel experimental data, Sackmann’s observations were largely ignored by the Life Sciences community until Kai Simons and Elina Ikonen (1997) published a seminal paper on the existence of so-called “lipid rafts” within biological membranes – a term coined almost a decade earlier by Simons and van Meer (1988), referencing the glycolipoprotein microdomains characteristic of native membrane organisation. To this day, lipid rafts represent an actively-researched area of cell membrane biology (Mouritsen, 2011a).

1.3. Model Membranes

Native membrane modelling has been known take on many different forms, depending on the examined membrane constituents and the types of assays involved in their study. Some of the most commonly-used models for membrane protein research are outlined throughout the following subsections.

1.3.1. Supported lipid membranes

The simplest model of a lipid membrane is represented by the monolayer formed at air-water or oil-water interfaces, useful for probing the interactions between the lipid components of biological membranes and the multitude of enzymes, solutes, peptides, drugs and other agents that come into contact with their surfaces (Mouritsen, 2011b). Lipid monolayers formed at air-water interfaces can be manipulated and studied with ease in a Langmuir trough (Figure 1.3.1.1), enabling the measurement and quantification of properties such as membrane thermodynamics (Dynarowicz-Łątka et al., 2001).

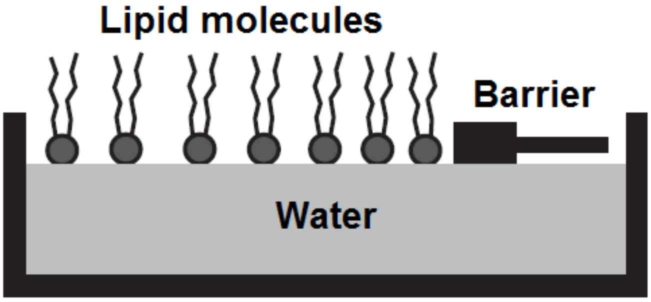

Figure 1.3.1.1. Lipid monolayer formation at the air-water interface in a Langmuir trough (adapted from Mouritsen, 2011b).

More advanced studies, including fluorescence spectroscopy, Brewster-angle microscopy, or X-ray and neutron scattering techniques can also be performed on an aqueous support, while equally benefiting from the transfer of the lipid monolayers onto a solid surface (Mouritsen, 2011b). On the other hand, alternative techniques such as atomic-force microscopy (AFM) require a solid support (e.g. mica or silica) in order to work at all. More complex models, including bilayer lipid membranes, can be formed directly on solid supports via Langmuir-Blodgett or Langmuir-Schaefer transfer (Rubinger et al., 2006), through spin-coated techniques followed by rehydration (Simonsen and Bagatolli, 2004) or by means of lipid vesicle dispersion and lysis on an appropriate hydrophilic substrate, such as gold or silica (Cho et al., 2010). There are also multiple examples of SSMs formed using proteoliposomes created through the reconstitution of purified membrane proteins into liposomes (Granéli et al., 2003), resulting in membrane models incorporating the proteins of interest (Figure 1.3.1.2).

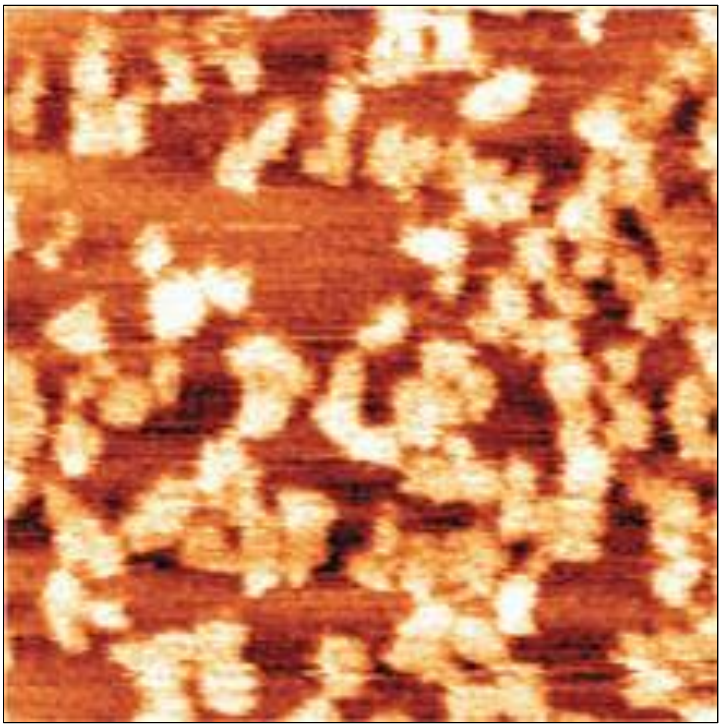

Figure 1.3.1.2. Atomic-force micrograph (100×100 nm) of the lateral structure of an SSM embedding reconstituted aquaporin channels (adapted from Mouritsen, 2011b).

However, studies by both Keller et al. (2005) and Jensen et al. (2007) reinforced the idea that "proximal" SSMs formed in direct contact with solid supports are under significant influence from electrostatic interactions occurring between the membranes and their hydrophilic substrates, which can in turn influence the internal thermodynamics, self-assembly kinetics and lateral organisation of the SSM. Mouritsen (2011b) added that these negative influences could be suppressed to a significant degree through the addition of a spin-coated distal bilayer on top of the proximal one. Knoll et al. (2000) and Tanaka and Sackmann (2005) described another solution, namely the use of ultrathin polymer supports as substrates for lipid bilayer formation. These polymers, mimicking the function of the extracellular matrix, are used to tether and/or cushion the reconstituted membrane proteins so as to not come into direct contact with the solid support and thus allow for their correct incorporation and folding within the SSM. This biological membrane model not only improved the diffusion capability and intrinsic activity of the embedded membrane proteins compared to the "proximal" model, but also preserved their lateral distribution as well (Figure 1.3.1.3 overleaf).

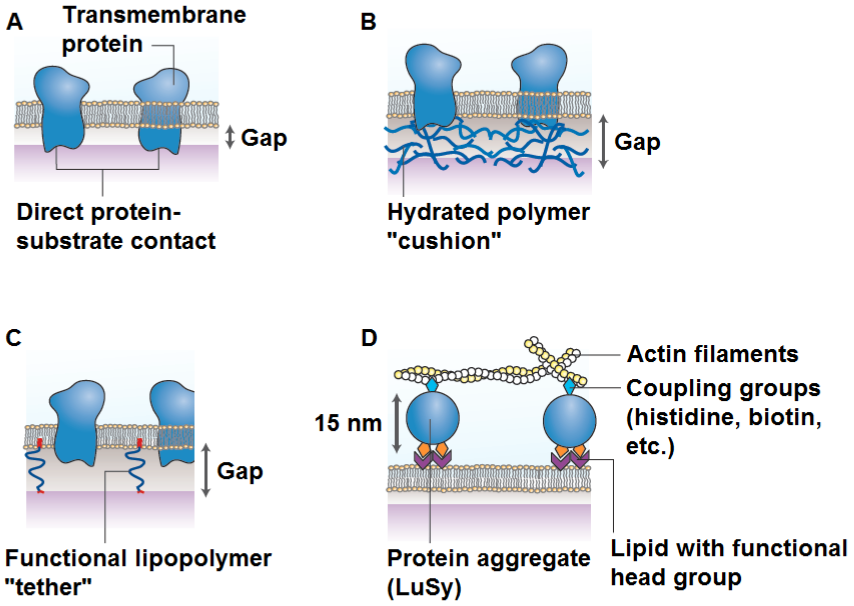

Figure 1.3.1.3. Different types of SSMs embedding reconstituted membrane proteins: A) Proximal SSM, with the proteins coming into direct contact with the substrate; B) Polymer-supported SSM, with the lipid bilayer resting on top of a hydrated polymer "cushion" that prevents the embedded proteins from interacting with the substrate; C) Lipopolymer-tethered SSM, with the lipid bilayer resting on functional lipopolymer "springs"; D) Spaced-out SSM, featuring large macromolecular spacers (here, the bacterial enzyme lumazine synthase (LuSy)) attaching entire protein complexes (here, actin filaments) via His- and Strep-tag coupling groups to the supported membrane (adapted from Tanaka and Sackmann, 2005).

1.3.2. Inserting membrane protein targets into solid-supported membranes

SSMs have proven to be powerful research tools in the hands of cell biologists, yet they have also demonstrated significant potential as remarkably versatile and robust analytical platforms for probing the function of multiple types of membrane proteins (Roder et al., 2011). Membrane protein targets that have already been successfully reconstituted into SSMs include transporters (Scalise et al., 2012), symporters (Newstead, 2011), GPCRs (Serebryany et al., 2012) and voltage-gated ion channels (Li et al., 2012).

Despite the fact that novel protein extraction techniques such as electrophoretic-electroosmotic focusing (EEF) (Liu et al., 2011) have emerged throughout recent years, membrane proteins are still routinely purified by first subjecting native cell membranes to detergent solubilisation, followed by their elution through a high-affinity column (e.g. Ni^{2+}-sepharose for His-tagged targets or streptavidin for Strep-tagged ones, respectively) (Scalise et al., 2012). However, alongside their stand-alone presentation in detergent solutions, purified membrane proteins can be reconstituted into proteoliposomes and then affixed onto solid supports, embedded within SSMs.

Two of the most successful membrane protein reconstitution methods involve the limited use of detergent solubilisation throughout their incipient stages, followed by the partial- or complete removal of detergent from solution after re-lipidation. The first method involves mixing detergent-solubilised membrane proteins with a liposomal solution and then gradually reducing the concentration of detergent below its CMC via repeated dilution so that the micelles shielding the membrane proteins fall apart and the latter integrate into the liposomes instead (Seddon et al., 2004). Conversely, the second method begins with the destabilisation of pre-formed liposomes using a non-ionic detergent (e.g. DDM or Triton X-100) titration to R_{sat} in order to render them more permeable to protein integration, followed by an incubation with the purified membrane proteins and the subsequent removal of detergent from the final solution via column chromatography, repeated dialysis or incubation with detergent-absorbing beads (e.g. Bio-Beads®) (Knol et al., 1998). While both of these methods effectively reach the same end-point (i.e. creating a proteoliposomal suspension with minimal or no detergent present), it is important to note that both processes are also completely reversible should more detergent be reintroduced into either solution (Seddon et al., 2004).

In order to better support the integration of purified membrane proteins, the liposomes used for reconstitution work should first be extruded through a porous polycarbonate membrane into unilamellar vesicles of the particular size needed for accommodating the protein targets of interest (Figure 1.3.2.1). Liposome diameters can therefore range from less than 100 nm (i.e. small unilamellar vesicles (SUVs)), to 1 μm (i.e. large unilamellar vesicles (LUVs)) and up to 100 μm (i.e. giant unilamellar vesicles (GUVs)), depending on the assay and membrane proteins found under examination (Wesołowska et al., 2009).

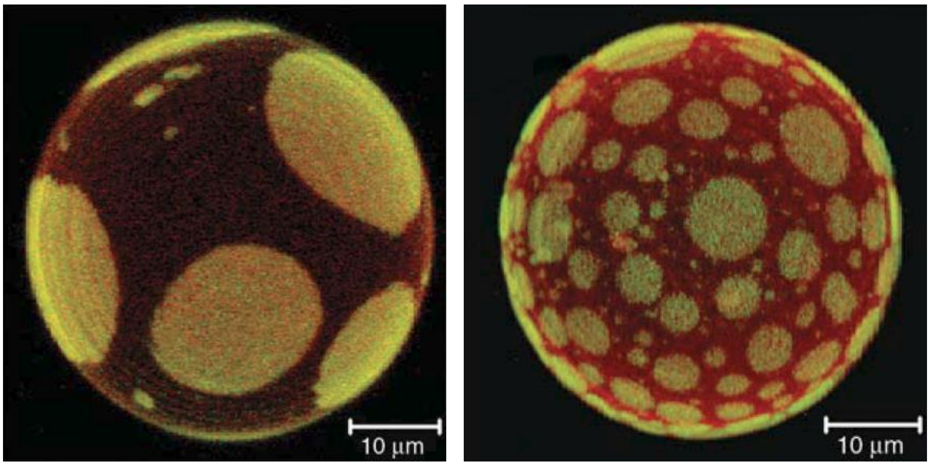

Figure 1.3.2.1. Fluorescence microscopy images of giant unilamellar vesicles (GUVs). Left: GUV formed using a DOPC/DPPC/Chol lipid mixture (2:2:1 (w/w) ratio). Right: GUV formed using native pulmonary surfactant mixtures (adapted from Mouritsen, 2011b).

Furthermore, since cellular membranes never comprise of singular bilayer-forming lipid species, mixtures of synthetic lipids are routinely used in the creation of liposomes so as to better mimic the membrane environment native to the protein targets, which normally features both bilayer- and non-bilayer-forming lipids. Two of the most widely-used lipids for modelling native membranes in a laboratory setting are 1,2-Dioleoyl-*sn*-glycerophosphocholine (DOPC) – a fluid lamellar bilayer-forming lipid – and 1,2-Dioleoyl-*sn*-glycerophosphoethanolamine (DOPE) – a non-bilayer-forming lipid whose presence complements the hydrophobicity of individual monolayer leaflets (Seddon et al., 2004).

Proteoliposomes represent versatile, robust platforms for the study of membrane protein kinetics, including their ability to ferry substrates of biological importance across lipid membranes (Nordlund et al., 2009). However, in order to maximise the success of such functional assays, the proteoliposomes must first be homogenous in size (i.e. should be re-extruded following protein reconstitution) and the reconstituted proteins should be embedded as evenly and equidirectionally as possible throughout the entire vesicle population. At the same time, the permeability of the lipid bilayer component towards the examined substrate should preferably be close to zero (Seddon et al., 2004).

Unfortunately, one of the main detriments of the proteoliposomal membrane model is that the orientation of the purified membrane proteins cannot be controlled during the reconstitution process, thereby leading to the formation of vesicles embedding both the correct and opposite orientations in equal measure (Schadauer et al., 2015). This limitation not only renders proteoliposomes as rather poor alternatives to live cells or organelles such as mitochondria or chloroplasts, whose membranes naturally feature only correctly-oriented proteins (Trépout et al., 2007), but can also skew the results of functional bioassays towards not accurately representing the full *in vivo* activity profiles of the reconstituted membrane protein targets (Schadauer et al., 2015).

Therefore, instead of directly assaying proteins embedded in a proteoliposomal suspension, one way through which the above issue can be overcome is by using the vesicles to form SSMs embedding the protein targets on a solid support that can be functionalised to favour a specific orientation (Richards et al., 2016). This procedure is not without its own caveats, however, since the amphiphilicity or even mere presence of reconstituted membrane proteins is often detrimental towards SSM formation compared to protein-free liposomes (Trépout et al., 2007). Several solutions were trialled in an attempt at reducing the rather strong non-specific interactions occurring between the hydrophilic extramembranous loops of the reconstituted membrane proteins and their solid supports, including the deposition of proteoliposomes onto polyethylene glycol (PEG)-functionalised surfaces (Wagner and Tamm, 2000), thiolated gold supports (Sévin-Landais et al., 2000) and hydrophilic spacers (Giess et al., 2004). Calcium ions (Ca^{2+}) have also been known to act as good bilayer formation adjuvants (Jass et al., 2000) and detergent-solubilised membrane proteins can also be directly incorporated into pre-formed SSMs by diluting the detergent concentration below its CMC (Salamon et al., 1996).

Alternatively, if the membrane protein targets can be genetically modified to express a high-affinity purification tag (e.g. His- or Strep-tag), then their orientation can also be much more tightly regulated following their deposition onto a suitably-functionalised substrate (i.e. nickel-nitrilotriacetic acid (Ni-NTA)-treated or biotinylated surfaces, respectively) (Ataka et al., 2004). With some membrane proteins, however, such genetic modification can unfortunately be conducive to expression defects and/or purification issues, therefore making a strong case for the development of new surface modifications or bilayer formation techniques (Figure 1.3.2.2) that do not rely on the availability of high-affinity chromatography tags for the oriented immobilisation of membrane protein targets (Trépout et al., 2007).

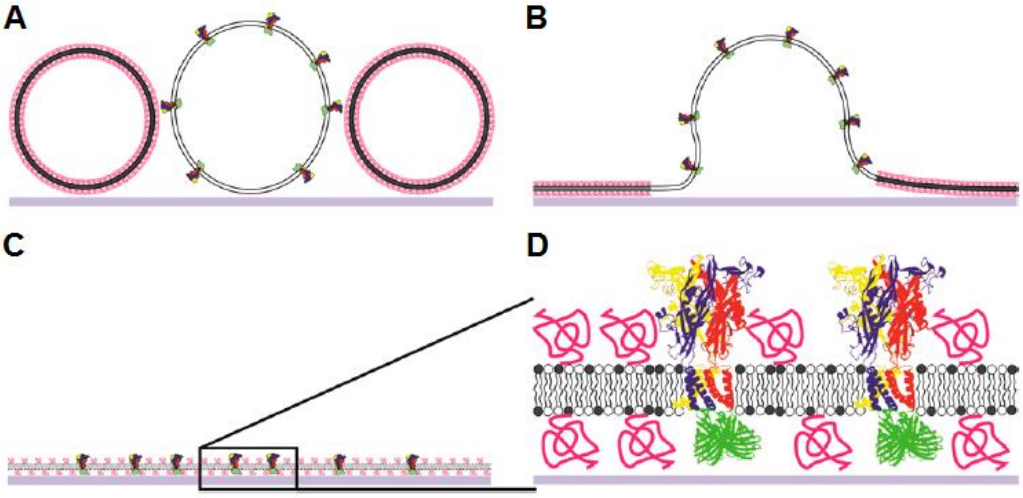

Figure 1.3.2.2. Diagram of the oriented reconstitution of P2X2-Neon membrane proteins into a PEGylated SSM: A) Native membrane vesicles (white) expressing P2X2-Neon are adsorbed onto a glass solid support, followed by the adsorption of PEGylated liposomes (lipids in black, polymers in magenta); B) Once the critical coverage point has been reached, the vesicles begin to rupture and form a continuous lipid bilayer on the glass surface; C) Since the system allows for the free mobility of the bilayer constituents, the P2X2-Neon membrane proteins distribute evenly throughout the newly-formed SSM; D) Magnification of the PEGylated SSM, highlighting the oriented embedding of P2X2-Neon membrane proteins (adapted from Richards et al., 2016).

Fortunately, recent successes observed with native cell membrane "blebs" (i.e. natural proteoliposomes formed via membrane budding following the chemical treatment of live cell cultures) deposited onto glass slides together with PEGylated liposomes (Figure 1.3.2.2 above) have demonstrated that the conserved protein mobility afforded by this system enabled the formation of SSMs embedding evenly-distributed membrane proteins that also preserved their natural *in vivo* orientation intact (Richards et al., 2016).

1.3.3. Current model membrane applications

Ever since their emergence, artificial model membranes have become an essential part of biological membrane studies, providing researchers with a native-like framework for reconstituting membrane proteins into that not only preserves their *in vivo* functions, but also facilitates the use of investigative and characterisation techniques and assays that could not be performed on live cells (Richards et al., 2016). These include quartz crystal microbalance with dissipation monitoring (QCM-D) (Cho et al., 2010), surface plasmon resonance (SPR) (Terrettaz et al., 1993), as well as atomic-force (Morandat et al., 2013), confocal (Korlach et al., 1999), fluorescence (Samsonov et al., 2001), scanning excitation (Dietrich et al., 2001) and total internal reflection fluorescence (TIRF) microscopy (Watts et al., 1986). SSM technology enables all of these high-resolution microscopy imaging techniques to monitor lateral membrane structure organisation and reconstituted protein arrangement on scales as small as a few micrometres or even nanometres (Figure 1.3.3.1).

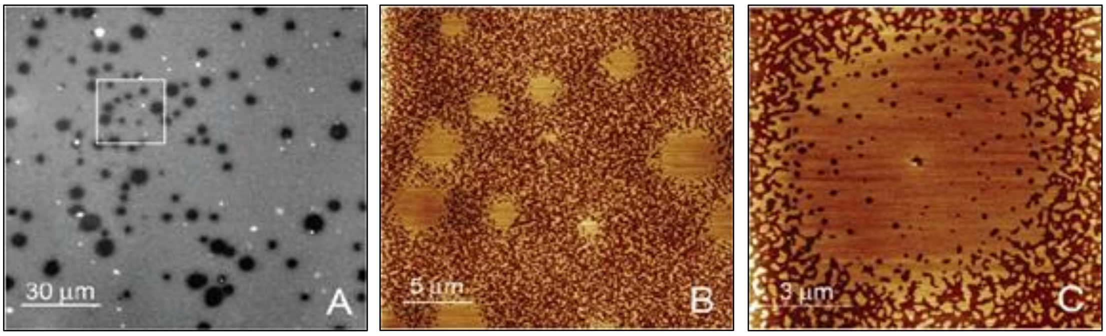

Figure 1.3.3.1. High-resolution microscopy images of different lipid raft domains present in SSMs formed using a DOPC/DPPC/Chol lipid mixture (2:2:1 (w/w) ratio): A) Fluorescence micrograph depicting large condensed domain features as dark spots; B) AFM scan of the region indicated in image A – domain features that were not previously visible via optical microscopy are now revealed; C) Atomic-force micrograph of a single condensed domain. The depicted height difference is 6.5 ± 2 Å, measured in a line scan (adapted from Jensen et al., 2007).

Over the last decade, SSMs have also provided stable and reliable patch clamps for electrophysiological studies (Yu and Groves, 2010) and contributed to the development of membrane array technology. Aiming to fully combine the functionality of native cell membranes with the simplicity and controllability of membrane models embedding reconstituted membrane proteins, SSM arrays can be used to perform antibody binding or competitive ligand displacement assays against membrane protein targets, as well as live cell adhesion assays in a high-throughput manner on an industrial scale, all while allowing both the cellular processes occurring within the membrane and the pharmacodynamics of the test compounds to be examined on a molecular level (Groves, 2002). In addition, plasmonic sensors developed using SSM technology are now capable of detecting and characterising biologically- and pharmacologically-relevant interactions occurring on cell membrane surfaces at similarly diminutive scales (Galush et al., 2009).

1.4. Providing Proof-of-Concept

The current project theorised that SSMs incorporating reconstituted membrane proteins also represented promising test beds for the screening of antibody libraries towards the discovery of binding candidates showing high affinity and specificity for their intended protein targets. The overarching aim of the project was, therefore, to incorporate SSMs embedding a specific membrane protein into the process of phage display screening and then raise antibody mimetics against this target presented in a close-to-native format that was also free from the undesirable consequences of detergent solubilisation. In order to provide proof-of-concept for this newly-proposed phage display screening platform, the bacterial nucleoside transporter NupC was chosen as the membrane protein of interest.

1.4.1. The bacterial nucleoside transporter NupC

Given sufficient extracellular concentrations, nucleosides can normally diffuse freely across *E. coli* outer membranes into the periplasmic space through associated porins. Otherwise, nucleosides can be actively transported inwardly at low concentrations (i.e. <1 nM) via the Tsx/T6 transporter (Hantke, 1976). Conversely, transport across bacterial inner membranes (IMs) is almost always performed against a concentration gradient and, as such, is facilitated by high-affinity nucleoside transport systems such as NupC, NupG and XapB (Loewen et al., 2004). NupC is a H^+-dependent nucleoside symporter commonly expressed in *E. coli* IMs (Miller et al., 2012) that belongs to the concentrative nucleoside transporter (CNT) family and shares a 22-26% amino acid sequence identity with its human analogues – hCNT1, hCNT2 and hCNT3 (Patching et al., 2005). While eukaryotic nucleoside transporters generally comprise of an intracellular N-terminal and an extracellular C-terminal capping 13 transmembrane helices that span the entire width of their native cellular membranes, NupC is believed to encompass only 10 such transmembrane helices arranged in a trimeric format around the central pore (Smith et al., 2005). Owing to its remarkable homology with its eukaryotic counterparts, as well as its biological significance towards correct cellular function (Craig et al., 1994), NupC represents a promising model for studying the transmembrane ferrying of nucleoside analogues bearing therapeutic payloads such as azidothymidine or gemcitabine (Loewen et al., 2004), respectively used in the treatment of life-threatening viral and neoplastic diseases (Thorn and Jarvis, 1996).

Micro-array experiments have demonstrated that NupC and NupG form the two predominant CNT species detected in *E. coli* expression systems under both aerobic and anaerobic conditions (Loewen et al., 2004). While NupC is mainly permeable to pyrimidine nucleosides, it also efficiently concentrates adenosine into the bacterial cytoplasm as a consequence of its evolutionary relation to hCNT1-3, to which the heterocyclic ring of adenosine is an easily-recognisable structural motif promoting the initiation of transmembrane delivery (Patching et al., 2005). Conversely, NupG is only distantly-related to its human counterparts (Patching et al., 2005) and instead shows high affinity for guanosine and inosine, both of which are only very poorly transported by NupC (Craig et al., 1994). Since the above-mentioned human nucleoside transporters represent important targets for drug delivery and therapeutic action (Damaraju et al., 2003), this important distinction ultimately led to NupC becoming the subject of the project at hand and the chosen membrane protein model for testing our proposed novel phage display screening platform against.

1.4.2. Spherical-supported bilayer lipid membranes

Knowing that membrane proteins cannot always be reconstituted into SSMs in their desired orientation (Trépout et al., 2007) and that specific detergents can drastically influence the success of the reconstitution process (Knol et al., 1998), in the case of phage display screening of antibodies or antibody mimetics against membrane protein targets it is crucial to use a platform that embeds as much of the target antigen as possible in order to ensure a maximal selection output featuring all of the potential binding candidates that can be identified from a given binder library. Therefore, in order to improve antigen availability – in this case, the amount of SSM-embedded NupC – and mitigate those scenarios where not enough membrane proteins are reconstituted in their native orientation, spherical-supported bilayer lipid membranes (i.e. SSBLMs) were assembled on commercially-available silica nanoparticles, whose vastly-increased surface areas compared to traditional screening supports (i.e. 96-well plates) enabled the presentation of much larger concentrations of NupC within the same close-to-native format afforded by planar SSMs. Several published studies have already proven the functionality of the SSBLM platform and its significant potential towards replacing live cells in bioassays involving membrane protein targets, even though the preferred nomenclature surrounding these novel particles varies from author to author.

For instance, Nordlund et al. (2009) created SSBLMs by mixing mesoporous silica nanoparticles (550 nm in diameter, 3 nm pore size) together with proteoliposomes formed using a DOPC, DOPE, 1,2-Dioleoyl-*sn*-glycero-3-[phospho-*rac*-(1-glycerol)] (DOPG) and 1,1’,2,2’-Tetraoleoyl cardiolipin (CA) lipid mixture, embedding the reconstituted redox-driven proton pump cytochrome *c* oxidase (Cyt*c*O) from *Rhodobacter sphaeroides*. After 1 hour of mixing at room temperature, the silica nanoparticles were fully enveloped in defect-free SSBLMs embedding 70% of the total Cyt*c*O used for the assay in its native orientation, as determined through the application of reducing agents operating selectively on either the extra- or intracellular side of the native bacterial membrane (i.e. hexaminerutheniumchloride and dithionite, respectively). Furthermore, O_2 consumption measurements performed on the SSBLM particles, along with their subsequent incubation with either valinomycin (K^+ ionophore) or carbonyl cyanide-*p*-trifluoromethoxyphenylhydrazone (FCCP) (H^+ ionophore), also revealed that the embedded Cyt*c*Os preserved their functionality towards O_2 reduction catalysis and transmembrane charge separation while presented in this novel format.

Trépout et al. (2007) focused on the membrane protein OprM – a component of the multidrug efflux pump OprM-MexA-MexB of *Pseudomonas aeruginosa* – and demonstrated its oriented reconstitution in DOPC, DOPG and 1,2-Dioleoyl-3-trimethylammonium-propane (DOTAP) SSBLMs formed on 80- and 175 nm silica nanoparticles. In order to ensure the correct orientation of the SSBLM-embedded OprM, Trépout et al. functionalised the nanoparticles with aminosilane prior to their incubation with OprM-containing proteoliposomes, which ultimately resulted in the protein adsorbing onto the nanoparticles in a single preferred orientation due to the electrostatic interactions occurring between the treated surface and the cylindrical base of the embedded protein. This singular protein orientation could not be replicated using regular, untreated silica nanoparticles as the SSBLM substrate. As shown via cryo-electron microscopy (cryo-EM) (Figure 1.4.2.1 overleaf), the correct orientation of the proteins and the large number of embedded units permitted the further study of OprM in an attempt at preventing the assembly of the OprM-MexA-MexB efflux pump and thus nullifying its undesirable effect towards antimicrobial drug treatments.

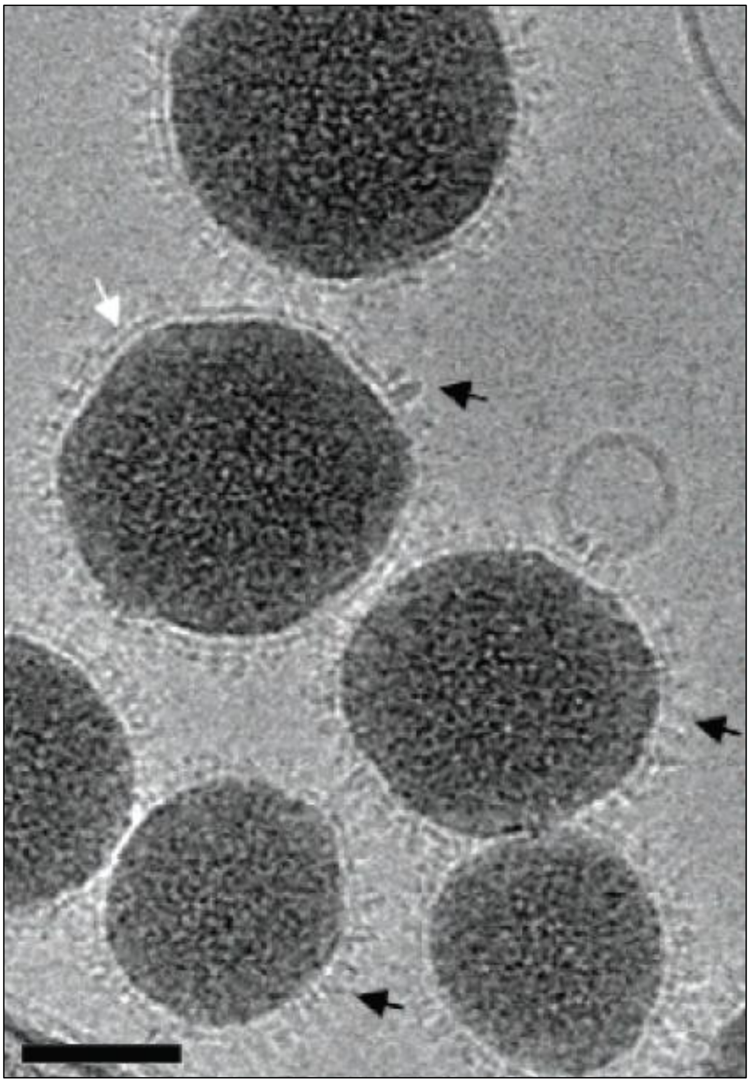

Figure 1.4.2.1. Cryo-EM image of SSBLM-embedded OprM (highlighted by the black arrows). The lipid bilayer component surrounding the nanoparticles was also revealed (indicated by the white arrow). The scale bar represents 50 nm (adapted from Trépout et al., 2007).

Finally, Schadauer et al. (2015) bound C-terminal-His-tagged Cyt*c*O constructs from *Paracoccus denitrificans* to 25 nm Ni-NTA-functionalised silica nanoparticles. After incubating these "composite beads" in the presence of 1,2-Diphytanoyl-*sn*-glycero-3-phosphocholine (DiPhyPC) vesicles, a continuous lipid bilayer was formed in-between the immobilised proteins, resulting in the creation of "proteo-lipobeads" (Figure 1.4.2.2 overleaf). These particles not only embedded Cyt*c*O in a native-like lipid membrane, but also did so strictly in its intended orientation, thus preserving the functionality of the protein towards initiating electron transfer in the presence of reduced cytochrome *c* or via light excitation of its ruthenium (Ru) complexes.

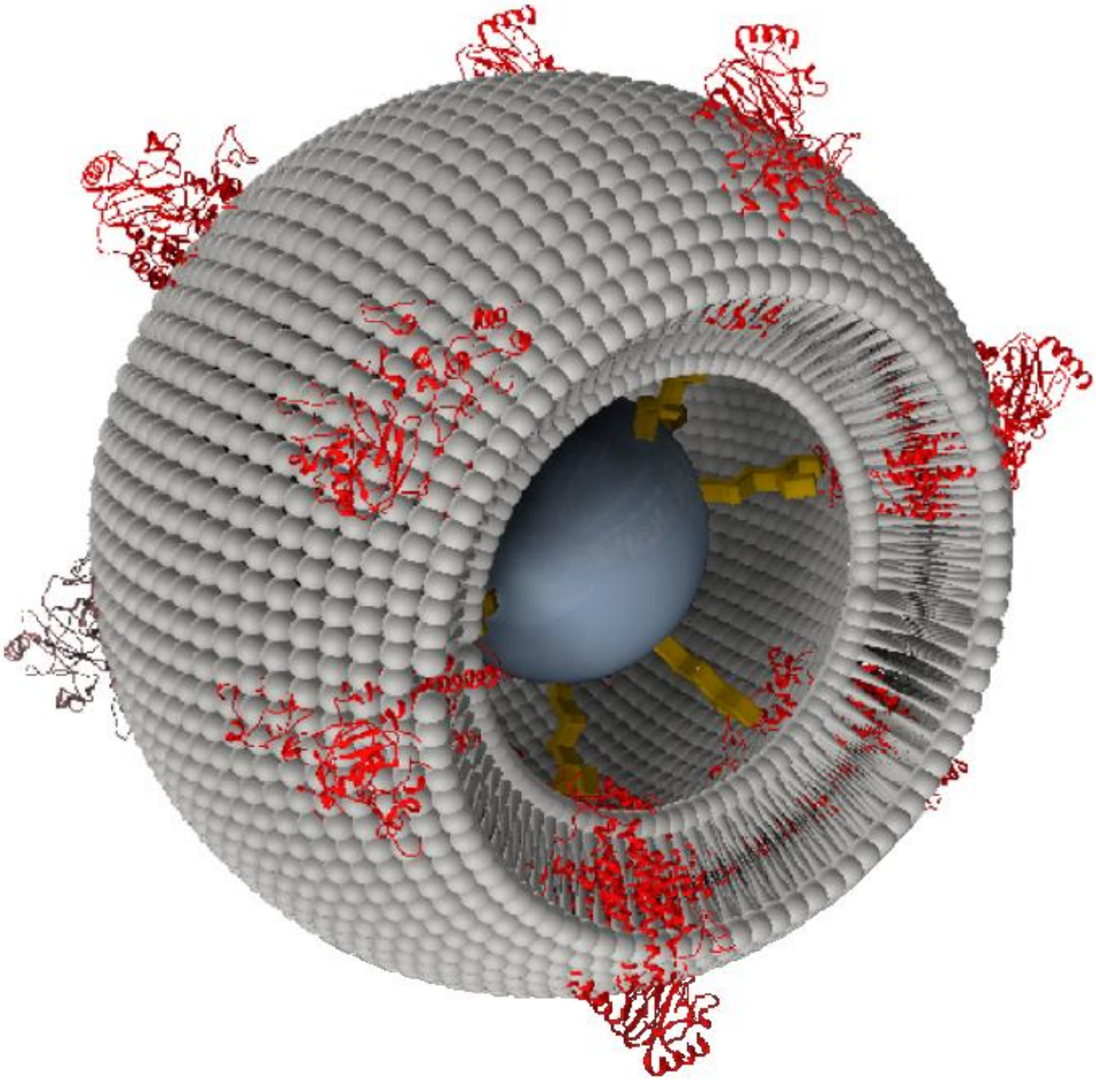

Figure 1.4.2.2. Diagram of a "proteo-lipobead": C-terminal-His-tagged membrane proteins (red) are first bound to Ni-NTA-functionalised silica nanoparticles (blue), after which phospholipid molecules (grey) are inserted in-between the immobilised membrane proteins to form the SSBLM lipid component (adapted from Schadauer et al., 2015).

The examples presented in the current subsection served to demonstrate the significant potential of the SSBLM platform towards the development of functional bioassays for the study of membrane protein targets. The formation of our proprietary NupC-embedding SSBLMs on silica nanoparticles will be described in Chapter 4, following an overview of the techniques involved in their characterisation and quality-assessment presented in the upcoming Chapter 2. So as to aid readers in following through the rather complex method development process, an illustrative summary of the overall project aims, as well as an experimental plan for materialising the SSBLM concept can also be found in Figure 1.4.2.3 overleaf.

SSBLM EXPERIMENTAL DEVELOPMENT PLAN

NupC construct expression and purification

- ➢ Choosing double Strep-tagged, His_6-tagged and untagged/wild-type NupC constructs
- ➢ Expressing and purifying NupC from *E. coli* according to established working protocols

↓

Purified NupC transport activity measurement

- ➢ Performing assays to confirm purified NupC *ex vivo* nucleoside transport activity
- ➢ Establishing whether the NupC constructs retained their conformation post-purification

↓

Planar SSM formation and characterisation

- ➢ Investigating model lipid SSM formation on planar silica substrates
- ➢ Testing the formation of planar SSMs embedding reconstituted purified NupC

↓

SSBLM formation and characterisation

- ➢ Determining the saturation thresholds resulting in full coverage of the tested nanoparticles
- ➢ Confirming the correct formation of SSBLMs on 100- and 200 nm silica nanoparticles

↓

Embedding NupC into the SSBLM platform

- ➢ Reconstituting purified NupC into proteoliposome LUVs and then forming SSBLMs
- ➢ Confirming the presence and epitope accessibility of SSBLM-embedded NupC

↓

Testing the SSBLM platform for phage display screening

- ➢ Interrogating antibody-mimetic binder libraries against SSBLM-embedded NupC
- ➢ Using different screening formats so as to compare SSBLMs to traditional methodologies

↓

Identifying and purifying the "lead candidate" binders

- ➢ Aligning the total selection output and establishing binder structural relationships
- ➢ Isolating the plasmids of phage-bound binders and purifying the chosen lead candidates

↓

Determining the success of the SSBLM platform

- ➢ Re-screening the purified lead candidates so as to confirm genuine binding to NupC
- ➢ Assessing the applicability of the SSBLM platform to other membrane protein targets

---

Figure 1.4.2.3. Workflow illustrating the overall project aims and experimental plan for the development of our proposed SSBLM phage display screening platform.

CHAPTER 2

Experimental Techniques

2.1. Quartz Crystal Microbalance with Dissipation Monitoring

At its core, any quartz crystal microbalance (QCM) comprises of a bulk acoustic wave transducer that uses piezoelectric quartz crystal sensors to detect a wide variety of surface interactions. By inducing electromechanical resonations throughout the sensor crystal, a wealth of information can be derived on the biological and physico-chemical properties of the material deposited onto the sensor surface (Tuantranont et al., 2011). In fact, the applications of this technology are so diverse that the term “microbalance” is somewhat of a misnomer, since QCMs can do much more than simply measure subtle changes in adsorbed mass. As will be seen throughout the following subsections, the descriptors “bulk acoustic wave sensor” or “thickness shear mode resonator” might be more appropriate for describing their expansive detection capabilities (Cheng et al., 2012).

2.1.1. Introduction to QCM-D technology

The technical principles underlying modern quartz crystal microbalances with added dissipation monitoring (QCM-Ds) were established through research started in 1976 at Chalmers University of Technology in Gothenburg, Sweden. After nearly two decades of experimentation, the technology was granted a patent in 1995 and Q-Sense AB was founded as a company developing QCM-D instruments a year later (Q-Sense, 2006). Since the launch of Q-Sense’s first commercial microbalance in 1999 (Biolin Scientific AB, 2016a), QCM-Ds have become widely-used research tools in applications as diverse as monitoring live lipid bilayer formation kinetics on a solid support (Richter et al., 2006), performing nanogram-sensitive measurements of molecules binding to a sensor surface (Heller et al., 2015) or investigating the interactions between different nanoparticle species and model cell membranes (Chen et al., 2016). All of these powerful measurement capabilities are made possible through the physical properties of the piezoelectric crystalline quartz that forms the basis of every sensor chip contained within a QCM-D flow cell (Figure 2.1.1.1).

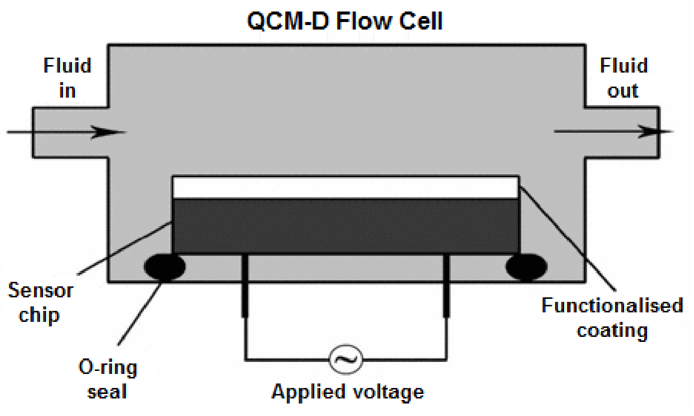

Figure 2.1.1.1. Diagram of a QCM-D flow cell featuring a singular flow module. A freshly-cleaned piezoelectric quartz crystal sensor is rested on a rubber O-ring fixed to the interior of the cell before the experiment is started and the buffers or sample solutions come into contact with its surface (adapted from Heller et al., 2015).

2.1.2. The QCM-D operating principle

The principle through which signals transduce through a QCM sensor is known as the “converse piezoelectric effect”: when a crystalline material is deformed through the application of pressure or torsion in a given direction, electrical charges will be generated on its opposing surfaces. In a QCM setup (Figure 2.1.2.1), the introduction of an alternating current (AC) across the surface electrodes transforms the sensor chip into an equivalent electrical circuit and causes the embedded quartz crystal to alternatingly expand and contract, generating bulk acoustic waves that produce mechanical oscillations at its fundamental resonance frequency (i.e. approximately 5 MHz) (Cheng et al., 2012).

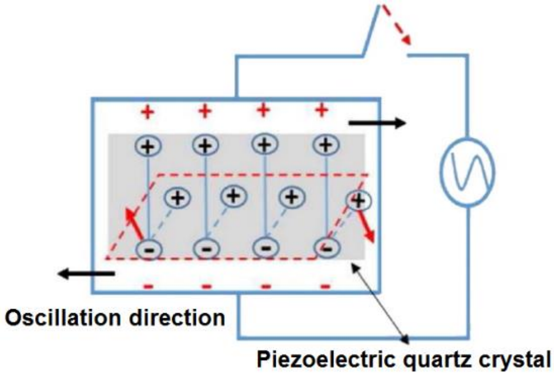

Figure 2.1.2.1. Diagram of the converse piezoelectric effect, illustrating the oscillations and electrical charges propagating through a piezoelectric quartz crystal sensor upon the application of an AC potential. For a coherent measurement to be registered, the charges at the top and bottom of the sensor must oppose one another to create a working electrical circuit (adapted from Chen et al., 2016).

Should an oscillating sensor then come into contact with foreign materials, the shear displacements inside the crystal will cause any adsorbed mass to move lateral of the quartz surface and resonate at a frequency other than its fundamental one. This property renders QCM sensors particularly suitable for conducting ultrasensitive measurements of the mass and viscosity of sensor-bound materials (Chen et al., 2016).

QCMs register frequency changes over a range of odd overtones (i.e. usually from the 3rd to the 13th crystal oscillation harmonic), since the shear displacements required for producing measurable responses are only triggered by acoustic waves propagating through the quartz crystal at odd overtones (Janshoff et al., 2000). While frequency measurements can give an indication of the total mass deposited onto the sensor chip, QCM-D instruments are also capable of determining changes in dissipation, thus offering information on the rigidity of the structure forming on the sensor surface as well. As opposed to frequency measurements, dissipation is measured by interrupting the current applied to the sensor chip and registering the damping oscillations of the resonating quartz crystal. If the deposited structure is rigid, the oscillations will dissipate more slowly and a low dissipation value will be reported. On the other hand, should the deposited structure be flexible, then the oscillations will dissipate faster and a high dissipation value will be registered. It is only when both frequency and dissipation are jointly monitored that changes within the mass adsorbed onto the surface of a sensor can be accurately correlated with the frequency measurement output of a QCM-D instrument (Heller et al., 2015).

2.1.3. QCM-D sensor design and sample loading

Modern microbalances generally use sensors featuring micrometre-thin, disk-shaped quartz crystals that can be cut at different angles depending on the type of induced mechanical vibration they are meant to resonate to, such as face shear mode (FSM), flexural mode (FM) or thickness shear mode (TSM) (Cheng et al., 2012). Given that QCMs generally operate in TSM, the AT-cut (i.e. 35° 10’ from the optical Z-axis of a crystal wafer) represents the preferred choice for the manufacturing of quartz sensor chips, since it allows them to resonate stably at room temperature with little to no frequency fluctuations arising from minor temperature changes (Marx, 2003).

A high surface quality is a vital characteristic of any QCM sensor and thus the underlying quartz crystals are usually optically-polished to produce an extremely smooth contact surface. This is especially important when studying the deposition of soluble materials, for instance, since the solvent can easily infiltrate any crevice found on the surface of a rough crystal and thus generate false-positive frequency changes that can be mistakenly interpreted as adsorbed mass (O'Sullivan and Guilbault, 1999). In order to avoid such anomalous results, most QCM sensors feature hydrophobic surfaces that do not wet easily, but rather attract pockets of air or vacuum, losing less energy in the process compared to sensors with hydrophilic surface chemistries (Janshoff et al., 2000).

The final components of a working QCM sensor are represented by the conducting metal film electrodes sandwiching the top and bottom of the functionalised quartz crystal disk. These normally comprise of evaporated nickel, aluminium, gold, silver or even platinum threads that interface with the contacts located inside a QCM flow module in order to establish a connection with the oscillator circuit of the microbalance (Cheng et al., 2012). Regarding the surface chemistry of QCM-D sensors, there are two main processes through which investigated samples can interact with the exposed quartz crystal – physisorption and chemisorption – and both involve the adsorption of solutes to its contact surface (Table 2.1.3.2).

QCM sensor surface chemistries	**Physisorption**	Hydrophobic bonds
		Ionic bonds
		Hydrogen bonds
	Chemisorption	Self-assembled monolayers
		Plasma-polymerised films
		Photochemistry
		Sensing ionic liquids

Table 2.1.3.2. Examples of QCM sensor surface chemistry interactions. Self-assembled monolayers can offer thiol, amine, amide, protein A, avidin-biotin, concanavalin A, click chemistry and mixed sensor surface functionalisations (adapted from Cheng et al., 2012).

The first of these two solute adsorption methods refers to the simple physical adsorption of materials to the sensor chip via non-specific interactions or non-covalent bonds, its direct advantage being a quick and easy experimental setup that also allows for a certain degree of reversibility given the poor strength of the interactions involved. By contrast, chemisorption relies on the adsorbed mass binding covalently to the sensor surface. Compared to the weak forces involved in the previous process, the considerably stronger covalent bonds aid in the deposition of larger amounts of material at the expense of binding reversibility. Furthermore, while physisorption is essentially disorganised and cannot account for the orientation of the adsorbed material, through chemisorption, test samples can be bound to the sensor surface in their intended orientation – a critically-important feature for experiments involving the creation of tethered supported bilayers or the monitoring of protein-protein interactions, where the accessibility of specific binding epitopes is key (Cheng et al., 2012).

Finally, the external loading of sample materials onto QCM-D sensors can also take one of two forms: gravimetric or viscoelastic. In the case of the former, the force of the crystalline shear gradient will balance out the gravimetric force exerted by the deposited mass on the sensor surface, which in turn will generate a measurable resonance frequency shift that can be calculated via the Sauerbrey equation (Sauerbrey, 1959). Provided that dissipation is either zero or close enough to be negligible, the equation effectively correlates any frequency shift with the mass of material adsorbed onto the QCM-D sensor surface:

$$\boldsymbol{\Delta f_g = -\frac{2f_0^2}{\sqrt{\rho_q \mu_q}} \frac{\Delta m}{A} \qquad f_0 = \frac{v}{2t_q} = \frac{\sqrt{(\mu_q/\rho_q)}}{2t_q}}$$

where Δf_g represents the resonance frequency shift, f_0 – the fundamental resonance frequency, m – the mass of the adsorbed material, ρ_q – the density of the quartz crystal (i.e. 2.648 g cm^{-3}), μ_q – the shear modulus of AT-cut quartz (i.e. 2.947×10^{11} g cm^{-1} s^{2}), A – the area of the sensor, v – the velocity of the acoustic wave and t_q – the thickness of the sensor crystal (Tuantranont et al., 2011).

The gravimetric approach is regularly used to monitor increases in adsorbed layer thickness during physical vapour deposition processes, for instance (Elliot et al., 2014). Another example of gravimetric loading is given by the “dip and dry” method, which involves taking measurements before and after the test material has adsorbed onto the sensor surface and any superficially-bound material has been removed via repeated washing (Cheng et al., 2012). While these approaches to sample loading normally result in the precise measurement of frequency changes – thus being particularly relevant to antibody binding studies – they are not without their drawbacks, represented by their laborious implementation, the impossibility of capturing live data and their susceptibility to humidity, solvent retention and sensor hydration conditions (Arce et al., 2007).

Conversely, during viscoelastic loading, the frequency shifts are triggered by the acoustic-fluid damping effects occurring when a quartz crystal oscillates inside a liquid medium (Tuantranont et al., 2011). One such example is represented by flow injection analysis (FIA), during which small sample volumes are applied to the QCM-D sensor via capillary laminar flow in an attempt at keeping turbulence and any other sensor disturbances originating as a result of fluid dynamics phenomena to a minimum (Cheng et al., 2012). While the real-time monitoring of adsorption kinetics is supported through the use of viscoelastic loading methods, major changes in both dissipation and resonance resistance can be registered due to the way shear waves travel through a non-rigid environment, resulting in potential energy losses. In such cases, where dissipation will almost always be greater than zero, the following equations ought to be used instead:

$$\boldsymbol{\Delta f_v = -f_0^{3/2}\sqrt{\frac{\eta_L\rho_L}{\pi\rho_q\mu_q}} \qquad \Delta D = 2f_0^{1/2}\sqrt{\frac{\eta_L\rho_L}{\pi\rho_q\mu_q}} \qquad \Delta R = \frac{(2\pi\eta_L\rho_L f_0)^{1/2}A}{k^2}}$$

where Δf_v, ΔD and ΔR represent the viscoelastic resonance frequency shift, dissipation factor and resonant resistance changes, respectively, while η_L, ρ_L and k signify the viscosity, density and electrochemical coupling factor of the adsorbate solution (Tuantranont et al., 2011).

2.1.4. The Q-Sense E4 QCM-D setup

As one of the most widely-used QCM-D instruments, the Q-Sense E4 (Figure 2.1.4.1 overleaf) features four QFM 401 flow modules that enable the live frequency and dissipation monitoring of up to four parallel experiments investigating separate molecular kinetics on each of their different sensor surfaces (Biolin Scientific Holding AB, 2016a). More specialised modules, such as the QEM 401 electrochemistry module or the QELM 401 ellipsometry module, can be installed in place of the standard QFM 401 flow modules to confer additional functionalities when performing experiments that require combination measurements to be taken (Biolin Scientific Holding AB, 2016b). The wide variety of different flow modules, combined with a multitude of metal, polymer and chemically-modified sensor surfaces allow for the detection of changes in the viscoelastic properties of the adsorbed materials with nanogram-sensitivity (Biolin Scientific Holding AB, 2016a).

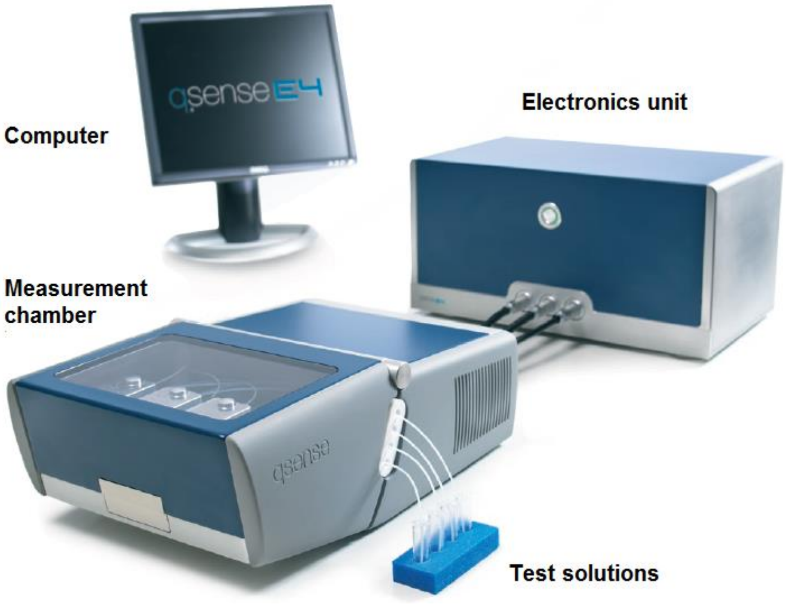

Figure 2.1.4.1. The Q-Sense E4 QCM-D setup, consisting of an electronics unit (responsible for applying the AC potential and the detection of any sensor surface changes), a measurement chamber (containing the four flow modules) and an attached computer (running the measurement software). Capillary tubes connected to a pump unit (not shown here) can deliver up to four separate test solutions to each of the four different sensor surfaces at adjustable flow rates ranging between 50-200 µL per minute (adapted from Biolin Scientific Holding AB, 2016a).

QCM-D experiments benefit from a high degree of stability and detection specificity while offering the possibility of providing real-time data on live and label-free binding kinetics at a relatively low operating cost using easy-to-follow experimental protocols (Tuantranont et al., 2011). The latter can be generally divided into four main steps: 1) sensor cleaning and mounting; 2) buffer and sample solution application; 3) live frequency and dissipation data collection and 4) data analysis. In a typical QCM-D experiment, ozone-cleaned sensors chips are mounted into either one of the four separate flow modules and their respective capillary tubes are connected in turn to the supplied pump unit. Buffer is then allowed to pass through the system until a stable baseline is achieved, after which the sample solutions are introduced. Any changes in the properties of the sensor surface caused by the deposition of soluble material will be reflected by the frequency and dissipation kinetics monitored via the measurement software. During the data analysis phase, these findings can then be translated into information regarding the mass, rigidity and viscoelastic properties of the sensor-bound material (Biolin Scientific Holding AB, 2016a).

2.1.5. Monitoring lipid bilayer formation kinetics via QCM-D

The QCM-D can also be a powerful tool for monitoring the formation of lipid SSMs on quartz crystal sensor chips. Measurements typically follow a two-step mechanism occurring spontaneously once specific conditions such as temperature, vesicle concentration, solution osmolarity and flow rate have been met. After a stable baseline has been established using plain buffer, the first step in a QCM-D experiment involves the introduction of lipid vesicles diluted in the same buffer to the flow module sensor. Contact with the sensor surface triggers the absorption of the vesicles, evidenced by a sudden drop in frequency and a mirrored increase in dissipation (Figure 2.1.5.1). The vesicles continue to accumulate on the sensor until critical vesicle coverage has been reached, as illustrated by the minimal frequency/maximal dissipation values, respectively.

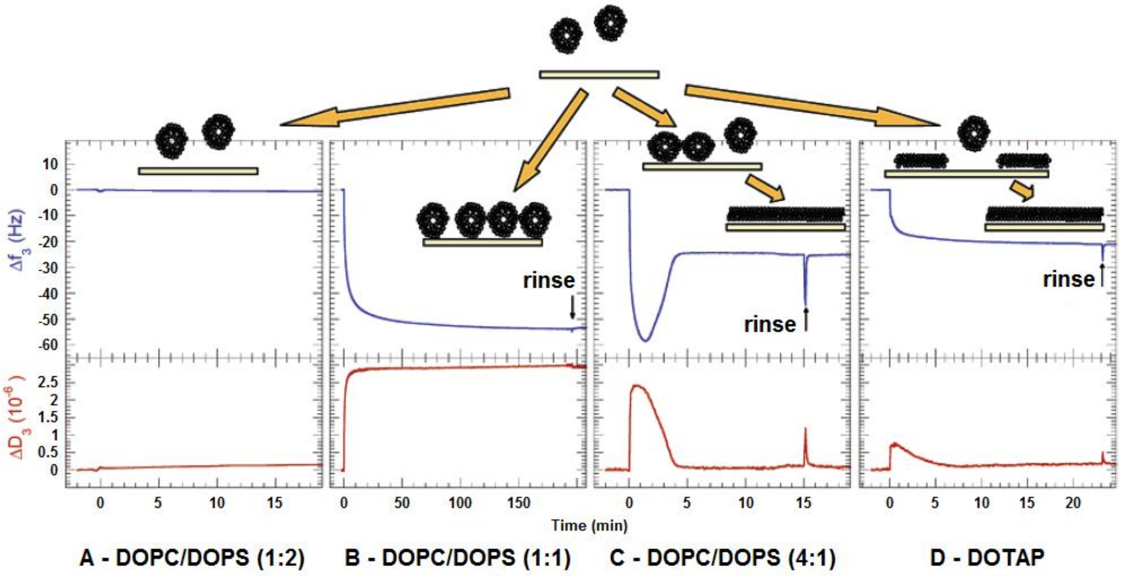

Figure 2.1.5.1. The frequency and dissipation changes brought on by the deposition of different lipid vesicles onto a silica-coated QCM-D sensor. DOPC, DOPS and DOTAP lipids were used to form vesicles at the specified molar mixing ratios and their adsorption onto the QCM-D sensor resulted in the following outcomes: A) DOPC/DOPS (1:2 molar ratio) vesicles did not adsorb onto the sensor; B) DOPC/DOPS (1:1 molar ratio) vesicles adsorbed onto the silica surface, but did not rupture; C) DOPC/DOPS (4:1 molar ratio) vesicles adsorbed and ruptured after reaching critical vesicular coverage, forming a lipid bilayer on the sensor surface; D) DOTAP-only vesicles ruptured and formed a bilayer almost immediately after coming into contact with the silica substrate (adapted from Richter et al., 2006).

Upon reaching critical coverage, the vesicles begin to rupture and form a planar lipid bilayer on the surface of the sensor (Figure 2.1.5.2 overleaf), as evidenced by the frequency and dissipation traces adopting new baselines. Following bilayer formation, the sensor-bound structure can be rinsed with deionised water in order to osmotically burst or remove any vesicles that may have adhered to the sensor, yet remained intact throughout the adsorption process. Finally, plain buffer is once again added through the system and a new baseline is established. Stable SSMs are typically characterised by a frequency change of approximately 25 Hz from the initial baseline, as well as a dissipation value of approximately 0.1×10^{-6} (Cho et al., 2010).

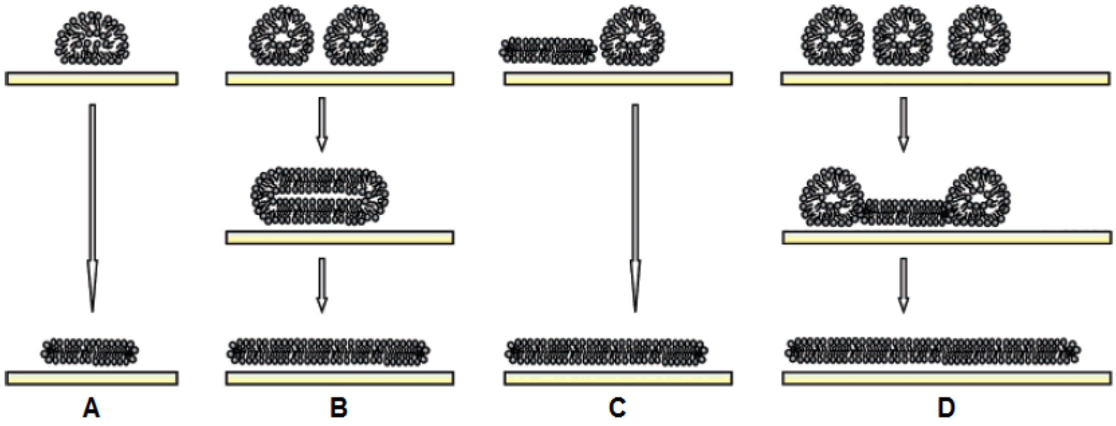

Figure 2.1.5.2. The different pathways leading to lipid bilayer formation after vesicles have been deposited onto a solid support: A) Isolated vesicles are deformed by the contact with the substrate and rupture spontaneously to form a lipid bilayer patch; B) Two adsorbed vesicles found in close proximity fuse and rupture, creating a lipid bilayer; C) Adsorbed vesicles coming into contact with the active edge of an already-existing lipid bilayer will rupture and add their mass to it; D) Upon reaching critical coverage, multiple vesicles come into contact and cause one of them to rupture, forming a lipid bilayer patch. The sudden appearance of an active edge sets off a chain reaction that ruptures all of the other neighbouring adsorbed vesicles, resulting in the formation of an extensive lipid bilayer (adapted from Richter et al., 2006).

2.1.6. The virtues and limitations of QCM-D technology

The remarkable sensitivity of QCM technology towards measuring surface changes renders it ideal for the creation of biosensors enabling the detection of compounds of medical interest. The existing literature on the subject already details a host of successful applications, such as the detection of volatile environmental pollutants (Tuantranont et al., 2011), of harmful extraneous compounds binding to α-oestrogen receptors attached to piezoelectric sensors (Carmon et al., 2005), of monoclonal antibodies binding to antigen-displaying biomimetic membrane vesicles tethered to silica-coated QCM-D crystals (Patel et al., 2009), as well as of single-base polymorphisms associated with hereditary diseases, identified through DNA strand displacement reactions performed on gold-coated sensor chips dotted with sample capture probes (Li et al., 2015). Furthermore, a QCM-based immunosensor was also successfully developed for the detection of phage-displayed antibodies binding to biotinylated antigens attached to streptavidin-coated gold surfaces. This novel approach for interrogating phage display libraries was shown to yield antigen-specific clones that demonstrated similar binding affinities to antibodies isolated via traditional plate-based screening protocols, thus highlighting once again the breadth of potential applications for QCM technology (Hengerer et al., 1999).

Unlike its counterpart techniques that rely on optical measurements, namely surface plasmon resonance (SPR) and dual polarisation interferometry (DPI), the QCM-D uses mechanical measurements to detect frequency changes. While all three techniques are capable of determining substrate binding affinities, only QCM-Ds can detect changes in mass caused by solvent trapped within the adsorbent material, which can prove useful in establishing the effects of sensor hydration when data sets from all three techniques are compared to one another (Heller et al., 2015). In particular, the combined usage of QCM-D and SPR when examining physical interactions at liquid-solid interfaces has grown in popularity over recent years due to its possibility of generating a comprehensive overview of the mass, orientation, thickness, lateral distribution and viscoelasticity of the adsorbed material (Fang et al., 2015). Similarly, the pairing of QCM-D and AFM techniques has led to the development of sensors functionalised with thin mica sheets that show none of the surface roughness of regular gold- or silicon dioxide (SiO_2)-coated QCM-D chips. These particular sensors can thus be readily used for performing highly stable and sensitive measurements yielding physicochemical and structural information than could only be derived by using both techniques in tandem on an identical support (Richter and Brisson, 2004).

Alternatively, when investigating the porosity of the sampled material – for instance, in the study of inward and outward ion fluxes arising within lithium-ion battery electrodes during charging and discharging (Shpigel et al., 2015) – the electrochemical quartz crystal microbalance (EQCM) suddenly becomes relevant (Buttry, 1992). Instead of relying on mechanical measurements, the EQCM uses electrochemical reactions to monitor not just mass changes occurring on its sensor surfaces, but also the amount of charge passing through their associated electrodes as well, thus being particularly well-suited for the study of underlying biological interactions towards biosensor development (Tuantranont et al., 2011), as well as for monitoring the physico-chemical interactions involved in processes such as metal electro-adsorption (i.e. electroplating) (Buttry, 1992).

However, one important limitation of QCM technology is given by its susceptibility to changes in environmental conditions, which can severely impact measurement accuracy. While AT quartz crystals are not as susceptible to temperature fluctuations (Marx, 2003), even this particular cut cannot account for all possible disruptive scenarios. An array of at least two independent QCMs operating in parallel under the same environmental conditions – one for taking reference measurements and the other(s) for running the actual experiment(s) – was therefore proposed to compensate for such disruptions, since the frequency fluctuations resulting from environmental changes could then be easily subtracted from the experimental measurements during the data analysis phase.

Unfortunately, this method came with hindrances of its own, one of the most pressing being an extremely bulky experimental setup that could also suffer from sensor uniformity issues caused by differences in quartz crystal manufacturing, which would undoubtedly render post-experimental fluctuation subtraction inaccurate and error-prone (Tuantranont et al., 2011). To this end, instruments featuring multiple QCM sensors embedded onto a singular monolithic quartz wafer have been developed specifically to alleviate both the experimental setup and sensor uniformity concerns (Tatsuma et al., 1999). Using one such monolithic quartz crystal microbalance (MQCM), at least one sensor can be dedicated exclusively to taking reference environmental readings, while the other identical electrodes can take the actual experimental measurements (Figure 2.1.6.1).

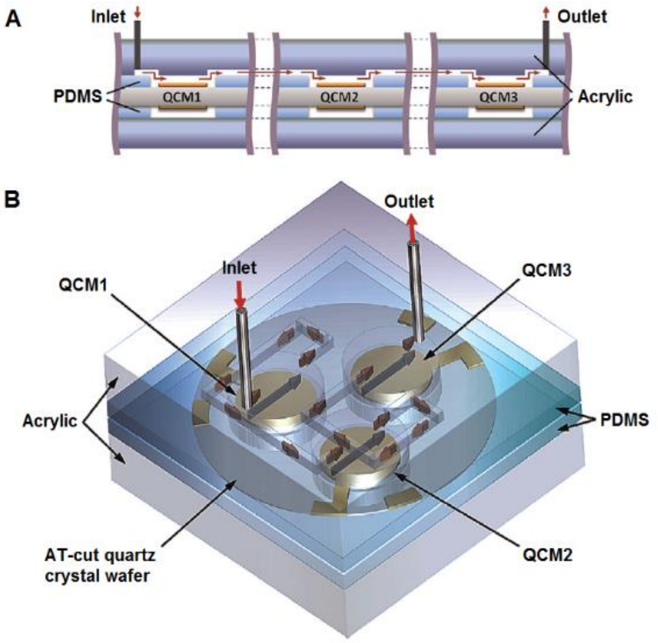

Figure 2.1.6.1. Diagram of an enhanced MQCM sensor design: A) Cross-section view of the three sensing electrodes, sandwiched between acrylic layers and shielded by polydimethylsiloxane (PDMS) walls; B) 3D conceptualisation of the same sensors arranged in a serial flow cell module (adapted from Jaruwongrungsee et al., 2015).

This miniaturisation not only significantly decreased the large footprint typical of a discrete QCM array, but also concurrently reduced sample consumption, as well as the time and effort required to perform each measurement. While concerns were initially raised over potential signal interference occurring between the different electrodes as a consequence of their close proximity, studies have shown that this phenomenon is negligible in real-life experimental settings (Jin et al., 2009) and recent improvements in MQCM design also saw the use of polydimethylsiloxane (PDMS) walls interposed between adjacent sensors (Figure 2.1.6.1 above) in order to effectively nullify TSM oscillation crossover (Jaruwongrungsee et al., 2015).

In spite of these minor limitations, its highly-sensitive means of monitoring SSM formation kinetics in real-time rendered QCM-D technology invaluable to the project at hand, as will be seen throughout the upcoming Chapter 3.

2.2. SURFE2R N1 Transport Activity Assay

The activity of proteins functioning as transporters, pumps and channels within living cell membranes can be characterised through a variety of electrophysiological methods. Historically, membrane proteins have been expressed in oocytes or mammalian cell lines and investigated using conventional electrophysiology techniques, such as patch- or voltage-clamp, which are laborious, time-consuming and require the help of highly-trained and experienced personnel (Schulz et al., 2009). Throughout the last decades, however, substantial developments in SSM technology have led to the development of quicker and less demanding approaches for assaying membrane protein activities. Following their expression in a suitable organism, membrane protein targets can now be tested for *ex vivo* substrate transport by forming proteoliposomes using harvested cell membranes and then applying modern, SSM-based electrophysiology techniques.

2.2.1. Introduction to SSM-based electrophysiology

Based on a technique perfected by previous pre-steady-state experiments studying membrane protein transport rates by measuring the electrical charge difference observed after a rapid introduction of charged substrate (Pintschovius and Fendler, 1999), the Nanion SURFE2R N1 workstation is capable of investigating the activity of membrane protein targets – such as anion or cation symporters and antiporters – reconstituted or embedded into multiple heterologous formats. The assay requires only microlitre-volumes of cell membrane preparations or purified membrane proteins reconstituted into proteoliposomes and has thus far been proven to work with targets originating from bacterial, insect and mammalian cell lines (Nanion Technologies GmbH, 2016b). The sensors used with the SURFE2R generally consist of a 3 mm-wide well capable of holding volumes of up to 400 µL, at the bottom of which lies a gold measurement electrode (Figure 2.2.1.1 overleaf). Prior to adsorbing the proteoliposomes or membrane preparations, however, an octadecanethiol monolayer is first covalently bound to the gold surface via its sulfhydryl groups, followed by a second phosphatidylcholine monolayer deposited directly on top of it. Taken together, the two stacked monolayers form a hybrid alkanethiol/phospholipid biomimetic SSM (Plant, 1993).

Figure 2.2.1.1. Top (left) and bottom (right) views of a SURFE2R N1 sensor chip, featuring a 3 mm-wide well. At its bottom lies a thin gold electrode coated with a hybrid biomimetic SSM to which the cell membrane preparations adhere (adapted from Nanion Technologies GmbH, 2016a).

2.2.2. The SURFE2R operating principle

In the first phase of a SURFE2R transporter assay, the proteoliposomes containing reconstituted purified membrane proteins or the cell membrane vesicles expressing the membrane protein targets are adsorbed onto the sensor-bound SSM component, creating a capacitively-coupled system (Figure 2.2.2.1) enabling the measurement of any transient electrical currents generated by the transport of permeant substrate (Bazzone et al., 2013).

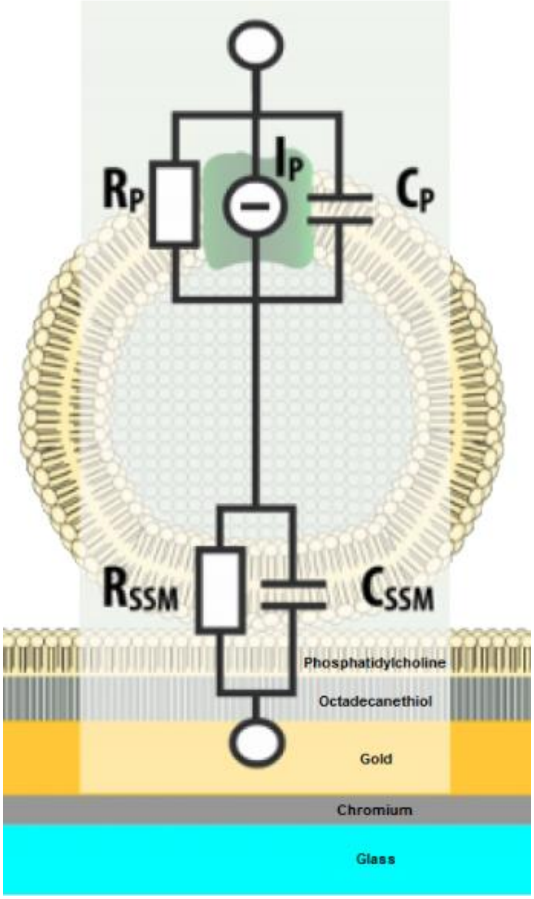

Figure 2.2.2.1. Proteoliposomes or cell membrane vesicles expressing the membrane protein targets (only one shown here for clarity, in green) are adsorbed onto the sensor-bound hybrid SSM, consisting of a phosphatidylcholine monolayer stacked on top of a gold-supported octadecanethiol basal monolayer. The resulting vesicle-SSM complex forms a capacitively-coupled system capable of measuring transient currents (adapted from Bazzone et al., 2013).

The adsorbed vesicles are then filled with a control solution (e.g. plain buffer) and a baseline is established, after which the activating solution containing the charged substrate is rapidly applied. Should the investigated protein still be capable of *ex vivo* transmembrane transport, the influx of transported substrate into the vesicles will cause a charge difference across the lipid membranes, giving rise to either a transient positive or negative current (for positively- or negatively-charged substrates, respectively). This inward current will be directly proportional to the concentration of substrate transported into the vesicles and will be registered by the workstation as a capacitive correction current at the surface of the gold measurement electrode (Figure 2.2.2.2). Once the adsorbed vesicles become saturated with substrate and the system reaches equilibrium, the transient inward current will disappear and the signal trace will return to its baseline level. Owing to the nature of measuring rapid transient currents in capacitively-coupled systems, the declining half of a positive inward current peak can sometimes be followed by a shallow negative overshoot phase that will slowly return to baseline given enough time (Bazzone et al., 2013). When the control solution is reintroduced to the sensor well, the substrate will be transported back out of the adsorbed vesicles, generating an outward transient current in the process. Finally, once all of the substrate has been removed from the vesicles, the trace will return to its baseline value measured at the beginning of the experiment (Nanion Technologies GmbH, 2016b).

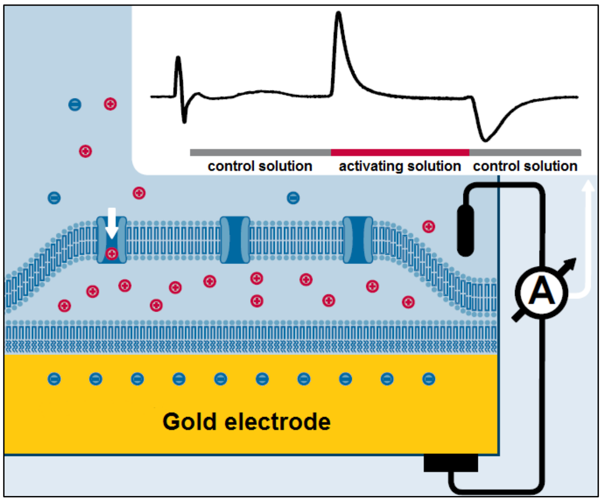

Figure 2.2.2.2. Diagram of the SURFE2R operating principle: after establishing a baseline using a control solution (e.g. plain buffer), the addition of an activating solution containing the charged transporter substrate will cause any active membrane proteins embedded within the adsorbed vesicles to initiate transmembrane transport, generating a transient inward current (in this case, positive). The resulting charge difference will be compensated by a capacitive correction current at the surface of the measurement electrode, represented by a sharp signal on the SURFE2R trace. When the control solution is reintroduced, a transient outward current (in this case, negative) will be registered as the substrate is transported back out of the adsorbed vesicles (adapted from Nanion Technologies GmbH, 2016b).

2.2.3. Successful applications of SURFE2R technology

One of the many success stories involving the SURFE2R assay revolves around the measurement and subsequent modulation of the ion transport capabilities exhibited by reconstituted uncoupling protein 1 (UCP1). This inner mitochondrial membrane-bound proton transporter, involved in adult human metabolism and non-shivering thermogenesis, was purified and subsequently reconstituted into phosphatidylcholine (PC), phosphatidylethanolamine (PE) and cardiolipin (CA) vesicles. These were then adsorbed onto a sensor-bound SSM and the transport activity of UCP1 was modulated through the use of activator (i.e. fatty acid) and inhibitor (i.e. purine nucleotide) compounds (Blesneac et al., 2012). Similarly, the nitrite/proton antiporter qualities of the NirC transporter from *Salmonella typhimurium* were also discovered using a custom SURFE2R-like assay. After the protein had been purified and reconstituted into *E. coli* polar phospholipid vesicles, the resulting proteoliposomes were adsorbed onto an octadecanethiol/diphytanoyl-phosphatidylcholine hybrid bilayer and subjected to the same control-activating-control solution exchange used in a traditional SURFE2R experiment (Rycovska et al., 2012).

Target membrane protein purification followed by reconstitution into lipid vesicles is not mandatory for an SSM-based electrophysiology assay to function, however, as native membrane vesicles or even membrane fragments have also been shown to produce measurable signals (Schulz et al., 2008). For instance, SURFE2R-like technology has been successfully used to develop an SSM-based electrophysiological assay for measuring the K^+ and Na^+ currents generated through the transport activity of the reversible murine neuronal glutamate transporter mEAAC1 expressed in whole plasma membrane vesicles. Bearing an impressive 90% amino acid sequence identity with the human glutamate transporters involved in neuronal pathology, the assay provided a fast, low-cost and highly-automated means of screening for novel anti-Parkinson’s disease drugs with therapeutic actions based on modulating the activity of this particular transporter (Krause et al., 2009).

Similarly, the ion transport kinetics of P-type ATPases were also studied in their native environment without the need for purification, while being expressed in either pig kidney outer medulla planar membranes (Pintschovius and Fendler, 1999) or vesicular fragments of animal sarcoplasmic reticulum (Tadini-Buoninsegni et al., 2008). These preparations were then adsorbed onto both black lipid membrane (BLM) and SSM platforms, highlighting once again the robustness and versatility of functional model membrane electrophysiology. While both BLMs and SSMs share a set of physical properties that make them ideal for measuring transient electrical currents, namely a low specific conductance (so as to control background noise) and a high specific capacitance (in order to produce large, easily-measurable signals), SSMs have been historically preferred over BLMs due to their increased mechanical stability against external vibrations, as well as their more expansive surface areas (Seifert et al., 1993).

2.2.4. The virtues and limitations of SURFE2R technology

The strengths of SSM-based electrophysiological techniques stem from their ability to measure the transport activities of membrane proteins embedded into very small structures, including sarcoplasmic reticulum and parietal cell vesicles (Schulz et al., 2008). This capability is further enhanced by their high degree of pliancy to different assay formats and asymmetrical experimental conditions, such as performing successive measurements under a pH gradient (Mager et al., 2011). However, these techniques also suffer from a share of limitations that need to be taken into consideration during the planning phase of future experiments.

When compared to the older patch- and voltage-clamp methodologies, SSM-based electrophysiology cannot be used to measure the transport activity of proteins relying on the application of a membrane potential or the aid of other intracellular components such as binding proteins (Schulz et al., 2009). Further limitations of SSM electrophysiological platforms arise from the possibility of encountering large current artefacts caused by the binding of lipophilic substrates directly onto the SSM sensor component, although this phenomenon can be largely mediated through the use of buffers with high salt concentrations. Proper sample preparation yielding homogenous proteoliposomes, followed by their thorough sonication and careful application to the measurement sensor are equally important, since the introduction of air bubbles to the system should be avoided at all times (Bazzone et al., 2013).

Given its established transport activity measurement capabilities, the SURFE2R assay was used to determine which of the NupC constructs employed throughout the project still retained their *in vivo* nucleoside transport activities following their expression and purification, as will be seen further on in Chapter 4.

2.3. Cryo-Electron Microscopy

With the advent of electron microscopy (EM) at the beginning of the 20th century (Figure 2.3.1.1), the high-resolution imaging of molecular structures and interactions all the way down to the atomic level quickly turned from mere pipe dream to scientific reality.

2.3.1. Introduction to electron microscopy

Similar to how conventional light microscopes make use of the visible spectrum of light for imaging samples, electron microscopes operate by focusing a high-powered electron beam through a set of electromagnetic and/or electrostatic lenses in order to pass it directly through sub-micrometre-thin sample preparations (Milne et al., 2013). As the beam travels through the immobilised specimen, regions of varying densities within the sample will scatter the incident electrons at different angles (e.g. fewer electrons will pass through sections comprised of heavier elements and will instead be redirected towards the walls and apertures of the specimen chamber), resulting in dark structures appearing on the final image formed on the attached imaging plate (Miranda et al., 2015). Since electrons propagate at much smaller wavelengths than visible light, greyscale images at magnifications thousands of times higher than those attainable with traditional light microscopes can thus be recorded. Depending on the means of interaction between the electron beam and the imaged specimen, the different types of electron microscopes available today (i.e. transmission or scanning) can provide a wealth of morphological and compositional information on virtually any suitably-prepared sample (Jensen, 2012).

Figure 2.3.1.1. Digitally-enhanced photograph of German physicists Max Knoll (left) and Ernst Ruska (right) working on the first electron microscope prototype in the 1930s (adapted from Williams and Carter, 2009).

2.3.2. The different types of electron microscopes

With EM, the resolution of the recorded images is inversely proportional to the wavelength of the electron radiation passing through the imaged specimen, as given by the accelerating voltage of the electron gun located at the top of the instrument. This critical parameter is normally measured in kilovolts (kV) and the higher it is set to, the lower the wavelength of the emitted beam will be, resulting in an enhanced image resolution and the ability to capture even smaller structures at magnifications of up to 2,000,000× (John Innes Centre, 2016). Based on the power and scattering angle of the electron beam, electron microscopes can be divided into two main categories – transmission and scanning – each with its own distinct virtues, limitations and applications (Jensen, 2012). The first of these (and the type used throughout the current project), transmission electron microscopes (TEMs) represent the original and, consequently, the oldest form of EM. Traditionally, such microscopes comprise of a cylindrical high-vacuum chamber featuring a top-mounted, down-facing electron gun. An array of solenoid-like electromagnetic condenser lenses and apertures concentrates the beam onto the immobilised sample, followed by a set of objective lenses and apertures that magnify and focus the resulting image onto a screen such as a photographic plate or, more modernly, a charged-coupled device (CCD) camera (Figure 2.3.2.1).

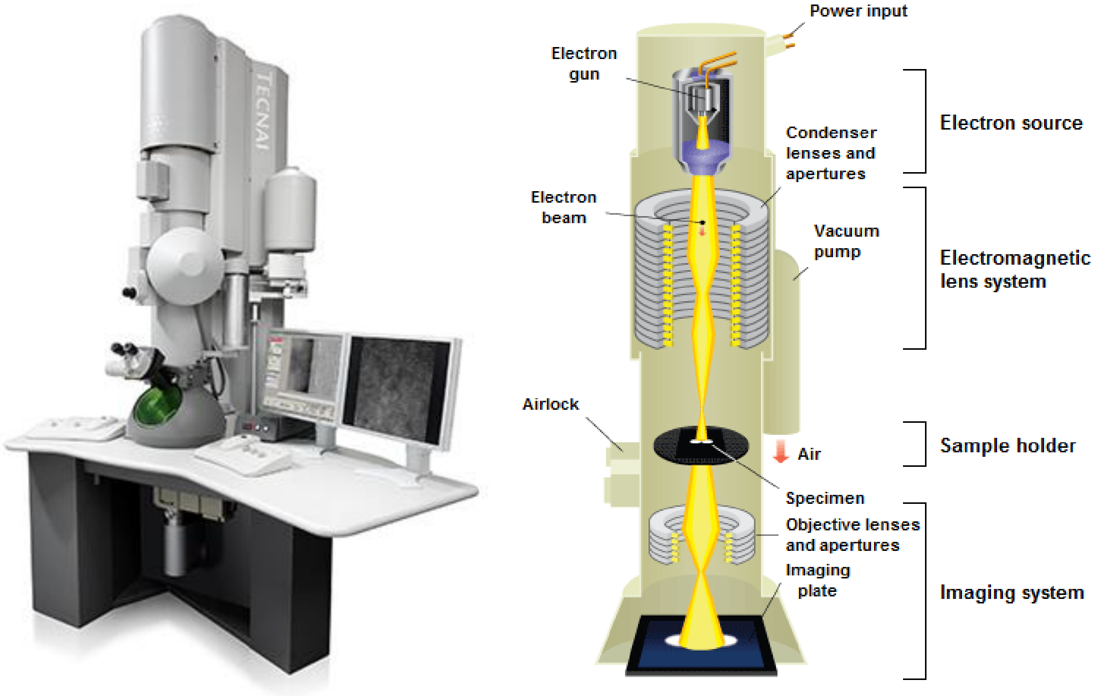

Figure 2.3.2.1. Left: the FEI Tecnai – a modern TEM (adapted from FEI, 2016a). Right: simplified diagram of the interior organisation of a typical TEM (adapted from the Department of Physics, The Chinese University of Hong Kong, 2016).

TEM instruments emit highly-powerful electron beams (i.e. up to 1,000 kV) that are focused into passing through sub-micrometre-thin sample preparations in order to produce 2D images of structures measuring up to less than 1 Å (i.e. 10^{-10} m) in size. This renders TEMs invaluable for any applications requiring imaging down to the atomic level (Erni et al., 2009). Of all of the different electron microscopes available today, TEMs offer the most powerful magnification capabilities – up to 50,000,000× (John Innes Centre, 2016) – and, consequently, the ability to produce the highest-quality images for biological and material science applications following a period of specialist training. However, these virtues do come at the cost of having to dedicate considerable time and effort towards preparing electron-transparent samples whose thinness also renders them particularly vulnerable to electron radiation damage (e.g. whole cell preparations) (Jensen, 2012). Nevertheless, TEMs have been instrumental over the years towards imaging key biological structures, including the various cellular organelles such as the Golgi apparatus (Dalton, 1951), mitochondria (Palade, 1953), nucleus (Bradfield, 1954) and the plasma membrane (Figure 2.3.2.2) (Stoeckenius, 1962), among many other biological entities and interactions.

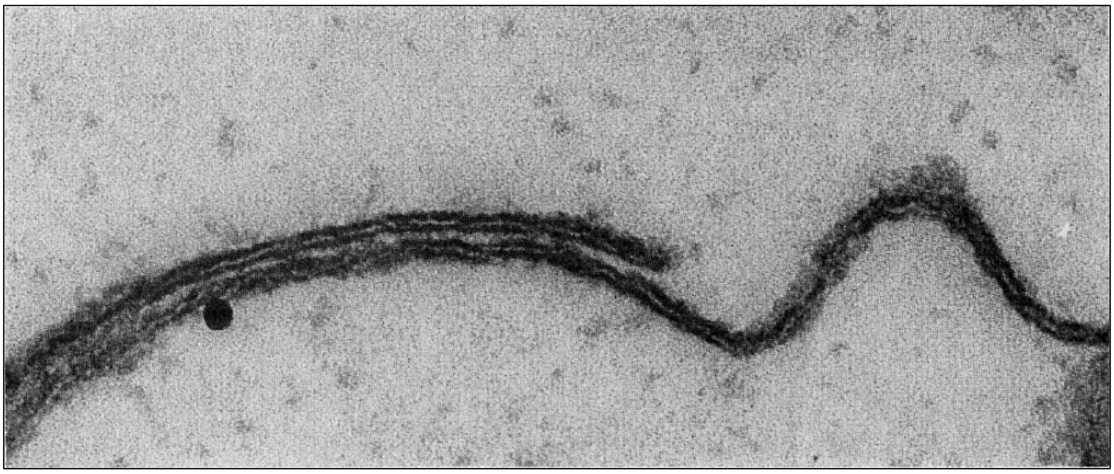

Figure 2.3.2.2. TEM image of the phospholipid bilayer component of the plasma membrane, magnified 280,000×. The sample was fixed using osmium tetroxide (OsO_4) and the contrast was enhanced via lead hydroxide ($Pb(OH)_2$) staining (adapted from Stoeckenius, 1962).

2.3.3. Cryofixation and the emergence of cryo-EM

Ever since their rise in popularity during the middle 20th century, various concerns were raised over using TEMs in the imaging of ultra-thin biological samples, with special consideration given to the precarious balance between achieving the lower wavelengths at which high resolutions were attainable and the sheer destructive force of even short-term exposure to high-power electron beams. Thankfully, a revolutionary method of TEM specimen preparation emerged towards the end of the same century, alleviating most, if not all of these concerns and ushering in an exciting new realm of potential biological and medical applications. Developed in 1981, the process of cryofixation involves flash-freezing EM samples in cryogens such as liquid propane or ethane in order to preserve them as close to their native state as physically possible (Dobro et al., 2010).

Whereas classic biological specimen fixation methods involved subjecting samples to lengthy chemical treatments (e.g. osmium tetroxide for preserving lipids and glutaraldehyde for fixing proteins) resulting in their dehydration and the subsequent generation of shrinkage artefacts, through cryofixation, micrometre-thin preparations are frozen in their entirety almost instantly (John Innes Centre, 2016). This procedure not only results in the effective vitrification of EM specimens, since water crystals do not have enough time to form in the surrounding solution, but the resulting preparations are preserved in their hydrated state while also only generating a minimal number of potential artefacts related to the quality of the newly-formed ice (Jensen, 2012). It is through cryofixation that cryo-electron microscopy (cryo-EM) came into being at the end of the 20th century and swiftly became the preferred means of harnessing the high resolving power characteristic of TEMs for capturing images of the ultrastructure of delicate biological preparations (Fitzpatrick et al., 2013).

2.3.4. Preparing samples for cryo-EM

The principle behind the preparation of cryo-EM samples via flash-freezing evolved little over the years since its inception, even after the introduction of automated vitrification devices such as the FEI Vitrobot (FEI, 2016b). Fundamentally, the process involves spreading microlitre-sized solubilised samples onto a specialised EM grid, after which any excess solution is removed via gentle blotting with filter paper. Once only a thin sample film remains, the grid is rapidly plunged into a cryogenic liquid to form vitreous ice, this also being the reason why this particular step is more commonly referred to as “plunge-freezing”. Finally, the flash-frozen grids are quickly, but carefully transferred into liquid nitrogen storage holders until they are ready to be imaged under a TEM (Dobro et al., 2010).

Although relatively straightforward, the successful creation of cryo-EM grids relies not only on the quality of both the applied samples and the EM grids themselves, but also on a correct blotting procedure followed by an extremely fast plunge into a suitable cryogen. Since the effectiveness of the technique is limited by the heat conductivity of the solvent solutions, cryo-EM preparations need to be as thin as possible in order to ensure that heat is quickly transferred out of the samples after they have been plunged into the cryogen. Similarly, the material and quality of both the grids and their support films constitute equally relevant attributes. Cryo-EM grids generally consist of a copper, nickel, aluminium, molybdenum, titanium or gold mesh upon which thin carbon films are deposited in either continuous or “holey” layers (Quantifoil, 2016). While thicker grid meshes can offer better support, they will also occupy additional space that could be dedicated to fixing more of the sample material instead. Furthermore, whereas continuous carbon films might be better at supporting samples in a specific orientation during imaging (e.g. protein crystals), holey and “lacey” films featuring either patterned or disorganised holes (Figure 2.3.4.2) can reduce background noise by immobilising individual specimens within the vitreous ice forming inside the gaps (Dobro et al., 2010).

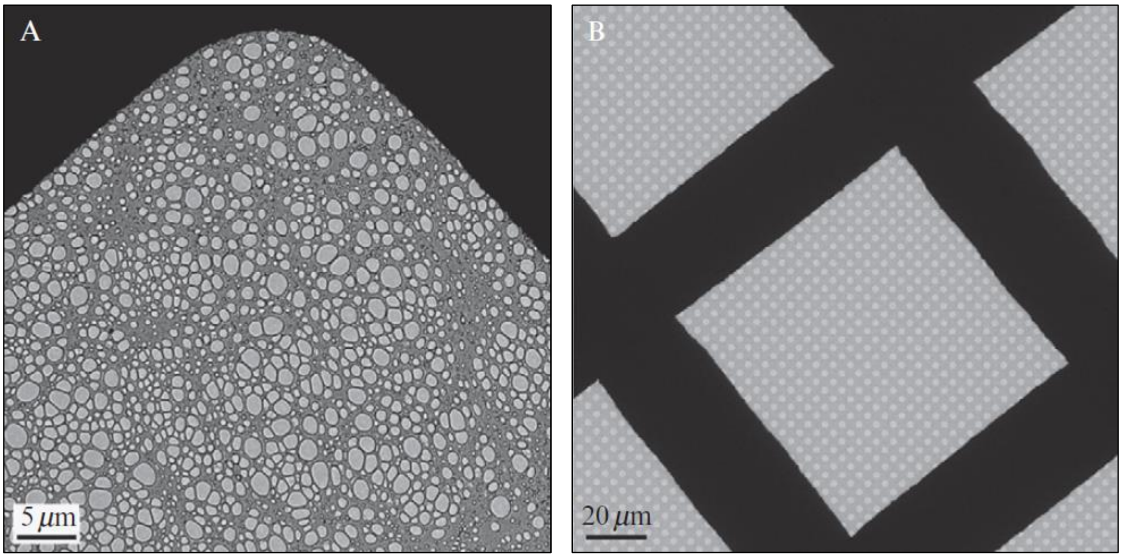

Figure 2.3.4.2. Different types of cryo-EM grids and their respective support films: A) Lacey grid with a carbon support film featuring different hole sizes in a disorganised pattern; B) Quantifoil grid with equally-sized holes arranged at regular intervals. Such grids typically feature micrometre-sized holes (adapted from Dobro et al., 2010).

In order to ensure the uniform distribution of liquid samples across the supporting films, the hydrophilicity of cryo-EM grids must be reinforced before use. Historically, this was achieved by cleaning previously-used grids via plasma glow discharging (Dubochet et al., 1971), but submerging them into solvents such as chloroform, acetone or ethanol, or simply replacing the carbon support film with a fresh one have also been proven as valid alternatives over the years (Quispe et al., 2007). Cell adhesion can also be facilitated by functionalising the grids with organic molecules (e.g. polylysine). Nevertheless, it is generally accepted that more extreme cleaning methods, such as overnight electron irradiation inside a TEM, should ultimately be avoided as they can lead to microfissures developing throughout the carbon support films, which future samples can inadvertently infiltrate following their application (Dobro et al., 2010).

Once the samples have been applied, the cryo-EM grids can be blotted either unilaterally – to reduce the chances of damaging delicate specimens – or bilaterally – to remove all of the excess fluids (Lepper et al., 2010). Achieving optimal ice thinness is particularly important, since insufficient ice coverage might cause the cells or particles contained within an applied sample to aggregate towards the edges of the grids upon plunge-freezing, which would in turn make their imaging rather problematic (Dobro et al., 2010). To this end, both the duration and pressure of blotting need to be optimised for the specimen at hand, since the integrity as well as the number of constituent entities (e.g. cells, sporozoites, nanoparticles, etc.) can be seriously compromised through the application of excessive or extensive force (Lepper et al., 2010).

Finally, the cryogenic liquids themselves must also meet very specific criteria before they can be used in the production of high-quality EM grids. These include high thermal conductivities and boiling points – to prevent vapour formation at the interface between the samples and the cryogen – as well as freezing points that are lower than the sample vitrification temperatures (Dobro et al., 2010). Given that aqueous solutions only vitrify at cooling rates of 10^5-10^6 K/s (Brüggeller and Mayer, 1980), liquid nitrogen has been deemed unsuitable for serving as a plunge-freezing cryogen due to its low thermal conductivity of only 400 K/s, which is not even nearly quick enough to prevent the formation of crystalline ice (Dobro et al., 2010). This prompted the use of liquid ethane or propane instead, since both of these feature much higher thermal conductivities. However, their different boiling points (i.e. -89 °C for ethane versus -42 °C for propane) meant that the latter cryogen suffers from a slower evaporation rate and is thus more prone to leave behind ice crusts on freshly-vitrified EM grids, which can in turn be a source of eventual imaging artefacts (Dubochet et al., 1988). It is for this additional reason that liquid ethane remains the most popular plunge-freezing cryogen for the production of high-quality cryo-EM specimens to date, while liquid nitrogen is only used as a coolant intended to keep the temperature of the primary cryogen constant throughout the grid preparation process. Even so, only pure cryogen should be used during the actual plunge-freezing step, since any impurities or contaminants can easily transfer onto the grids and show up as artefacts during imaging (Dobro et al., 2010).

2.3.5. The virtues and limitations of cryo-EM

While its limitations closely follow those of TEMs in general, cryo-EM benefits from significant advantages that have rendered it an essential tool for studying biological specimens at ultra-high resolutions (Muench et al., 2009). For one, cryofixation preserves biological samples in a hydrated, close-to-native state without the need for any of the old chemical staining or stabilising agents. Additionally, vitrified samples are more stable when exposed to the harsh conditions encountered inside a cryo-EM and low-powered electron beams (<100 kV) can therefore be used over longer periods of time without compromising the quality of the final images (Jensen, 2012). This not only effectively limits the total radiation absorbed by the preparations throughout an entire imaging run, but also enables prolonged measurements to be taken of fragile specimens such as adenoviruses and T4 bacteriophages (Adrian et al., 1984).

The versatility of cryo-EM also enables it to be successfully used in place of older, more established techniques. X-ray crystallography has long been a staple of structural biology, but it nevertheless requires the use of large, well-ordered and highly-pure protein crystals that must also be able to withstand the radiation damage inflicted by prolonged exposure to focused X-ray beams. While short X-ray pulses can minimise this to an extent, a significant number of crystals is nevertheless required and, unfortunately, not all proteins can be purified to a high-enough standard for crystallography work. Furthermore, some formats such as membrane proteins reconstituted into proteoliposomes or expressed in total membrane extract preparations cannot even be crystallised at all. Electron crystallography, on the other hand, operates via the same principle (i.e. an electron beam is scattered by the examined protein crystal into a quantifiable diffraction pattern), but given that electrons interact much more strongly with the crystal matrix than X-rays, higher resolution data sets can be gathered from smaller and even less pure crystals (Boekema et al., 2009). Furthermore, while the potential electron radiation damage is indeed proportionately higher than that inflicted through X-ray exposure, following a reduction in the total electron dose down to 0.1 $e^{-}/Å^{2}/s$, up to 90 individual diffraction patterns could be obtained from singular crystals via cryo-EM crystallography (Shi et al., 2013). Termed “MicroED”, this particular technique proved capable of determining the structure of lysozyme with a resolution of only 2.9 Å, thus reiterating the advantages of utilising cryo-EM in structural biology studies.

With respect to the current project, cryo-EM was also successfully used towards imaging SSBLM formation on silica nanoparticles. Mornet et al. (2005) achieved this by sonicating mixed DOPC/DOPS SUVs (4:1 (w/w) ratio) together with 100 nm silica nanoparticles for 1 hour and then inspecting the vitrified solution under a FEI Tecnai F20 TEM operating at 200 kV. Their images, taken at a resolution of 2 nm using a CCD camera, captured the newly-formed SSBLMs as 4-5 nm electron-dense rings enveloping the silica nanoparticle substrates (Figure 2.3.5.1).

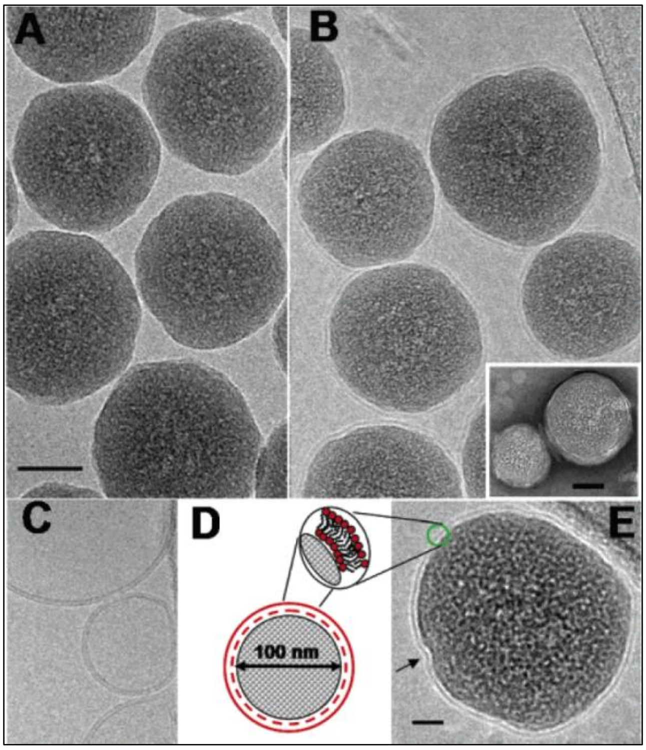

Figure 2.3.5.1. Evidence of SSBLM formation around 100 nm silica nanoparticles as determined via cryo-EM: A) 100 nm bare silica nanoparticles (scale bar: 50 nm); B) Following a 1-hour sonication with DOPC/DOPS SUVs (4:1 (w/w) ratio), the nanoparticles became enveloped in SSBLMs, as evidenced by the surrounding rings of electron-dense material represented schematically in (D). Inset: negative-staining comparison revealing the dehydration damage typical of this method of EM sample preparation (scale bar: 50 nm); C) Stand-alone DOPC/DOPS SUVs; E) Close-up of a DOPC/DOPS SSBLM, highlighting the twin leaflets of the supported lipid bilayer, whose polar head groups scatter electrons more strongly than the hydrocarbon chains sandwiched in-between (scale bar: 20 nm) (adapted from Mornet et al., 2005).

As will be seen later on, Chapter 4 will describe yet another successful cryo-EM application, namely the imaging of NupC embedded into the lipid bilayer component of SSBLMs formed on 200 nm silica nanoparticles.

2.4. Small-Angle X-Ray Scattering

Another technique capable of offering structural information on microscopic specimens is represented by small-angle X-ray scattering (SAXS). Since any inhomogeneities present within a given sample solution – be they amorphous or crystalline solids, liquids of varying densities or even gases – will invariably diffract an incident X-ray radiation from its initial course, the analysis of the small angle of scattered radiation can reveal substantial information on the examined specimen at hand (Pauw, 2013).

2.4.1. Introduction to X-ray scattering

Through SAXS, the shape and distribution of kDa-to-GDa biomolecules can be rapidly derived under a multitude of experimental conditions, ranging from close-to-native hydrated protein solutions to cryofixed specimens, especially upon harnessing high-intensity X-rays sources such as those found in synchrotrons. The widespread popularity of SAXS in fields as diverse as medical, materials and even food sciences stems from its capability of quantitatively characterising the polydispersity of both ordered and disordered particles, such as intrinsically-disordered proteins (IDPs). Furthermore, since the technique is performed in a time-resolved manner, the dynamics and kinetics of various biomolecular interactions can also be studied at the same time (Kikhney and Svergun, 2015). With a basic operating principle shared with alternative small-angle scattering techniques based on other forms of radiation, such as SAGS (gamma rays), SAES (electrons), SANS (neutrons) and LS (visible light) (Pauw, 2013), and in spite of having a relatively lower structural resolving power compared to staple techniques such as X-ray crystallography (Pérez and Nishino, 2012), SAXS nevertheless offers a powerful means of studying close-to-native-state biomolecular morphologies in hydrated, non-crystalline samples and has thus become an integral part of structural biology research laboratories around the world.

2.4.2. The SAXS experimental setup and operating principle

Following their inception in the first half of the 20th century, a majority of SAXS setups were custom-made and as such varied considerably between individual laboratories. Thankfully, a multitude of present-day industrial manufacturers, including Bruker, Rigaku and Xenocs, now offer a wide range of commercial X-ray scattering instruments. With that being said, the basic SAXS operating principle has not changed fundamentally over the years and at their core, all modern setups still consist of an X-ray emitter, a beam collimation section, a sample chamber, an evacuated flight tube fitted with a beam stopper and, most importantly, a detector for capturing and recording the scattered X-rays (Figure 2.4.2.1 overleaf). Based on the process through which the initially-disordered X-rays are collimated (i.e. arranged into a parallel, non-dispersible beam), SAXS instruments can be categorised into one of several classes: pinhole-collimated, slit-collimated and Bonse-Hart-collimated (Pauw, 2013).

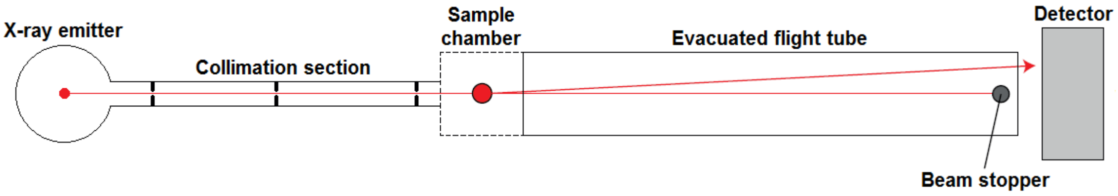

Figure 2.4.2.1. Diagram of the basic components of a pinhole-collimated SAXS instrument (adapted from Pauw, 2013).

SAXS experiments usually comprise of three successive phases, all of them referring to the stage the experimental data is in: data collection, data correction and data analysis (Pauw, 2013). The first step in any classic SAXS experiment involves pipetting microlitre-sized volumes of the sample solution into a quartz capillary tube, which is then secured in place within the sample chamber of the instrument and irradiated with a collimated, monochromatic X-ray beam (Figure 2.4.2.2).

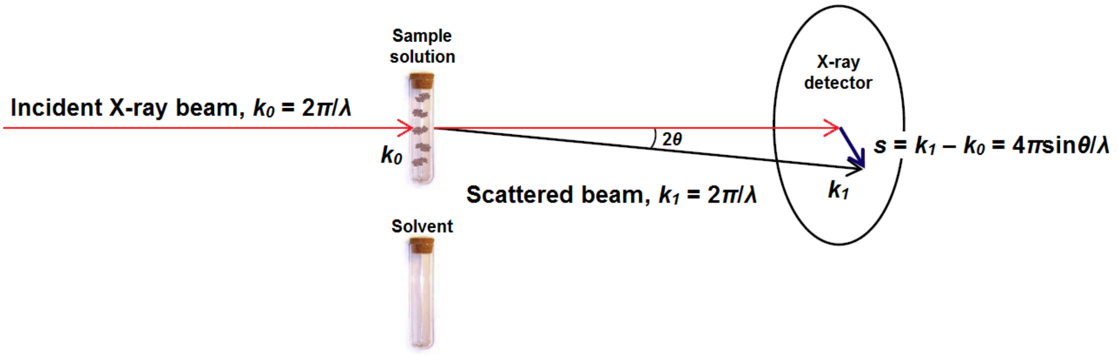

Figure 2.4.2.2. Diagrammatic representation of the SAXS operating principle (adapted from Kikhney and Svergun, 2015).

As incident X-rays pass through the sample chamber, a number of them will be elastically scattered by the electrons of the solubilised particles present in the sampled solution (Pérez and Nishino, 2012). The scattered X-rays will then travel on different vectors throughout the evacuated flight tube and will ultimately be captured by the detector located beyond, instead of simply being stopped at the end of the tube like the remainder of the undeviated incident radiation. After subtracting the signal generated by a sample of pure solvent, a scattering profile of just the solubilised particles can be determined, holding information on the size and morphology of the examined solute (Kikhney and Svergun, 2015).

Whereas the data collection step is relatively straightforward, the collected scattering profiles must first be corrected by factoring out any potential noise or distortions generated by the X-ray detection system, accounting for sample polarisation and self-absorption, as well as scaling results to absolute units, since only by using corrected data sets can the intensity of solute-exclusive scattering profiles be accurately determined (Pauw, 2013). Finally, it is during data analysis that the intensity of the scattered X-rays, $I(s)$, can be calculated as a function of the momentum transfer $s = 4\pi \sin\theta/\lambda$, where 2θ represents the scattering angle and λ signifies the wavelength of the X-ray beam:

$$\boldsymbol{I(s) = [I(s)]_{\Omega} = [A(s)A^{*}(s)]_{\Omega}}$$

Next, by applying a Fourier transformation to the excess electron density, the scattering amplitude, $A(s)$, can now be calculated:

$$\boldsymbol{A(s) = \int \Delta\rho(r) \exp(isr)\, dr}$$

where $\Delta\rho(r) = \rho(r) - \rho_s$ (i.e. the electron density of the sampled particles minus the electron density of the solvent itself) and $[\,]_{\Omega}$ represents the spherical average (Kikhney and Svergun, 2015). Given that soluble particles can be contained in any number of orientations within a sample solution, their scattering patterns can be plotted as isotropic, one-dimensional $I(s)$ curves depicting the averaged signatures of all of the sampled particles, whose number will be proportional to the detected X-ray scattering intensity (Pérez and Nishino, 2012).

When performing SAXS studies of virtually any sample solution, the three main parameters that researchers usually aim to gather information on are the morphology (i.e. shape/size), heterogeneity (i.e. polydispersity) and distribution (i.e. packing) of the sampled particles. While not all of these parameters might become readily available by the end of the data correction phase, if only two of them are known or even just reasonably assumed, then they can be used to infer on the quality of the missing third. For instance, assuming a monodisperse solution at an infinite dilution (so that any possibility of aggregation can be eliminated altogether), the morphology of its solubilised particles could be deduced using shape-resolving computational techniques, at the expense of a lower final resolution. Similarly, structure-resolving techniques can be used to determine the distribution of solute in a specified volume, should information on its shape and polydispersity be made available through other means such as TEM (Pauw, 2013).

Apart from the above, several other sample parameters can be derived directly during the data analysis phase. These include the maximum dimension of the sampled particles, D_{max}, their molecular weight, as well as the radius of gyration, R_g. It is important to note that while these values will pertain to every single particle contained within a monodisperse solution (i.e. harbouring identical particles), a scattering profile derived from a polydisperse sample (i.e. containing particles of different shapes and sizes) will instead give averages of the above values for the entire heterogeneous solute population taken as a whole. Although not as immediately useful as for monodisperse solutions, these parameters can still be used to structurally characterise polydisperse samples based on properties other than size (Kikhney and Svergun, 2015).

Expressed as an average of the root-mean-squared distance to the centre of density of a given particle, weighted by the density of the scattering length, R_g is actually one the most important and best-known SAXS-derived parameters, since it can be used directly towards determining the overall size of the sampled particles. For example, in the case of protein molecules featuring an identical number of amino acids, R_g will be reduced for compact (e.g. globular) proteins and increased for extended (e.g. unfolded) proteins. By knowing R_g and $I(s)$, the Guinier approximation ($s < 1/R_g$) and the equation $I(s) = I(0)\exp(s^2 R_g^2/-3)$ can then be used to determine the forward scattering, $I(0)$, which will be directly proportional to both the concentration and molecular weight of a sampled protein (Kikhney and Svergun, 2015).

Finally, the flexibility of the examined molecules (e.g. the degree of folding observed throughout a protein sample) can also be determined directly from analysing SAXS data sets and constructing a Kratky plot. Knowing that the scattering intensity of a solid particle will decay at a high angle (i.e. $I(s) = \sim 1/s^4$), globular or folded proteins will be represented on Kratky plots as marked peaks followed by downward phases, whereas unfolded proteins with large s values will be represented as plateaus (Figure 2.4.2.3 overleaf). Furthermore, should only the folding states of the different proteins contained within a polydisperse solution be important to know, then the resulting Kratky plot can be normalised by assuming $I(0) = 1$ and multiplying s by R_g, which will in turn reveal the requested information at the expense of disregarding the molecular weights of the investigated proteins. This is also the reason why normalised Kratky curves are also referred to as “dimensionless” plots (Kikhney and Svergun, 2015).

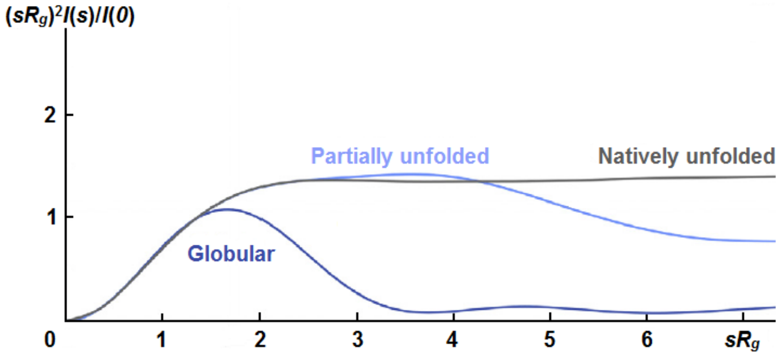

Figure 2.4.2.3. Normalised Kratky plot of the $(sR_g)^2I(s)/I(0)$ versus sR_g parameters obtained from the scattering profiles of three globular (dark blue), half-unfolded (light blue) and natively unfolded (grey) 60 kDa proteins (adapted from Kikhney and Svergun, 2015).

2.4.3. The virtues and limitations of SAXS

Some of the significant advantages of performing X-ray scattering experiments include their straightforwardness and time-efficiency compared to running MD simulations in scenarios such as determining the 3D distribution of ion and water content surrounding a target biomolecule (Nguyen et al., 2014). In addition, SAXS experiments only require minimal sample volumes per measurement (e.g. 10-100 µL) and the higher the particle concentration, the better the scattering profiles and, consequently, the quality of the resulting data will be (Kikhney and Svergun, 2015). Another major advantage of SAXS is represented by the fact that it can be used to investigate a very wide range of specimens. Most of these take the form of two-phase systems (e.g. a solvent carrying a single type of solute), but even multiphase systems in which the electron density of one phase significantly outweighs those of all other sample phases can be analysed as a two-phase system. Such approximations are regularly used in materials science (e.g. when verifying the composition of metal alloys or monitoring particle growth in solution), during the quality control phase of industrially-manufactured items (e.g. identifying defects in the structure of glass and diamonds or voids in the structure of ceramics), as well as in chemical engineering (e.g. isolating combustible hydrocarbons from coal, crude oil and other fuel sources), alongside many other fields in which performing similar studies via in-depth techniques such as TEM would ultimately prove a great deal costlier in both time and funding (Pauw, 2013).

Additionally, through its facile complementarity with advanced computational processing and other high-resolution techniques such as NMR and X-ray crystallography (Pérez and Nishino, 2012), SAXS permits the *ab initio* modelling of sampled particles and the study of complex biomolecular dynamics without requiring any prior knowledge of the examined specimens beforehand (Kikhney and Svergun, 2015). SAXS measurements are also frequently paired with wide-angle scattering (WAXS) ones, for example in the study of lipid raft models comprised of phosphatidylcholine, sphingomyelin and cholesterol (Quinn and Wolf, 2010).

Unfortunately, combining SAXS with other techniques can also hide its notable shortcomings, including the absence of an objective and undisputable means of determining whether the information provided by a SAXS-derived curve is accurate and true-to-life, even in simple scenarios such as working with background-corrected scattering profiles of monodisperse particle solutions. This ambiguity is felt even harder when studying polydisperse samples such as protein oligomer solutions (Kikhney and Svergun, 2015). The uncertainty surrounding the collected data stems primarily from the fact that typical SAXS experiments only focus on measuring the scattering intensity of a given sample while forgoing other parameters such as the phase of the incident X-ray radiation, usually resulting in the construction of scattering profiles that can match an entire host of potential sample configurations. In cases such as these, it is only by cross-referencing SAXS results with those obtained using other high-resolution techniques such as TEM and atom probe (AP) that the information collected via X-ray scattering can be considered reliable enough to be incorporated into a structural study (Pauw, 2013). Similarly, while significant particle agglomeration would be immediately apparent during SAXS data analysis, a minor yet still potentially relevant amount of aggregation would only result in a slightly raised R_g and, by association, an inaccurately extrapolated $I(0)$ value, which would nevertheless still give an incorrect impression on the morphology of the sampled particles (Pérez and Nishino, 2012).

In spite of these shortcomings, SAXS has been employed with great success in studies as diverse as developing novel molecular rulers for providing quantitative distance measurements between macromolecules labelled with gold nanocrystal probes (Mathew-Fenn et al., 2008), monitoring the deposition of positively-charged nanoparticles in a layer at a silica-water interface (Brenner et al., 2012) and determining the aggregation and sedimentation rates of silica nanoparticles in solution after interacting with globular proteins such as lysozyme (Bharti et al., 2011). Furthermore, SAXS was also successfully used in the current project towards providing additional confirmation of correct SSBLM formation on the surfaces of silica nanoparticles, as will be seen further on in Chapter 4.

2.5. Phage Display Screening

Drug discovery has long resorted to the high-throughput screening of million-strong candidate molecule libraries in search of “hits” that can perform a desired therapeutic action with as high affinity and specificity as possible (Hoogenboom, 2002). Throughout recent years, however, the focus of the pharmaceutical industry has gradually shifted from traditional small molecule drugs, obtained via the screening of combinatorial chemistry libraries, to antibody-based therapeutics involving “protein-binding proteins”. These compounds not only exhibit higher specificities and affinities for their designated targets, but do so while also provoking less side effects in patients as well (Stumpp et al., 2008).

The members of this novel drug class, which includes monoclonal antibodies (Clementi et al., 2012), single-chain variable fragment antibodies (scFvs) (Ahmad et al., 2012) and designed ankyrin repeat proteins (DARPins) (Hausammann et al., 2013) are routinely identified via phage display screening – a powerful technique capable of interrogating vast candidate libraries in order to identify nanomolar-affinity binders without the traditional need for animal immunisation and antisera extraction (Hanes et al., 2000).

2.5.1. Introduction to phage display screening

Initially developed more than 30 years ago for the selection of peptide binders (Smith, 1985), phage display technology revolves around the expression of exogenous antibody fragments and other such protein-binding proteins on the extracellular surface of a suitable bacteriophage vector following genetic manipulation (Figure 2.5.1.1).

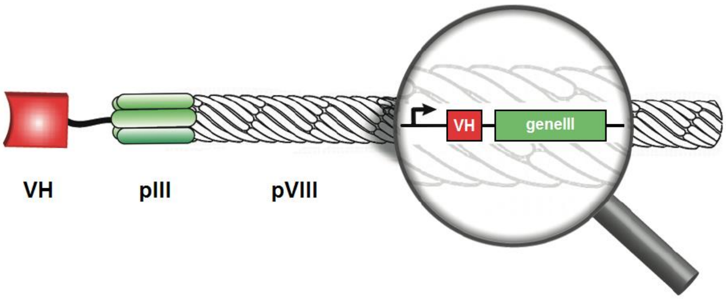

Figure 2.5.1.1. Diagram of a typical filamentous bacteriophage displaying a binder. The DNA encoding the antibody fragment, in this case a variable heavy chain (red), is fused with the bacteriophage gene encoding the pIII coat protein (green). Once the modified pIII protein is expressed, the V_H paratope will also be displayed on the bacteriophage surface. For the purpose of clarity, only the pIII and pVIII coat proteins are depicted here (adapted from Lee et al., 2007).

While other methods such as ribosome display have been successfully used for isolating numerous high-affinity binders since the concept was first introduced (Hanes and Plückthun, 1997), filamentous bacteriophages represent the original vehicles used in the display and screening of binding peptides and antibody fragments (Chasteen et al., 2006).

The creation of diverse libraries of phages expressing "naïve" binders and their subsequent screening against a given antigen is in fact not entirely dissimilar to the immune-triggered secretion of specific antibodies in an infected host (Hanes et al., 2000). Phage display libraries are regularly created by inserting the coding oligonucleotides or gene sequences of the candidate binders into the genome of filamentous bacteriophages, specifically within the genes responsible for encoding either of their five different coat proteins – pIII, pVI, pVII, pVIII and pIX (Baek et al., 2002). The necessary genetic manipulation can be performed by either fusing the ligand genes onto the phage genome itself (i.e. using phage vectors) or by working with a plasmid harbouring only the genes of the chosen coat protein and then transfecting the recombinant DNA into a helper phage via phagemid vectors (Lee et al., 2007). Out of the five coat proteins that have been used for binder display thus far, pIII remains one of the most commonly employed, partly due to its role in bacterial infectivity (Hoogenboom, 2002). Through the phage format approach, all recombinant pIII proteins will be expressed from geneIII-binder fusions and will usually display 3-5 copies of the respective binder on their surface (i.e. "low-level" multivalent display). Should "high-level" multivalent display be desired, then the genes encoding the pVIII protein should be modified instead, since this particular coat protein can display more than 1,000 binder copies per unit on account of its increased surface area. Conversely, the phagemid format yields binder copies derived from the helper phage, which are then displayed monovalently (i.e. in single copies) on the surface of each individual phage (Lee et al., 2007).

Just as natural antibodies undergo several cycles of somatic mutation in order to bind their antigens with increasingly higher affinities, so too are phage-displayed binders subjected to multiple rounds of selection or "panning" before ligands with near-picomolar affinities for their targets can be identified (Figure 2.5.1.2 overleaf). After the phages have been modified with the binder genes, they are infected into *E. coli* and cultured to express vast binder libraries, which are then screened against their designated immobilised antigens through recursive binding and washing cycles (i.e. selection rounds). Following multiple rounds of selection (usually 3-5), only those phages displaying the highest affinity binders will be eluted and amplified in *E. coli* for further testing (Hoogenboom, 2002).

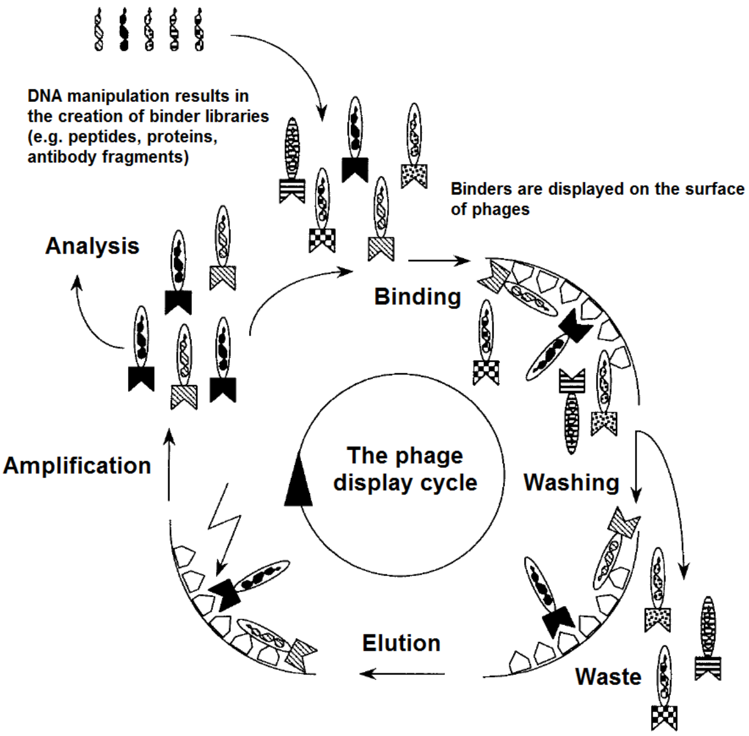

Figure 2.5.1.2. Schematic representation of the phage display screening process, also known as the "phage display cycle". The DNA of the candidate ligands (e.g. peptides, proteins) is batch-cloned into the phage genome as part of one of the coat proteins (i.e. pIII, pVI, pVII, pVIII or pIX). Subsequent infection and virion replication in *E. coli* results in phage libraries numbering millions of candidates, which are then screened against the immobilised targets of interest through recursive binding and washing cycles. Identified "lead candidate" binders are then eluted, re-infected into *E. coli* and amplified for further testing (adapted from Hoogenboom, 2002).

During routine phage display screening, it is common to use libraries created using the phage format for the initial selection rounds since the multivalently-displayed paratopes will have a higher chance at binding the target antigen. Once high-affinity binders have been identified, the phagemid format can be employed instead so as to promote the enrichment of phages that monovalently-display only those binders deemed to be "lead candidates". This way, investigators can more accurately characterise the affinity of a single binder molecule against its target of interest and not that of several molecules binding collectively to the same antigen (Beaber et al., 2012).

2.5.2. Types of phages used in the display of antibody binders

Since the first binder-coat fusion protein that started this entire field was displayed on an M13 bacteriophage following the insertion of *Eco*RI genes into the genome encoding its pIII coat protein (Smith, 1985), the vectors commonly associated with phage display screening are still represented by the *E. coli* bacteriophages M13, fd and f1, which together form the Ff filamentous phage class (Chasteen et al., 2006). Sharing a staggering 98% sequence identity, these phages feature a single-stranded DNA conformation organised inside a 7 nm-wide, 900-2,000 nm-long cylindrical structure. Thus far, they have been successfully used in selecting a multitude of high-affinity binders against targets as diverse as membrane-bound receptors, enzymes and nucleic acids (Baek et al., 2002).

Throughout recent years, however, T-even bacteriophages have enjoyed increasing popularity as alternative vehicles for binder display (Gamkrelidze and Dąbrowska, 2014). Classified as members of the order *Caudovirales*, and more specifically the *Myoviridae* family, the T-even phages T2, T4 and T6 are easily-recognisable by their lunar-lander shapes (Figure 2.5.2.1). Structurally, these are tailed viruses comprising of a prolate icosahedral head containing the ~170 kbp double-stranded DNA, followed by a contractible tail sheath protecting the internal DNA delivery tube and finally ending in a baseplate featuring six protruding tail fibers involved in bacterial cell membrane recognition and binding (Gamkrelidze and Dąbrowska, 2014).

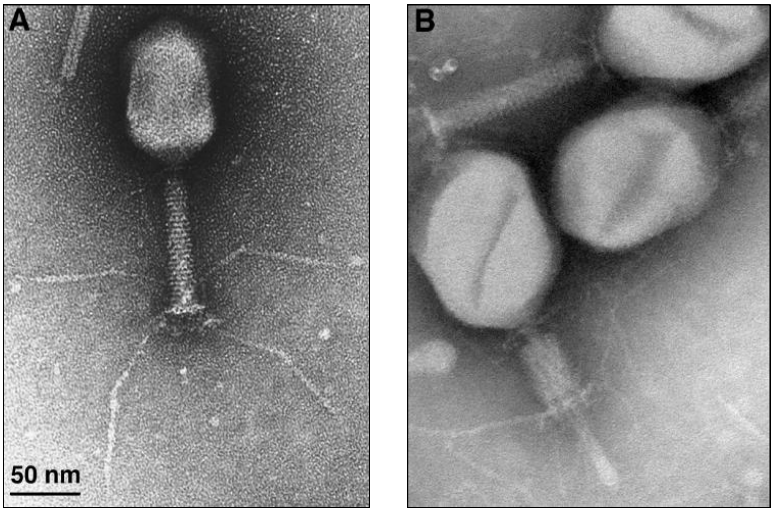

Figure 2.5.2.1. Transmission electron micrographs showcasing the famous NASA lunar lander shape of the T4 bacteriophage: A) The 168,903 bp double-stranded DNA is contained within its prolate icosahedral head, while the six protruding tail fibres are used to search for the membranes of potential bacterial hosts; B) Once the virus has bound to a bacteria, the tail sheath contracts in order to reveal the internal delivery tube through which the viral DNA will be released into the cytoplasm of the host cell (adapted from Miller et al., 2003).

T-even bacteriophages have been studied extensively since the 1940s and were involved in many seminal developments, including the discovery of mRNA, of the connection between nucleic acids and genetic information and the fact that the genetic code is organised in nucleoside triplets. Of the three members of the T-even phage class, T4 has seen the most extensive use due to its capability of completely inhibiting the gene expression mechanisms of a bacterial cell, which greatly aids in the discrimination of viral molecular dynamics from those of its host (Miller et al., 2003).

Upon their attachment and infection of a host cell, bacteriophages can reproduce according to one of two cycles: lytic or lysogenic (Figure 2.5.2.2). Whereas through the lytic cycle the viral DNA ends up co-existing with the bacterial DNA as a separate cytoplasmic entity until the replicated viral clones escape the host cell via membrane lysis, through the lysogenic cycle the viral DNA becomes a part of the bacterial genome, integrating non-destructively into the nucleus of its host without affecting its ability to live and divide normally (Domingo-Calap et al., 2016). Since T4 bacteriophages fall into the former category and replicate hundreds of times before their host cell is ultimately destroyed, their exclusively lytic lifecycle constitutes an ideal phage amplification strategy requiring only minimal volumes of *E. coli* culture (Kutter et al., 1995).

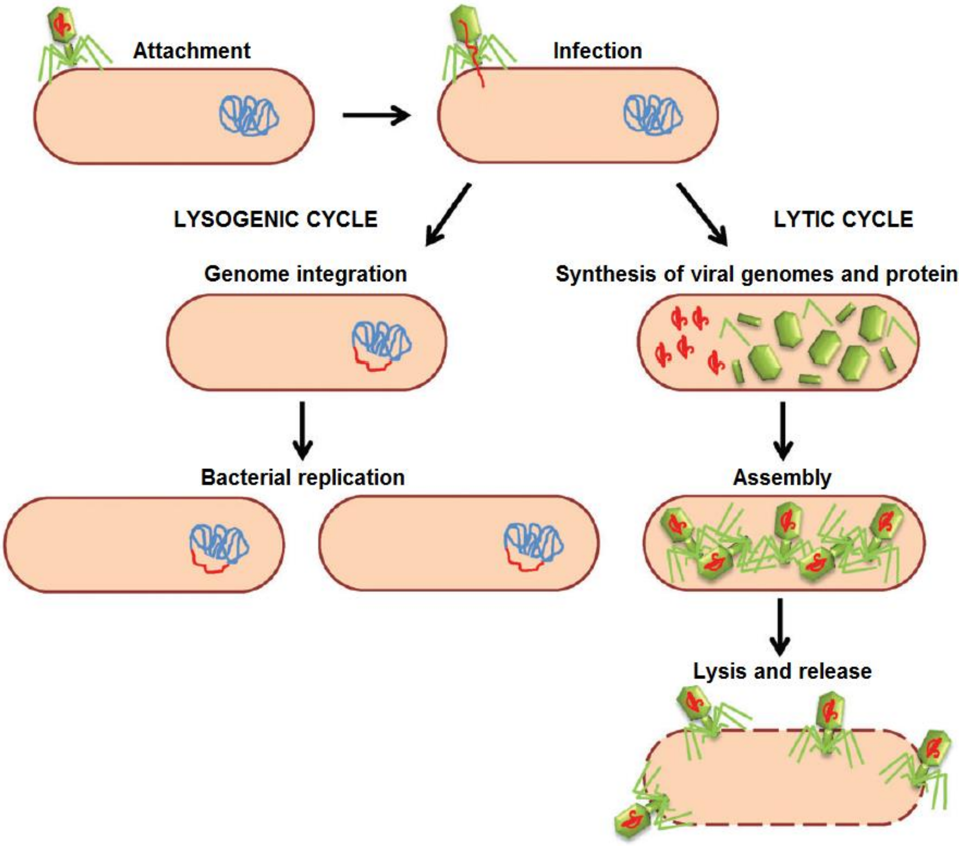

Figure 2.5.2.2. The two possible bacteriophage life cycles. Left: the lysogenic cycle, during which the viral DNA inserts into the bacterial genome and replicates alongside the bacterium without producing progeny. Right: the lytic cycle, during which the viral DNA subjugates the replication machinery of its host in order to create more virions that ultimately escape through the cell membrane in search of other hosts to infect (adapted from Domingo-Calap et al., 2016).

2.5.3. Phage versus phagemid library creation

The two pathways leading to the creation of phage libraries expressing recombinant binding proteins each come with their own virtues and limitations. Using the phage format, the genes encoding the ligands are inserted directly into the phage genome and, as such, amplifying a single clone will yield viral vectors that are both genotypically and phenotypically identical and will all display the ligand-coat fusion proteins multivalently. Phage libraries are considerably less laborious to produce than phagemid libraries, which depend not only upon the availability of helper phage, but also upon their infection into bacterial cultures at specific growth stages. The amplification of phage library members is also straightforward and only requires the culturing of more infected bacteria, which represents a major advantage for high-throughput applications where large numbers of binders are simultaneously screened against dozens of different antigens. Furthermore, the multivalent nature of binder display among phage library members translates into multiple copies of identical paratopes being expressed on the surface of the same phage, ultimately leading to the recovery of more binders after a round of selection, as well as the potential discovery of more diverse ligands by the end of the screening phase. This comes into stark contrast with phagemid particles, since these only incorporate their recombinant proteins in as a little as 1-10% of all library members due to their monovalent display capabilities, which conversely also form a prerequisite for subsequent affinity maturation studies (Chasteen et al., 2006).

Phagemid vectors thus represent the second pathway through which phage display libraries encoding recombinant binding proteins can be built, but in their case this can only be accomplished with the help of other phages that must provide them with additional proteins without which they cannot create fully-functional, binder-displaying clones. Given their role, these protein-donor particles are commonly referred to as “helper phages” and generally comprise of Ff-class filamentous bacteriophages that have been engineered with a specific antibiotic resistance, an additional origin of replication and a disabled packaging signal. Phagemid particles represent the preferential choice for displaying larger binding molecules such as antibody fragments and, compared to phage vectors, are not only easier to genetically-engineer additional properties into, but also enjoy a more efficient ligation-transformation process, resulting in the possibility of building larger binder libraries than through the use of the phage format (Chasteen et al., 2006).

In order to create a phagemid vector, the nucleotide sequences encoding the binding proteins are cloned in-frame into a plasmid containing not only the genes responsible for the expression of one of the phage coat proteins, but also the phage replication and packaging signals required for the subsequent inclusion of the phagemid into the helper phage particles (e.g. M13KO7 or VCSM13), whose own packaging signals have been disabled to promote the expression of the ligand-coat recombinant binding proteins (Baek et al., 2002). Once the phagemid has been transformed into *E. coli*, the cells are infected with helper phage, which triggers the packaging of the phagemid genome together with the genes encoding the wild-type coat proteins of the helper phage. Upon amplification, the resulting virions will ultimately display the ligand-coat recombinant binding proteins instead of the wild-type ones – a process known as "phage rescue" (Beaber et al., 2012).

In practice, however, it has been observed that although the disabled packaging signal of helper phages generally prevents them from outnumbering the phagemid particles, any newly-amplified phages will still heterogeneously display both the ligand-coat fusion proteins, as well as the wild-type proteins endogenous to the helper phage itself. While this could potentially reduce the number of negative avidity-related interactions occurring during the subsequent selection rounds, the ratio between the recombinant and wild-type displayed proteins is, unfortunately, regularly skewed towards the expression of the latter due to the proteolytic degradation occurring within the *E. coli* periplasmic space. This directly translates into a majority of the ligand-coat fusion proteins being degraded well before the phages can even be subjected to antigen screening. Because of this, most phages created using a typical phagemid vector will not display the encoded ligands at all and will unfortunately only serve to further hinder the already-difficult discovery of high-affinity binders originating from a naïve phage library. The number of these "bald" phages can, however, be lessened by capitalising on the antibiotic resistance conferred to newly-amplified phages expressing the phagemid-encoded recombinant proteins. By only selecting those cells harbouring the same antibiotic resistance, the chances of recovering fully-functional phages displaying the ligand-coat proteins are significantly increased (Chasteen et al., 2006). A similarly beneficial outcome can also be reached if the helper phage themselves have been genetically-engineered beforehand to encode cleavable wild-type coat proteins (Baek et al., 2002) or to feature rare codon clusters and ribosome binding site spacing alterations that promote a reduction in the overall expression levels of wild-type coat proteins, such as those employed by the novel XP5 helper phage class (Beaber et al., 2012).

In the end, it becomes evident that libraries created using either phage or phagemid vectors will differ from one another in several important ways. If the effort attributed to the initial genetic manipulation is to be considered (i.e. the cloning and transfection of binder-encoding genes), then working with phagemids instead of directly modifying phages would represent the preferred choice, especially since libraries built via phagemid vectors usually number many more binding candidates (e.g. 10^{10}-10^{12}). Concurrently, the identical genetic arrangement present within libraries created via direct phage manipulation would invariably be affected by the low copy number of the phage vectors and the poor functionality of the wild-type gene promoter. Finally, filamentous phage vectors also suffer from another issue in the form of a low resistance to exogenous gene sequence deletions, which can lead to the selective growth of only those phages that possess an optimal genetic make-up. This would mean that while only those recombinant phages featuring minimal genetic manipulation would ultimately be allowed to develop into functional particles, phagemid vectors – being comprised of circular DNA – would be affected to a much lesser extent by unpredictable DNA deletions and their encoded binders will have a better chance at being ultimately displayed on amplified phages (Chasteen et al., 2006).

2.5.4. The virtues and limitations of phage display screening

In diametric opposition to raising hybridoma-based antibodies inside immunised animals, the main advantage of phage display screening is given by its capability of expressing potentially millions of different proteinaceous binders and then selecting only those showing the most promising affinities against virtually any antigen, biological or otherwise, in a highly efficient manner and without ever requiring any sort of animal involvement throughout the entire process (Lee et al., 2007). Furthermore, as opposed to *in vitro*-exclusive display methodologies such as ribosome display, phage display can also be successfully performed *in vivo* as well, by injecting live animals with entire phage-bound binder libraries and then identifying which candidate ligands remain bound to the tissue of interest (Stumpp et al., 2008).

Other virtues of this technique are represented by its significant time- and cost-effectiveness, both during the relatively straightforward creation of phage libraries and the rapid selection of high-affinity binders, as well as by its complementarity with other high-throughput protein interaction techniques such as yeast hybrid systems (Gamkrelidze and Dąbrowska, 2014). If any further improvements to phage display screening are to be considered, then the overall quality of the binder libraries themselves and the speed of their selection become the rate-limiting steps in need of additional optimisation before phage display screening can be implemented wholly into high-throughput industrial scenarios (Schilling et al., 2014).

When considering the potential pitfalls of the technique, however, it is important to be aware that a synthetically-created, naïve phage library might not always include high-affinity binders to a given antigen. This shortcoming is further compounded by the often-poor display of ligand-coat fusion proteins (e.g. only 1-10% of phagemid library members might express them) or their proteolytic degradation over multiple rounds of selection, resulting in “bald” phages that outnumber functional clones by factors as high as 200:1 (Beaber et al., 2012). In order to minimise these negative aspects, phage display libraries usually encompass between 10^7-10^{10} different members and any high-affinity binders identified within a selection round will be routinely amplified up to $10^5\times$ so as to bolster the efficacy of any future panning or binding characterisation steps (Baek et al., 2002). Further limitations of phage display technology stem from the use of helper phage, which need to be continuously produced and added to growing bacterial cultures within very specific D_{600nm} intervals in order to maintain a steady rate of phage production. Upon considering the inclusion of phage display into applications requiring the high-throughput screening of millions of potential binding candidates, it becomes easy to imagine the many delays that such a laborious rate-limiting step would cause. Fortunately, alternatives to helper phages have become available during the past decade in the form of novel helper plasmids that allow bacteria to be transformed with the phagemid and then be cultured overnight without the need for any D_{600nm} measurements at all. Instead, the following day the replicated particles can simply be harvested by centrifuging the cell debris and collecting the phage-rich supernatant (Chasteen et al., 2006).

To date, phage display technology has led to the development of several blockbuster antibody drugs incorporating high-affinity binders (Reichert et al., 2005). These include the anti-neoplastic monoclonal antibodies bevacizumab (Avastin), cetuximab (Erbitux), rituximab (Rituxan) and trastuzumab (Herceptin), all of which have been approved by the US Food and Drug Administration (FDA) for the treatment of cancer patients (Adams and Weiner, 2005). The following subsections, describing the major classes of binders selectable via phage display screening, will only further highlight the relevance of this technique in the fields of immunology, protein engineering and novel antibody-based drug development.

2.5.5. Immunoglobulins

To this day, natural antibodies or immunoglobulins (Igs) remain the most widely recognised binding proteins. Based on their distinct immunological activities and distribution throughout the body, they can generally be categorised into one of five main antibody classes: IgG (main serum antibody involved in protection against bacteria and viruses), IgE (triggers histamine release following the detection of allergenic compounds and protects against parasitic helminth infections), IgA (prevents pathogens from colonising mucosal linings), IgM (involved in early bacterial and fungal infection response) and IgD (stimulates the production of antimicrobial and proinflammatory factors in basophils) (Woof and Burton, 2004; Chen et al., 2009). Other antibody classes not present in mammals have also been identified, including IgY – found in non-galliform birds such as ducks (Lundqvist et al., 2006) and IgW – discovered in cartilaginous fish such as sharks (Bernstein et al., 1996). Regularly secreted as antigen receptors on the surfaces of vertebrate plasma cells in response to intruding foreign pathogens (Borghesi and Milcarek, 2006), immunoglobulin molecules feature a distinctive “Y”-shaped structure (Figure 2.5.5.1) comprised of identical pairs of light and heavy polypeptide chains connected via disulfide bridges (Schilling et al., 2014).

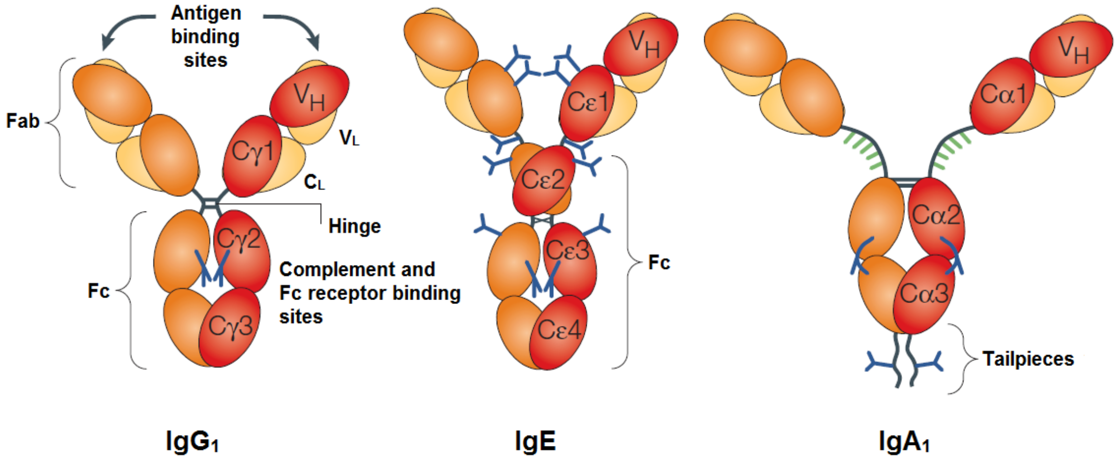

Figure 2.5.5.1. Structures of three human antibody classes: IgG, IgE and IgA. The number of red and orange heavy chain domains varies between the different classes, while the pair of yellow light chains is identical and shared between all immunoglobulins. N-linked oligosaccharides (blue) are also featured across the chains of IgG and IgE antibodies, while O-linked oligosaccharides (green) form part of the hinge region of the IgA$_1$ molecule. The amino-acid, carboxy-terminal tailpiece extensions of IgA antibodies grant them the ability to assemble into polymeric immunoglobulin structures (adapted from Woof and Burton, 2004).

The peptide sequences identified within each light and heavy chain region have led to the classification of their respective domains as either variable (V) or constant (C) (Litman et al., 1993). Therefore, immunoglobulin light chains each comprise of one variable domain (V_L) and one constant domain (C_L), while their heavy counterparts feature one variable domain (V_H) and multiple constant domains (C_H) (Woof and Burton, 2004). Both domain types can be even further subdivided into lambda (λ) and kappa (κ) light chain domains and alpha (α), delta (δ), epsilon (ε), gamma (γ) and mu (μ) heavy chain domains (Syndercombe Court et al., 2009, p. 266). Since the pair of light chains is identical and conserved between all antibody classes, immunoglobulins are thus classified according to the type and number of their heavy chain domains, ranging from just three in human IgG and IgA antibodies, to four in IgE molecules, to five in duck IgY antibodies (Lundqvist et al., 2006) and as many as seven in carcharhine shark IgW immunoglobulins (Bernstein et al., 1996). A distinct hinge region was also identified within the structures of antibody molecules featuring only three constant domains, varying in length and structure between the different antibody classes (Woof and Burton, 2004) and likely conferring increased flexibility to their associated heavy chain domains (Syndercombe Court et al., 2009, p. 266).

Immunoglobulin antigen specificities are dictated by the light and heavy variable domains located on the two "arms" of their "Y"-shaped molecules. Taken together, the two arms form the Fab (fragment-antigen binding) or hypervariable regions (Al-Lazikani et al., 1997) displaying the antigen-binding sites at the tip of each arm (Syndercombe Court et al., 2009, p. 266). Conversely, the basal half of immunoglobulin molecules, comprised exclusively of disulfide-linked heavy chain constant domains, forms the Fc (fragment-crystallisable) region, which facilitates their interaction with effector molecules such as complement in order to dictate the role of a plasma cell within the overall immune activity of the host organism (Woof and Burton, 2004).

2.5.6. Monoclonal antibodies

The strength of interaction between the different immunoglobulin classes and their respective antigens – termed binding "affinity" when describing the strength of individual antibody-antigen bonds or "avidity" when referring to the number of antigens that a certain immunoglobulin can bind (Syndercombe Court et al., 2009, p. 267) – is so high that antibody-based drugs have become widely researched and developed by the pharmaceutical industry. While classic antibodies or "antisera" are still collected from the blood of humans or animals that have developed natural immunities to specific antigens, so that passive immunity might then be conferred upon other patients or animals as well, such methods of immunisation are ultimately limited in their scope due to their reliance on polyclonal antibodies. Since antibodies are secreted by the entire plasma cell population of the particular donor that came into contact with the respective antigen, antisera actually comprise of an entire host of antibodies with mixed affinities and specificities and, thus, the efficacy of such treatments will always be dependent upon the quality and amount of collected antibody serum (Rang et al., 2007, p. 772).

Fortunately, all of these limitations became avoidable in 1975, when Georges Köhler and César Milstein from the Medical Research Council (MRC) Laboratory of Molecular Biology in Cambridge, UK, first developed a “hybridoma” cell line (Figure 2.5.6.1) by fusing immortalised mouse myeloma cells with spleen B lymphocytes from an immunised specimen secreting anti-sheep red blood cell (SRBC) antibodies (Köhler and Milstein, 1975).

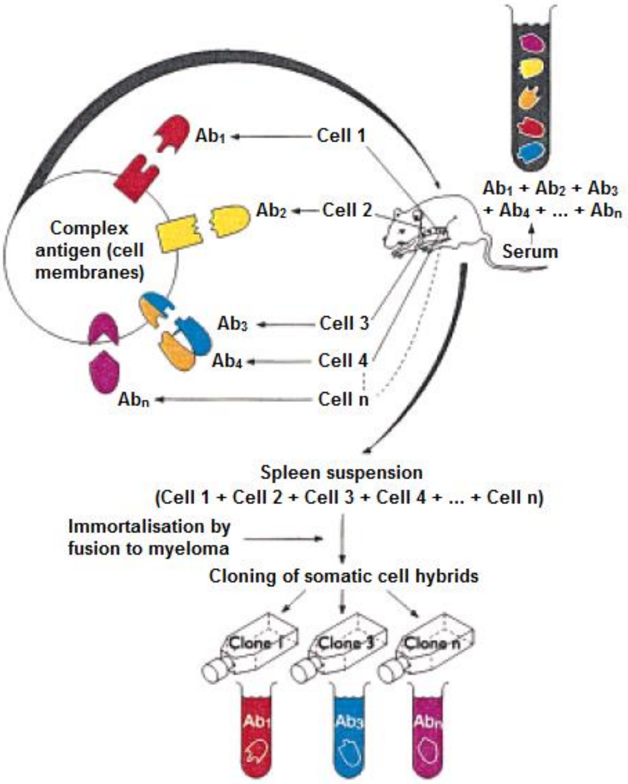

Figure 2.5.6.1. Schematic of a hybridoma cell line producing monoclonal antibodies against a complex antigen. A mouse is injected with foreign cell membranes and thus generates a multitude of different antibodies. Its antibody-rich serum is then extracted and the antibody-secreting B lymphocytes are immortalised via fusion to myeloma cells. Through the cloning of the resulting hybridomas, the selection of monoclonal antibodies against the individual antigens expressed by the injected immunogenic cell membranes now becomes possible (adapted from Milstein, 1999).

The fusion process effectively transferred the immortal quality of the myeloma cell line to the spleen B lymphocytes, which could afterwards be perpetually cultured *in vitro*. By diluting the growth medium until a single lymphocyte could be selected, a vast number of monoclonal anti-SRBC antibodies could thus be derived from the same B cell and therefore share the same elevated specificity and affinity for their designated antigen. Since monoclonal antibodies displaying high affinities and specificities could then be raised against virtually any antigen, they were quickly introduced to clinical trials after their emergence in the early 1980s. Unfortunately, by virtue of being expressed in an animal system, fully murine antibodies also triggered immune responses in approximately 75% of human patients and thus had to undergo “humanisation” before they could be effectively used for their intended therapeutic purposes. This was achieved by modifying the antibody expressor genes to include cDNA encoding human Fc domains while preserving the mouse Fab regions responsible for antigen binding, which resulted in not only a much better integration into the human immune system, but also a markedly improved serum half-life (Rang et al., 2007, p. 773). As the pharmaceutical industry gradually moved towards developing fully human monoclonal antibodies, the chimeric human-murine molecules were improved to the point of only including murine paratopes on otherwise fully human Fab and Fc regions. Similarly, throughout recent years hybridoma cell lines have also been steadily phased out by recombinant antibody production in transgenic mammalian cells (Reichert et al., 2005).

Since their humanisation, a total of 23 monoclonal antibodies have already been approved by the FDA for use in a clinical environment (Toporkiewicz et al., 2015). These include treatments for Crohn’s disease (natalizumab), psoriasis (efalizumab), asthma (omalizumab), rheumatoid arthritis (adalimumab) and multiple sclerosis (alemtuzumab) (Reichert et al., 2005). Several monoclonal antibodies have also been selected against cancer markers such as CD20 (rituximab) and HER2 (trastuzumab), becoming staples of human anti-cancer treatments. Moreover, through their capability of being coupled to cytotoxins, radioisotopes and other such conjugates, monoclonal antibodies have steadily increased their therapeutic and diagnostic versatility, leading to the development of commercialised immunoconjugated antibody drugs such as Mylotarg (gemtuzumab ozogamicin), Zevalin (ibritumomab tiuxetan) and Bexxar (131I-tositumomab). Considering all of the above developments, it should come as no surprise that, since their inception, over 150 different monoclonal antibodies have undergone clinical trials across the world (Toporkiewicz et al., 2015).

2.5.7. Designed ankyrin repeat proteins

For many years, monoclonal antibodies and the newer antibody fragments such as single-chain variable fragments (scFvs) represented prime examples of protein binders displaying high affinities and specificities for their intended therapeutic targets. Unfortunately, their successful application *in vivo* has always been constrained by both their poor conformational stability under adverse biological conditions, as well as their propensity for aggregation in solution due to their antiparallel β-sheet domain arrangement (Schilling et al., 2014). Luckily, more recent developments in synthetic antibody library design and selection have managed to improve upon these limitations quite significantly.

Newer, scaffold-based binding proteins feature a modular assembly process that not only dramatically expands their potential applications horizon, but also imbues them with very desirable biophysical characteristics that confer significant advantages over traditional monoclonal antibodies in both *in vitro* and, more importantly, *in vivo* scenarios. These include low to non-existent aggregation in solution, a high potential for chemical coupling to functional conjugates such as fluorophores and cytotoxins, the absence of structural disulfide bonds (a requisite for functional *E. coli* cytoplasmic expression systems), high levels of secretion for both mono- and multimeric assemblies and the possibility of extending their *in vivo* half-lives through site-specific PEGylation or fusion to long-lived serum proteins (Boersma and Plückthun, 2011). With the advent of phage and ribosome display, *in vitro* production of antibody-like binders has become not only possible, but highly pursued throughout the entire pharmaceutical industry. These techniques enabled biological drug divisions to select scaffold binding proteins such as adnectins, avimers, anticalins and affibodies with high affinities against a variety of target antigens at a mere fraction of the production cost of monoclonal antibodies (Stumpp et al., 2008).

Developed in the early ‘00s through research conducted by Prof. Andreas Plückthun’s group from the Biochemistry department at the University of Zurich, Switzerland (Molecular Partners, 2016a), designed ankyrin repeat proteins (DARPins) represent a novel class of binding proteins that have overcome the limitations of traditional monoclonal antibodies, namely expensive formulation, difficult extraction and low tissue penetration (Stumpp et al., 2008). Furthermore, while monoclonal antibodies can be either murine, primatised or, in the best of cases, chimeric or humanised (Reichert et al., 2005), DARPins are derived from naturally-occurring ankyrin repeat proteins that are abundantly encoded throughout the human genome (International Human Genome Sequencing Consortium, 2001), contributing to a multitude of high-affinity protein-protein interactions courtesy of their intriguing modular architecture (Schilling et al., 2014). DARPins capitalise upon this property by being comprised of a varying number of protein motifs (i.e. library modules) that stack together to form the target binding domain (Figure 2.5.7.1 overleaf). Typical DARPin molecules regularly feature between 4-6 motifs, but examples of single proteins consisting of up to 29 library modules have also been documented in the literature (Tamaskovic et al., 2012). Their facile modularity grants DARPins an enormous degree of potential diversity that can lead to the creation of binder libraries numbering billions of different ligand combinations (Stumpp et al., 2008).

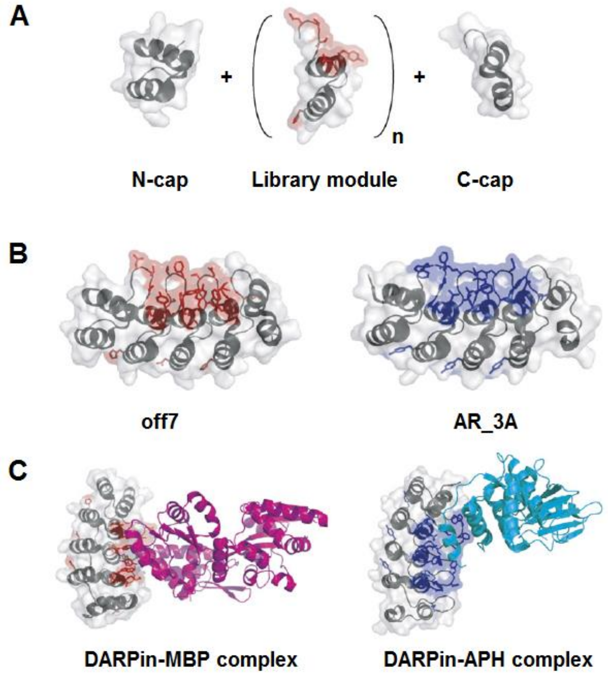

Figure 2.5.7.1. Diagram of DARPin library design: A) DARPins comprise of two hydrophilic ends (N- and C-), capping varying numbers of internal library modules (n, shown here in grey). Every library module is comprised of 33 amino acids featuring 7 variable side chains (red); B) Examples of two DARPins – "off7" and "AR_3A" – composed of three library modules each and with their randomised target binding regions coloured in red and blue, respectively; C) DARPins off7 and AR_3A forming complexes with maltose binding protein (MBP) (PDB ID: 1SVX) and aminoglycoside phosphotransferase (APH) (PDB ID: 2BKK), each of them connected at their respective red and blue randomised target binding regions (adapted from Stumpp et al., 2008).

From early on in their inception, DARPin libraries were constructed around a consensus design approach that helped define what their smallest building block – the library module – should contain. Originating from a desire to determine the occurrence of particular amino acids at specific positions based on multiple amino acid sequence alignments (Kajander et al., 2006), the repeat protein consensus design was applied to DARPins based on an initial alignment of 229 naturally-occurring ankyrin repeat proteins, each comprising of 33 amino acids of which 7 were variable (Stumpp et al., 2008). Upon further refinement, a total of 2,200 amino acid sequences were established as consensus-approved DARPin library modules (Binz et al., 2003). The consensus design approach ultimately resulted in the possibility of creating highly stable and extremely versatile binders that could have modules added, deleted or exchanged on a case-by-case basis so as to better suit their intended purposes. Furthermore, their known amino acid sequences opened them towards even further manipulation, such as conjugation to specialised functional groups (Boersma and Plückthun, 2011). These include PEG for extending DARPin *in vivo* half-lives, electrophilic moieties for binding target proteins covalently, cytotoxic compounds for targeted anti-cancer therapies and fluorophores, radiolabels or contrast agents for *in vivo* magnetic resonance imaging (MRI) (Moody et al., 2014).

When generating a DARPin library, the modules are genetically engineered to feature hydrophilic N- and C-caps that flank the otherwise hydrophobic central binding domain, giving rise to potentially billions of "N×C" binders, where "×" represents the number of library modules employed in the creation of a specific binder. The 7 variable amino acid positions grant individual modules millions of different sequence variations and, as such, a DARPin library created using only two of these modules can reach diversities of up to 10^{14} unique binders (Stumpp et al., 2008). Their consensus design enables DARPins to closely resemble human ankyrin repeat proteins (i.e. 67-71% sequence identity) (Stumpp et al., 2008), while the absence of an Fc domain renders them far less prone to trigger unfavourable immune responses in human patients compared to antibody fragments, monoclonal antibodies, aptamers, folates, lectins or transferrins (Toporkiewicz et al., 2015). Since a single library module only weighs approximately 3.5 kDa, conventional DARPins featuring 4-6 modules are thus ten times smaller than classic immunoglobulin molecules, which greatly favours their serum solubility (>100 mg/mL), half-life (>60 days) and tissue penetration. DARPins are also much less susceptible to both thermal and chemical denaturation (>100 °C or 5 M guanidine hydrochloride, respectively) and their stability actually increases proportionally to their number of constituent repeats. Furthermore, they express to a very high degree even in low expression bacterial strains such as XL1-blue *E. coli*, generating yields upwards of 200 mg of purified protein per litre of shake flask culture (Stumpp et al., 2008) – a result that can be improved upon even further through the use of specialised expression strains (e.g. the BL21 *E. coli* used in the current project) along with cell culture fermentation technologies.

Coupled with modern *in vitro* selection technologies such as phage display, DARPin binders with low-nanomolar to picomolar affinities can be successfully selected against a variety of different protein targets (e.g. cytokines, proteases, kinases and membrane-bound transporters and pumps) following a minimal number of selection rounds (Jost and Plückthun, 2014). Their diminutive sizes allow DARPins to be primed for vaccination (Wallmann et al., 2010) and to be administered *in vivo* through a variety of possible routes, including topically, orally and nasally (Stumpp et al., 2008), while also benefitting from a rapid clearance via the kidneys (Weidle et al., 2013). Given their high stability, serum solubility and broad functionalisation capabilities, DARPin-based drugs can be readily formulated from either monovalent DARPins, harbouring no additional modifications, or from molecules that have been chemically or genetically conjugated to other useful moieties (Figure 2.5.7.2), enabling them to serve either as agonists, antagonists or inhibitors at their designated therapeutic targets (Stumpp et al., 2008).

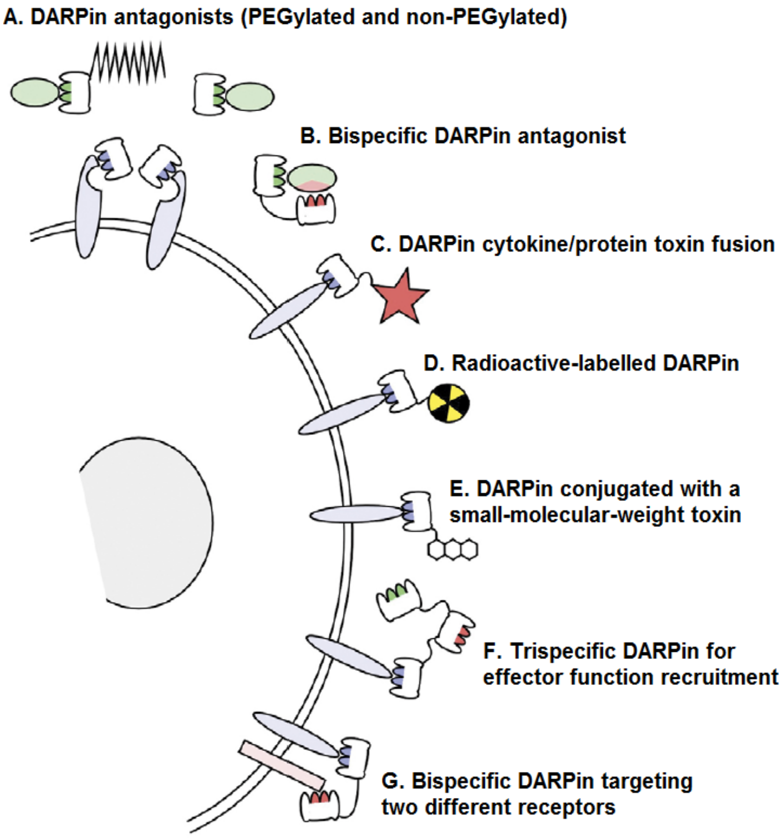

Figure 2.5.7.2. Functionalisation capabilities of therapeutic DARPins: A) Monovalent DARPin antagonists binding to either a ligand (green) or a membrane-bound receptor (blue). One of the DARPins has been PEGylated for extended serum half-life; B) Bispecific DARPin conjugate capable of binding two epitopes on the same target for improved efficacy; DARPins targeting cell surface antigens while being fused to either (C) another protein such as a cytokine, (D) a radioactive label for diagnostic purposes or (E) a small-molecular-weight toxin for added cytotoxic activity; F) Trispecific DARPin conjugate capable of binding a tumour antigen, as well as additional effector cells and serum proteins; G) Bispecific DARPin binding two different cell-surface antigens in hopes of demonstrating increased tumour selectivity compared to monovalent binders (adapted from Stumpp et al., 2008).

Thus far, multiple DARPin-based therapeutic compounds have shown safety and efficacy in preclinical models when used for diagnostic purposes (Stumpp et al., 2008), such as detecting coagulation factor VIII inhibitory antibodies in haemophilia A patients (Hausammann et al., 2013) and binding to HER2 factors in solid tumours (Zahnd et al., 2010). Cancer immunotherapy also benefitted from the use of DARPin technology via the adoptive transfer of T lymphocytes expressing DARPin-based chimeric receptors for the recognition of solid tumour antigens (Hammill et al., 2015).

Anti-cancer DARPins have also been successfully conjugated to both cytotoxins for tumour-specific payload delivery, as well as modified serum albumin modules for extended half-life (Simon et al., 2013), while other binders still have been displayed on the capsids of adeno-associated viral vectors targeted against the tumour antigen HER2/neu. These DARPin-viral complexes were able to reach 75% of all tumour sites and extend patient survival rates beyond the capabilities of the cytostatic antibody Herceptin, while also demonstrating none of the associated off-target accumulation in unaffected tissues caused by the latter drug (Münch et al., 2015). DARPins were also found to prevent amyloid-β peptide aggregation and its resulting neurotoxicity *in vivo*, leading to improved cognitive abilities in murine Alzheimer models (Hanenberg et al., 2014). Furthermore, off7 (Figure 2.5.3.1 above) was used as a starting point for developing a reagentless fluorescent biosensor whose fluorescence intensity increases proportionally to the concentration of bound MaIE maltose binding protein from *E. coli* (Brient-Litzler et al., 2010).

Their high binding affinities not only enable DARPins to act as input domains towards the creation of rapid modular protein switches in the fields of novel biosensor and highly-selective protein therapeutics development (Nicholes et al., 2016), but to also be formulated for intraocular administration against vascular endothelial growth factor (VEGF) in the treatment of diabetic macular oedema (Campochiaro et al., 2013) and wet age-related macular degeneration (Tamaskovic et al., 2012) (Figure 2.5.7.3).

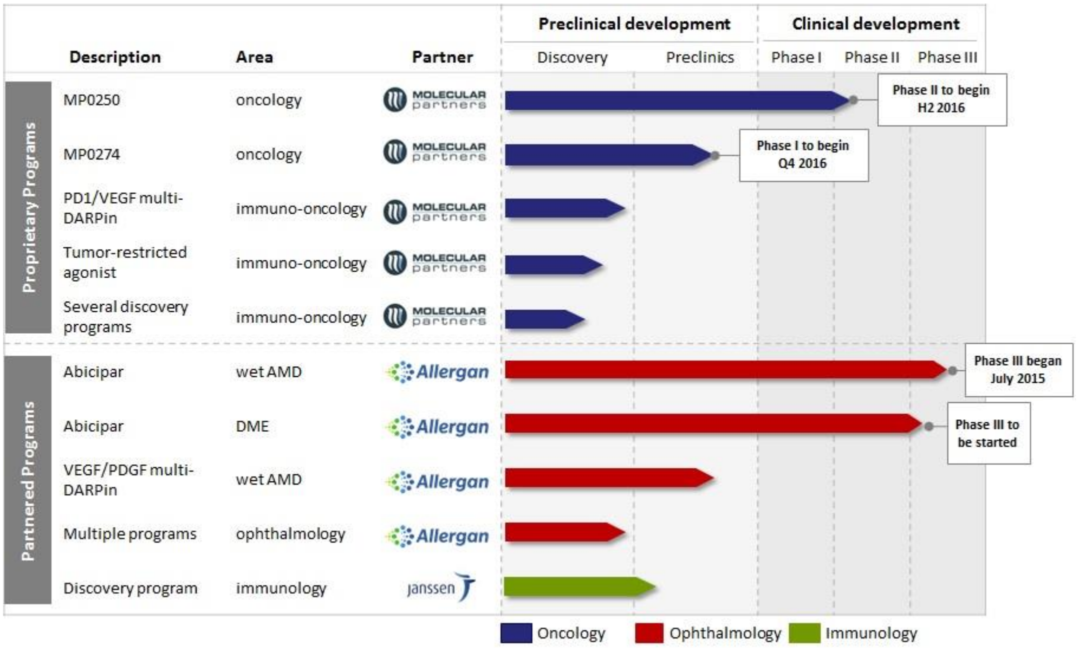

Figure 2.5.7.3. Examples of DARPin-based drugs currently undergoing clinical trials in a multitude of therapeutic interest areas (adapted from Molecular Partners, 2016b).

Lastly, DARPins binding endogenous IgE immunoglobulins in the low nanomolar range were found to inhibit the release of proinflammatory mediators with higher efficacy than the commercial anti-IgE monoclonal antibody omalizumab (Xolair), demonstrating significant potential towards forming the basis of future anti-allergy medications (Baumann et al., 2010).

Unfortunately, while also being responsible for their very high degrees of stability, the rigid and concave DARPin structures can actually restrict their spectrum of potential therapeutic applications, especially when their modular hydrophobic regions are incompletely randomised (Jost and Plückthun, 2014). In an attempt at circumventing this limitation, a new class of “LoopDARPins” (Figure 2.5.7.4 overleaf) was recently engineered to include a convex paratope normally displayed within the complementarity-determining regions (CDRs) of classic immunoglobulin variable domains. Through the substitution of the central DARPin β-turn with an extended, 19-amino-acid CDR-H3-like loop demonstrating high conformational diversity, a total of 10 additional variable amino acid positions became available for antigen binding without affecting the overall stability of the protein scaffold. Furthermore, the upper part of the introduced loop is flexible and can thus readily expose its randomised binding domains to previously-unreachable antigen epitopes. Even more interestingly, the original consensus library design was expanded for LoopDARPins to also cover randomised N- and C-caps, which only served to increase their available antigen binding surfaces even further (Schilling et al., 2014).

LoopDARPins preserve many of the favourable characteristics that made conventional DARPins so exciting and actually managed to surpass them in several key areas. First of all, they readily express in *E. coli* systems, giving high yields of protein binders that can remain folded over several weeks at 4 °C and are much less susceptible to forming dimers and oligomers in solution than regular DARPins. In fact, a higher percentage of monomers was actually detected in LoopDARPin populations that had been subjected to rigorous rounds of ribosome display compared to untested library members. Finally, it was found that a single round of ribosome display was enough to yield LoopDARPins demonstrating low-nanomolar to mid-picomolar affinities towards their designated targets – a surprising result, given that regular DARPin libraries usually require multiple rounds of interrogation before binders with similar affinity levels can be identified (Jost and Plückthun, 2014). Despite some minor self-complementarity issues arising as an unfortunate consequence of the added flexibility of their extended loops, LoopDARPins represent an evolved scaffold protein platform that exceeds the capabilities of traditional

DARPins while also offering a substantial enrichment potential and an unprecedented selection speed against similar types of protein-based antigens (Schilling et al., 2014). While LoopDARPins were sadly not available for the project at hand, the binding capabilities of traditional DARPins against NupC were investigated as described further on in Chapter 5, after presenting the materials and methods in the upcoming Chapter 3.

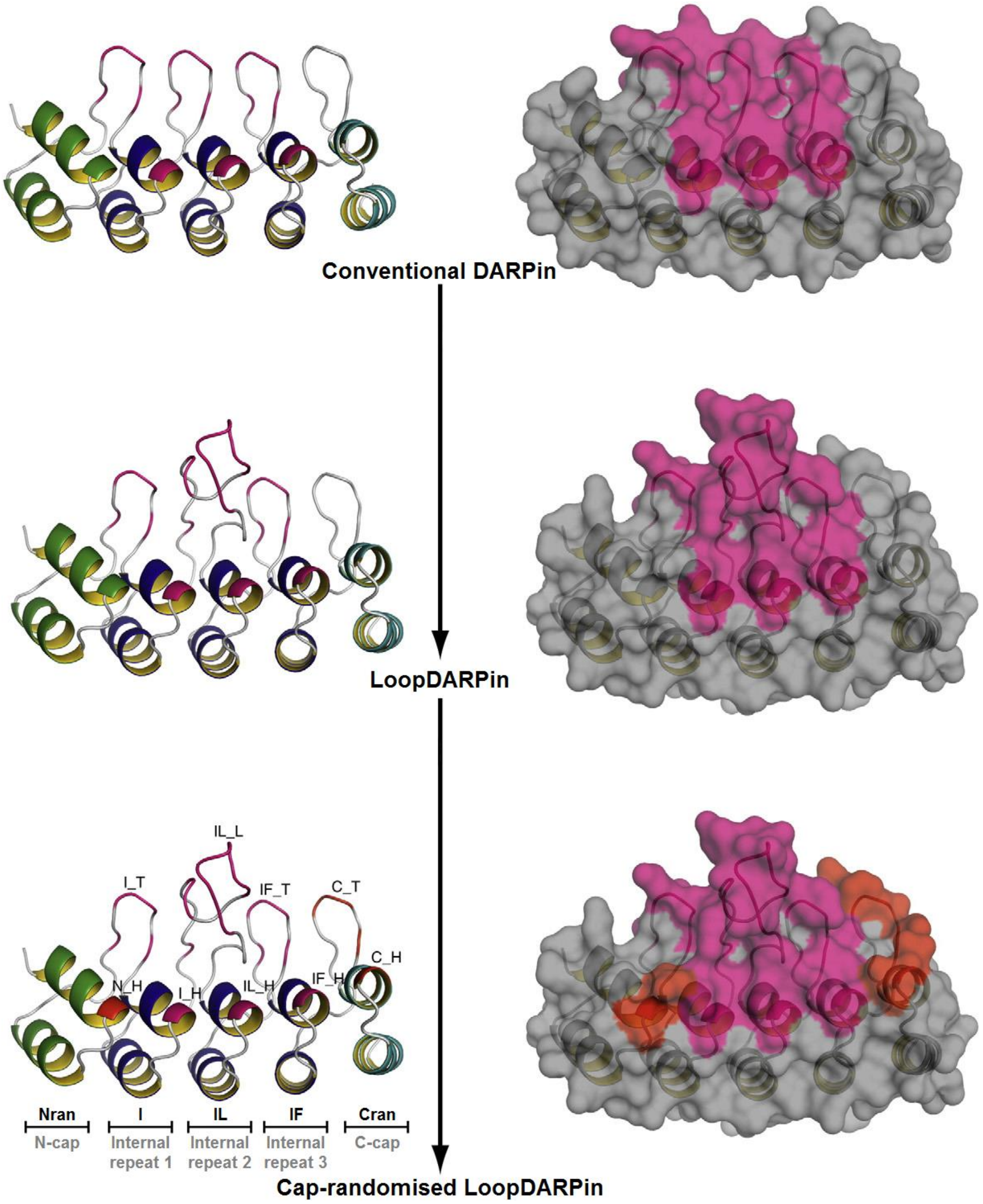

Figure 2.5.7.4. Diagram detailing the process of transforming regular DARPins into cap-randomised LoopDARPins. Top: a conventional DARPin (PDB ID: 2XEE) harbouring three consensus library modules undergoes modification with an extended CDR-like loop. Middle: a LoopDARPin integrating the extended loop into its second library module is thereby created. Bottom: randomised N- and C-terminal caps (Nran and Cran, respectively, depicted in red on the ribbon structure and in orange on the surface structure) are added to flank the three library modules I (internal module), IL (loop-containing internal module) and IF (internal module following loop), depicted here in pink (adapted from Schilling et al., 2014).

CHAPTER 3

Materials and Methods

3.1. Reiterating the Overall Experimental Plan

Three NupC constructs (i.e. C-terminal double Strep-tagged (II), intrinsic His_6-tagged and untagged/wild-type NupC) were used to provide proof-of-concept for the proposed SSBLM phage display screening platform. Following their expression and purification from *E. coli*, their *ex vivo* nucleoside transport activities were measured via a transporter assay in order to establish whether the purified NupC constructs retained their original conformations and were still correctly folded.

The formation and characterisation of model lipid SSMs on planar silica surfaces was then investigated via QCM-D in order to test the virtues of this particular substrate towards forming SSMs embedding reconstituted membrane protein targets. Planar SSM creation was afterwards followed by the deposition and characterisation of SSBLMs on the chosen 100- and 200 nm silica nanoparticle substrates.

Finally, the presentation of the three SSBLM-embedded NupC constructs was examined alongside the characterisation of their orientations and epitope accessibility prior to using this novel platform towards the phage display screening of DARPin binders against NupC.

3.2. Materials

The BL21, C43 (DE3) and OmniMAX *E. coli* cell cultures and the pBPT-0217-CS2T, pLH13, pGJL16 and pMPSIL0079A plasmids (see Appendix), respectively encoding double Strep-tagged, His_6-tagged and untagged NupC, as well as His_6-tagged PepTSo, were kindly provided by Dr. Vincent Postis (The School of Biomedical Sciences, University of Leeds). The DARPin library, TG1 *E. coli* cell cultures and M13K07trp helper phage stock solutions were kindly provided by MedImmune Ltd.

Cell culture and protein expression materials included ampicillin sodium salt (Melford, A0104), bacteriological agar (Agar No. 1) (Oxoid, LP0011), carbenicillin disodium salt (Melford, C0109), Corning® non-treated culture (Petri) dishes (Sigma-Aldrich, CLS430589), Corning® square bioassay dishes (Sigma-Aldrich, CLS431111), glucose (VWR, 101174Y), HisPur™ cobalt resin (Thermo Fisher Scientific, 89965), isopropyl β-D-thiogalactoside (IPTG) (Generon, GEN-S-02122), kanamycin monosulfate (Melford, K0126), Pierce™ disposable columns (5 mL) (Thermo Fisher Scientific, 29922), Slide-A-Lyzer™ dialysis cassettes (3 mL, 10K MWCO) (Thermo Fisher Scientific, 66380), sodium chloride (NaCl) (Melford, S0520), Strep-Tactin® Superflow® 50% (w/v) resin suspension (IBA, 2-1206-002), StrepTrap HP columns (5×1 mL) (GE Healthcare Life Sciences, 28-9075-46), tryptone (Melford, T1332), Vivaspin® 6 and Vivaspin® 20 centrifugal concentrators (10K MWCO) (Sartorius, VS0601 and VS2001, respectively) and yeast extract powder (Melford, Y1333).

Buffer materials included 3-(N-Morpholino)propanesulfonic acid (MOPS) (Sigma-Aldrich, M1254), bovine serum albumin (BSA) fraction V (Melford, A1302), cOmplete™ (EDTA-free) mini protease inhibitor cocktail tablets (Sigma-Aldrich, 04693159001), *d*-Desthiobiotin (Sigma-Aldrich, D1411), ethylenediaminetetraacetic acid (EDTA) disodium salt (Melford, E0511), glycerol (Sigma-Aldrich, G6279), glycine (Melford, G0709), imidazole (Sigma-Aldrich, I202), Marvel Original dried skimmed milk (Tesco, 340 g), N-(2-Hydroxyethyl)piperazine-N′-(2-ethanesulfonic acid) (HEPES) (Sigma-Aldrich, H3375), *n*-Dodecyl β-D-maltoside (DDM) (Anatrace, D310LA), potassium chloride (KCl) (Sigma-Aldrich, P9541), potassium phosphate dibasic (K_2HPO_4) (Sigma-Aldrich, P3786-M), potassium phosphate monobasic (KH_2PO_4) (Sigma-Aldrich, P9791), sodium dodecyl sulfate (SDS) (Sigma-Aldrich, L3771), sodium phosphate dibasic (Na_2HPO_4) (Sigma-Aldrich, S7907), sodium sulfate (Na_2SO_4) (Sigma-Aldrich, 239313-M), sucrose (Melford, S0809), *threo*-1,4-Dimercapto-2,3-butanediol (DTT) (Sigma-Aldrich, 43819), tris(hydroxymethyl)aminomethane (Tris) (Melford, B2005), trypsin (Sigma-Aldrich, T2600000) and Tween® 20 (Sigma-Aldrich, P2287).

Bicinchoninic acid (BCA) assay materials included BCA solution (Sigma-Aldrich, B9643), copper (II) sulfate pentahydrate ($CuSO_4 \cdot 5H_2O$) (Sigma-Aldrich, 203165) and Corning® Costar® flat-bottomed 96-well plates (Sigma-Aldrich, CLS3599).

SDS-polyacrylamide gel electrophoresis (SDS-PAGE) materials included 2-Mercaptoethanol (Acros Organics, 125470100), acetic acid (Sigma-Aldrich, 71251), acrylamide (40% (w/v) solution) (Melford, A2440), ammonium persulfate (APS) (Melford, A1512), bis-acrylamide (2% (w/v) solution) (Melford, A2502), bromophenol blue (SLS, CHE1342), Coomassie Brilliant Blue G solution (Sigma-Aldrich, B8522), methanol (Sigma-Aldrich, 322415), N,N,N',N'-Tetramethylethylenediamine (TEMED) (Melford, T3100), PageRuler™ Plus prestained protein ladder (10-250 kDa) (Thermo Fisher Scientific, 26619) and PageRuler™ unstained broad range protein ladder (5-250 kDa) (Thermo Fisher Scientific, 26630). DNA gel electrophoresis materials included 1 kb DNA ladder (New England BioLabs, N3232S) and agarose (Sigma-Aldrich, A9414).

Western blotting materials included 1-Step™ Ultra TMB-blotting solution (Thermo Fisher Scientific, 37574), precut nitrocellulose membranes (0.45 μm, 15×15 cm) (Bio-Rad, 1620116) and precut thick blot filter paper (18×34 cm) (Bio-Rad, 1650921). Double Strep-tagged NupC detection employed StrepMAB-Classic mouse anti-Strep (II) primary antibodies (IBA, 2-1507-001) and peroxidase-conjugated AffiniPure goat anti-mouse IgG (H+L) secondary antibodies (Jackson ImmunoResearch Laboratories, 115-035-003). His_6-tagged NupC detection employed HRP-conjugated mouse IgG_1 anti-His antibodies (R&D Systems, MAB050H). Formyl peptide receptor (FPR) detection employed IgG 0165 primary antibodies (MedImmune Ltd, proprietary) and goat anti-human IgG (Fc-specific) peroxidase-conjugated antibodies (Sigma-Aldrich, A0170).

Protein reconstitution materials included 1-Palmitoyl-2-oleoyl-*sn*-glycero-3-phosphocholine (POPC) lipids (Avanti Polar Lipids, 850457), *α*-[4-(1,1,3,3-Tetramethylbutyl)phenyl]-*w*-hydroxy-poly(oxy-1,2-ethanediyl) (Triton X-100) (10% (w/v) solution) (Anatrace, APX100), Bio-Beads® SM-2 adsorbent beads (Bio-Rad, 1523920), *E. coli* polar lipid extracts (67% phosphatidylethanolamine, 23.2% phosphatidylglycerol, 9.8% cardiolipin) (Avanti Polar Lipids, 100600), isopropanol (2-Propanol) (Sigma-Aldrich, I9516), Mini-Extruder set with holder/heating block and two Hamilton Gastight #1001 (1 mL) syringes (Avanti Polar Lipids, 610000), Nuclepore™ polycarbonate extrusion membranes (50-, 100-, 200- and 400 nm) (GE Healthcare Life Sciences, 800308, 800309, 800281 and 800282, respectively) and polyester extruder drain discs (10 mm) (GE Healthcare Life Sciences, 230300).

SURFE2R N1 transporter assay materials included adenosine (Sigma-Aldrich, A9251), guanosine (Sigma-Aldrich, G6752), N1 gold sensors (Nanion Technologies), Parafilm M® laboratory film (Bemis, PM999), as well as Sensor Prep A (1-octadecanethiol in isopropanol (1 mM)) and Sensor Prep B (DiPhyPC in decane (7.5 mg/mL)) solutions (Nanion Technologies).

QCM-D materials included silicon dioxide (SiO_2)-coated Q-Sensors (Biolin Scientific).

Fluorescence spectroscopy materials included 1,2-Dihexadecanoyl-*sn*-glycero-3-phosphoethanolamine triethylammonium salt (Texas Red$^{®}$) (Thermo Fisher Scientific, T1395MP), chloroform (Sigma-Aldrich, 288306) and methanol (Sigma-Aldrich, 322415).

The SSBLM substrates comprised of solid silicon dioxide (SiO_2) nanospheres with diameters of 100- and 200 nm (10 mg/mL aqueous solutions) (nanoComposix, SISN100 and SISN200, respectively).

The peroxidase assay materials were included in a SensoLyte$^{®}$ 10-Acetyl-3,7-dihydroxyphenoxazine (ADHP) peroxidase assay kit (fluorimetric) (AnaSpec, AS-71111).

Cryo-EM materials included 5 nm Ni-NTA-Nanogold$^{®}$ probes (0.5 µM stock solution in 50 mM MOPS buffer, pH 7.9) (Nanoprobes, 2082) and lacey carbon film/copper mesh cryo-grids (Agar Scientific, AGS166).

DNA molecular biology materials included BamHI restriction digest enzyme (New England BioLabs, R0136S), ChargeSwitch$^{®}$-Pro plasmid miniprep kit (Thermo Fisher Scientific, CS30250), KOD DNA polymerase (Merck Millipore, 71085-3), NdeI restriction digest enzyme (New England BioLabs, R0111S), NEBuffer 3.1 (New England BioLabs, B7203S), nuclease-free water (Thermo Fisher Scientific, R0581), pET-16b expression vector (Merck Millipore, 69662-3), pET-16b forward and reverse primers (Eurofins, custom-made), T4 DNA ligase (New England BioLabs, M0202S), T4 DNA ligase reaction buffer (New England BioLabs, B0202S) and Wizard$^{®}$ SV gel and polymerase chain reaction (PCR) clean-up system (Promega, A9281).

Enzyme-linked immunosorbent assay (ELISA) materials included 3,3′,5,5′-Tetramethylbenzidine (TMB) liquid substrate system for ELISA (Sigma-Aldrich, T0440), Corning$^{®}$ Costar$^{®}$ V-bottomed 96-well plates (Sigma-Aldrich, CLS3897), Nunc™ MaxiSorp™ flat-bottomed 96-well plates (Thermo Fisher Scientific, 442404) and sulfuric acid (H_2SO_4) (Fisher Scientific, A300-212).

3.3. Buffers, Media and Solutions

The following tables (3.3.1.1a-o) detail all of the buffers, media and solutions used for the experimental work described throughout the current thesis. Unless specified otherwise, MilliQ® water (18.2 MΩ·cm) represented the solvent for all of the recipes presented below.

General buffers and solutions
KPi buffer (pH 6.8/7.4, adjusted with NaOH) - 20% (w/w) KH_2PO_4 - 80% (w/w) K_2HPO_4
MOPS/Na_2SO_4 buffer (pH 7.0, adjusted with NaOH) - 20 mM MOPS - 30 mM Na_2SO_4
PBS buffer (pH 7.5, adjusted with HCl) - 137 mM NaCl - 2.7 mM KCl - 10 mM Na_2HPO_4 - 1.8 mM KH_2PO_4
HEPES buffer (pH 7.4, adjusted with NaOH) - 30 mM HEPES - 25 mM NaCl - 100 mM KCl
TAE buffer (pH 7.6, adjusted with HCl) - 40 mM Tris - 20 mM acetic acid - 1 mM EDTA
Deep-freeze storage solution - 50% (w/v) glycerol
Peroxidase reaction stop solution - 0.5 M H_2SO_4

Table 3.3.1.1a. General buffers and solutions used for the experimental work described throughout the current thesis.

Bacterial growth media
Luria-Bertani (LB) bacterial growth medium - 1% (w/v) tryptone - 0.5% (w/v) yeast extract - 1% (w/v) NaCl

Luria-Bertani (LB) agar - LB bacterial growth medium - 1.25% (w/v) bacteriological agar
2×TY growth medium - 1.6% (w/v) tryptone - 1% (w/v) yeast extract - 0.5% (w/v) NaCl
2×TYAG growth medium - 2×TY growth medium - 100 µg/mL ampicillin - 2% (w/v) glucose
2×TYAK growth medium - 2×TY growth medium - 100 µg/mL ampicillin - 50 µg/mL kanamycin

Table 3.3.1.1b. The bacterial growth media used for the cell culture work described throughout the current thesis.

Double Strep-tagged NupC expression and purification buffers
Double Strep-tagged NupC Tris/EDTA buffer (pH 7.5, adjusted with HCl) - 20 mM Tris - 0.5 mM EDTA - 5% (w/v) glycerol
Double Strep-tagged NupC solubilisation buffer (2×, pH 7.0, adjusted with HCl) - 100 mM Tris - 2 mM EDTA - 200 mM NaCl - 2% (w/v) DDM - 1 cOmplete™ (EDTA-free) mini protease inhibitor cocktail tablet per 50 mL
Double Strep-tagged NupC wash buffer (pH 7.0, adjusted with HCl) - 50 mM Tris - 1 mM EDTA - 100 mM NaCl - 5% (w/v) glycerol - 0.05% (w/v) DDM
Double Strep-tagged NupC binding dilution buffer (pH 7.0, adjusted with HCl) - 50 mM Tris - 1 mM EDTA - 100 mM NaCl - 10% (w/v) glycerol

Double Strep-tagged NupC elution buffer - Double Strep-tagged NupC wash buffer (pH 7.0) - 2.5 mM *d*-Desthiobiotin

Table 3.3.1.1c. The buffers used for the expression and purification of double Strep-tagged NupC.

His$_6$-tagged NupC expression and purification buffers
His$_6$-tagged NupC solubilisation buffer - 50 mM KPi buffer (pH 7.4) - 150 mM NaCl - 5 mM imidazole - 10% (w/v) glycerol - 1% (w/v) DDM
His$_6$-tagged NupC wash buffer - 50 mM KPi buffer (pH 7.4) - 150 mM NaCl - 5 mM imidazole - 10% (w/v) glycerol - 0.05% (w/v) DDM
His$_6$-tagged NupC elution buffer - 50 mM KPi buffer (pH 6.8) - 150 mM NaCl - 300 mM imidazole - 10% (w/v) glycerol - 0.05% (w/v) DDM

Table 3.3.1.1d. The buffers used for the expression and purification of His$_6$-tagged NupC.

Untagged NupC expression and membrane extraction buffers and solutions
Untagged NupC Tris/EDTA buffer (pH 7.5, adjusted with HCl) - 20 mM Tris - 0.5 mM EDTA
Sucrose gradient solutions - Untagged NupC Tris/EDTA buffer (pH 7.5) - 25%, 30%, 40%, 45%, 50% and 55% (w/w) sucrose, respectively

Table 3.3.1.1e. The buffers and solutions used for the expression and inner membrane extraction of untagged NupC.

BCA assay solutions
Reagent A - BCA solution (commercial stock)

Reagent B - 4% (w/v) $CuSO_4 \cdot 5H_2O$

Table 3.3.1.1f. The solutions used for the BCA assays performed throughout the entire project.

SDS-PAGE buffers and solutions
Tris buffer (pH 6.8/8.8, adjusted with HCl) - 0.5 M Tris (pH 6.8) or 1.5 M Tris (pH 8.8)
SDS-PAGE stacking gel solution (4% (v/v)) - 0.77 mL of stock 40% (w/v) acrylamide solution - 0.39 mL of stock 2% (w/v) bis-acrylamide solution - 0.75 mL of 0.5 M Tris buffer (pH 6.8) - 0.05 mL of 10% (w/v) SDS solution - 3.2 mL of MilliQ® water - 30 µL of 10% (w/v) APS solution - 18 µL of stock TEMED solution
SDS-PAGE resolving gel solution (12.5% (v/v)) - 3.745 mL of stock 40% (w/v) acrylamide solution - 0.45 mL of stock 2% (w/v) bis-acrylamide solution - 2.81 mL of 1.5 M Tris buffer (pH 8.8) - 0.1 mL of 10% (w/v) SDS solution - 4.265 mL of MilliQ® water - 37 µL of 10% (w/v) APS solution - 24 µL of stock TEMED solution
SDS-PAGE loading buffer (4×, pH 7.5, adjusted with HCl) - 200 mM Tris - 400 mM DTT - 8% (w/v) SDS - 0.4% (w/v) bromophenol blue - 40% (w/v) glycerol - 20% (v/v) 2-Mercaptoethanol
SDS-PAGE running buffer (5×, pH 7.5, adjusted with HCl) - 1.5% (w/v) Tris - 7.2% (w/v) glycine - 0.5% (w/v) SDS
SDS-PAGE destaining solution - 7.5% (v/v) methanol - 5% (v/v) acetic acid
SDS-PAGE staining solution - 40 mL of SDS-PAGE destaining solution - 2 mL of Coomassie Brilliant Blue G solution

Table 3.3.1.1g. The buffers and solutions used for SDS-PAGE.

Western blotting buffers
TBS buffer (10×, pH 7.5, adjusted with HCl) - 0.5 M Tris - 1.5 M NaCl
TBS-T buffer - 1× TBS buffer (pH 7.5) - 0.1% (v/v) Tween® 20
Western blotting blocking buffer - TBS-T buffer (pH 7.5) - 3% (w/v) BSA

Table 3.3.1.1h. The buffers used for Western blotting.

SURFE2R assay solutions
SURFE2R activating solutions - PBS buffer (pH 7.5) - increasing concentrations of adenosine (μM range)
SURFE2R control solutions - PBS buffer (pH 7.5) - increasing concentrations of guanosine (μM range)

Table 3.3.1.1i. The solutions used for the purified NupC nucleoside transport SURFE2R assays.

Phage display screening buffers
Phage display blocking buffer - PBS buffer (pH 7.5) - 3-6% (w/v) Marvel Original dried skimmed milk
Phage display wash buffer - PBS buffer (pH 7.5) - 0.1% (v/v) Tween® 20
Phage display elution buffer (pH 7.5, adjusted with NaOH) - 0.1 M Na_2HPO_4 - 1:500 (v/v) trypsin

Table 3.3.1.1j. The buffers used for the phage display screening of DARPin binders against NupC.

DARPin DNA molecular biology reaction mixtures
DARPin double restriction digest reaction mixture - 50 µL of pET-16b expression vector - 10 µL of NEBuffer 3.1 - 2 µL of BamHI - 2 µL of NdeI - 36 µL of nuclease-free water
DARPin ligation reaction mixture - 1:10 vector/insert molar ratio (8 µL in total) - 1 µL of T4 DNA ligase buffer - 1 µL of T4 DNA ligase
DARPin PCR reaction mixture - 5 µL of KOD DNA polymerase buffer - 1 µL of pET-16b forward primer - 1 µL of pET-16b reverse primer - 5 µL of DARPin plasmid DNA - 1 µL of KOD DNA polymerase - 37 µL of nuclease-free water

Table 3.3.1.1k. The reaction mixtures used for manipulating the plasmids of the lead candidate DARPins selected against NupC.

Lead candidate DARPin purification buffers
DARPin purification wash buffer - 2× PBS buffer (pH 7.5) - 30 mM imidazole
DARPin purification elution buffer - 2× PBS buffer (pH 7.5) - 200 mM imidazole

Table 3.3.1.1l. The buffers used for the purification of the lead candidate DARPins selected against NupC.

Detergent-solubilised NupC ELISA buffers
Detergent-solubilised NupC ELISA wash buffer - 2× PBS buffer (pH 7.5) - 0.05% (w/v) DDM
Detergent-solubilised NupC ELISA blocking buffer - Detergent-solubilised NupC ELISA wash buffer - 3% (w/v) BSA

Detergent-solubilised NupC ELISA antibody wash buffer - 2× PBS buffer (pH 7.5) - 0.1% (v/v) Tween® 20

Table 3.3.1.1m. The buffers used for the ELISAs screening the purified lead candidate DARPins against detergent-solubilised double Strep-tagged NupC.

SSBLM-embedded NupC ELISA buffers
SSBLM-embedded NupC ELISA wash buffer - 2× PBS buffer (pH 7.5) - 1% (w/v) POPC LUVs
SSBLM-embedded NupC ELISA blocking buffer - SSBLM-embedded NupC ELISA wash buffer - 3% (w/v) BSA

Table 3.3.1.1n. The buffers used for the ELISAs screening the purified lead candidate DARPins against detergent-free (i.e. SSBLM-embedded) untagged NupC.

SSBLM-embedded FPR ELISA buffers
SSBLM-embedded FPR ELISA wash buffer - HEPES buffer (pH 7.4) - 1% (w/v) POPC LUVs
SSBLM-embedded FPR ELISA blocking buffer - SSBLM-embedded FPR ELISA wash buffer - 3% (w/v) Marvel Original dried skimmed milk

Table 3.3.1.1o. The buffers used for the SSBLM-embedded mammalian FPR ELISA.

3.4. Methods

The following subsections describe the general experimental methods, as well as the expression and purification of the membrane protein targets used throughout the current project towards providing proof-of-concept for the SSBLM phage display screening platform.

3.4.1. General methods

The BL21, C43 (DE3) and OmniMAX *E. coli* cell culture stocks were made competent by Dr. Vincent Postis (The School of Biomedical Sciences, University of Leeds) via the rubidium chloride (RbCl) method developed by Hanahan (1983). The TG1 *E. coli* cell culture stocks were made competent by MedImmune technicians using the same method.

The “heat-shock” transformation method involved incubating 50 µL of competent cells with 1 µL of the chosen plasmid (i.e. 50 ng of DNA) at 4 °C for 30 minutes, then at 42 °C for 30 seconds and finally at 4 °C for another 2 minutes. Sterile, pre-warmed LB medium (250 µL) lacking antibiotics was then added to the cells, followed by another 1-hour incubation at 37 °C.

All roller, rocking platform and magnetic mixing steps were performed on a Stuart Scientific SRT6 roller mixer, Grant Bio PS-3D Sunflower mini-shaker and Stuart Scientific magnetic stirrer SM1, respectively.

All BCA assays were performed in triplicate in Costar® flat-bottomed 96-well plates using 10 µL sample volumes. A 400 µg/mL BSA solution – diluted 1:5, 1:2.5, 1:1.6 and 1:1.25 (v/v) in deionised water to give 10 µL volumes per well – was used to build the standard curve. The BCA working reagent was prepared by adding Reagent A (i.e. BCA solution at stock concentration) to Reagent B (i.e. 4% (w/v) $CuSO_4{\cdot}5H_2O$ solution in MilliQ® water) at a 1:50 (v/v) ratio, followed by vortexing until the resulting mixture became light green. The working reagent was then added to each well in 200 µL volumes and the plate was left to incubate at 37 °C for 30 minutes, after which the absorbances were measured at a wavelength of 551 nm using a Thermo Scientific Multiskan™ FC spectrophotometer.

All lipid extrusion steps were performed by first rehydrating desiccated lipid aliquots in the specified buffer at the stated concentration. The lipid suspensions were then passed 11 times through a fully assembled Avanti Mini-Extruder fitted with a polycarbonate extrusion membrane of specified pore size, sandwiched between four extruder drain discs (i.e. two on each side of the membrane). Prior to assembly, all extrusion membranes and drain discs were hydrated in MilliQ® water for at least 2 minutes. Both 1 mL Hamilton syringes were washed first in isopropanol, then in MilliQ® water and the buffer used to rehydrate the lipids was passed 11 times through the full assembly before any extrusion.

The “freeze-thaw” mixing method consisted of snap-freezing lipid solutions in liquid nitrogen and then allowing them to thaw while floating on MilliQ® water at room temperature to ensure the proper mixing of the different lipid types present in solution.

All polyacrylamide gels (12.5% (w/w)), comprising of stacking and resolving gel solutions, were freshly cast prior to each round of SDS-PAGE. The resolving gel solution was first pipetted into the Bio-Rad gel casting assembly and left to polymerise at room temperature until solid (e.g. 45 minutes) before the stacking gel solution was added on top. A 10-toothed plastic comb was used for moulding the gel wells. All SDS-PAGE samples were normalised to 5 µg of protein, made up to total volumes of 15 µL and then incubated with 5 µL of 4× SDS-PAGE loading buffer for 2 hours at 37 °C before being loaded into the wells of the solidified gels. Electrophoresis was performed in a Bio-Rad Mini-PROTEAN Tetra vertical electrophoresis cell filled with 1× SDS-PAGE running buffer under a 100 V-current applied for 2 hours through a Bio-Rad Powerpac Basic 300 V power supply. The electrophoresed gels were then rinsed in MilliQ® water and incubated with the Coomassie Blue staining solution overnight at room temperature under gentle rocking mixing. The following day, the gels were once again rinsed in deionised water and left to incubate with destaining solution under similar conditions until all bands were clearly visible.

Western blotting was performed by first semi-dry blotting an electrophoresed SDS-PAGE gel onto a nitrocellulose membrane using a MilliBlot Graphite Electroblotter II under a 150 mA-current applied for 1 hour through a Bio-Rad Powerpac Basic 300 V power supply. The semi-dry blotting assembly comprised of (from bottom-to-top): two gel-sized blot filter paper sheets, one gel-sized nitrocellulose membrane, one electrophoresed SDS-PAGE gel and two additional gel-sized blot filter paper sheets. The electrophoresed SDS-PAGE gel, the gel-sized filter paper sheets and the nitrocellulose membrane were first left to soak in TBS buffer for at least 15 minutes prior to running any semi-dry blot. After each run, the blotted nitrocellulose membrane was left to incubate overnight with 20 mL of blocking buffer at 4 °C under gentle roller mixing, while the blotted SDS-PAGE gel was placed in staining solution to determine the quality of the semi-dry blotting process. The next day, the blotted membrane was left to incubate with 5 mL of HRP-conjugated antibodies diluted in blocking buffer (at the manufacturer-specified ratio) for 1 hour at room temperature with gentle roller mixing. The membrane was then washed four times with 25 mL of TBS-T buffer (for 10 minutes each time, at room temperature with gentle roller mixing) before being placed in a tray, covered in 1-Step™ Ultra TMB-blotting solution and incubated at room temperature until fully-coloured bands were readily visible (usually after 15 minutes of incubation).

The cryo-EM grids were prepared using a FEI Vitrobot by first applying 3 µL of sample per grid, followed by the blotting of the excess solution for 2 seconds before plunging the grids into liquid ethane for vitrification. The grids were then studied under a FEI F20 cryo-EM and all of the resulting images were taken with a Gatan 4K×4K CCD camera.

The protocols for phage display screening, as well as expressing and purifying the lead candidate DARPins isolated against NupC, were kindly provided by Dr. Stacey Chin (MedImmune Ltd).

All DNA molecular biology reactions were performed using a Bio-Rad Dyad® DNA Engine PCR machine. DARPin double restriction digests were performed by incubating the respective reaction mixtures at 37 °C for at least 2 hours, followed by the inactivation of the restriction enzymes through 15-minute incubations, first at 65 °C (i.e. the NdeI inactivation temperature) and then at 80 °C (i.e. the BamHI inactivation temperature). The vector:insert ligation calculations were performed online at http://www.insilico.uni-duesseldorf.de/Lig_Input.html, while the ligation reactions themselves were performed overnight at 16 °C. DNA amplification consisted of incubating the reaction mixtures first at 94 °C for 3 minutes, then through 32 recursive cycles of 94 °C (for 30 seconds), then 50 °C (for another 30 seconds) and 72 °C (for 105 seconds), before finally undergoing a last 5-minute incubation at 72 °C, followed by overnight storage at 10 °C.

The TAE DNA agarose gels were cast by first mixing the specified concentration of agarose with TAE buffer (pH 7.6), then placing the mixtures in a microwave oven and heating them up for 2 minutes at maximum power. The heated gel mixtures were then poured into either a Bio-Rad Mini-Gel or Gel caster and left to polymerise at room temperature until completely solid (usually after 20 minutes). All DNA gels were submitted to electrophoresis in a Bio-Rad Sub-Cell® GT horizontal electrophoresis cell powered through a Bio-Rad Powerpac Basic 300 V power supply. Current was applied at a constant 100 V until the dye fronts reached the bottom edge of the gels (generally after 45-60 minutes).

All Eppendorf tube-based SSBLM centrifugations were performed in a Thermo Scientific Heraeus Fresco 17 centrifuge for 1 minute at 17,000 *g* and 4 °C. All plate-based SSBLM ELISA centrifugations were performed in an Eppendorf 5810 R table-top centrifuge for 5 minutes at 3,220 *g* and 4 °C.

Finally, the protocols for expressing and purifying all of the membrane protein constructs used throughout the project were developed, optimised and kindly provided by Dr. Vincent Postis (The School of Biomedical Sciences, University of Leeds).

3.4.2. Double Strep-tagged NupC expression and purification

C43 (DE3) *E. coli* competent cells (50 µL) harbouring the chloramphenicol-resistance plasmid pRARE2 (Novagen) were first transformed via the heat-shock method with 1 µL of the plasmid pBPT-0217-CS2T (i.e. 50 ng of DNA) encoding double Strep-tagged NupC. The transformed cells were then spread onto an LB-agar plate supplemented with carbenicillin (100 µg/mL) and incubated overnight at 37 °C.

LB medium (100 mL) supplemented with carbenicillin (100 µg/mL) and 1% (w/v) glucose was inoculated the following day with a single colony from the overnight plate and the resulting inoculation culture was once again incubated overnight at 37 °C with 200 rpm orbital shaking. The bacterial density was determined by measuring the D_{600nm} value of the overnight culture using a Shimadzu UV-2450 spectrophotometer, after which the culture was used to inoculate 8×500 mL volumes of carbenicillin-supplemented (100 µg/mL) LB medium contained in 8×2.5 L baffled flasks, so as to give starting D_{600nm} values of 0.05. The new flask cultures were then incubated at 37 °C with 200 rpm orbital shaking and their D_{600nm} values were monitored every hour until they reached 0.7, after which protein overexpression was induced via IPTG addition (0.5 mM per flask). Following that, the flask cultures were incubated for an additional 3 hours under similar conditions before the cells were harvested using a Sorvall Evolution RC centrifuge fitted with an SLC-6000 rotor (9,000 *g* spin for 20 minutes at 4 °C). The resulting cell pellets were resuspended in Tris/EDTA buffer supplemented with 5% (w/v) glycerol (i.e. 6 mL of buffer per gram of cells) and then stored overnight at -20 °C.

The next day, the cell suspensions were thawed in a water bath set to 25 °C and one cOmplete™ (EDTA-free) mini protease inhibitor cocktail tablet was added per 50 mL of suspension so as to protect the overexpressed membrane proteins from being catabolised by the cytoplasmic proteases released during the following steps of the purification process. The cell suspensions were then pooled together and supplemented with Tris/EDTA buffer to give a final volume of 100 mL, before being homogenised using a T18 basic ULTRA-TURRAX® homogeniser and disrupted twice using a Constant Systems TS series continuous cell disruptor operating at 30 kpsi and 4 °C. The resulting cell debris was removed using a Sorvall Evolution RC centrifuge fitted with an SLA-1500 rotor (14,000 *g* spin for 45 minutes at 4 °C), while the cell membranes were harvested by ultracentrifuging the resulting supernatant using a Beckman Coulter L-80XP ultracentrifuge fitted with a Ti45 rotor (100,000 *g* spin for 2 hours at 4 °C). The cell membrane pellets were then resuspended in Tris/EDTA buffer at a concentration of 1 g/mL, snap-frozen in liquid nitrogen and stored at -80 °C overnight. Small-volume test samples (i.e. <1 mL) were taken throughout the entire process so as to enable the measurement of membrane protein concentration at each expression and purification stage.

The total protein content of the cell membrane suspension was evaluated via BCA assay and the determined protein concentration was used for creating the membrane solubilisation solution (i.e. cell membranes mixed at 2 mg of protein/mL with 1× double Strep-tagged NupC solubilisation buffer). This mixture was then supplemented with 1% (w/v) DDM and incubated for 1 hour at 4 °C with gentle magnetic mixing. The insoluble membrane fraction was pelleted in a Beckman Coulter L-80XP ultracentrifuge fitted with a Ti45 rotor (100,000 *g* spin for 1 hour at 4 °C), while the solubilised membranes contained in the supernatant were stored on ice. The Strep-Tactin® Superflow® 50% (w/v) resin suspension (1 mL) was then washed three times through subsequent resuspensions in MilliQ® water, followed by re-pelleting in an Eppendorf 5810 R table-top centrifuge (700 *g* spins for 5 minutes each at 4 °C). After the washed resin was also pre-equilibrated with double Strep-tagged NupC wash buffer via the same procedure, a 1:1 volume of binding dilution buffer was added to the solubilised membrane fraction and the resulting solution was mixed with the buffer-equilibrated resin. Protein-to-resin binding was then allowed to occur overnight at 4 °C with gentle roller mixing.

The following day, the protein binding solution was poured through a 5 mL Pierce™ disposable column and the captured resin was washed dropwise under gravity with 1 column volume (CV) of wash buffer (i.e. 1 drop every 1-2 seconds). With the column outlet closed, the resin was gently treated with 0.3 mL of elution buffer in order to remove any residual wash buffer. After this initial fraction was collected and stored separately on ice, the column outlet was once again closed and the resin was resuspended in 0.5 mL of elution buffer. The column was then incubated for 10 minutes at 4 °C with gentle roller mixing before the outlet was reopened and the first eluate, plus a further addition of 0.5 mL of elution buffer, were allowed to pour through and be collected into a single Eppendorf tube.

The elution steps outlined above were repeated until all of the protein had been eluted, as determined by measuring the A_{280nm} values of each eluate against the elution buffer as blank. The "peak" fractions – containing the highest concentrations of purified double

Strep-tagged NupC – were then pooled together and dialysed overnight at 4 °C in a 3 mL Slide-A-Lyzer™ dialysis cassette (10K MWCO) against 500 mL of wash buffer, so as to eliminate any remaining *d*-Desthiobiotin. The dialysed protein solution was subsequently concentrated at 3,220 *g* and 4 °C using an Eppendorf 5810 R table-top centrifuge fitted with a Vivaspin® 20 centrifugal concentrator (10K MWCO) and the total amount of purified protein was determined via BCA assay. The concentrated double Strep-tagged NupC solution was then aliquoted and stored at -80 °C following snap-freezing in liquid nitrogen, while SDS-PAGE and western blotting were used to assess the quality of the purification process (see Figure 4.1.1.1 in Chapter 4).

In the case of double Strep-tagged NupC, the semi-dry-blotted nitrocellulose membranes were incubated with 5 mL of StrepMAB-Classic mouse anti-Strep (II) primary antibodies (diluted 1/2,500 in blocking buffer) for 1 hour at 4 °C with gentle roller mixing. The membranes were then washed four times by incubating them with 25 mL volumes of TBS-T buffer for 10 minutes per wash, before being incubated with 5 mL of peroxidase-conjugated AffiniPure goat anti-mouse IgG (H+L) secondary antibodies (diluted 1/50,000 in TBS-T buffer) for 1 hour at 4 °C with gentle roller mixing. After four additional TBS-T buffer washes, the blotted membranes were incubated with 1-Step™ Ultra TMB-blotting solution and imaged according to the protocol detailed in subsection 3.4.1.

The low purification yields typical of membrane proteins prompted the need for growing larger bacterial cultures via bioreactor fermentation in order to express and purify double Strep-tagged NupC to the high levels necessary for supporting its intended applications throughout the project at hand. Thus, the cell membranes originating from a 30 L C43 (DE3) *E. coli* fermentation culture overexpressing double Strep-tagged NupC were harvested and solubilised according to the protocol described above, after which the overexpressed protein was eluted under a step gradient (0.5 mL/min) using the same elution buffer in a GE Healthcare ÄKTA pure 25 fitted with a 1 mL StrepTrap™ HP column.

In order to reduce the overlong column loading times, the dilution of the solubilised membranes using binding dilution buffer – a requirement for the protein-resin binding step preceding gravity-column elutions – was omitted from all ÄKTA purifications. The *d*-Desthiobiotin was, however, still dialysed from the pooled elution fractions as previously described. A BCA assay performed on the dialysed ÄKTA eluates revealed that the purified protein yields per litre of bacterial culture were proportionate to those reported with the gravity-column elutions described earlier, originating from the smaller 4 L cultures.

3.4.3. His$_6$-tagged NupC expression and purification

Following the same steps outlined in subsection 3.4.2, C43 (DE3) *E. coli* competent cells were transformed via the heat-shock method with plasmid pLH13 encoding intrinsically His$_6$-tagged NupC and then subsequently cultured in 4 L of LB media.

After determining the overall concentration of overexpressed membrane proteins via BCA assay, the harvested cell membranes were mixed with solubilisation buffer at 5 mg of protein per mL. The resulting solubilisation solution was incubated for 1 hour at 4 °C with gentle magnetic mixing before the insoluble membrane fraction was pelleted in a Beckmann Coulter L-80XP ultracentrifuge fitted with a Ti45 rotor (100,000 *g* spin for 1 hour at 4 °C). The solubilised membranes contained in the supernatant were stored on ice while the HisPur™ cobalt resin (80 µL per mg of membrane protein) was washed in MilliQ® water and then pre-equilibrated with His$_6$-tagged NupC wash buffer via the previously-described technique. The solubilised membranes were then mixed with the resin and protein binding was allowed to occur overnight at 4 °C with gentle roller mixing.

The next day, the protein binding solution was poured through a 5 mL Pierce™ disposable column and the captured resin was washed dropwise under gravity with 1 CV of wash buffer (i.e. 1 drop every 1-2 seconds), after which the His$_6$-tagged NupC was eluted at room temperature using 500 µL of elution buffer per fraction. The elution steps were repeated until all of the protein had been eluted, as determined by measuring the A_{280nm} values of each fraction against the elution buffer as blank. The peak fractions were then pooled and dialysed overnight at 4 °C in a 3 mL Slide-A-Lyzer™ dialysis cassette (10K MWCO) submerged in 500 mL of wash buffer, in order to remove any remaining imidazole.

The dialysed protein solution was subsequently concentrated via centrifugation at 3,220 *g* and 4 °C in an Eppendorf 5810 R table-top centrifuge fitted with a Vivaspin® 20 centrifugal concentrator (10K MWCO). The total amount of purified protein was ultimately determined via BCA assay, after which the concentrated His$_6$-tagged NupC solution was aliquoted and stored at -80 °C following snap-freezing in liquid nitrogen.

Small-volume test samples (i.e. <1 mL) were taken throughout the entire process in order to evaluate the expression and purification of His_6-tagged NupC.

3.4.4. Untagged NupC expression and *E. coli* inner membrane extraction

Following the same steps outlined in subsection 3.4.2, C43 (DE3) *E. coli* competent cells were transformed via the heat-shock method with the plasmid pGJL16 encoding untagged/wild-type NupC and then subsequently cultured in 4 L of LB media. After the cell membranes were harvested via ultracentrifugation, the inner membrane (IM) fraction overexpressing untagged NupC was also separated from the outer membrane (OM) fraction through a sucrose density gradient ultracentrifugation.

The harvested membranes were first resuspended in a 25% (w/w) sucrose solution, pipetted into a Ti45 ultracentrifuge tube layered with increasingly-concentrated sucrose gradients (30-55% (w/w)) and then ultracentrifuged at minimal acceleration with no braking in a Beckmann Coulter L-80XP ultracentrifuge fitted with a Ti45 rotor (100,000 *g* spin for 16 hours at 4 °C). Following separation, the inner (lighter) and outer (darker) membrane fractions were extracted from the sucrose gradient via pipetting and then resuspended in minimal volumes of Tris/EDTA buffer. In order to remove the residual sucrose present in both of the separated membrane fractions, these were alternatingly pelleted via ultracentrifugation (100,000 *g* spins for 1 hour each at 4 °C) and then resuspended in similar volumes of Tris/EDTA buffer twice. The washed inner and outer membrane pellets were finally resuspended in minimal volumes of Tris/EDTA buffer, snap-frozen in liquid nitrogen and stored at -80 °C. Small-volume test samples (i.e. <1 mL) were taken throughout the entire process in order to evaluate the expression of untagged NupC.

3.4.5. His_6-tagged PepTSo expression and purification

The NupC-homologous bacterial peptide transporter PepTSo (Newstead et al., 2011) was deemed a suitable negative control for the SURFE2R N1 transport activity assay, as well as determining the specificity of any potential binding candidates to NupC.

To this extent, a His_6-tagged PepTSo construct was also expressed in C43 (DE3) *E. coli* by transforming competent cells with the plasmid pMPSIL0079A via the heat-shock method and then following the expression protocol outlined in subsection 3.4.2. The harvested cell membranes overexpressing His$_6$-tagged PepTSo were then mixed with a 25% (w/w) sucrose solution prepared in Tris/EDTA buffer and added to a 30-55% (w/w) sucrose density gradient in order to separate the inner and outer membrane fractions through the same procedure described for untagged NupC.

3.4.6. Measuring nucleoside transport activity via the SURFE2R N1

Desiccated POPC aliquots (5 mg) were rehydrated with 1 mL of PBS buffer each and subsequently extruded through a 200 nm polycarbonate filter using the Avanti Mini-Extruder to create 5 mg/mL LUV suspensions. These were then titrated at room temperature with 1 µL volumes of Triton X-100 at stock concentration (i.e. 10% (w/v) in ultrapure water) until R_{sat} was reached. At this point, an additional 5 µL of Triton X-100 were added to ensure that the LUVs had been optimally destabilised. Purified double Strep-tagged or His$_6$-tagged NupC were then added to the destabilised LUVs to give protein/lipid ratios of 1% (w/w). The resulting proteoliposomes were vortexed for 60 seconds using a Heidolph Reax Top test tube shaker, then left to incubate at room temperature for 15 minutes with gentle roller mixing. Bio-Beads® SM-2 were then added to a concentration of 50 mg/mL and the proteoliposomes were left to incubate for another 30 minutes under similar conditions in order to remove the Triton X-100 from solution. Following that, the Bio-Beads were left to sediment and the proteoliposomes were transferred into a new Eppendorf tube along with 50 mg of fresh Bio-Beads®. After an additional 60-minute incubation at 4 °C with gentle roller mixing, the proteoliposomes were once again transferred into a new Eppendorf tube containing 50 mg of fresh Bio-Beads® and then incubated overnight under identical conditions. The next day, the Bio-Beads® were removed and the proteoliposomes were harvested using a Beckmann ultracentrifuge fitted with a Ti45 rotor (100,000 *g* spin for 1 hour at 4 °C). The proteoliposomes were finally resuspended in PBS buffer to give concentrations of 5 mg/mL POPC and 50 µg/mL NupC (assuming a 100% recovery rate) and then re-extruded through a 200 nm polycarbonate filter to ensure their homogeneity.

In order to construct the hybrid alkanethiol/phospholipid biomimetic SSMs required for proteoliposomal adsorption, the stock N1 gold sensors were first incubated with 50 µL of Sensor Prep A (i.e. 1-octadecanethiol in isopropanol (1 mM)) for 15 minutes at room temperature while covered by a Petri dish, so as to ensure that the self-assembled thiol monolayer already present on their surface (as supplied by Nanion Technologies) was of sufficiently-high quality at the start of the SURFE2R N1 transport activity measurements.

The Sensor Prep A solution was removed by tapping on the up-ended sensors, after which their surfaces were rinsed thoroughly with MilliQ® water, then dried under a nitrogen stream. Any remaining solvents were allowed to evaporate from the uncovered sensors during an additional 15-minute incubation at room temperature. Sensor Prep B was then added in 3 µL volumes on top of the thiol layers while avoiding direct contact between the pipette tip and the thiolated gold surfaces. Immediately after, the sensors were filled with 50 µL of PBS buffer supplemented with 0.2 mM DTT and incubated at 4 °C covered in Parafilm M® to avoid desiccation.

Following that, the sensors were drained as previously described and immediately re-filled with 100 µL of PBS buffer. The proteoliposomes (1% (w/w) protein/lipid ratio) were then pipetted into the sensor wells in 5 µL volumes without disturbing the SSMs. So as to ensure their complete adsorption and the correct formation of the vesicle-SSM capacitively-coupled systems, the loaded sensors were subjected to centrifugation in an Eppendorf 5810 R table-top centrifuge (2,500 *g* spins for 30 minutes at 4 °C). After another 15-minute incubation at 4 °C, the sensors were finally ready to be used with the SURFE2R N1 workstation.

3.4.7. Traditional plate-based phage display screening

For performing a traditional plate-based phage display screening round against detergent-solubilised NupC, 100 µL of a purified His_6-tagged NupC solution (10 µg/mL) were added to the well of a Nunc™ MaxiSorp™ flat-bottomed 96-well plate and left to adsorb overnight at 4 °C. The following day, a TG1 *E. coli* cell culture was set up by using one colony from a TG1 *E. coli* stock Petri dish to inoculate 20 mL of 2×TY growth medium, which was then left to incubate at 37 °C with 200 rpm orbital shaking until it reached log-phase (i.e. D_{600nm} = 0.5-1.0). The MaxiSorp™ well containing the adsorbed His_6-tagged NupC was washed three times with 300 µL volumes of PBS buffer, then incubated with 300 µL of blocking buffer for 1 hour at room temperature with gentle rocking mixing so as to block any potential non-specific binding sites. Concomitantly, a 50 µL DARPin library aliquot was also blocked with a 1:1 volume of blocking buffer under similar conditions. Following the blocking incubations, the NupC-containing well was once again washed three times with 300 µL volumes of PBS buffer, after which the blocked DARPin library solution (100 µL) was added to the well. The plate was then left to incubate for another hour at room temperature before being washed five times with 300 µL of wash buffer, as well as five times with 300 µL of regular PBS buffer.

A 100 µL volume of elution buffer was then added to the well and left to incubate at 37 °C for 30 minutes with 600 rpm orbital shaking. Following that, the eluted DARPins were extracted from the well and infected into 900 µL of log-phase TG1 *E. coli* cell culture. This was then left to incubate at 37 °C for 1 hour with 200 rpm orbital shaking before being diluted 1:10, 1:100 and 1:1,000 (v/v) using 2×TY growth medium and plated onto separate 2×TYAG agar Petri dishes. All of the leftover cells were pelleted via centrifugation, resuspended in 3 mL of 2×TY growth medium and spread onto a 2×TYAG bioassay dish. After an overnight incubation at 30 °C, the colonies on the diluted Petri dish cultures were counted in order to determine the phage input titre, serving as an indication of the degree of overnight amplification and the number of phages that will be carried forward into the next round of selection. The bioassay dish was then scraped clean using 10 mL of 2×TY growth medium supplemented with 50% (w/v) glycerol. The scraped cells were used to create a 2 mL backup for storage at -80 °C, while the remaining 8 mL of infected TG1 *E. coli* were stored at -20 °C in preparation for phage rescue.

The following day, the phage rescue procedure involved inoculating 25 mL of 2×TYAG growth medium with infected TG1 *E. coli* to give a starting D_{600nm} value of 0.1. This phage rescue culture was then incubated at 37 °C with 280 rpm orbital shaking until it reached log-phase, after which it was superinfected with 2.5 µL of M13K07trp helper phage stock solution. Following that, the culture was left to incubate for one additional hour at 37 °C with 150 rpm orbital shaking before the cells were harvested via centrifugation (3,220 *g* spin for 10 minutes at 4 °C). While the supernatant was ultimately discarded, the cell pellet was resuspended in 0.5 mL of 2×TYAK growth medium and used to further inoculate 25 mL of the same media. Phage production was then left to occur overnight at 25 °C with 280 rpm orbital shaking. The next day, 1 mL of the overnight culture was pelleted at maximum speed in a table-top centrifuge and the resulting supernatant – containing the replicated phages – was transferred into a new Eppendorf tube and stored on ice in preparation for the next round of selection.

At the end of a second round of selection (performed by repeating the same steps outlined above), the colonies from the 1:10, 1:100 and 1:1,000-diluted Petri dish cultures were counted to give the phage output titre (i.e. an indication of the total phage selection output for the tested screening format). Individual colonies were then transferred onto a Costar® flat-bottomed 96-well plate containing 120 µL of 2×TYAG growth medium per well and left to incubate overnight at 37 °C with 150 rpm orbital shaking. The next day, 40 µL samples were taken from each well and transferred onto a new Costar® flat-bottomed 96-

well plate that was later sent for binder sequencing and diversity assessment, while the remaining well contents were each supplemented with 40 µL of 50% (w/v) glycerol so as to create another backup for storage at -80 °C.

3.4.8. Plasmid DNA extraction

In order to extract the plasmid DNA encoding each of the phage-bound DARPin binders selected against NupC, 5 mL of 2×TY growth medium supplemented with carbenicillin (100 µg/mL) were inoculated with thawed TG1 *E. coli* glycerol backups harbouring the respective phages. The 5 mL cultures were then left to incubate overnight at 37 °C with 200 rpm orbital shaking. The following day, the cells were pelleted in a table-top centrifuge (3,220 *g* spin for 15 minutes at room temperature) and then resuspended in 250 µL of resuspension buffer (provided in the ChargeSwitch®-Pro miniprep kit). After that, 250 µL of provided lysis buffer were added on top and left to incubate for 4 minutes at room temperature before 250 µL of provided precipitation buffer were added to the lysed cells. The resulting white precipitates were pelleted in a table-top centrifuge (17,000 *g* spin for 1 minute at room temperature), while the supernatants were transferred to the provided spin columns and re-centrifuged under similar conditions. The flowthroughs were then discarded and 750 µL of provided wash buffer 1 were added to the spin columns, followed by re-centrifugation. The flowthroughs were once again discarded and the centrifugation was repeated using 250 µL of provided wash buffer 2. After the last flowthroughs were discarded, the individual plasmids were eluted via centrifugation under similar conditions using 100 µL of provided elution buffer. In order to maximise the DNA yield, each eluate was transferred back into their original spin column and re-centrifuged one final time under similar conditions before being stored at -20 °C.

Having described all of the materials and general methods used throughout the experiments presented in the current thesis, the following chapter will begin showcasing the concept development work that led to the creation of the SSBLM platform embedding reconstituted purified NupC.

CHAPTER 4

SSBLM Formation and Characterisation

4.1. Target Protein Expression and Purification

Since the current chapter will focus on the step-by-step formation and characterisation of the SSBLM screening platform, the following subsections will present the quality-control results ensuring that the target proteins expressed and purified to a high-enough degree.

4.1.1. Double Strep-tagged NupC expression and purification

After using the protocol described in subsection 3.4.2, SDS-PAGE and Western blotting were used to assess the quality of purified double Strep-tagged NupC (Figure 4.1.1.1).

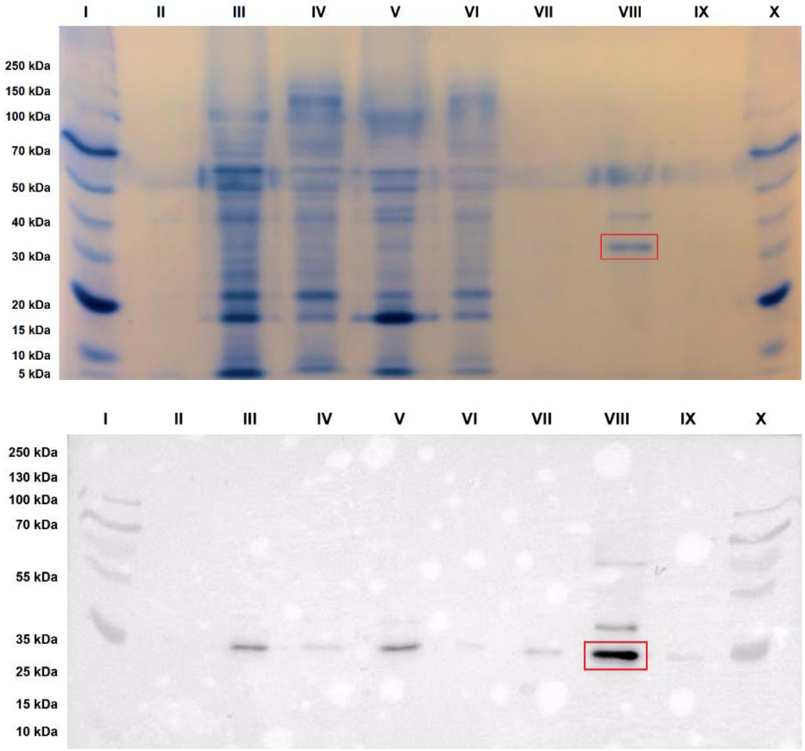

Figure 4.1.1.1. Coomassie Blue-stained polyacrylamide gel (top) and corresponding Western blot (bottom) stained to detect the Strep-tags of key samples taken during the expression and purification of double Strep-tagged NupC. The lanes represent, from left to right: I. Protein ladder; II. Pre-IPTG induction cell culture sample; III. Cell membrane pellet; IV. Soluble membrane fraction; V. Insoluble membrane fraction; VI. Overnight protein binding solution; VII. Elution fraction 1; VIII. Elution fractions 2, 3 and 4 (pooled); IX. Elution fraction 5; X. Protein ladder. The two red rectangles highlight the bands representative of purified double Strep-tagged NupC.

Ultimately, the purification of double Strep-tagged NupC was clearly successful, amounting to yields of approximately 0.5 mg of pure protein per 4 L of C43 (DE3) *E. coli* cell culture. Apart from the expected NupC monomer band at approximately 35 kDa, both SDS-PAGE and Western blotting also revealed the presence of NupC oligomers which co-eluted during the final stages of the purification process (Hao et al., 2016).

4.1.2. His_6-tagged NupC expression and purification

SDS-PAGE and Western blotting revealed that His_6-tagged NupC also expressed and purified successfully (Figure 4.1.2.1), amounting to average yields of 3 mg of pure protein per 4 L of C43 (DE3) *E. coli* cell culture. Oligomeric His_6-tagged NupC states (clearly visible on the Western blot) were also detected.

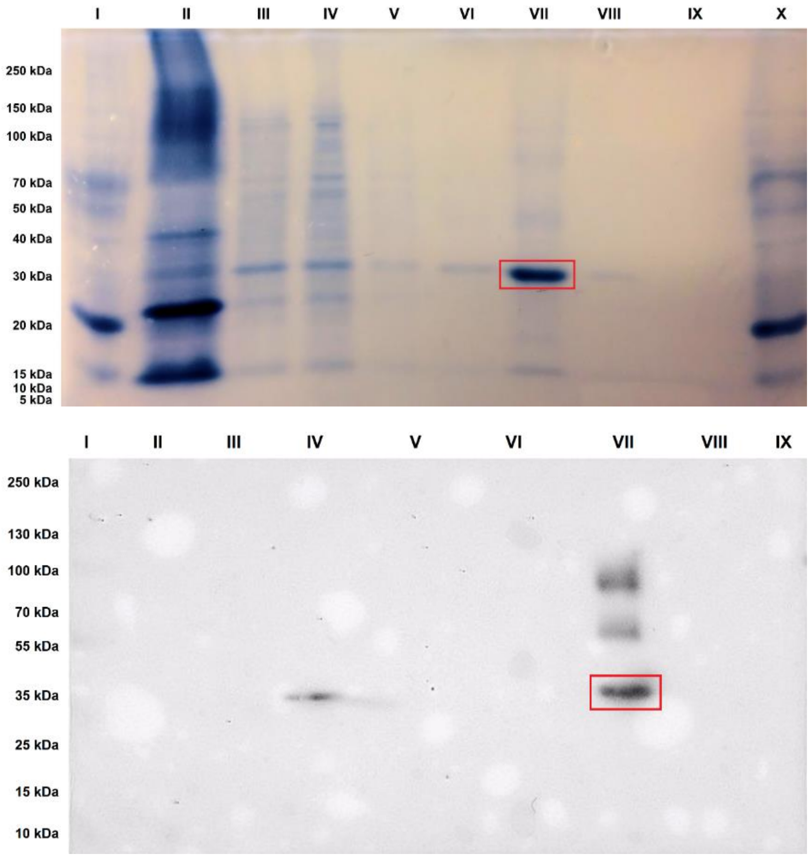

Figure 4.1.2.1. Coomassie Blue-stained polyacrylamide gel (top) and corresponding Western blot (bottom) stained to detect the His_6-tags of key samples taken during the expression and purification of His_6-tagged NupC. The lanes represent, from left to right: I. Protein ladder; II. Insoluble membrane fraction; III. Soluble membrane fraction; IV. Elution fraction 1; V. Elution fraction 2; VI. Elution fraction 3; VII. Elution fractions 2, 3 and 4 (pooled); VIII. Elution fraction 5; IX. Vivaspin® concentrator filtrate; X. Protein ladder. The two red rectangles highlight the bands representative of purified His_6-tagged NupC.

4.1.3. Untagged NupC expression and *E. coli* inner membrane extraction

Subjecting these key samples to SDS-PAGE revealed the presence of untagged NupC at each step of the protein expression and membrane harvesting processes (Figure 4.1.3.1). A BCA assay also indicated that the total protein content of the separated IM fraction amounted to 48 mg per 4 L of C43 (DE3) *E. coli* cell culture. The differences between the inner and outer membrane fractions with respect to their different protein contents were also highlighted via SDS-PAGE, confirming that – apart from some minor band overlap – the sucrose density separation was overall successful.

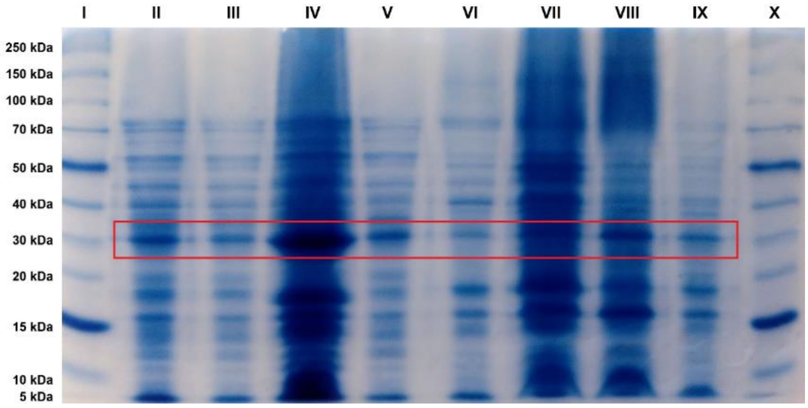

Figure 4.1.3.1. Coomassie Blue-stained polyacrylamide gel of key samples taken during the expression of untagged NupC. The lanes represent, from left to right: I. Protein ladder; II. Disrupted cells; III. Cell debris supernatant; IV. Cell debris pellet; V. Cytoplasmic protein fraction; VI. Cell membrane pellet; VII. Separated IM fraction; VIII. Separated OM fraction; IX. Control IM fraction; X. Protein ladder. The red rectangle highlights the bands representative of untagged NupC.

4.1.4. His$_6$-tagged PepTSo expression and purification

The NupC-homologous bacterial peptide transporter PepTSo (Newstead et al., 2011) was deemed a suitable negative control for the SURFE2R N1 transport activity assay, as well as any future assays determining the specificity of isolated binding candidates to NupC.

Key samples taken throughout the expression of a His$_6$-tagged PepTSo construct were loaded onto polyacrylamide gels and subjected to both SDS-PAGE and Western blotting (Figure 4.1.4.1 overleaf). Instead of purifying the protein via high-affinity chromatography, a sucrose density gradient was once again used towards separating the inner and outer bacterial membrane fractions, ultimately resulting in a total IM protein yield of 34 mg per 4 L of C43 (DE3) *E. coli* cell culture, as revealed by a BCA assay.

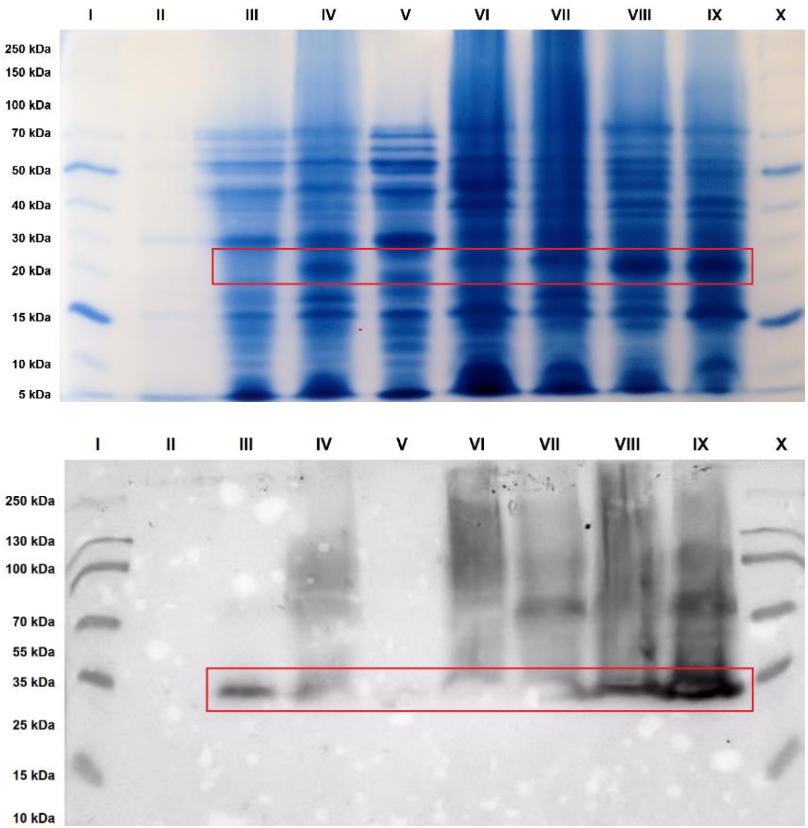

Figure 4.1.4.1. Coomassie Blue-stained polyacrylamide gel (top) and corresponding Western blot (bottom) stained to detect the His_6-tags of key samples taken during the expression and purification of His_6-tagged PepTSo. The lanes represent, from left to right: I. Protein ladder; II. Pre-IPTG induction cell culture sample; III. Cell debris supernatant; IV. Cell debris pellet; V. Cytoplasmic protein fraction; VI. Cell membrane pellet; VII. Separated IM fraction; VIII. Separated OM fraction; IX. Control IM fraction; X. Protein ladder. The red rectangles highlight the bands representative of His_6-tagged PepTSo.

4.2. Assaying the Transport Activity of Purified NupC

So as to determine whether the nucleoside transport activities of the three NupC constructs were preserved following their purification or IM extraction, several samples were prepared for use with the SURFE2R N1 workstation. Double Strep-tagged and His_6-tagged NupC/POPC LUVs (200 nm, 1% (w/w) protein/lipid ratios) were formed according to the protocol outlined by Geertsma et al. (2008), reproduced in subsection 3.4.6. At first, the SURFE2R did not detect any signals representative of nucleoside transport from either proteoliposome sample (data not shown here), suggesting that these two constructs might not be active when reconstituted into lipid vesicles post-purification. Furthermore, 200 nm untagged NupC-embedding LUVs extruded directly from *E. coli* IMs overexpressing this particular construct also failed to produce signals indicative of nucleoside transport (Figure 4.2.1.1 overleaf).

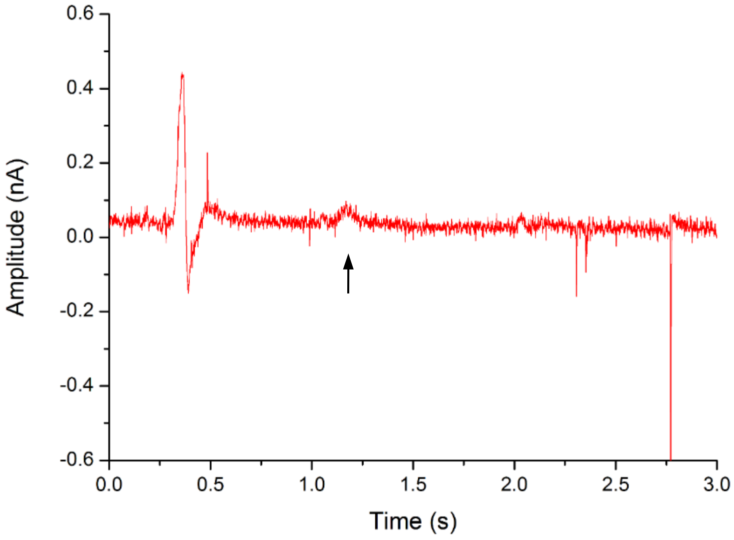

Figure 4.2.1.1. SURFE2R N1 trace of the measured nucleoside transport activity of untagged NupC embedded in native IM LUVs (200 nm in diameter). The addition of the activating solution (i.e. PBS buffer containing 5 µM adenosine at t = 0 s) did not trigger any transient currents indicative of nucleoside transport into the sensor-bound LUVs (black arrow).

In order to determine whether the lack of transport activity was an unintended consequence of NupC overexpression, the IMs were mixed 1:50 (w/w) with *E. coli* polar lipid extracts (PLEs) dissolved in PBS buffer (5 mg/mL), then tip-sonicated 100× using a Hielscher UP50H (0.5 cycles, 20% amplitude) before using the same SURFE2R protocol. With these untagged NupC-embedding IM/PLE LUVs, transient currents suggestive of bidirectional adenosine transport became readily apparent (Figure 4.2.1.2).

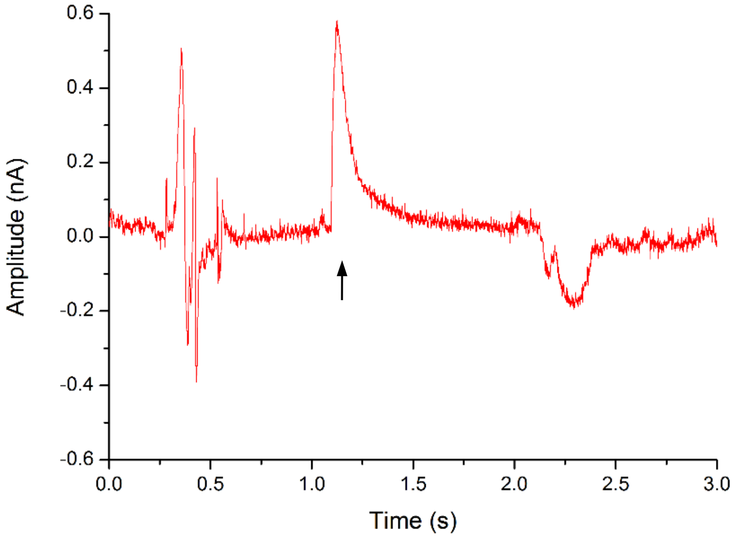

Figure 4.2.1.2. SURFE2R N1 trace of the measured nucleoside transport activity of untagged NupC embedded in 200 nm IM/PLE LUVs. The addition of the activating solution (i.e. PBS buffer containing 5 µM adenosine at t = 0 s) triggered a transient inward current (black arrow) indicative of nucleoside transport into the sensor-bound LUVs. The reintroduction of the control solution (i.e. regular PBS buffer at t = 2 s) caused the substrate to be transported back out of the adsorbed LUVs and thus generate a transient outward current (i.e. the depression at t = 2.25 s).

The amplitudes of the measured transient currents were expectedly found to be directly proportional to the substrate concentrations of the activating solutions, which helped generate a Michaelis-Menten-like activity profile with a K_m of 3.9 µM (Figure 4.2.1.3).

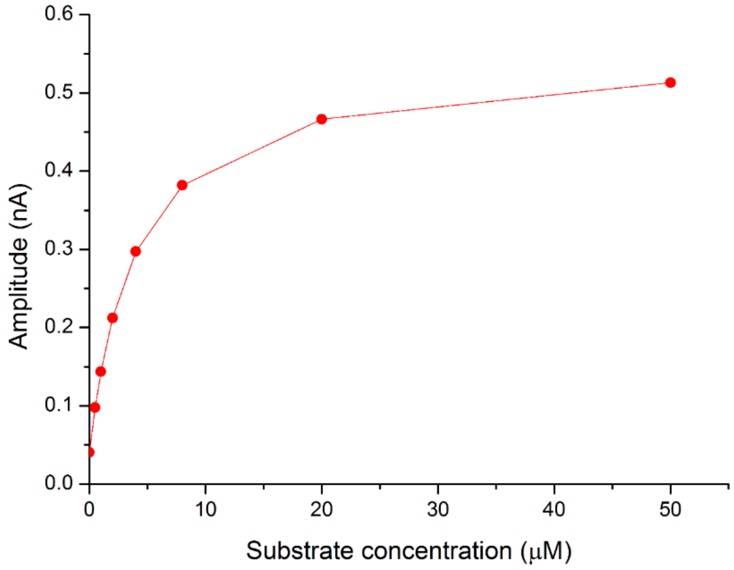

Figure 4.2.1.3. Michaelis-Menten curve of transient inward current peak amplitudes generated by increasing substrate concentrations using IM/PLE LUVs embedding untagged NupC. The following values have been calculated using this curve: V_{max} = 0.54 nA, K_m = 3.9 µM.

The above results confirmed that untagged NupC was still functional while overexpressed in *E. coli* IM fractions. Further measurements were performed during a summer internship by an undergraduate student – Katrina Moisley – using the double Strep- and His$_6$-tagged NupC constructs presented in the same IM/PLE LUV format. Although no transport activity was ever detected from double Strep-tagged NupC presented in either format, IM-bound His$_6$-tagged NupC did ultimately show signs of nucleoside transport, albeit at much lower levels compared to untagged NupC (data not shown here). While this was not investigated any further, the most likely culprit behind these unfavourable results was probably the His$_6$-tag itself (Mohanty and Wiener, 2004), whose insertion into one of the extramembranous loops could have disrupted the conformation of the central pore and thus hampered the transport capabilities of this particular NupC construct.

4.3. Planar SSM Formation and Characterisation

Following the purification or IM extraction of the above membrane protein constructs, the focus of the project shifted towards characterising and optimising the formation of lipid SSMs on planar silica substrates towards the goal of ultimately embedding the purified membrane protein targets in a native-like antibody screening platform.

4.3.1. Monitoring planar SSM formation via QCM-D

Initial attempts at forming planar SSMs on SiO_2 sensor chips involved running 200 nm POPC LUVs diluted to 0.5 mg/mL in MOPS buffer through a Q-Sense E4 QCM-D set to a constant temperature of 22 °C and a pump flow rate of 100 µL/min. These attempts were met with consistent success and one such example is depicted in Figure 4.3.1.1 below. After the addition of the POPC LUV solution to the SiO_2 QCM-D sensor (A), the measured frequency dropped rapidly while dissipation increased proportionately due to the adsorption of increasing numbers of vesicles to the sensor surface (Richter et al., 2006). After the critical concentration of adsorbed LUVs had been reached (B), the vesicles began to fuse together and burst, increasing frequency as buffer was released from the ruptured LUVs. These then reassembled into a continuous lipid bilayer on the sensor surface (C) and, once the surplus vesicles were washed off with MilliQ® water (D) and plain MOPS buffer was reintroduced to the system (E), the resulting stable SSM was characterised by a frequency shift of -25 Hz, mirrored by a dissipation value of approximately 0.1×10^{-6} (Cho et al., 2010).

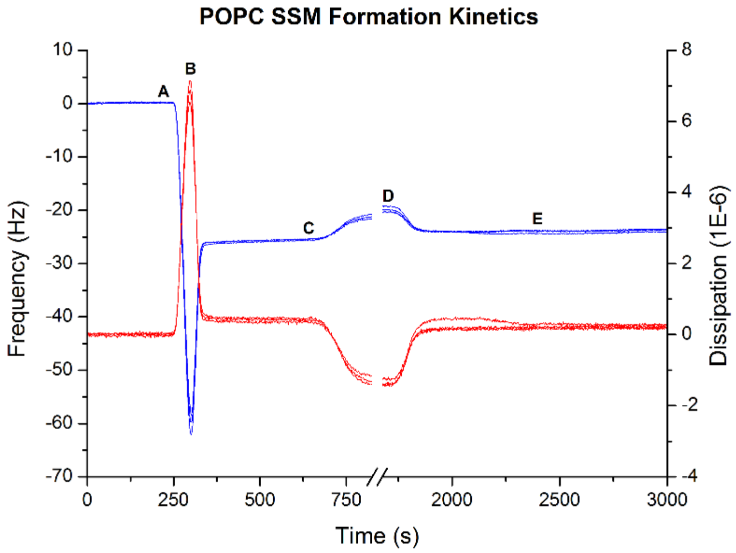

Figure 4.3.1.1. Planar lipid SSM formation kinetics given by frequency (blue, left Y-axis) and dissipation (red, right Y-axis) as monitored via QCM-D using POPC LUVs suspended in MOPS buffer at a concentration of 0.5 mg/mL: (A) The POPC LUV solution is introduced; (B) Critical LUV coverage is reached and lipid bilayer formation begins; (C) Intact LUVs are washed off with MilliQ® water; (D) Plain MOPS buffer is re-introduced; (E) Stable SSM formation is reached. The data was presented at the 7th, 9th and 11th resonance overtones of the SiO_2 QCM-D sensor.

Due to providing a better representation of the native membrane environment of NupC, 200 nm LUVs were also extruded from *E. coli* PLEs towards replicating the favourable POPC SSM formation results on identical SiO_2 sensors. Unfortunately, this proved significantly more difficult, in no small part due to the considerable electrostatic repulsion occurring between the negatively-charged *E. coli* phospholipid head groups and the similarly-charged SiO_2 substrate, which impeded the adsorption of the LUVs to the sensor surface. In order to circumvent this issue, a divalent cation solution (i.e. 10 mM $CaCl_2$) was mixed with the LUV suspension so as to promote vesicle-substrate interactions and, consequently, facilitate SSM formation (McMillan et al., 2013). Further attempts also included running the *E. coli* PLE LUVs through the QCM-D at higher temperatures that were closer to the ideal *E. coli* proliferation conditions (i.e. 37 °C).

While applying the above-mentioned protocol iterations did ultimately result in *E. coli* PLE SSMs forming on the SiO_2 sensors, their formation kinetics were unfortunately extremely slow, as stable SSMs were only formed after more than 2 hours of running time. This contrasted sharply with POPC SSM formation, during which LUVs readily formed lipid bilayers on the SiO_2 surface not only without the need for any supplementary chemical intervention, but also within a significantly shorter time frame as well (i.e. less than 40 minutes of running time). The much quicker bilayer formation kinetics reported with POPC LUVs ultimately rendered them as the better choice for fast and reliable SSM formation over their *E. coli* PLE counterparts.

4.3.2. Planar SSM formation using NupC-embedding proteoliposomes

In order to form POPC SSMs featuring embedded NupC, the purified double Strep-tagged and His_6-tagged constructs were reconstituted into 400 nm POPC LUVs (1% (w/w) protein/lipid ratios) diluted in KPi buffer (5 mg/mL) following the protocol described in subsection 3.4.6. Unfortunately, the first attempts at forming SSMs using either proteoliposomes on identical SiO_2 sensors proved unsuccessful. While the measurements did indicate LUV adhesion to the sensor surfaces (data not shown here), SSM formation could not be achieved even after the forced osmotic lysis brought on by the MilliQ® water wash. Proteoliposomes extruded through polycarbonate filters with smaller pore sizes (i.e. 200-, 100- and 50 nm) were also tested, but without any success. Fortunately, limiting the Triton X-100 titrations to the bare minimum required to reach R_{sat} during the NupC reconstitution phase ultimately resolved SSM formation using both the double Strep- and His_6-tagged NupC/POPC proteoliposomes (Figures 4.3.2.1b and 4.3.2.1c overleaf). Not only that, but their different dissipation values reported to that of the POPC negative control SSM (Figure 4.3.2.1a overleaf) also confirmed the presence of embedded protein.

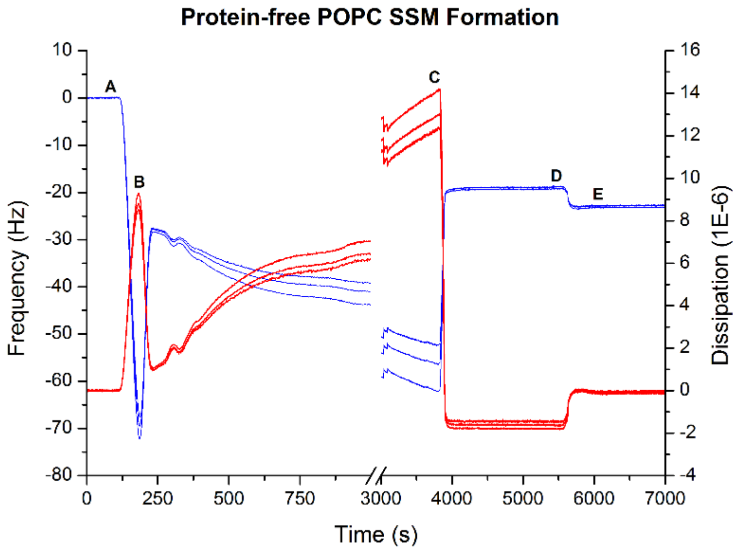

Figure 4.3.2.1a. SSM formation kinetics given by frequency (blue, left Y-axis) and dissipation (red, right Y-axis) as monitored via QCM-D using protein-free, 50 nm negative control POPC SUVs: (A) The POPC SUV solution is introduced; (B) Critical SUV coverage is reached and lipid bilayer formation begins; (C) Intact SUVs are washed off with MilliQ® water; (D) Plain KPi buffer is re-introduced; (E) Stable SSM formation is reached. The final dissipation value of approximately 0 suggested that the SSM formed a rigid structure on the sensor surface. The data was presented at the 7th, 9th and 11th resonance overtones of the SiO_2 sensor.

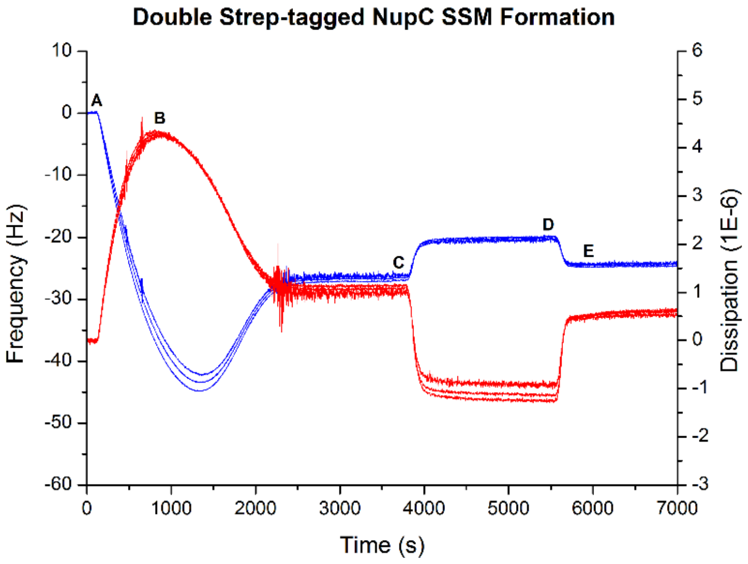

Figure 4.3.2.1b. SSM formation kinetics given by frequency (blue, left Y-axis) and dissipation (red, right Y-axis) as monitored via QCM-D using 50 nm double Strep-tagged NupC/POPC SUVs (1% (w/w) protein/lipid ratio): (A) The NupC/POPC SUV solution is introduced; (B) Critical SUV coverage is reached and lipid bilayer formation begins; (C) Intact SUVs are washed off with MilliQ® water; (D) Plain KPi buffer is re-introduced; (E) Stable SSM formation is reached. The final dissipation value of approximately 0.6×10^{-6} suggested that the formed SSM also embedded double Strep-tagged NupC. The data was presented at the 7th, 9th and 11th resonance overtones of the SiO_2 sensor.

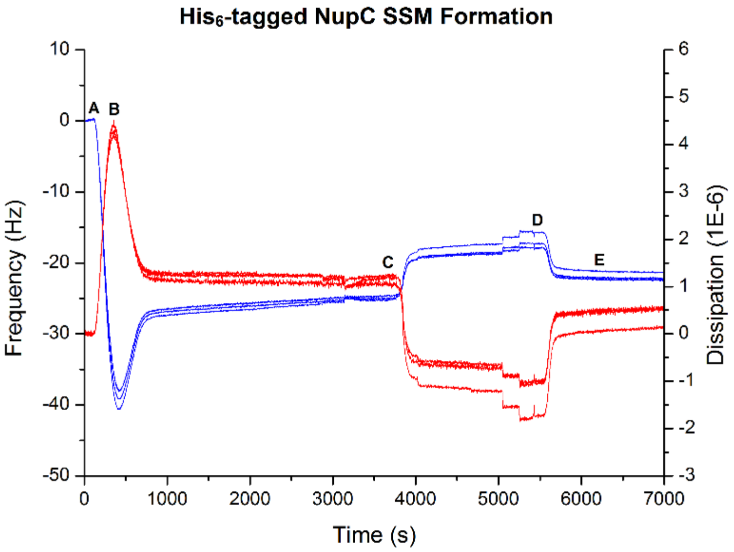

Figure 4.3.2.1c. SSM formation kinetics given by frequency (blue, left Y-axis) and dissipation (red, right Y-axis) as monitored via QCM-D using 50 nm His$_6$-tagged NupC/POPC SUVs (1% (w/w) protein/lipid ratio): (A) The NupC/POPC SUV solution is introduced; (B) Critical SUV coverage is reached and lipid bilayer formation begins; (C) Intact SUVs are washed off with MilliQ® water; (D) Plain KPi buffer is re-introduced; (E) Stable SSM formation is reached. The final dissipation value of approximately 0.6×10^{-6} suggested that the formed SSM also embedded His$_6$-tagged NupC. The data was presented at the 7th, 9th and 11th resonance overtones of the SiO_2 sensor.

While SSM formation using native membrane vesicles is complicated not only by the presence of non-bilayer-forming lipids, but also that of a myriad of other naturally-occurring membrane constituents (Elie-Caille et al., 2005), positive results have nevertheless been reported with proteoliposomes formed after mixing harvested native membranes with bilayer-forming model lipids such as phosphatidylcholine (Dodd et al., 2008).

In order to test this with NupC, *E. coli* IMs overexpressing the untagged construct were mixed with 50 nm POPC SUVs at a 1:50 (w/w) ratio via the freeze-thaw method and were fortunately also found to form bilayers on SiO_2 QCM-D sensors (Figure 4.3.2.1d overleaf). This result was particularly encouraging towards the future formation of SSMs embedding other classes of potential membrane protein targets while still being expressed in their original native membrane environments, without any need to spend additional time and effort on purifying and subsequently reconstituting them into model lipid vesicles.

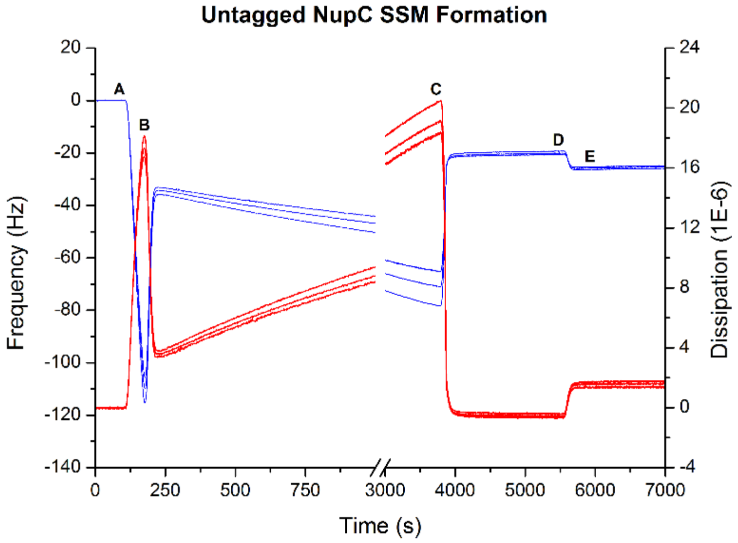

Figure 4.3.2.1d. SSM formation kinetics given by frequency (blue, left Y-axis) and dissipation (red, right Y-axis) as monitored via QCM-D using 50 nm *E. coli* IM/POPC SUVs overexpressing untagged NupC: (A) The IM/POPC SUV solution is introduced; (B) Critical SUV coverage is reached and lipid bilayer formation begins; (C) Intact SUVs are washed off with MilliQ® water; (D) Plain KPi buffer is re-introduced; (E) Stable SSM formation is reached. The final dissipation value of approximately 1.5×10^{-6} suggested that the formed SSM also embedded untagged NupC. The data was presented at the 7th, 9th and 11th resonance overtones of the SiO_2 sensor.

4.4. SSBLM Formation and Characterisation

Since the positive QCM-D results presented above were found to be reproducible, the focus of the project shifted towards replicating SSM formation – first lipid-only, then protein-embedding – on the surfaces of spherical silica nanoparticles.

4.4.1. Confirmation of substrate saturation via fluorescence spectroscopy

SSBLM formation was initially attempted on 100- and 200 nm silica nanoparticles using fluorescently-labelled POPC LUVs, so as to enable the detection of the newly-formed SSBLMs via spectrofluorometry. The fluorescent labelling of POPC was achieved by first dissolving Texas Red® (TR)-modified lipids in a 1:1 (v/v) mixture of chloroform and methanol (0.5 mg/mL). A 100 µL volume of the resulting TR solution was then added to a desiccated 5 mg POPC aliquot, followed by a vigorous 60-second vortexing to ensure the proper mixing of the different lipid types. The solvent mixture was removed at room temperature by placing the vial first under a nitrogen stream for 60 seconds, then under vacuum for 2 hours. The desiccated TR/POPC lipids (1% (w/w) ratio) were then finally rehydrated using 1 mL of PBS buffer and extruded through a 200 nm polycarbonate filter.

In order to determine the LUV/nanoparticle (w/w) ratios that would saturate the chosen substrates (i.e. achieve 100% lipid bilayer coverage), fluorescent SSBLMs were formed on 100- and 200 nm silica nanoparticles by mixing 25 μL of each nanoparticle stock solution (i.e. 10 mg/mL in deionised water) with increasing amounts of TR/POPC LUVs, ranging from 0-100% (w/w) LUVs/nanoparticles for the 100 nm nanoparticles and 0-50% (w/w) LUVs/nanoparticles for the 200 nm nanoparticles. The resulting mixtures were then each made up to 100 μL using MilliQ® water and subjected to 60 seconds of vigorous vortexing, causing the LUVs and nanoparticles to collide with one another. Ultimately, this lead to the former collapsing and re-forming into SSBLMs enveloping the latter.

The SSBLM samples were then left to incubate for 1 hour at room temperature with gentle roller mixing before the particles were pelleted in a Thermo Scientific Heraeus Fresco 17 centrifuge (13,000 *g* spin for 30 seconds at 4 °C). The supernatants were transferred into separate Eppendorf tubes and stored at 4 °C, while the SSBLM pellets were washed in similar volumes of MilliQ® water during a 30-minute incubation at 4 °C with gentle roller mixing before being re-pelleted and resuspended in 100 μL of PBS buffer each. The particle samples were then diluted 20× further in a Hellma Quartz SUPRASIL precision cuvette using MilliQ® water, after which a Perkin Elmer LS 55 spectrofluorometer was used to measure their emissions at 615 nm with excitation set to 595 nm (Figure 4.4.1.1).

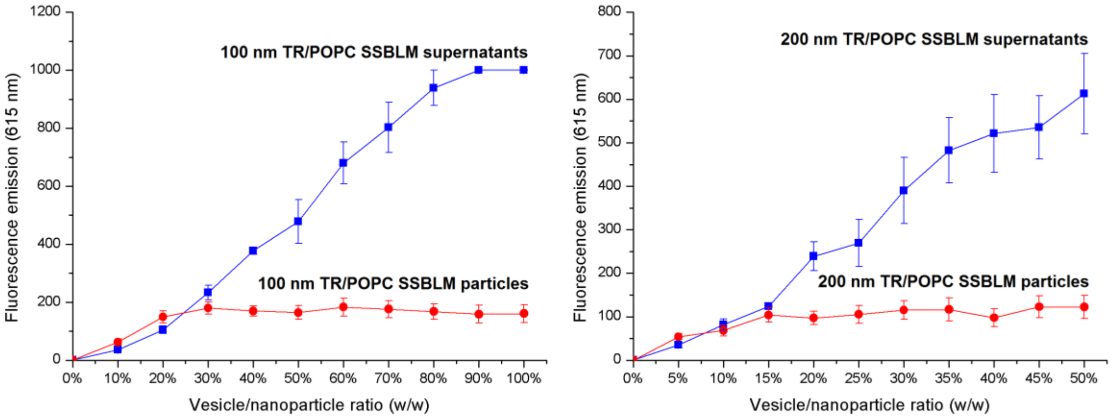

Figure 4.4.1.1. The fluorescence emissions resulting from 100 nm (left) and 200 nm (right) silica nanoparticles coated with SSBLMs formed using TR-labelled POPC liposomes (red), as well as from their respective supernatants (blue) after pelleting the particles. The saturation thresholds at which 100% SSBLM coverage was achieved were 30- and 15% (w/w) for the 100- and 200 nm silica nanoparticles, respectively. The error bars represent the standard error of the mean, n = 2.

In the case of the 100 nm silica nanoparticles, the minimal LUV/nanoparticle ratio that appeared to saturate the substrate was 30% (w/w). Increasing the LUV concentration beyond this point resulted in the surplus fluorescent material remaining in the sample supernatants and thus leading to a mirrored increase in emission that ultimately saturated the spectrofluorometer at the top-end of the spectrum. A similar result was observed for the 200 nm silica nanoparticles, where substrate saturation occurred beyond an LUV/nanoparticle ratio of 15% (w/w).

Having determined the saturation thresholds for both particle sizes, all subsequent SSBLM experiments were performed at LUV/nanoparticle ratios of at least 50- and 25% (w/w) for the 100- and 200 nm particles, respectively, in order to ensure the saturation of the silica substrate. This provided not only maximal antigen coverage, but also minimised the chances of any potential non-specific interactions occurring between the experimental solutions and areas of silica left bare as consequence of incomplete SSBLM formation.

4.4.2. Characterisation of SSBLM formation via SAXS

While fluorescence spectroscopy did indicate that the POPC lipid material was attaching to the silica substrate to the point of saturation, it could not also be used to discriminate the correct formation of actual SSBLMs around the nanoparticles from the mere adhesion of intact lipid vesicles to the available silica surface. It is for this reason then that SAXS – a technique capable of deriving structural information from nanosized objects suspended in solution – was subsequently used for the detection and characterisation of silica-bound SSBLMs. All of the SAXS measurements described in this section were taken at room temperature by Dr. Amin Sadeghpour from the School of Food Science and Nutrition at the University of Leeds.

Prior to starting the SAXS measurements, the optimal beam exposure time was determined after vigorously vortexing both the SSBLM and negative control (i.e. bare silica nanoparticle) samples for 60 seconds and then measuring the time needed for both particle types to sediment at room temperature under normal gravity. It was thus revealed that the minimal time required for the complete sedimentation of both samples was in excess of 2-3 hours, thereby ensuring that the SAXS measurements could be performed using longer beam exposure times in order to improve the resolution of the individual scattering profiles.

Having determined the above, POPC SSBLMs were formed on 100 nm silica nanoparticles at a 60% (w/w) LUV/nanoparticle ratio according to the protocol described in subsection 4.4.1, after which the washed SSBLM pellets were resuspended in PBS buffer at particle concentrations of 30 mg/mL. These were then measured together with their bare stock counterparts at room temperature and a significant difference was noted between the two scattering profiles (Figure 4.4.2.1).

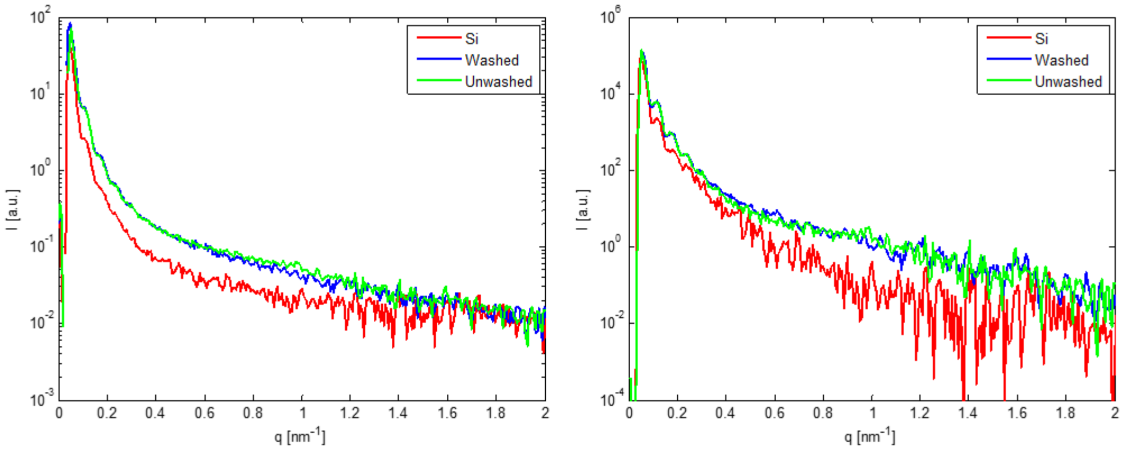

Figure 4.4.2.1. Left: the scattering profiles obtained from stock 100 nm silica nanoparticles (red), as well as POPC SSBLMs before and after washing away the excess LUV material (green and blue, respectively). Right: the same data after deconvoluting the scattering curves with the beam profile in order to increase curve resolution (courtesy of Dr. Amin Sadeghpour, The School of Food Science and Nutrition, University of Leeds).

The data analysis for the SAXS measurements comparing the 100 nm POPC-coated nanoparticles to the negative control ones offered confirmation of correct SSBLM formation. By fitting the data from the stock nanoparticles and including a Gaussian size distribution, a radius (R) with a value of 47.8 ± 3.5 nm was determined, which proved consistent with manufacturer nanoComposix's specifications for the stock 100 nm silica nanoparticles used throughout the project (Figure 4.4.2.2).

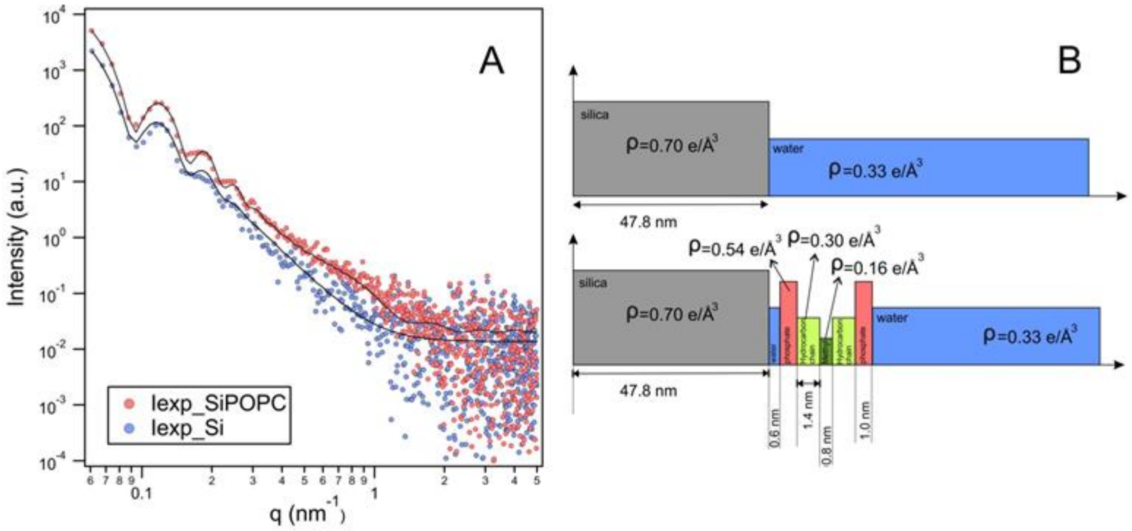

Figure 4.4.2.2. The scattering profiles obtained from 100 nm bare silica nanoparticles (blue) and POPC SSBLM samples (red), alongside their corresponding fit functions (A) and electron density profiles presented according to the fitting parameters deduced from the raw data (B) (courtesy of Dr. Amin Sadeghpour, The School of Food Science and Nutrition, University of Leeds).

The data from the POPC-coated samples was then fitted with the fixed silica nanoparticle radius according to a strip model. All electron densities of the modelled SSBLM layers were set to their literature values and the radial dimensions of the lipid bilayer were kept free. While this resulted in a correct fit, the lipid bilayer thickness – specifically the phosphate-to-phosphate distance – appeared higher than normal (i.e. 4.6 nm, compared to 3.9 nm at room temperature (Kučerka et al., 2011)).

Unfortunately, the very high nanoparticle concentrations required for obtaining high-resolution scattering profiles (i.e. 30 mg/mL) were prohibitive towards taking SAXS measurements of SSBLMs embedding either of the three NupC constructs due to the sheer amount of purified membrane protein required to create such highly-concentrated samples. This ultimately prevented the use of SAXS as a means of confirming the presence of SSBLM-embedded NupC and thus alternative methods had to be used to this end instead.

4.5. Formation and Characterisation of SSBLMs Embedding NupC

After demonstrating the successful formation of SSBLMs on the silica nanoparticle substrates, the presence of the embedded protein was confirmed using a suite of techniques described throughout the following subsections.

4.5.1. Confirmation of SSBLM-embedded NupC via Western blotting

Western blotting represented one of the more straightforward methods explored for confirming the presence of SSBLM-embedded (His_6-tagged) NupC. After multiple protocol iterations, a protein/lipid reconstitution ratio of 2.4% (w/w) was used to create 200 nm NupC/POPC proteoliposomes from which 100 μL SSBLM samples were formed at LUV/nanoparticle ratios of 20- and 50% (w/w) for the 100 nm nanoparticles and 10- and 25% (w/w) for their 200 nm counterparts. The supernatant solutions resulting from pelleting the SSBLMs – containing all of the excess proteoliposomal material – were also included on the Western blot.

Upon imaging the blotted membrane following its incubation with 5 mL of HRP-conjugated mouse IgG_1 anti-His antibodies diluted 1:5,000 (v/v) in PBS buffer, several bands were revealed at a molecular weight consistent with that of purified His_6-tagged NupC, which was used as a positive control in lane X (Figure 4.5.1.1 overleaf). The appearance of the bands confirmed that Western blotting represents a viable means of detecting SSBLM-embedded NupC. Furthermore, the direct relationship between the LUV/nanoparticle ratios and the intensity of the bands encouraged the predominant use of the 100 nm nanoparticles in all subsequent experiments, in order to maximise the available surface area for antigen presentation on the SSBLM particles.

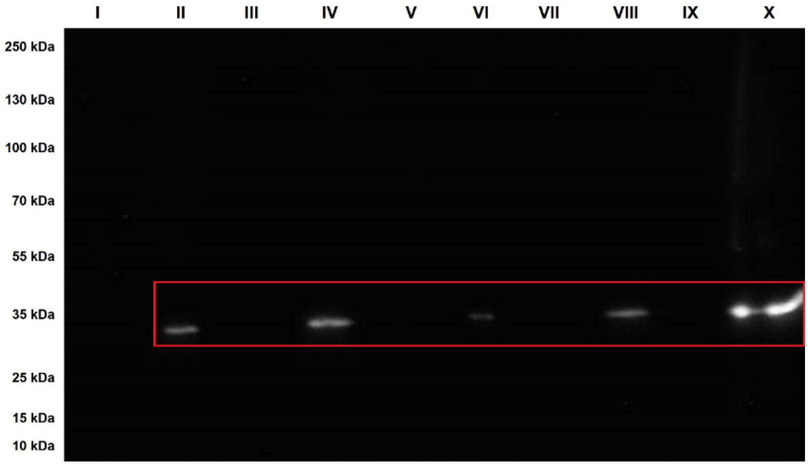

Figure 4.5.1.1. Western blot of 100- and 200 nm POPC SSBLMs embedding His$_6$-tagged NupC. The lanes represent, from left to right: I. Protein ladder (not visible as chemiluminescence); II. 100 nm, 20% (w/w) SSBLMs; III. 100 nm, 20% (w/w) SSBLM supernatant; IV. 100 nm, 50% (w/w) SSBLMs; V. 100 nm, 50% (w/w) SSBLM supernatant; VI. 200 nm, 10% (w/w) SSBLMs; VII. 200 nm, 10% (w/w) SSBLM supernatant; VIII. 200 nm, 25% (w/w) SSBLMs; IX. 200 nm, 25% (w/w) SSBLM supernatant; X. Purified His$_6$-tagged NupC positive control. The red rectangle highlights the bands representative of His$_6$-tagged NupC.

It was certainly interesting to note, however, that the supernatant-containing lanes (i.e. III, V, VII and IX) did not produce any bands on the Western blot at all, especially given that their respective SSBLM samples had been created using an excess of proteoliposomal material (as determined in subsection 4.4.1). While this occurrence was not investigated any further, the absence of any supernatant bands suggested that the entire membrane protein content of the excess proteoliposomes had instead been completely adsorbed onto the nanoparticle substrates, resulting in SSBLMs embedding a higher NupC content than anticipated. This, in turn, would imply that using LUV/nanoparticle ratios exceeding the established saturation thresholds during SSBLM formation could ultimately prove beneficial towards maximising the total antigen presented by a given particle population.

4.5.2. Confirmation of SSBLM-embedded NupC via peroxidase assay

The second method of detecting NupC presented in the SSBLM format focused on determining the accessibility of the embedded protein towards antibody binding. This involved the use of a peroxidase assay to detect the presence of HRP-conjugated anti-His antibodies bound to SSBLM-embedded His_6-tagged NupC.

To this extent, a 1% (w/w) reconstitution of purified His_6-tagged NupC into detergent-destabilised 200 nm POPC LUVs yielded proteoliposomes that were subsequently used towards forming 100- and 200 nm SSBLM samples at 50- and 25% (w/w) LUV/nanoparticle ratios, respectively. POPC-only LUVs of similar sizes were also used to create protein-free SSBLMs for negative control purposes. The washed SSBLM particles were then incubated with 1:1 volumes of HRP-conjugated mouse IgG_1 anti-His antibodies (diluted 1:5,000 (v/v) in PBS buffer) for 1 hour at room temperature under gentle roller mixing before the SSBLMs were pelleted via centrifugation (13,000 *g* spin for 30 seconds at 4 °C) and the supernatant solutions were removed alongside any unbound antibodies. The particles were then washed twice via two 10-minute incubations at room temperature with gentle roller mixing in 1:1 volumes of PBS buffer supplemented with 2.5% (w/v) POPC LUVs – so as to patch-up any potential areas of exposed silica substrate – followed by re-centrifugation.

The SSBLMs were finally resuspended in 50 µL of PBS buffer, transferred to a Costar® flat-bottomed 96-well plate in 1, 2, 4, 8, 16, 20, 30, 40 and 50 µL volumes and supplemented with ADHP working reagent solution (50 µL/well, prepared according to the protocol supplied by AnaSpec). The developing fluorescence emission was then measured at 590 nm using a Perkin Elmer Victor X3 Multilabel fluorescent plate reader throughout a total reagent incubation time of 30 minutes (Figure 4.5.2.1 overleaf).

Measuring the fluorescence at regular intervals revealed an almost linear increase in detected emission that was directly proportional to the SSBLM sample volumes. The surprisingly high background signal emitted by the protein-free negative controls was attributed to the non-specific binding of HRP-conjugated anti-His antibodies to either patches of exposed silica following incomplete substrate coverage or to the SSBLM lipid component itself, likely coupled with an insufficiently-thorough wash of any remaining unbound antibodies prior to the ADHP reagent incubation and fluorescence measurement phases.

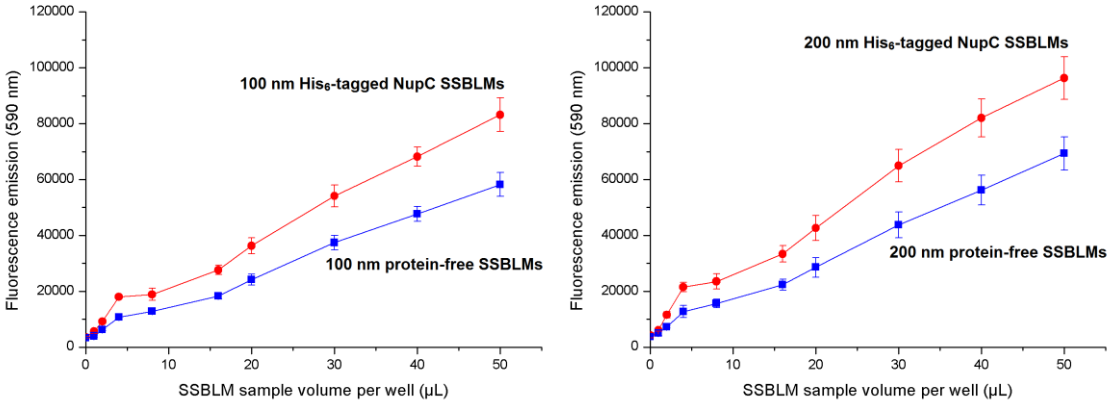

Figure 4.5.2.1. The fluorescence emissions resulting from 100 nm (left) and 200 nm (right) silica nanoparticles coated with SSBLMs formed using protein-free POPC LUVs (blue) and proteoliposomes embedding His$_6$-tagged NupC (red) after 30 minutes of incubation with the ADHP working reagent. The error bars represent the standard error of the mean, n = 2.

Several protocol optimisations were tested towards reducing non-specific antibody binding in hopes of eliminating the significant background fluorescence emission. Thus, new 100- and 200 nm SSBLM samples were respectively formed at 50- and 25% (w/w) LUV/nanoparticle ratios using 200 nm His$_6$-tagged NupC/POPC proteoliposomes created at 2.4% (w/w) protein/lipid ratios. POPC-only SSBLMs were once again formed at similar ratios to serve as protein-free negative controls. Following the MilliQ® water wash, the SSBLM solutions were divided into 50 µL volumes, pelleted via centrifugation (13,000 *g* spin for 30 seconds at 4 °C) and resuspended in increasing volumes (i.e. 1, 2, 4, 8, 12, 16, 20, 30, 40 and 50 µL) of HRP-conjugated mouse IgG$_1$ anti-His antibodies diluted 1:5,000 (v/v) in PBS buffer. In an attempt at blocking any available non-specific binding sites, each SSBLM solution was then further supplemented with 1 mg/mL BSA and 1% (w/v) POPC LUVs before being made up to a final volume of 50 µL using MilliQ® water, followed by vigorous vortexing for 60 seconds.

The SSBLM solutions were left to incubate with their respective anti-His antibody solutions for 1 hour at room temperature with gentle roller mixing before the particles were washed twice in 1:1 volumes of the above-mentioned blocking buffer via two 10-minute incubations under similar conditions, followed by pelleting and resuspension in the same buffer. The washed SSBLM particles where once again vortexed vigorously for 60 seconds before being transferred onto a Costar® flat-bottomed 96-well plate and mixed with 50 µL of ADHP working reagent to give final volumes of 100 µL per well. The fluorescence emission of the SSBLM samples was then measured using the same fluorescent plate reader setup as before (Figure 4.5.2.2 overleaf).

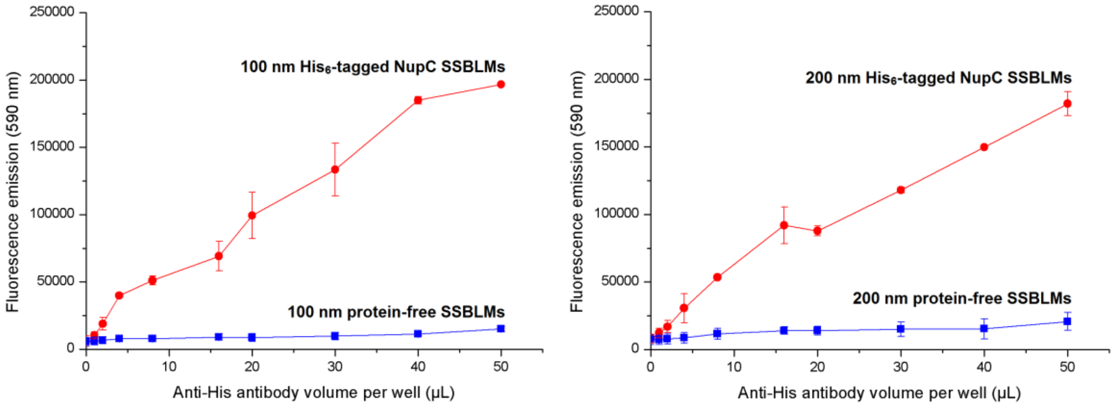

Figure 4.5.2.2. The fluorescence emissions resulting from 100 nm (left) and 200 nm (right) silica nanoparticles coated with SSBLMs formed using protein-free POPC LUVs (blue) and proteoliposomes embedding His$_6$-tagged NupC (red) after 30 minutes of incubation with the ADHP working reagent. The samples were formed according to the optimised SSBLM peroxidase assay protocol. The error bars represent the standard error of the mean, n = 2.

The results depicted above in Figure 4.5.2.2 not only confirmed the presence of SSBLM-embedded His$_6$-tagged NupC, but also the elimination of the abnormally high background fluorescence. The addition of BSA and protein-free POPC LUVs to the PBS buffer used during the antibody binding and washing steps proved greatly beneficial towards keeping the negative control emission close to baseline levels. This was likely due to the extra POPC lipids repairing potential defects within the formed SSBLMs and thus covering up any patches of exposed silica, while the BSA served to block any remaining non-specific binding sites (as in the case of Western blotting), thereby maximising the correct binding of the HRP-conjugated antibodies to the SSBLM-embedded His$_6$-tagged NupC. The iterative changes that led to the development of the optimised peroxidase assay protocol are reflected by the workflow presented in Table 4.5.2.3 below.

Final SSBLM-embedded NupC peroxidase assay detection protocol
SSBLM sample creation - 50% (w/w) 100 nm NupC/POPC and POPC-only SSBLMs (2.5 mg particles/1 mL sample) - 25% (w/w) 200 nm NupC/POPC and POPC-only SSBLMs (2.5 mg particles/1 mL sample)
↓ 60-second vortexing ↓
MilliQ® water wash - 1 mL of MilliQ® water per sample - one wash during a 10-minute incubation at room temperature with gentle roller mixing
↓ 60-second vortexing ↓
SSBLM sample division - use half of the total sample volumes (i.e. 500 µL) - divide these further into a total of 40×50 µL smaller working samples
↓ 60-second vortexing ↓

Anti-His antibody incubation - 1:5,000 (v/v) in PBS buffer supplemented with 1 mg/mL BSA and 1% (w/v) POPC LUVs - 1, 2, 4, 8, 12, 16, 20, 30, 40 and 50 µL of antibody solution added per sample
↓ 60-second vortexing ↓
Antibody wash - PBS buffer supplemented with 1 mg/mL BSA and 1% (w/v) POPC LUVs - two washes during 10-minute incubations at room temperature with gentle roller mixing
↓ 60-second vortexing ↓
Plating - 50 µL of sample transferred per well of a Costar® flat-bottomed 96-well plate - 50 µL of ADHP working reagent added per well to give 100 µL final sample volumes
↓ 30-second shaking ↓
Results - NupC-embedding SSBLM emission significantly higher than that of POPC-only SSBLMs - Fluorescence emission of protein-free negative controls reduced to expected baseline levels

Table 4.5.2.3. Workflow illustrating the optimised protocol for the peroxidase assay detection of SSBLM-embedded His_6-tagged NupC.

The optimised peroxidase assay protocol detailed above was also used to test whether SSBLMs formed using IM/POPC LUVs overexpressing His_6-tagged NupC represented a viable method for performing antibody binding studies against protein targets embedded in their original biological membranes, since this approach could prove particularly useful towards the future assaying of membrane proteins that are difficult to purify and/or reconstitute into lipid vesicles. To this end, 200 nm POPC LUVs (diluted to 5 mg/mL in PBS buffer) were mixed via the freeze-thaw method with *E. coli* IMs overexpressing His_6-tagged NupC at increasing IM/POPC (w/w) ratios (i.e. total IM protein content versus model lipid weight). Additional POPC LUVs were also mixed at identical w/w ratios with *E. coli* IMs overexpressing untagged NupC to serve as negative controls.

The resulting IM/POPC solutions were re-extruded through another 200 nm polycarbonate filter to ensure LUV size homogeneity, then mixed with 100- and 200 nm silica nanoparticles to respectively form 100 µL SSBLM samples at 50- and 25% (w/w) LUV/nanoparticle ratios. Following the MilliQ® water wash, the SSBLMs were resuspended in 1:1 volumes of HRP-conjugated mouse IgG_1 anti-His antibodies diluted 1:5,000 (v/v) in PBS buffer supplemented with 1 mg/mL BSA and 1% (w/v) POPC LUVs, then incubated for 1 hour at room temperature with gentle roller mixing. After that, the SSBLMs were washed twice in the above blocking buffer to remove any unbound antibodies, then resuspended in the same buffer, transferred onto a Costar® flat-bottomed

96-well plate (50 µL of sample per well) and supplemented with 50 µL of ADHP working reagent. The fluorescence emission was finally measured using a BMG LABTECH FLUOstar OPTIMA spectrofluorometer at a wavelength of 590 nm. The assay yielded reproducible results that consistently saturated the spectrofluorometer beyond the 20-minute reagent incubation mark (Figure 4.5.2.4).

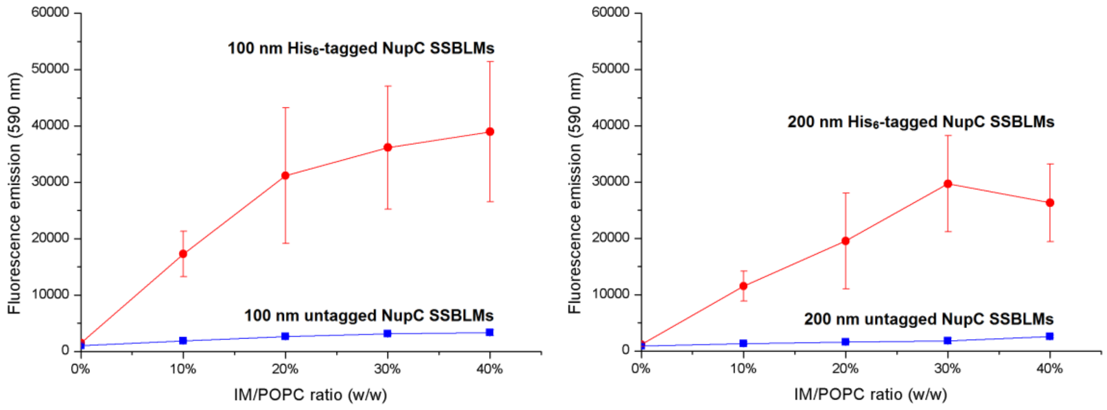

Figure 4.5.2.4. The fluorescence emissions resulting from 100 nm (left) and 200 nm (right) silica nanoparticles coated with SSBLMs formed using IM/POPC LUVs embedding untagged (blue) and His$_6$-tagged NupC (red) after 20 minutes of incubation with the ADHP working reagent. The samples were formed according to the optimised SSBLM peroxidase assay protocol. The error bars represent the standard error of the mean, n = 3.

Based on the results presented above in Figure 4.5.2.4, it was decided that all future mixed membrane LUVs be formed at the highest (i.e. 40% (w/w)) protein/lipid ratio. This specific ratio was also employed by Dodd et al. (2008), who successfully formed and characterised mixed membrane SSMs on planar silica surfaces and ultimately reported that this distribution of native membrane to model lipids allowed for an optimal balance between facile bilayer formation and embedded membrane protein coverage.

4.5.3. Confirmation of SSBLM-embedded NupC via cryo-EM

While the previous subsections confirmed that NupC could indeed be successfully embedded into the SSBLM format, the spectrofluorometric detection methods presented above still could not differentiate between protein-rich SSBLMs correctly enveloping the nanoparticles and intact proteoliposomes merely attaching to the silica substrate without actually forming a bilayer. The high-resolution imaging of NupC-embedding SSBLM samples was thus attempted via cryo-EM towards demonstrating correct bilayer formation with embedded protein around the chosen silica nanoparticles.

Fresh SSBLM samples were thus formed by mixing 200 nm His$_6$-tagged NupC/POPC proteoliposomes (2% (w/w) protein/lipid ratio) with 200 nm silica nanoparticles at a 25%

(w/w) LUV/nanoparticle ratio. POPC-only SSBLMs were also formed at the same w/w ratio to serve as protein-free negative controls. After the SSBLMs were washed in MilliQ® water, the particles were resuspended in 1:1 volumes of PBS buffer supplemented with 1 mg/mL BSA and 1% (w/v) POPC LUVs and incubated for 1 hour at room temperature with gentle roller mixing.

The SSBLMs were then pelleted via centrifugation (13,000 *g* spin for 30 seconds at 4 °C) and resuspended in identical volumes of a 5 nm Ni-NTA-Nanogold® probe solution prepared in the above blocking buffer at a 2:1 probe/protein molar ratio. Following another 30-minute incubation at room temperature with gentle roller mixing, the SSBLMs were washed twice – first in blocking buffer and then in regular PBS buffer – for 10 minutes per wash under similar conditions. The washed SSBLM solutions were then diluted 10× in PBS buffer and applied to the cryo-EM grids as described in subsection 3.4.1 before finally being imaged at a magnification of 35,000× using a FEI Tecnai F20 TEM fitted with a Gatan 4K×4K CCD camera (Figure 4.5.3.1).

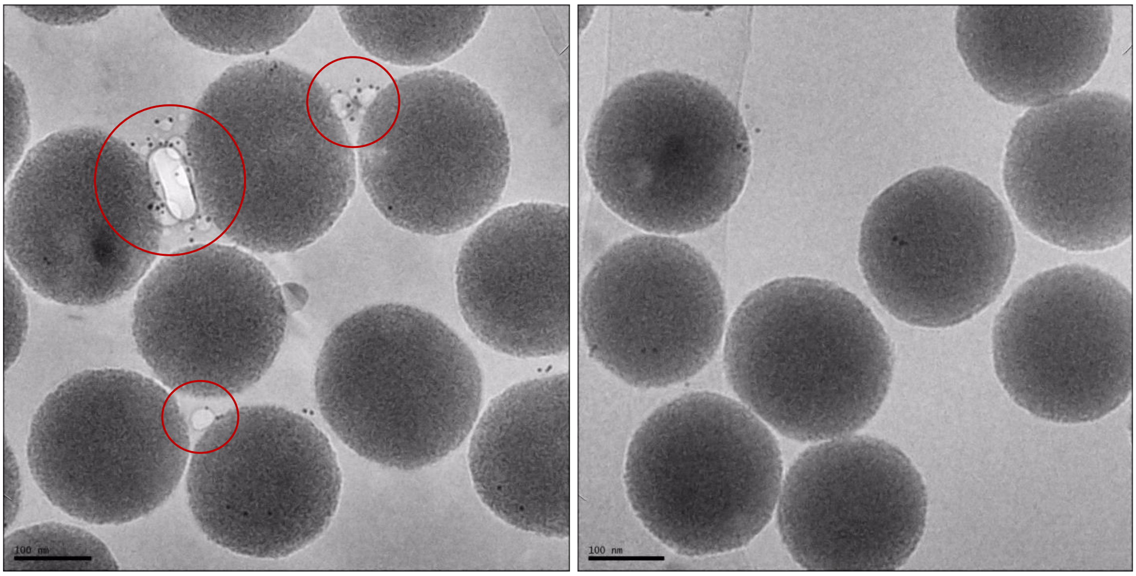

Figure 4.5.3.1. Left: 200 nm silica nanoparticles coated with POPC SSBLMs embedding His$_6$-tagged NupC, imaged at a 35,000× magnification using a FEI Tecnai F20 TEM fitted with a Gatan 4K×4K CCD camera. The particles had been pre-incubated with Ni-NTA-Nanogold® probes at a 2:1 probe/protein molar ratio in order to reveal the presence of SSBLM-embedded His$_6$-tagged NupC, as evidenced by the black dots representative of the 5 nm probe-conjugated gold molecules. The red circles highlight unfused NupC/POPC LUVs. Right: 200 nm silica nanoparticles coated with POPC-only SSBLMs for negative control purposes (courtesy of Dr. Stephen Muench, The School of Biomedical Sciences, University of Leeds).

The cryo-EM images presented above in Figure 4.5.3.1 revealed not only poor Ni-NTA probe coverage (possibly as a consequence of unequal blotting and/or poor vitrification of the cryo-grids by the FEI Vitrobot), but also unfused LUV remnants, prompting the need for more stringent washing and a higher probe/protein molar ratio in subsequent attempts. While very few probes were visible in this first instance, they were nevertheless found in close proximity to (i.e. less than 5-10 nm) or even on top of the imaged nanoparticles, suggesting that the SSBLMs were indeed present, even though the discrete structure of their lipid components could not be resolved using the TEM setup available at our disposal.

The imaging was therefore repeated using new 200 nm SSBLM samples pre-incubated with Ni-NTA probes at a higher 10:1 probe/protein molar ratio. Concurrently, the blocking and PBS buffer washing steps were each supplemented with 1-minute rounds of vigorous vortexing before and after each pelleting and resuspension. While the resulting images suffered from less-than-ideal vitreous ice quality, the abundance of Ni-NTA probes dotting the surface of the NupC-embedding nanoparticles – but not that of the POPC-only negative controls – nevertheless confirmed the presence of SSBLM-embedded His$_6$-tagged NupC, even though the lipid membrane components revealed by Mornet et al. (2005) or Trépout et al. (2007) still remained unresolved (Figure 4.5.3.2).

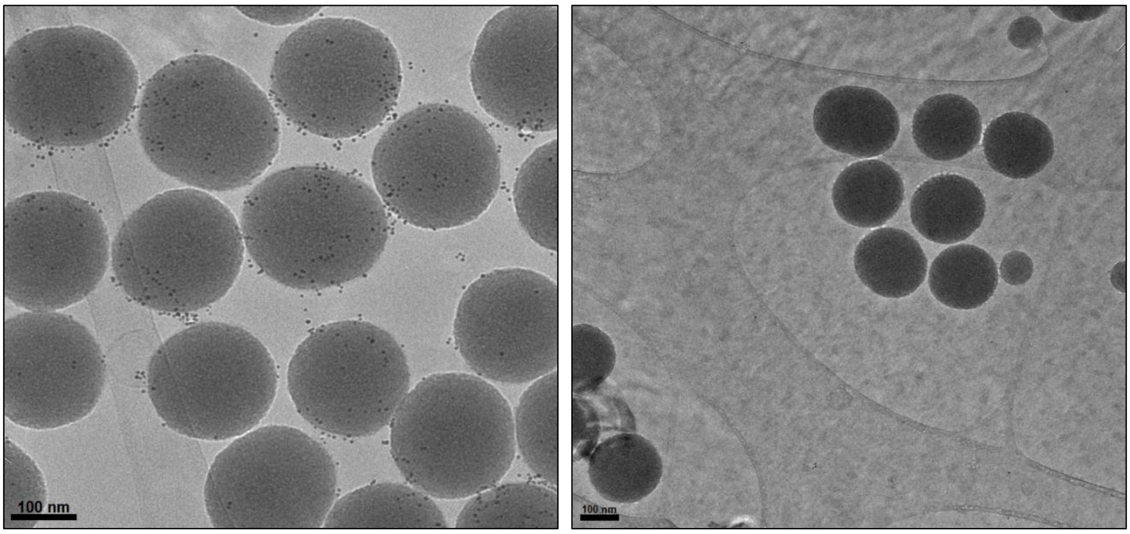

Figure 4.5.3.2. Left: 200 nm silica nanoparticles coated with POPC SSBLMs embedding His$_6$-tagged NupC, imaged at a 30,000× magnification using a FEI Tecnai F20 TEM fitted with a Gatan 4K×4K CCD camera. The multitude of gold-conjugated Ni-NTA probes (black dots) detected either on the surface or in the immediate vicinity of the imaged nanoparticles confirmed the presence of SSBLM-embedded His$_6$-tagged NupC. Right: 200 nm silica nanoparticles coated with POPC-only SSBLMs for negative control purposes showing no signs of Ni-NTA probe binding (courtesy of Dr. Stephen Muench, The School of Biomedical Sciences, University of Leeds).

Having established not only the successful formation of SSBLMs embedding the different NupC constructs on the 100- and 200 nm silica nanoparticles, but also the accessibility of the target protein towards high-affinity antibody binding, the platform was deemed suitable for the phage display screening of DARPin binders against NupC presented in this novel format. For a recapitulative look at the overall platform development plan, a summary of the experimental findings presented in the current chapter can be found in Figure 4.5.3.3 below.

SSBLM FORMATION AND CHARACTERISATION CONCLUSIONS

NupC construct expression and purification

- ✓ Overexpressed double Strep-tagged, His$_6$-tagged and untagged NupC in *E. coli*
- ✓ Purified or isolated each NupC construct according to the described protocols

↓

Purified NupC transport activity measurement

- ✓ SURFE2R assays confirmed that IM-bound untagged NupC retained its transport activity
- ✓ IM-bound His$_6$-tagged NupC also demonstrated some activity, albeit at much lower levels

↓

Planar SSM formation and characterisation

- ✓ Successfully formed POPC SSMs on planar silica substrates as reported via QCM-D
- ✓ Achieved successful planar SSM formation embedding each of the three NupC constructs

↓

SSBLM formation and characterisation

- ✓ Established the saturation thresholds resulting in full coverage of the chosen nanoparticles
- ✓ Confirmed the correct formation of SSBLMs around the silica nanoparticles via SAXS

↓

Embedding NupC into the SSBLM platform

- ✓ Successfully formed SSBLMs on the chosen nanoparticles using reconstituted NupC LUVs
- ✓ Confirmed the presence and accessibility of SSBLM-embedded NupC via antibody binding

---

Figure 4.5.3.3. Workflow summarising the experimental findings presented in the current chapter regarding the development of our proposed SSBLM phage display screening platform.

CHAPTER 5

SSBLM-Based Phage Display Screening

5.1. Introduction to SSBLM-Based Screening against NupC

Following the successful characterisation of the SSBLM platform embedding the different NupC constructs, this novel target presentation format was used towards the selection of DARPin binders against His_6-tagged NupC. While phage display screening generally requires between 3-5 panning rounds before high-affinity binders can be isolated against a given antigen (Hoogenboom, 2002), for the purposes of this project only two rounds of selection were performed against His_6-tagged NupC across each of the different screening formats detailed in the following subsections. In short, these included traditional "solid" selections performed against detergent-solubilised His_6-tagged NupC adsorbed onto regular 96-well plates, as well as "soluble" selections performed against the SSBLM-embedded protein suspended in small-volume liquid samples. For providing even better comparisons between the traditional and SSBLM-based screening approaches, the solid selections were performed both with and without extra detergent added to the screening buffers (so as to determine the extent of epitope occlusion caused by the detergent micelles), while the soluble selections were carried out both with and without a prior deselection step performed on protein-free, POPC-only SSBLMs (so as to eliminate any non-specific binders from the final selection output).

After completing all of the selection rounds across each of the different screening formats described above, the amino acid sequences encoding the DARPins forming the final selection output were aligned and examined in order to identify those candidates which showed the highest potential binding affinity for His_6-tagged NupC. Following that, the top 20 most promising DARPins (i.e. the lead candidates) were purified and subjected to further binding validation assays against the two other constructs (i.e. double Strep-tagged and untagged NupC), in order to isolate any binders that might have actually targeted the His_6-tag of the NupC construct used during screening and not its natural epitopes that would normally also be accessible *in vivo*. To this end, the 20 lead candidate DARPins were re-screened against detergent-solubilised double Strep-tagged NupC presented in the traditional plate-bound format, as well as untagged NupC embedded within SSBLMs formed using mixed membrane IM/POPC LUVs.

5.2. The Different DARPin Screening Formats Tested against NupC

DARPin binders were selected against His_6-tagged NupC presented in a variety of different formats so as to better allow for comparisons to be drawn between the traditional method of performing phage display screening against detergent-solubilised membrane protein targets and the novel detergent-free SSBLM platform. The individual formats will be described in further detail throughout the subsections below.

5.2.1. Traditional plate-based screening against detergent-solubilised NupC

Before trialling the novel SSBLM-based screening method, a traditional selection against detergent-solubilised His_6-tagged NupC adsorbed onto a classic 96-well plate support was performed according to the protocol detailed in subsection 3.4.7 for comparison purposes. Following the completion of the two selection rounds, the sequencing results revealed a DARPin diversity of 67% after panning the library against His_6-tagged NupC presented in this format. Two new rounds of selection were then performed against the plate-bound detergent-solubilised protein following the same protocol while also supplementing all of the screening solutions and buffers with 0.05% (w/w) DDM. A summary of the traditional selections performed against detergent-solubilised His_6-tagged NupC and their respective outcomes can be found in Table 5.2.1.1 below.

Antigen presentation format	Deselected against	Phage input titre	Phage output titre	DARPin diversity
Detergent-solubilised His_6-tagged NupC	No deselection	1.8×10^{12} cfu/mL	3.4×10^{5} cfu/mL	67%
Detergent-solubilised His_6-tagged NupC with additional 0.05% (w/w) DDM present	No deselection	4.5×10^{12} cfu/mL	6.5×10^{6} cfu/mL	93%

Table 5.2.1.1. Details and outcomes of the traditional plate-based DARPin selections performed against detergent-solubilised His_6-tagged NupC.

5.2.2. Novel SSBLM-based screening against detergent-free NupC

In order to provide proof-of-concept for this novel phage display screening platform, 1 mL SSBLM samples were respectively formed on both 100- and 200 nm silica nanoparticles at 60- and 30% (w/w) saturation ratios, embedding His_6-tagged NupC at a 4% (w/w) protein/lipid ratio. Protein-free SSBLMs were also created at identical saturation ratios from POPC-only LUVs for use during the deselection phases.

Two rounds of soluble DARPin selection were then performed against the SSBLM-embedded His_6-tagged NupC suspensions held in 1.5 mL Eppendorf tubes, each round using only 500 µL (i.e. half) of each SSBLM solution. To begin with, both the protein-free and NupC-embedding SSBLMs were first pelleted via centrifugation (3,220 *g* spin for 1 minute at 4 °C) and had their supernatants replaced with 1:1 volumes of blocking buffer. The SSBLMs were then left to incubate for 1 hour at room temperature with gentle roller mixing, alongside the DARPin library solutions undergoing the same procedure (i.e. two 50 µL DARPin library aliquots mixed with 450 µL of blocking buffer each).

Deselection was then performed by pelleting the protein-free SSBLMs via centrifugation (3,220 *g* spin for 1 minute at 4 °C) and then replacing their supernatants with the 500 µL blocked DARPin library aliquots, followed by another hour of incubation under the above conditions. After that, both the protein-free and NupC-embedding SSBLMs were re-pelleted, the supernatants of the latter samples were discarded and the supernatants of the former ones – containing the deselected DARPin libraries – were added to the NupC-embedding SSBLM pellets. The resuspended protein-rich SSBLMs were then left to incubate for another hour under the previously-stated conditions to allow for the deselected DARPins to bind to the SSBLM-embedded His_6-tagged NupC.

Following this incubation, the NupC-embedding SSBLMs were pelleted via centrifugation, their supernatants were discarded and the particles were washed five times in regular PBS buffer via 5-minute incubations at room temperature with gentle roller mixing. The bound phages were then eluted by resuspending the SSBLMs in elution buffer and leaving them to incubate for 30 minutes at 37 °C with gentle roller mixing. The eluted phages were amplified by adding each of the particle supernatants to 4.5 mL of TG1 *E. coli* cultured to log-phase in 2×TY growth medium and incubating the resulting mixtures for 1 hour at 37 °C with 150 rpm orbital shaking. Finally, the phage-infected TG1 cell cultures were serially-diluted in 2×TY growth medium from 1:10 to 1:1,000 (v/v) and 100 µL volumes of each dilution were spread onto 2×TYAG agar Petri dishes.

The remaining TG1 cells were then harvested via centrifugation (3,220 *g* spin for 1 minute at 4 °C), resuspended in 1 mL of 2×TY growth medium per pellet and spread onto separate 2×TYAG bioassay dishes. An identical volume of a non-infected, log-phase TG1 cell culture was also spread onto its own 2×TYAG Petri dish to serve as a negative control. All of the Petri and bioassay dishes were then left to incubate overnight at 30 °C.

The following day, the TG1 cells harbouring the eluted phages were scraped off the bioassay dishes using 10 mL 2×TY growth medium volumes supplemented with 50% (w/v) glycerol and used to create 2 mL -80 °C backups. The remainder of the scraped bacteria were then transferred into 25 mL volumes of 2×TYAG growth medium to give starting D_{600nm} values of 0.1. These cultures were incubated at 37 °C with 150 rpm orbital shaking until log-phase was reached, at which point they were each superinfected with 2.5 µL of M13K07trp helper phage stock and left to incubate for an additional hour under similar conditions. Following that, the cells were harvested via centrifugation (3,220 *g* spin for 10 minutes at 4 °C), their supernatants were discarded and the pellets were each resuspended in 0.5 mL of 2×TYAK growth medium. These cell suspensions were then used to further inoculate 25 mL volumes of 2×TYAK growth medium, after which the phage rescue was allowed to take place overnight at 25 °C with 280 rpm orbital shaking.

Finally, 1 mL volumes were taken from each overnight culture and the harboured cells were pelleted at maximum speed in a table-top centrifuge. The supernatants – containing the amplified phages – were then used during the second round of selection performed against the remaining 500 µL volumes of each initial SSBLM solution. Once the second round of selection was also completed, colonies were picked from the serially-diluted Petri dish cultures, transferred to Costar® flat-bottomed 96-well plates containing 120 µL of 2×TYAG growth medium per well and incubated overnight at 37 °C with 150 rpm orbital shaking. The next day, 40 µL samples were taken from each well and transferred onto new Costar® flat-bottomed 96-well plates that were later sent for binder sequencing and diversity assessment, while the remaining well contents were each supplemented with 40 µL of 50% (w/v) glycerol so as to create further backups for storage at -80 °C.

Two rounds of DARPin selection were also performed against SSBLM-embedded His_6-tagged NupC without a prior deselection done on protein-free particles, so as to evaluate the usefulness of this step towards isolating high-affinity binders against membrane protein targets presented in the SSBLM format. The final sequencing results revealed

DARPin diversities in the range of 91-95% across all of the selections performed against SSBLM-embedded His$_6$-tagged NupC (Table 5.2.2.1).

Antigen presentation format		Deselected against	Phage input titre	Phage output titre	DARPin diversity
SSBLM-embedded His$_6$-tagged NupC (with deselection)	100 nm	POPC-only SSBLMs	4.9×10^{12} cfu/mL	4.7×10^{4} cfu/mL	93%
	200 nm	POPC-only SSBLMs	4.6×10^{13} cfu/mL	5.2×10^{5} cfu/mL	91%
SSBLM-embedded His$_6$-tagged NupC (without deselection)	100 nm	No deselection	5.9×10^{12} cfu/mL	5.1×10^{5} cfu/mL	93%
	200 nm	No deselection	6.4×10^{12} cfu/mL	1.1×10^{5} cfu/mL	95%

Table 5.2.2.1. Details and outcomes of the novel SSBLM-based DARPin selections performed against detergent-free His$_6$-tagged NupC.

5.3. Identifying the Lead Candidate DARPin Binders

Following the completion of the DARPin selections across all of the above screening formats, the lead candidate binders were isolated for further validation in order to confirm their genuine affinity for NupC.

5.3.1. Aligning the amino acid sequences of the total selection output

Upon aligning the amino acid sequences of the 707 unique DARPin binders selected against His$_6$-tagged NupC (Figure 5.3.1.1 overleaf), it was discovered that a number of these repeated between 3-20× not only throughout the total selection output, but also across the different screening formats as well. Therefore, the isolated candidates encoded by these recurring sequences were believed to have the highest chances of representing genuine NupC binders.

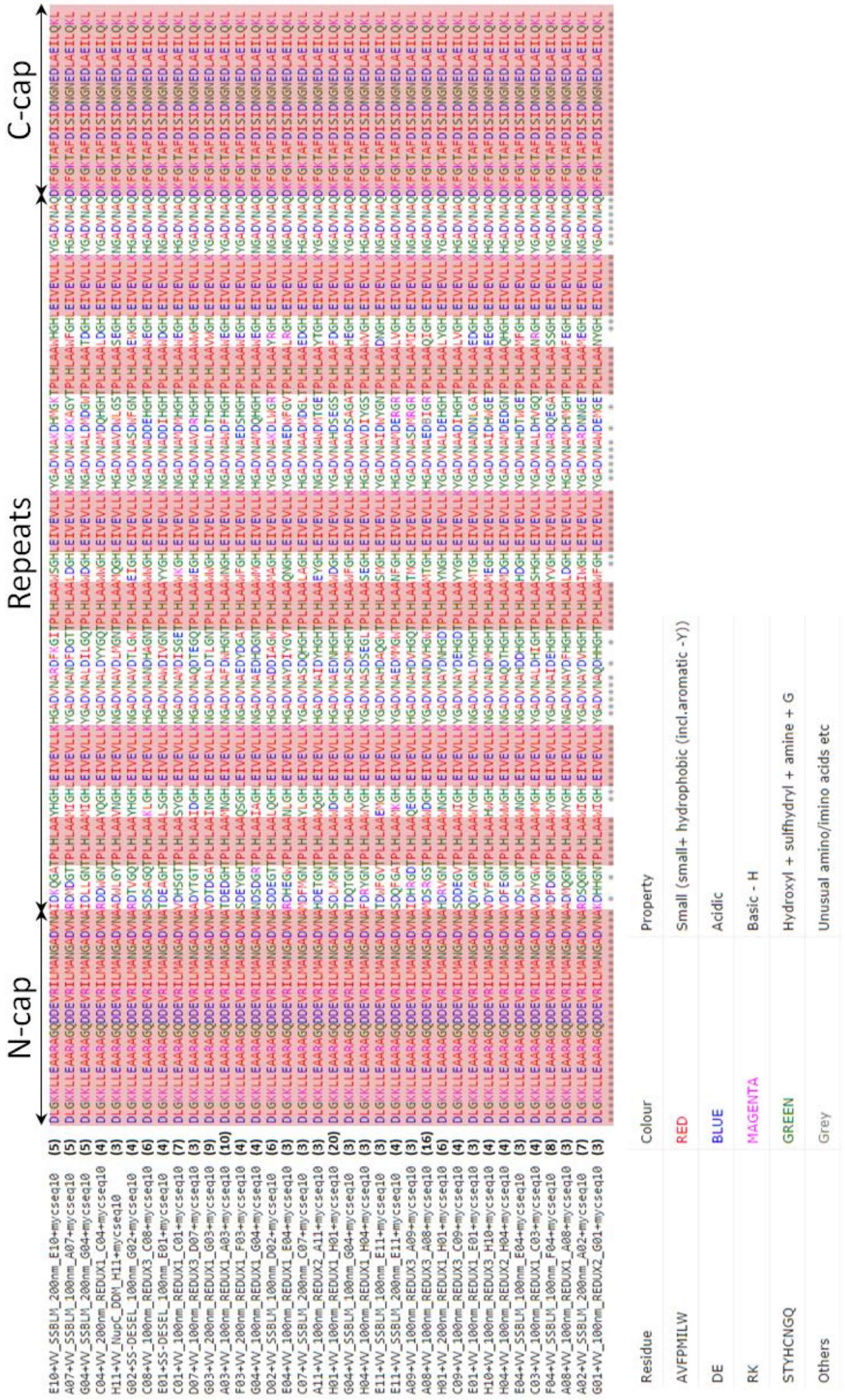

Residue	Colour	Property
AVFPMILW	RED	Small (small+ hydrophobic (incl.aromatic -Y))
DE	BLUE	Acidic
RK	MAGENTA	Basic - H
STYHCNGQ	GREEN	Hydroxyl + sulfhydryl + amine + G
Others	Grey	Unusual amino/imino acids etc

Figure 5.3.1.1. The DARPin amino acid sequences featuring the highest number of repeats throughout the total selection output (shown here in brackets), as aligned using Clustal Omega. The highlighted areas represent conserved regions shared by every consensus-built DARPin, while the variable regions unique to each binder have been left white for enhanced readability.

After examining the amino acid sequences presented above in Figure 5.3.1.1, it became clear that a majority of the most promising DARPins featured tryptophans heavily, which could have translated into a potential affinity for the lipid bilayer components of the SSBLMs in addition to that against the embedded His_6-tagged NupC. Positively-charged amino acids such as asparagine were also prominently displayed, which likely facilitated binding to the negative regions of the protein or protein-membrane interfaces, as well as being indicative of a strong affinity for any negatively-charged patches of exposed silica. Therefore, in order to highlight the structural relationships identified between each chosen candidate, a phylogenetic tree was also constructed as shown in Figure 5.3.1.2 below.

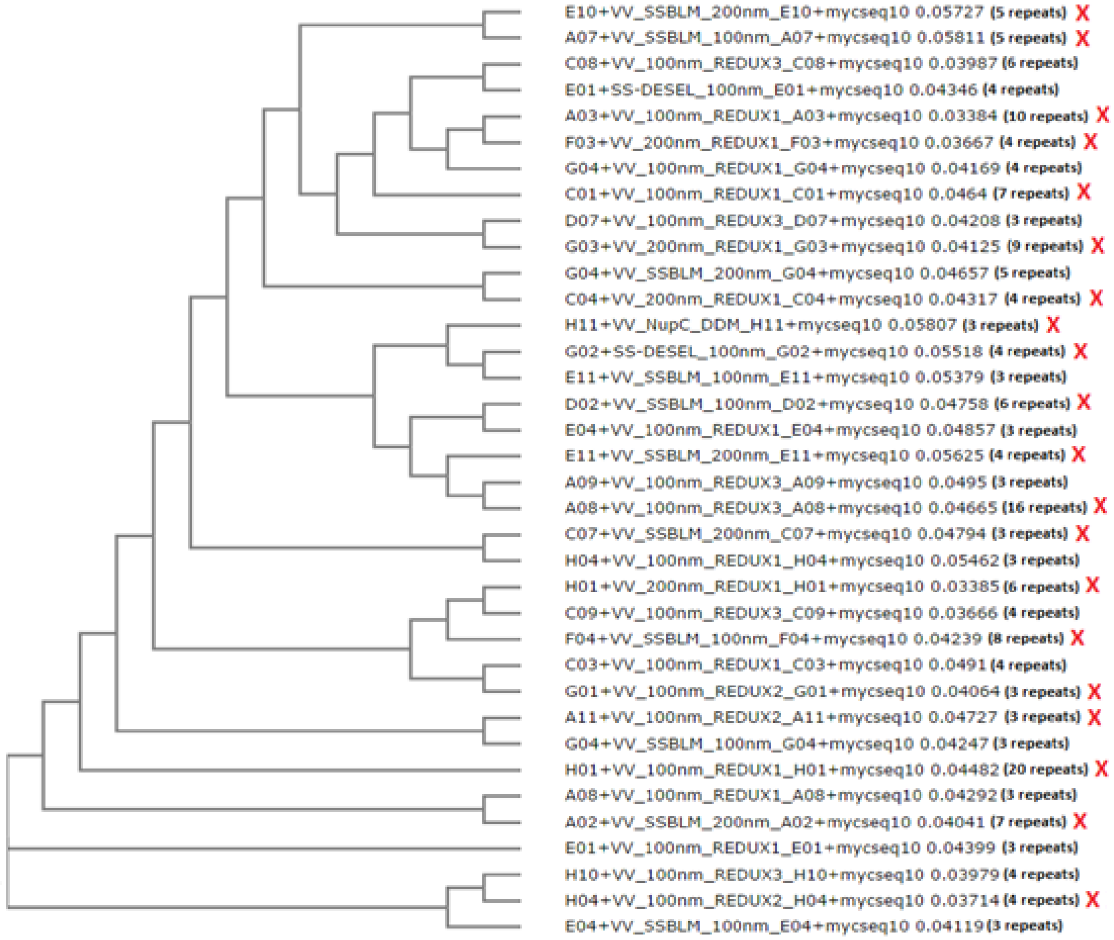

Figure 5.3.1.2. The phylogenetic tree resulting from aligning the most recurring DARPin amino acid sequences using Clustal Omega. The clones marked with a red "X" were chosen as the lead candidate binders selected against His_6-tagged NupC across all of the different screening formats.

Out of the 36 DARPins presented above in Figure 5.3.1.2, a "shortlist" of the 20 clones showing the highest number of repeats throughout the total alignment (each marked with a red "X") were ultimately designated as the lead candidate binders and taken forward for purification and affinity re-assessment against the other available NupC constructs.

5.4. Purifying the Lead Candidate DARPin Binders

The steps involved in purifying each of the chosen lead candidates – from binder plasmid isolation to high-affinity chromatography – will be presented throughout the following subsections.

5.4.1. Isolating the plasmid DNA encoding the lead candidate DARPins

The plasmids encoding the 20 lead candidate DARPins were purified using a ChargeSwitch®-Pro plasmid miniprep kit according to the protocol supplied by the manufacturer, reproduced in subsection 3.4.8.

The purified DARPin plasmids contained a pC6 expression vector that Dr. Vincent Agboh (The School of Biomedical Sciences, University of Leeds) discovered to be unsuitable for the purification of the selected binders due to a malfunctioning amber stop codon leading to the expression of the entire ligand-coat fusion protein instead. Therefore, each of the isolated DARPin plasmids had to be subcloned into a new pET-16b expression vector in order to bypass this issue. To this end, a double restriction digest was performed on commercially-sourced pET-16b for a minimum of 2 hours at 37 °C before the product was run on a 1% (w/v) TAE agarose gel and the relevant band – containing the digested vector – was cut from the gel and cleaned using a Wizard® SV gel and PCR clean-up system, then stored at -20 °C. After that, PCRs were performed on the DARPin DNA and the amplified plasmids were run on 2% (w/v) TAE agarose gels. The bands containing the PCR products were then extracted, cleaned up using the same Wizard® system and subjected to an overnight double restriction digest so as to remove the DARPin DNA fragments from the pC6 vector. The resulting digests were run on and subsequently cut out of 1% (w/v) TAE agarose gels, applied to the Wizard® clean-up system and then ligated with the digested pET-16b overnight at a 1:10 vector/insert molar ratio. The ligation products were transformed into competent OmniMAX *E. coli* (i.e. 5 µL of ligation product per 20 µL of cell culture) which were finally spread onto 2×TY agar Petri dishes supplemented with carbenicillin (100 µg/mL) and left to incubate overnight at 37 °C.

A double restriction digest control was used to confirm the presence of the DARPin fragments before an expression trial was attempted. Figure 5.4.1.1 overleaf showcases the DNA fragments encoding seven of the lead candidate DARPins, confirming that they had been successfully ligated with pET-16b. The other thirteen lead candidate plasmids showed similar bands on identical 1% (w/v) TAE agarose gels (not shown here). For extra validation, all DARPin plasmids were sent to Source Bioscience for sequencing and the results confirmed that all of the DNA fragments encoding the 20 lead candidates were present within their respective plasmids after their subcloning into the pET-16b vector.

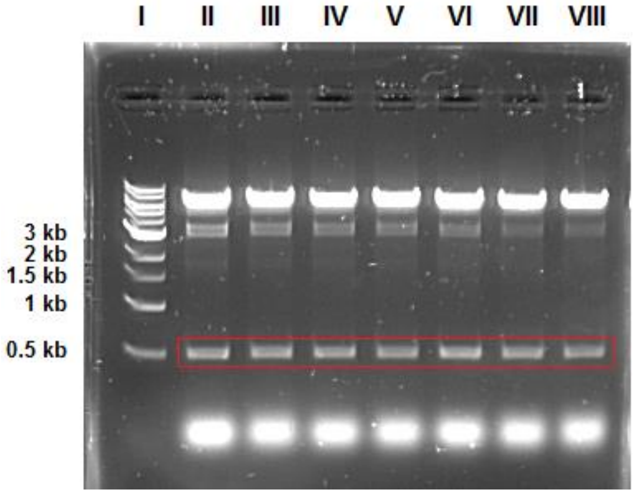

Figure 5.4.1.1. TAE agarose gel of 7 lead candidate DNA fragments subcloned into a pET-16b expression vector. The lanes represent, from left to right: I. 1 kb DNA ladder; II. A11 100 nm REDUX2; III. C04 200 nm REDUX1; IV. G02 SS-DESEL 100 nm; V. A07 SSBLM 100 nm; VI. H04 100 nm REDUX2; VII. C07 SSBLM 200 nm; VIII. E11 SSBLM 200 nm. The red rectangle highlights the bands representative of the DARPin-encoding DNA fragments.

5.4.2. Small-scale expression trial of the lead candidate DARPins

A small-scale trial was used to verify the expression levels of the chosen lead candidate DARPins before tackling their full-scale purification. To this end, all 20 DNA fragments subcloned into a pET-16b expression vector were transformed into competent BL21 *E. coli* (i.e. 1 µL of pET-16b/DARPin plasmid per 10 µL of cell culture), after which they were spread onto 2×TY agar Petri dishes supplemented with carbenicillin (100 µg/mL) and left to incubate overnight at 37 °C.

The following day, 1 mL volumes of 2×TY growth medium supplemented with carbenicillin (100 µg/mL) were inoculated with one colony from each plate and the resulting cultures were left to incubate overnight at 37 °C with 280 rpm orbital shaking. The next day, other 5 mL volumes of 2×TY growth medium supplemented with carbenicillin (100 µg/mL) were inoculated with 250 µL from the overnight cultures and incubated for 2 hours at 37 °C with 280 rpm orbital shaking. After that, the cultures were separated into 2.5 mL volumes, 0.5 mM IPTG was added to half of these and then all of the cultures were left to incubate for an additional 4 hours under the same conditions. Following protein overexpression, 1 mL volumes were taken from each culture and the cells were harvested via centrifugation (17,000 *g* spin for 10 minutes at 4 °C). The supernatants were discarded and the cell pellets were each resuspended in 1 mL of 2× PBS buffer before being diluted 1:10 (v/v) using the same buffer. SDS-PAGE loading buffer (4×) was then added in 2.5 µL volumes per 10 µL of diluted cell suspension, after which all of the samples were left to incubate at 95 °C for 10 minutes. Finally, given that all of the DARPin fragments also encoded His$_6$-tags for purification purposes, both SDS-PAGE and Western blotting were performed in order to verify the outcome of the small-scale expression trial using a purified E3-5 DARPin supplied by MedImmune as a positive control (Figure 5.4.2.1).

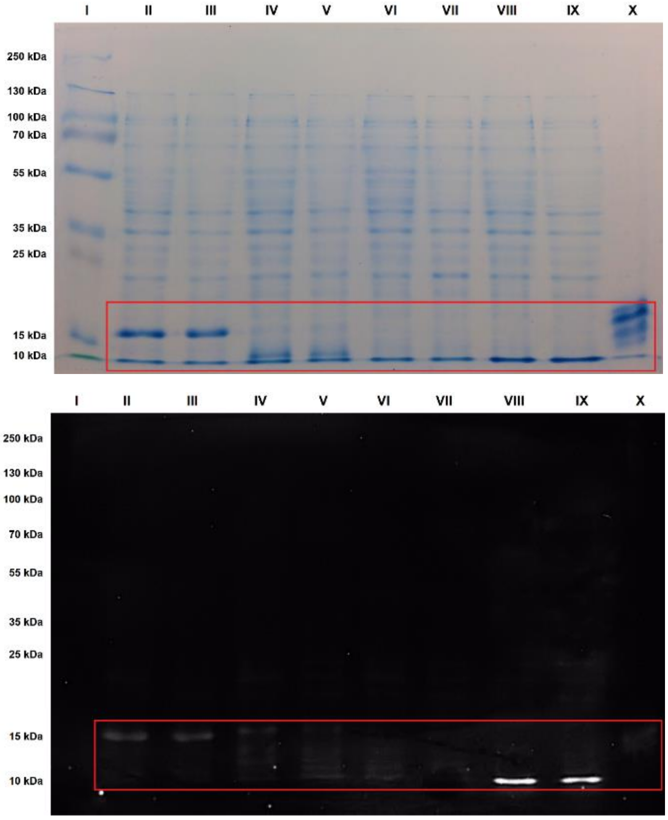

Figure 5.4.2.1. Coomassie Blue-stained polyacrylamide gel (top) and corresponding Western blot (bottom) stained to detect the His$_6$-tags of the DARPin samples resulting from the small-scale expression trial. The lanes represent, from left to right: I. Protein ladder; II. H01-; III. H01+; IV. C01-; V. C01+; VI. H11-; VII. H11+; VIII. A08-; IX. A08+; X. E3-5. The "+" lanes contain samples that had been incubated with 0.5 mM IPTG, whereas the "-" lanes contain samples that had been kept uninduced.

Judging from the results depicted above in Figure 5.4.2.1, it became clear that the isolated DARPins were not readily visible on Western blots incubated with our commercially-sourced anti-His antibodies. Nevertheless, all 20 constructs did ultimately express according to the purified DARPin concentrations revealed via BCA assay and despite the fact that all of the lead candidates showed slightly different migration patterns on otherwise identical SDS-PAGE gels. IPTG induction also did not appear to significantly influence DARPin expression, although this finding was not explored any further.

5.4.3. Full-scale expression and purification of the lead candidate DARPins

Following the successful small-scale expression trial, the 20 lead candidate DARPins were expressed and purified in larger volumes according to a MedImmune protocol optimised by Dr. Vincent Agboh (The School of Biomedical Sciences, University of Leeds), reproduced here for clarity. Firstly, competent BL21 *E. coli* were transformed with each lead candidate plasmid (i.e. 1 µL of pET-16b/DARPin DNA per 10 µL of cell culture), then spread onto 2×TY agar Petri dishes supplemented with carbenicillin (100 µg/mL) and subjected to an overnight incubation at 37 °C. The next day, a single colony from each plate was used to create inoculation cultures comprising of 30 mL volumes of carbenicillin-supplemented 2×TY growth medium. These cultures were also left to incubate overnight at 37 °C with 280 rpm orbital shaking, after which they were subsequently used to inoculate even larger 500 mL volumes of carbenicillin-supplemented 2×TY growth medium with starting D_{600nm} values of 0.1. The 500 mL cultures were then incubated for 2 hours at 37 °C with 280 rpm orbital shaking before 0.5 mM IPTG was added to each flask and DARPin overexpression was allowed to occur over an extra 4 hours of incubation under similar conditions. A 1 mL volume of 2×TY growth medium without any antibiotics was also inoculated with 50 µL of stock BL21 competent cells as a negative control.

The cells of the IPTG-induced cultures were harvested via centrifugation in a JLA-10.500 rotor (9,000 *g* spin for 30 minutes at 4 °C), the supernatants were discarded and the cell pellets were stored at -20 °C overnight. After being thawed the next day, each pellet was resuspended in 25 mL of 2× PBS buffer and disrupted twice through a Constant Systems TS series cell disruptor operating at 30 kpsi and 4 °C. The resulting cell debris was pelleted via ultracentrifugation in a Ti50.2 rotor (100,000 *g* spin for 1 hour at 4 °C) and a BCA assay was used to determine the total protein content of the supernatants harbouring the expressed lead candidate DARPins. Owing to their His_6-tagged N-terminals, each supernatant solution was further mixed with 1 mL of HisPur™ cobalt resin (first washed in 10 mL volumes of MilliQ® water, then pre-equilibrated with 2× PBS buffer) and left to incubate overnight at 4 °C with gentle roller mixing in the presence of 10 mM imidazole, so as to prevent other cytoplasmic proteins from adhering non-specifically to the added resin.

The following day, the mixtures were loaded into 5 mL Pierce™ disposable columns and allowed to flow through twice, in order to maximise the retention of all of the material from the overnight incubation. The resin was then washed dropwise with 10 CVs of wash buffer before 600 µL of elution buffer were added and allowed to flow through so as to remove any residual wash buffer. After that, the column ends were sealed and 400 µL of elution buffer were added, then left to incubate with the resin for 10 minutes at 4 °C with gentle roller mixing. These 400 µL volumes were afterwards collected separately and the remaining DARPins were eluted in 10×1 mL subsequent fractions. Based on their A_{280nm} values, the first four "peak" fractions were pooled together and dialysed extensively in 2× PBS buffer so as to remove any residual imidazole. Quality control was then performed on the purified DARPins via SDS-PAGE and Western blotting, as shown below in Figure 5.4.3.1 for the H01 100 nm REDUX1 clone. Although each of the lead candidates ultimately showed different levels of expression, in the end all appeared to have purified to a high degree, resulting in average yields of 1 mg of pure protein per 100 mL of cell culture.

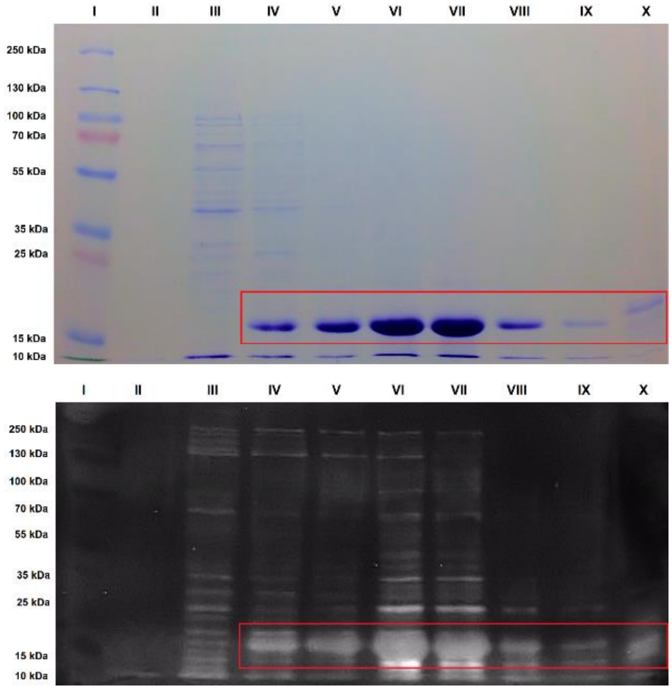

Figure 5.4.3.1. Coomassie Blue-stained polyacrylamide gel (top) and corresponding Western blot (bottom) stained to detect the His_6-tags of the H01 100 nm REDUX1 DARPin purification samples. The lanes represent, from left to right: I. Protein ladder; II. Pre-IPTG induction cell culture sample; III. Column flowthrough; IV. Column wash; V. Fraction 0; VI. Fraction 1; VII. Fraction 2; VIII. Fraction 3; IX. Fraction 4; X. E3-5 positive control. The red rectangle highlights the bands representative of the H01 100 nm REDUX1 DARPin clone.

5.5. Characterising the Purified Lead Candidate Binders

Following their purification, all of the 20 lead candidate DARPins were re-screened against the other available NupC constructs presented in both detergent-solubilised (i.e. plate-based), as well as detergent-free (i.e. SSBLM-embedded) formats in order to assess their binding affinities against native NupC epitopes.

5.5.1. Re-screening against detergent-solubilised double Strep-tagged NupC

In an attempt at uncovering any potential His_6-tag binders isolated throughout the numerous DARPin selection phases, the 20 lead candidates were re-screened against detergent-solubilised double Strep-tagged NupC using an ELISA protocol optimised with the help of Dr. Vincent Agboh (The School of Biomedical Sciences, University of Leeds), reproduced here below.

Purified double Strep-tagged NupC was first diluted in wash buffer to a concentration of 1 mg/mL, then added to the wells of Nunc™ MaxiSorp™ flat-bottomed 96-well plates in 50 µL volumes so as to bind 5 µg of protein per well. Identically-diluted His_6-tagged NupC was also added to a few empty wells as a positive control. The plates were then covered with adhesive plastic lids and NupC was left to adsorb overnight at 4 °C. The next day, the coating solutions were removed and the plates were washed three times with 200 µL of wash buffer per well. The wells were then each filled with 200 µL of blocking buffer and the plates were once again covered and left to incubate for 1 hour at 4 °C. After three more washes with 200 µL of wash buffer per well, a serial dilution of the purified lead candidate binders – ranging from 10 µM to 1 pM – was prepared in the same buffer.

Three of the blocked wells seeded with double Strep-tagged NupC were then filled with 50 µL volumes of wash buffer to serve as negative controls, while the serially-diluted DARPin solutions were added to the remaining test wells in identical volumes. In order to provide additional negative controls, the assayed binders were likewise added at 10 µM, 1 µM and 100 nM concentrations to protein-free wells that had also undergone blocking, after which the plates were covered once more and left to incubate for 1 hour at 4 °C.

After the plates were washed with three additional volumes of 200 µL of wash buffer per well, HRP-conjugated mouse IgG_1 anti-His antibodies (diluted 1:5,000 (v/v) in blocking buffer) were added to each well in 50 µL volumes. The covered plates were then left to incubate for 1 more hour at 4 °C before the wells were washed three times with 200 µL of antibody wash buffer each. Finally, pre-warmed TMB liquid substrate system for ELISA was added in 50 µL volumes per well and the covered plates were left to incubate at room temperature with gentle rocking mixing. After 30 minutes of colour development, the conjugated HRP was inactivated by dispensing similar volumes of 0.5 M H_2SO_4 into each well. Their respective absorbance values were then measured at a wavelength of 450 nm using a Thermo Scientific Multiskan™ FC spectrophotometer, revealing that a majority of DARPins showed signs of weak (i.e. micromolar) binding to double Strep-tagged NupC. The top five candidates with the highest affinities for this detergent-solubilised construct were presented in Figure 5.5.1.1 below.

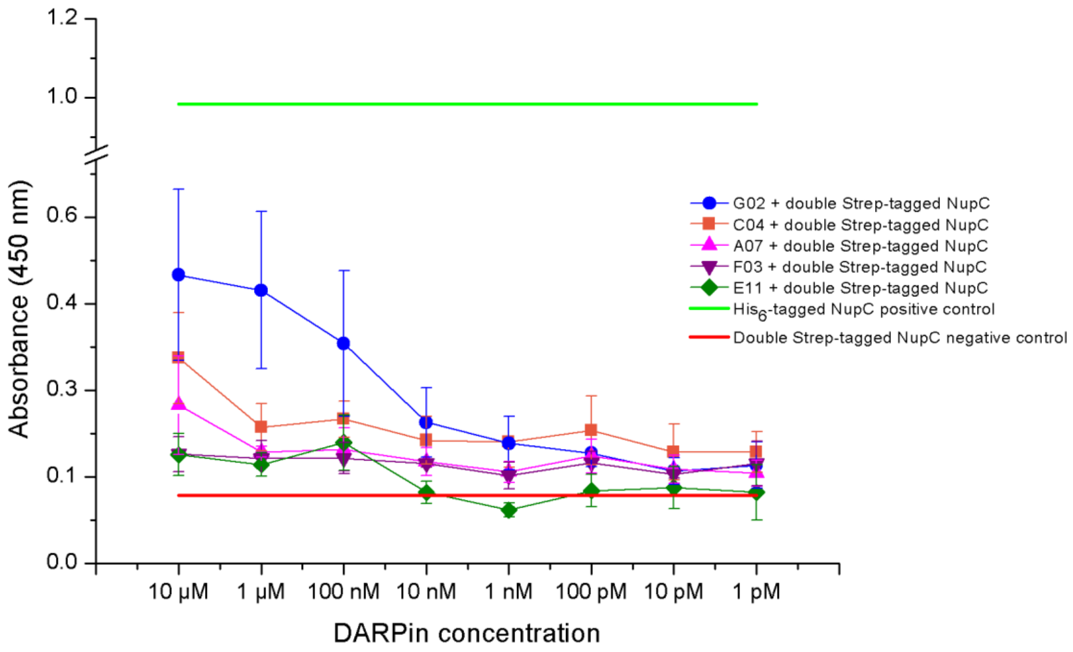

Figure 5.5.1.1. The absorbances resulting from the DARPins with the highest affinities for detergent-solubilised double Strep-tagged NupC: G02 SS-DESEL 100 nm, C04 200 nm REDUX1, A07 SSBLM 100 nm, F03 200 nm REDUX1 and E11 SSBLM 200 nm. The averaged His$_6$-tagged NupC positive controls and double Strep-tagged NupC negative controls are presented as green and red lines, respectively. The error bars represent the standard error of the mean, n = 3.

5.5.2. Re-screening against detergent-free untagged NupC

Having assayed all of the purified DARPins against detergent-solubilised double Strep-tagged NupC, the lead candidates were also re-screened against untagged NupC presented in the SSBLM format so as to obtain further validation over the above binding results. The protocols for creating the requisite samples and then running the SSBLM-based ELISAs will be reproduced below for consistency.

In order to create the SSBLM particles embedding untagged NupC, 5 mg POPC aliquots were first rehydrated with 1 mL of PBS buffer each, then subjected to a 60-second round of vigorous vortexing. *E. coli* IMs overexpressing untagged NupC, as well as His_6-tagged PepTSo (acting as the positive control), were also diluted to 5 mg/mL of total protein content using PBS buffer before being vortexed with the POPC solutions to create 40% (w/w) IM/POPC mixtures via the freeze-thaw method. The NupC/POPC and PepTSo/POPC suspensions were then subjected to an additional 2 minutes of vigorous vortexing alongside the leftover POPC solution before being extruded through separate polycarbonate filters to yield 400 nm LUVs. Following that, the resulting IM/POPC and protein-free vesicles were mixed with 100 nm silica nanoparticles (10 mg/mL in deionised water) to produce SSBLMs at 50% (w/w) LUV/nanoparticle ratios. The particle solutions were then vigorously vortexed for another 2 minutes before being left to incubate overnight at 4 °C with gentle roller mixing. The next day, the SSBLMs were once again subjected to 2 minutes of vigorous vortexing before being harvested via centrifugation (17,000 *g* spin for 1 minute at 4 °C) and washed in 1:1 volumes of MilliQ® water through a 30-minute incubation at 4 °C with gentle roller mixing. Finally, the washed particles were once again vortexed vigorously for 120 seconds, re-pelleted via centrifugation and resuspended in similar volumes of blocking buffer.

The SSBLM-based DARPin ELISAs consisted of adding the sample solutions to the wells of Costar® V-bottomed 96-well plates in 50 µL volumes, then supplementing these with an additional 150 µL of blocking buffer per well and leaving the covered plates to incubate for 1 hour at 4 °C with gentle rocking mixing. The SSBLMs were then pelleted via centrifugation (3,220 *g* spin for 5 minutes at 4 °C) and washed twice via resuspension in 200 µL of wash buffer per well followed by 5-minute centrifugations under similar conditions. The washed SSBLMs were then re-pelleted via centrifugation and resuspended in 50 µL of serially-diluted DARPins per well (i.e. 10 µM to 1 pM). Following a 1-hour incubation at 4 °C with gentle rocking mixing, the SSBLMs were washed twice as previously described and resuspended in 50 µL volumes of HRP-conjugated mouse IgG_1 anti-His antibodies (diluted 1:5,000 (v/v) in blocking buffer) per well. After an additional 1-hour incubation at 4 °C with gentle rocking mixing, the SSBLMs were once again washed twice in wash buffer and resuspended in 50 µL of plain PBS buffer before being transferred onto Costar® flat-bottomed 96-well plates. Pre-warmed TMB liquid substrate system for ELISA was then added to the wells in 50 µL volumes and the plates were left to incubate at room temperature with gentle rocking mixing. Following sufficient colour development (i.e. after approximately 15 minutes of incubation), 50 µL volumes of 0.5 M H_2SO_4 were added to each well to stop the reaction.

The absorbance values were ultimately measured at a wavelength of 450 nm using the same Thermo Scientific Multiskan™ FC spectrophotometer, yet the new results appeared polarising: a number of clones that previously demonstrated micromolar affinity for detergent-solubilised double Strep-tagged NupC did not appear to bind to the untagged construct at all (e.g. C04 200 nm REDUX1), while other candidates that showed no affinity for double Strep-tagged NupC now appeared to bind SSBLM-embedded untagged NupC within the same micromolar range observed previously (Figure 5.5.2.1).

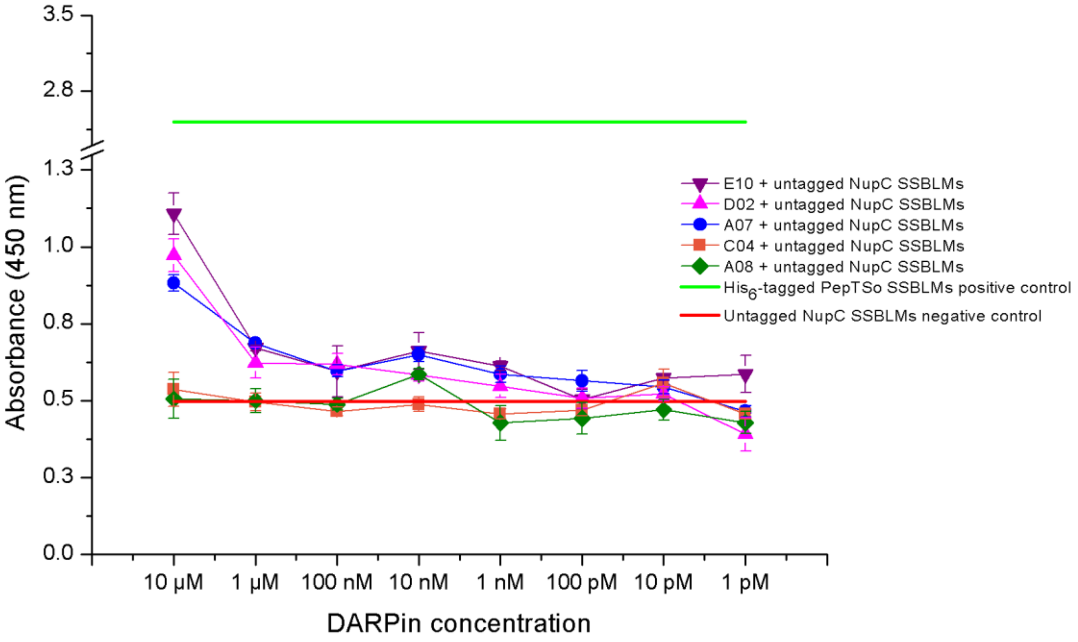

Figure 5.5.2.1. The absorbances resulting from the DARPins with the highest affinities for detergent-free (i.e. SSBLM-embedded) untagged NupC: E10 SSBLM 200 nm, D02 SSBLM 100 nm, A07 SSBLM 100 nm, C04 200 nm REDUX1 and A08 100 nm REDUX3. The averaged His$_6$-tagged PepTSo positive controls and untagged NupC negative controls are presented as green and red lines, respectively. The error bars represent the standard error of the mean, n = 3.

The results presented above in Figure 5.5.2.1 appear to indicate that several NupC epitopes that had been previously occluded by detergent micelles during the first ELISAs performed against detergent-solubilised NupC became readily accessible when the protein was embedded within the SSBLM format. On the other hand, the possibility of the lipid bilayer component shielding yet another epitope subset could also explain why the clones showing affinity for detergent-solubilised NupC were no longer able to bind the SSBLM-embedded protein. This would likewise explain why the affinities of a number of promising DARPins identified via the previous ELISAs were reduced when the same clones were re-screened against the embedded untagged NupC.

5.6. Evaluating the Outcome of the DARPin Selections

The results of the DARPin phage display screening performed against NupC and their significance towards the future development of the SSBLM antigen presentation format will be examined throughout the following subsections.

5.6.1. The phage display screening of antibodies against membrane proteins

The DARPin selections presented earlier in the chapter ultimately yielded a number of weak, micromolar-affinity binders against NupC mainly due to the fact that the time spent at MedImmune only allowed for two rounds of panning for each of the different screening formats. Unfortunately, a binding validation assay could also not be developed in time for re-screening the total selection output of 707 unique DARPins against NupC in a high-throughput manner before the most promising binders had to undergo expression and purification. With that being said, even though phage display screening typically requires between 3-5 rounds of selection before high-affinity binders can be identified (Hoogenboom, 2002), it is important to remember that the aim of the project was never to discover strong ligands against NupC. Rather, the focus was on developing the SSBLM platform and comparing it to the traditional antigen presentation methods with special regard given to the issues caused by the presence of detergents during antibody screening.

This goal was clearly supported by the results presented throughout the current chapter, with the data from Tables 5.2.1.1 and 5.2.2.1 being especially interesting. Significant differences in clone diversity were registered between the traditional plate-based selections performed against detergent-solubilised His$_6$-tagged NupC with and without extra detergent present in the screening buffers (i.e. 67% versus 93% binder diversity, respectively). Given that higher diversity numbers generally reflect selection outputs featuring lower-affinity binders, it would appear that the addition of even more detergent to successive panning rounds is clearly detrimental towards antibody binding, likely due to the detergent occlusion of target epitopes. The subsequent selections performed against the same NupC construct embedded within the SSBLM format showed similarly-high diversities (i.e. >90% for both particle sizes), but in this case they came as a consequence of the greatly increased surface area dedicated to antigen binding offered by the nanosized substrates compared to the wells of traditional assay plates. Moreover, the insignificant differences arising from the inclusion or omission of the deselection step performed against protein-free particles questioned its usefulness towards future selections and could potentially vouch for its complete removal so as to reduce the time cost of the already-lengthy screening rounds. Finally, it is important to note that none of the binders identified through the ELISA performed against detergent-solubilised double Strep-tagged NupC were found to be repeated throughout the total selection output or across the different screening formats. This would, in turn, suggest that even though the DARPins selected against detergent-solubilised NupC without DDM supplementation enjoyed the lowest clone diversity and, consequently, the highest potential binding affinities for their intended target, these particular binders likely favoured an epitope that is normally occluded by the lipid bilayer component of the SSBLM particles and – most probably – living cell membranes as well. This finding sheds considerable light on the importance of using a close-to-native antigen presentation method for screening antibodies against membrane protein targets, so as to ultimately maximise the chances of isolating candidates that actually target epitopes normally accessible *in vivo*.

Additionally, the facile adaptability and versatility of the SSBLM platform allows for the complete coverage of not just nanoparticles, but also micrometre-sized beads in continuous lipid bilayers mimicking the spherical architecture of living cells (Schadauer et al., 2015). This model can be even further improved upon through the use of surface treatments that can direct the orientation of reconstituted membrane proteins (Trépout et al., 2007) and allow targets to retain their natural mobility throughout the supporting bilayers (Richards et al., 2016). Furthermore, using mesoporous particles as substrates for SSBLM formation could create artificial cytoskeletons whose aqueous interspaces would connect with the cytoplasmic sides of the embedded membrane proteins and thus allow these constructs to also be successfully used in functional assays as advanced substitutes for the proteoliposomes routinely used up until now (Nordlund et al., 2009). Coupled with straightforward protocols, as well as easy manipulation with only minimal training, the results presented throughout the past chapters show great promise for continuing the research on SSBLMs and testing them on a wider variety of membrane protein targets.

5.6.2. Testing the SSBLM format on new membrane protein targets

In order to further validate SSBLMs as versatile antigen-immobilisation platforms for the screening of binder candidates against membrane protein targets originating from more advanced expression systems, MedImmune provided us with mammalian cell pellets overexpressing a formyl peptide receptor (FPR) that they had already raised a high-affinity antibody against. SSBLMs were therefore created using mixtures of POPC and FPR-expressing mammalian cell membranes, then subjected to another ELISA performed according to the protocol detailed in subsection 5.5.2, reproduced below for clarity.

To begin with, the supplied FPR-expressing and uninduced (i.e. negative control) mammalian cell pellets were resuspended in 2 mL of HEPES buffer each and disrupted by passing the mixtures 11 times through an isobiotec cell homogeniser. The resulting cell debris and organelles were pelleted via centrifugation (6,000 *g* spin for 10 minutes at 4 °C) and the cell membranes were harvested by ultracentrifuging the supernatants (100,000 *g* spin for 2 hours at 4 °C). The membrane pellets were then each resuspended in 500 µL of HEPES buffer and a BCA assay was used to determine their overall protein concentrations before they were snap-frozen in liquid nitrogen and stored at -80 °C overnight. The two different membrane suspensions were diluted the next day to 5 mg/mL of total protein content using HEPES buffer, then mixed at a 40% (w/w) ratio via the freeze-thaw method with a similarly-concentrated POPC solution prepared in the same buffer. The resulting mixtures were subsequently extruded into 400 nm LUVs and used towards the formation of 100 nm SSBLMs at a 50% (w/w) LUV/nanoparticle ratio.

The SSBLM-based FPR ELISAs then followed the same steps outlined in subsection 5.5.2 up until the antibody incubation, at which point the blocked nanoparticle pellets were each resuspended in 100 µL of anti-FPR IgG 0165 primary antibodies (diluted to 1 µg/mL in HEPES buffer) and left to incubate for 1 hour at 4 °C with gentle rocking mixing. Afterwards, the particles were once again washed twice in wash buffer, followed by pelleting via centrifugation and resuspension in 100 µL of goat anti-human IgG (Fc-specific) peroxidase-conjugated antibodies diluted 1:2,000, 1:6,000, 1:12,000, 1:24,000 and 1:48,000 (v/v) in blocking buffer. Following an additional 1-hour incubation at 4 °C with gentle rocking mixing, the SSBLMs were washed twice once more, re-pelleted via centrifugation and finally resuspended in 50 µL of plain HEPES buffer per well before being transferred onto a Costar® flat-bottomed 96-well plate.

Pre-warmed TMB liquid substrate system for ELISA was then added to each well in 50 µL volumes and the SSBLMs were left to incubate at room temperature with gentle rocking mixing until sufficient colour development had occurred (i.e. after approximately 15 minutes). Following that, 50 µL volumes of 0.5 M H_2SO_4 were added per well to stop the reaction and the absorbances were ultimately measured at a wavelength of 450 nm using a Thermo Scientific Multiskan™ FC spectrophotometer (Figure 5.6.2.1 overleaf).

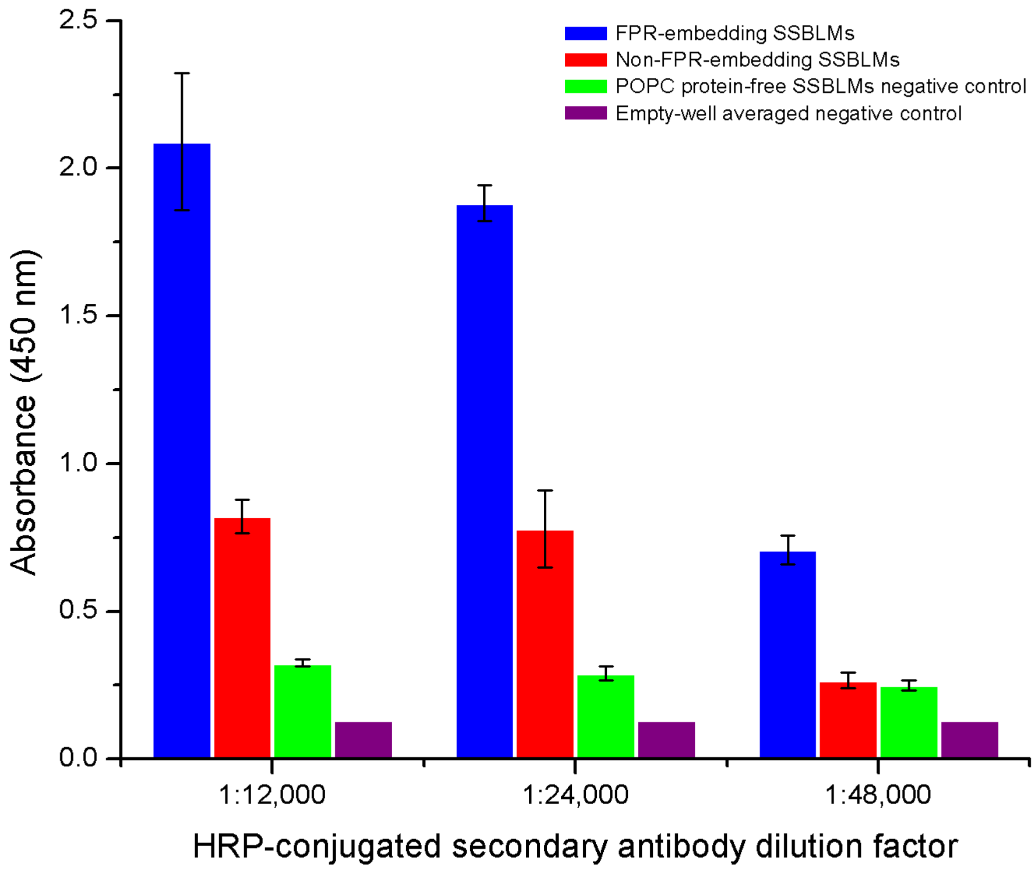

Figure 5.6.2.1. The absorbances resulting from an ELISA testing the epitope accessibility of membrane-bound mammalian FPR embedded into the SSBLM format. Uninduced membrane and POPC-only particles (red and green, respectively) were used as negative controls, alongside the averaged absorbances of empty wells (purple). Only the data points for the 1:12,000, 1:24,000 and 1:48,000 (v/v) secondary antibody dilution factors were presented here, in order to keep background absorbance levels to a minimum and also avoid reaching the saturation limit of the employed spectrophotometer. The error bars represent the standard error of the mean, n = 3.

The results presented in Figure 5.6.2.1 confirmed that the embedded mammalian FPR was accessible towards high-affinity antibody binding and that the SSBLM format was suitable for screening candidate libraries against not just prokaryotic membrane proteins such as NupC, but also eukaryotic ones as well. By also taking into account that a density gradient was not used to separate the lysosomal membranes from the plasma membranes prior to creating the FPR/POPC particles, it is very likely then that the results presented above can be improved upon even further with additional protocol optimisation. To conclude, a more detailed discussion regarding the applicability of the SSBLM platform towards membrane protein research in general will be presented throughout the final Chapter 6.

Until then, a summative perspective on the SSBLM-based phage display screening of DARPin binders against NupC, alongside the other experimental findings presented in the current chapter, can be found in Figure 5.6.2.2 overleaf.

SSBLM-BASED PHAGE DISPLAY SCREENING CONCLUSIONS

Testing the SSBLM platform for phage display screening

✓ Screened MedImmune's DARPin library against His$_6$-tagged NupC across different formats
✓ Only performed two rounds of selection per screening format for comparison purposes

↓

Identifying and purifying the "lead candidate" binders

✓ Aligned the total selection output via Clustal Omega and discovered repeating sequences
✓ Isolated the plasmids, then purified the lead candidates with the highest number of repeats

↓

Determining the success of the SSBLM platform

✓ Re-screened the purified lead candidates against the other available NupC constructs
✓ Tested the SSBLMs with FPR and confirmed their applicability to other protein targets

---

Figure 5.6.2.2. Workflow summarising the experimental findings presented in the current chapter regarding the SSBLM-based phage display screening of DARPin binders against NupC.

CHAPTER 6

Discussion and Conclusions

6.1. Discussion

The impact screening supports have on selecting antibody binders against reconstituted membrane protein targets, as well as the virtues and limitations of the novel SSBLM format, will be evaluated throughout the following subsections.

6.1.1. Presenting targets for screening in a close-to-native format

Model membranes represent valuable tools for the study of membrane proteins *in vitro*, but their successful application is closely linked to the characteristics of not only the protein targets themselves, but also to those of the assay at hand. Depending on the type of membrane protein being studied, certain models such as lipid bilayers formed on Ni-NTA-treated surfaces could facilitate target relipidation in a preferred orientation, while other membrane models such as proteoliposomes would not. Conversely, the latter model could allow a membrane protein such as an integral transporter to preserve its function post-purification, while the former SSM model would not. This is especially noteworthy considering that the solvent-filled gap formed between the solid support and the deposited lipid bilayer might not even permit the correct integration of certain membrane protein targets whose extramembranous domains extend further than a few nanometres (Richards et al., 2016). Nevertheless, even following successful SSM integration, coming into contact with the underlying substrate would undoubtedly affect protein fluidity within the model membrane and, in turn, lead to an unequal target distribution throughout the antigen presentation area.

In order to circumvent the issues caused by target immobility, as well as the need for finding an optimal detergent for membrane destabilisation ahead of protein reconstitution (Seddon et al., 2004), several alternatives to the traditional method of SSM formation via proteoliposome deposition have already been trialled. These included the self-insertion of membrane protein targets into an already-formed SSM (Diaz et al., 2008) or the sonication of native cell membranes together with PEGylated synthetic lipids, followed by the deposition of the resulting mixed vesicles onto a solid substrate to form a polymer-supported lipid bilayer (Pace et al., 2015). Unfortunately, neither of these methods is without its own drawbacks, since the former has only been tested for a specific class of membrane proteins (i.e. annexins), while the sonication step required by the latter would invariably disturb the orientation of the embedded protein targets (Richards et al., 2016).

Beyond its long-term denaturating effect and the potential occlusion of target epitopes, the detergent solubilisation of membrane proteins comes with several other issues not pertaining directly to antibody screening. Firstly, detergent monomers seldom arrange into neatly-packaged micelles and it is therefore possible that their inability to solubilise certain membrane protein classes arises from the defects inherent to monomer packing, which can ultimately lead to protein aggregation and inactivation following purification (Garavito and Ferguson-Miller, 2001). Furthermore, the complete delipidation of membrane proteins – long pursued by X-ray crystallographers and NMR experts striving to obtain high-purity samples – has also been linked to increased chances of protein denaturation and, consequently, loss-of-function post-purification (le Maire et al., 2000). It is because of these undesirable side effects that a new "purer is not always better" paradigm has emerged in modern Structural Biology, paving the way for the purification of protein-lipid complexes rather than just the membrane protein targets by themselves (Garavito and Ferguson-Miller, 2001). Several approaches have already been made available to this end through the use of apolipoprotein nanodiscs (Hagn et al., 2013) and styrene-maleic acid copolymer lipid particles (SMALPs) (Lee et al., 2016), both of which can extract protein targets from their native membrane environments along with a proximal portion of their associated lipid bilayer components as well. Hopefully, these emergent technologies will help bolster the number of membrane protein structures available to date – unfortunately representing less than 1% of all submissions to the Protein Data Bank (PDB) (Mancia and Love, 2010) – and thus refine our understanding of membrane proteins and the treatment of their related disorders at the same time.

6.1.2. Current limitations of the SSBLM screening format

While highly versatile and clearly adaptable to membrane protein targets originating from both prokaryotic and eukaryotic expression systems, rapid SSBLM sedimentation under normal gravity (i.e. <10 minutes) was nevertheless observed for both particle sizes below vesicle/nanoparticle ratios of 20% (w/w) for the 100 nm nanoparticles and 10% (w/w) for their 200 nm counterparts. However, upon increasing the vesicle concentrations above said ratios, both samples remained suspended in solution over much longer periods of time (i.e. >3 hours). The rapid sedimentation was therefore likely caused by the incomplete SSBLM formation observed below the two experimentally-determined saturation ratios, since non-functionalised nanoparticles tend to aggregate in high ionic strength buffers (Moore et al., 2015), such as the PBS buffer used for resuspending the particles following the MilliQ® water washing step. However, once the SSBLMs are completely enveloping the silica nanoparticles, their aggregation is prevented due to the altered surface chemistries of the particles promoting dispersion in solution.

Our attempts at reproducing the results obtained by Mornet et al. (2005) and Trépout et al. (2007) towards resolving the lipid component of the SSBLMs via cryo-EM have, unfortunately, not been met with the same level of success. Luckily, the SAXS measurements detailed in subsection 4.4.2 did provide similarly-strong evidence of correct SSBLM formation around the nanoparticle substrates. Moreover, even though the cryo-EM images presented in subsection 4.5.3 did not reveal the lipid bilayers surrounding the depicted 200 nm nanoparticles, the positioning of the gold-labelled Ni-NTA probes – either on top of or within lipid-bilayer proximity to the silica substrate – strongly suggested that the SSBLMs were indeed present, but simply remained unresolved using the TEM setup we had at our disposal at the time. It should also be noted that Mornet et al. (2005) used vesicles of a different lipid composition to our own, in addition to the fact that we aimed to match the quality of their results using proteoliposomes embedding reconstituted membrane proteins, whose mere presence undoubtedly impacts SSBLM formation in ways that are not yet fully understood at the moment (Granéli et al., 2003).

6.2. Future Directions

Throughout recent years, the study of membrane protein targets embedded in detergent-free, close-to-native formats such as SSBLMs, SMALPs and nanodiscs has become more and more commonplace, fostering a deeper understanding of the complex proteolipid interactions affecting their conformations and functions in relation to the lipid bilayer component of native cell membranes. These novel research platforms will undoubtedly pave the way for new exciting contributions in the near future as well. Considering their performance during the phage display screening of DARPin binders against His_6-tagged NupC, it has become clear that SSBLMs represent a valuable new means of assaying antibody binding to membrane proteins embedded in a close-to-native format that not only mimics the biological environment from which the screening targets originated, but also elegantly circumvents the undesirable consequences of traditional detergent-based selection methods.

With that being said, the SSBLM format would certainly benefit from faster washing steps that do not rely on centrifugation for the removal of particles from solution. Rather, the use of iron oxide-core, silica-shell nanoparticles for the formation of future SSBLM samples would undoubtedly save considerable time due to the increased pelleting speed afforded by a high-power magnetic separator compared to a table-top centrifuge. Ultimately, even more advanced levels of automation would very likely be possible in an industrial setting, allowing the true value of the SSBLM platform to be fully appreciated.

It was certainly unfortunate that the available project time did not allow for an examination of the potential effects the lead candidate DARPins might have had on the *ex vivo* nucleoside transport activity of purified NupC. Nevertheless, the SURFE2R measurements did reveal that said activity was mainly dependent on the level of NupC expression relative to that of other *E. coli* IM proteins and not necessarily on the concentration of NupC-embedding vesicles loaded onto a prepared N1 sensor. This observation helped reinforce the idea that an unambiguous comparison between the post-purification transport activities demonstrated by the three NupC constructs used throughout the project would be quite difficult to perform, especially given that membrane protein expression levels can vary substantially between different purification runs.

In the end, should high-affinity antibody binders be selected via phage display screening against future SSBLM-embedded targets, then the optimal number of selection rounds must be rigorously observed (i.e. 3-5 instead of just 2). Furthermore, a high-throughput method of detecting phage-bound antibody binding to the embedded membrane proteins must also be developed in order to ensure that only those candidates displaying the highest affinities towards their intended targets are carried forward though the laborious and time-consuming full-scale expression and purification processes.

6.3. Conclusions

With greatly varied applications and still-untapped potential, model membranes have already contributed substantially to our understanding of native membrane biophysics and biochemistry and have helped researchers translate theoretical knowledge into real-life technological applications in fields as diverse as micro- and nanoarray sensor development (Wittenberg et al., 2011), novel functional materials (Collins et al., 2016), advanced drug delivery methods (Lockhart et al., 2016) and even nanoscale encapsulation for the preservation of foodstuffs and drugs (Ghorbanzade et al., 2016).

Research into membrane biology is especially relevant at present given that a majority of the pharmaceuticals available today target membrane proteins exclusively (Hopkins and Groom, 2002). While these drugs regularly take the form of antibodies or antibody mimetics, the screening procedures employed in their discovery require the fragile membrane protein targets to be detergent-solubilised for post-purification stability prior to their immobilisation onto a screening support. Unfortunately, the presence of detergent micelles during antibody selection can prevent the isolation of high-affinity binders through the occlusion of key epitopes on the target protein surface.

Therefore, the main objective of the project at hand revolved around adapting SSM technology featuring reconstituted membrane protein targets into a novel research platform that could bring several improvements to the traditional process of phage display screening while simultaneously circumventing the issues caused by detergent solubilisation. As the results presented throughout the current thesis have already demonstrated, SSBLMs embedding reconstituted membrane proteins represent an enhanced format for presenting antigens to binding candidates that could potentially act as therapeutics by modulating the function of their bound targets.

SSBLMs combine the desirable properties of both nanomaterials and model membranes, representing objects of great scientific and even commercial interest, especially for the drug discovery industry. They constitute a versatile, native-like format for the embedding of phenotypically-diverse membrane proteins while significantly reducing or outright eliminating the screening issues associated with target denaturation, antigen availability or epitope accessibility. SSBLMs also facilitate research and development opportunities such as the creation of nanovectors capable of delivering therapeutic payloads to drug targets (Mornet et al., 2005). Furthermore, there is already convincing evidence to support applying the SSBLM formation strategies presented thus far to nanoparticles coated with shells of a different composition, such as superparamagnetic ferrite nanoparticles (Mornet et al., 2002) or fluorescent quantum dots (Rochard et al., 2002), so as to expand the physical properties of the platform in any way that might prove useful towards manipulating biomolecules of varying sizes and functions.

The future development of this novel format specifically for use in phage display screening would also undoubtedly benefit the selection of novel antibody-based therapeutics for a number of reasons. By embedding membrane protein targets into SSBLMs, a resilient support for the high-throughput screening of vast candidate libraries can be constructed in a time-efficient manner with minimal effort and no specialist training. Coupled with the substantially increased surface area and feasibility offered by nanoscopic redispersible substrates, this technology shows promise towards becoming a genuine boon for the screening of novel protein-binding therapeutics such as the DARPins selected against NupC during the current project. Moreover, the fact that fully-functional SSBLMs can be also created from vesicles extruded from native cell membranes mixed with model lipids supports their use towards performing binding validation assays in a semi-*in vivo* fashion as well.

In conclusion, the nanoscale SSBLM model represents a highly promising platform for the selection of antibody binders against a multitude of potential membrane protein targets and, as such, it rightfully deserves to be further explored and refined in the near future.

BIBLIOGRAPHY

Adams, G.P. and Weiner, L.M. 2005. Monoclonal antibody therapy of cancer. *Nat. Biotechnol.* **23**(9), pp. 1147-1157.

Adrian, M., Dubochet, J., Lepault, J. and McDowall, A.W. 1984. Cryo-electron microscopy of viruses. *Nature*. **308**, pp. 32-36.

Ahmad, Z.A., Yeap, S.K., Ali, A.M., Ho, W.Y., Alitheen, N.B.M. and Hamid, M. 2012. scFv antibody: principles and clinical application. *Clin. Dev. Immunol.* **2012**, article no: 980250 [no pagination].

Al-Lazikani, B., Lesk, A.M. and Chothia, C. 1997. Standard conformations for the canonical structures of immunoglobulins. *J. Mol. Biol.* **273**, pp. 927-948.

Andersen, J.P., Verstergaard, A.L., Mikkelsen, S.A., Mogensen, L.S., Chalat, M. and Molday, R.S. 2016. P4-ATPases as phospholipid flippases – structure, function, and enigmas. *Front. Physiol.* **7**, article no: 275 [no pagination].

Aperia, A. 2007. Membrane transport proteins in health and disease. *J. Intern. Med.* **261**(1), pp. 2-4.

Arce, L., Zougagh, M., Arce, C., Moreno, A., Ríos, A. and Valcárcel, M. 2007. Self-assembled monolayer-based piezoelectric flow immunosensor for the determination of canine immunoglobulin. *Biosens. Bioelectron.* **22**(12), pp. 3217-3223.

Ataka, K., Giess, F., Knoll, W., Naumann, R., Haber-Pohlmeier, S., Richter, B. and Heberle, J. 2004. Oriented attachment and membrane reconstitution of His-tagged cytochrome *c* oxidase to a gold electrode: in situ monitoring by surface-enhanced infrared absorption spectroscopy. *J. Am. Chem. Soc.* **126**(49), pp. 16199-16206.

Baek, H., Suk, K., Kim, Y. and Cha, S. 2002. An improved helper phage system for efficient isolation of specific antibody molecules in phage display. *Nucleic Acids Res.* **30**(5), article no: e18 [no pagination].

Bagatolli, L.A., Ipsen, J.H., Simonsen, A.C. and Mouritsen, O.G. 2010. An outlook on organization of lipids in membranes: searching for a realistic connection with the organization of biological membranes. *Prog. Lipid Res.* **49**(4), pp. 378-389.

BIBLIOGRAPHY

Bangham, A.D. and Horne, R.W. 1964. Negative staining of phospholipids and their structural modification by surface-active agents as observed in the electron microscope. *J. Mol. Biol.* **8**, pp. 660-668.

Baumann, M.J., Eggel, A., Amstutz, P., Stadler, B.M. and Vogel, M. 2010. DARPins against a functional IgE epitope. *Immunol. Lett.* **133**(2), pp. 78-84.

Bazzone, A., Costa, W.S., Braner, M., Călinescu, O., Hatahet, L. and Fendler, K. 2013. Introduction to solid supported membrane based electrophysiology. *J. Vis. Exp.* **75**, article no: e50230 [no pagination].

Beaber, J.W., Tam, E.M., Lao, L.S. and Rondon, I.J. 2012. A new helper phage for improved monovalent display of Fab molecules. *J. Immunol. Methods.* **376**(1-2), pp. 46-54.

Benson, A.A. 1964. Plant membrane lipids. *Annu. Rev. Plant Physiol.* **15**, pp. 1-16.

Benson, A.A. 1966. On the orientation of lipids in chloroplast and cell membranes. *J. Am. Oil Chem. Soc.* **43**(5), pp. 265-270.

Bernstein, R.M., Schluter, S.F., Shen, S. and Marchalonis, J.J. 1996. A new high molecular weight immunoglobulin class from the carcharhine shark: implications for the properties of the primordial immunoglobulin. *Proc. Natl. Acad. Sci. USA.* **93**(8), pp. 3289-3293.

Bharti, B., Meissner, J. and Findenegg, G.H. 2011. Aggregation of silica nanoparticles directed by adsorption of lysozyme. *Langmuir.* **27**(16), pp. 9823-9833.

Bill, R.M., Henderson, P.J.F., Iwata, S., Kunji, E.R.S., Michel, H., Neutze, R., Newstead, S., Poolman, B., Tate, C.G. and Vogel, H. 2011. Overcoming barriers to membrane protein structure determination. *Nat. Biotechnol.* **29**(4), pp. 335-340.

Binz, H.K., Stumpp, M.T., Forrer, P., Amstutz, P. and Plückthun, A. 2003. Designing repeat proteins: well-expressed, soluble and stable proteins from combinatorial libraries of consensus ankyrin repeat proteins. *J. Mol. Biol.* **332**(2), pp. 489-503.

Biolin Scientific Holding AB. 2016a. *Q-Sense.* [Online]. [Accessed 28 March 2016]. Available from: http://www.biolinscientific.com/q-sense/.

Biolin Scientific Holding AB. 2016b. *Q-Sense E4 Product Brochure*. [Online]. [Accessed 9 March 2016]. Available from: http://www.biolinscientific.com/zafepress.php?url=%2Fpdf%2FQ-Sense%2FProducts%2FE4%2FQS_P_E4%20Brochure.pdf.

Blesneac, I., Ravaud, S., Machillot, P., Zoonens, M., Masscheylen, S., Miroux, B., Vivaudou, M. and Pebay-Peyroula, E. 2012. Assaying the proton transport and regulation of UCP1 using solid supported membranes. *Eur. Biophys. J.* **41**(8), pp. 675-679.

Boekema, E.J., Folea, M. and Kouřil, R. 2009. Single particle electron microscopy. *Photosynth. Res.* **102**(2-3), pp. 189-196.

Boersma, Y.L. and Plückthun, A. 2011. DARPins and other repeat protein scaffolds: advances in engineering and applications. *Curr. Opin. Biotechnol.* **22**(6), pp. 849-857.

Borghesi, L. and Milcarek, C. 2006. From B cell to plasma cell: regulation of V(D)J recombination and antibody secretion. *Immunol. Res.* **36**(1-3), pp. 27-32.

Bradfield, J.R.G. 1954. Electron microscopic observations on bacterial nuclei. *Nature.* **173**(4396), pp. 184-186.

Brenner, T., Paulus, M., Schroer, M.A., Tiemeyer, S., Sternemann, C., Möller, J., Tolan, M., Degen, P. and Rehage, H. 2012. Adsorption of nanoparticles at the solid-liquid interface. *J. Colloid Interface Sci.* **374**(1), pp. 287-290.

Brient-Litzler, E., Plückthun, A. and Bedouelle, H. 2010. Knowledge-based design of reagentless fluorescent biosensors from a designed ankyrin repeat protein. *Protein Eng. Des. Sel.* **23**(4), pp. 229-241.

Brown, A.D. 1965. Hydrogen ion titrations of intact and dissolved lipoprotein membranes. *J. Mol. Biol.* **12**, pp. 491-508.

Brüggeller, P. and Mayer, E. 1980. Complete vitrification in pure liquid water and dilute aqueous solutions. *Nature.* **288**, pp. 569-571.

Buttry, D.A. 1992. Measurement of interfacial processes at electrode surfaces with the electrochemical quartz crystal microbalance. *Chem. Rev.* **92**(6), pp. 1355-1379.

BIBLIOGRAPHY

Campochiaro, P.A., Channa, R., Berger, B.B., Heier, J.S., Brown, D.M., Fiedler, U., Hepp, J. and Stumpp, M.T. 2013. Treatment of diabetic macular edema with a designed ankyrin repeat protein that binds vascular endothelial growth factor: a phase I/II study. *Am. J. Ophthalmol.* **155**(4), pp. 697-704.

Carmon, K.S., Baltus, R.E. and Luck, L.A. 2005. A biosensor for estrogenic substances using the quartz crystal microbalance. *Anal. Biochem.* **345**(2), pp. 277-283.

Chasteen, L., Ayriss, J., Pavlik, P. and Bradbury, A.R.M. 2006. Eliminating helper phage from phage display. *Nucleic Acids Res.* **34**(21), article no: e145 [no pagination].

Chen, K., Xu, W., Wilson, M., He, B., Miller, N.W., Bengtén, E., Edholm, E.S., Santini, P.A., Rath, P., Chiu, A., Cattalini, M., Litzman, J., Bussel, J.B., Huang, B., Meini, A., Riesbeck, K., Cunningham-Rundles, C., Plebani, A. and Cerutti, A. 2009. Immunoglobulin D enhances immune surveillance by activating antimicrobial, proinflammatory and B cell-stimulating programs in basophils. *Nat. Immunol.* **10**(8), pp. 889-898.

Chen, Q., Xu, S., Liu, Q., Masliyah, J. and Xu, Z. 2016. QCM-D study of nanoparticle interactions. *Adv. Colloid Interface Sci.* **233**, pp. 94-114.

Cheng, C.I., Chang, Y.P. and Chu, Y.H. 2012. Biomolecular interactions and tools for their recognition: focus on the quartz crystal microbalance and its diverse surface chemistries and applications. *Chem. Soc. Rev.* **41**(5), pp. 1947-1971.

Cho, N.J., Frank, C.W., Kasemo, B. and Höök, F. 2010. Quartz crystal microbalance with dissipation monitoring of supported lipid bilayers on various substrates. *Nat. Protoc.* **5**(6), pp. 1096-1106.

Cho, W. and Stahelin, R.V. 2005. Membrane-protein interactions in cell signaling and membrane trafficking. *Annu. Rev. Biophys. Biomol. Struct.* **34**, pp. 119-151.

Clementi, N., Mancini, N., Solforosi, L., Castelli, M., Clementi, M. and Burioni, R. 2012. Phage display-based strategies for cloning and optimization of monoclonal antibodies directed against human pathogens. *Int. J. Mol. Sci.* **13**(7), pp. 8273-8292.

Collins, A.M., Timlin, J.A., Anthony, S.M. and Montaño, G.A. 2016. Amphiphilic block copolymers as flexible membrane materials generating structural and functional mimics of green bacterial antenna complexes. *Nanoscale.* **8**(32), pp. 15056-15063.

Craig, J.E., Zhang, Y and Gallagher, M.P. 1994. Cloning of the *nupC* gene of *Escherichia coli* encoding a nucleoside transport system, and identification of an adjacent insertion element, IS*186*. *Mol. Microbiol.* **11**(6), pp. 1159-1168.

Dalton, A.J. 1951. Observations of the Golgi substance with the electron microscope. *Nature*. **168**(4267), pp. 244-245.

Damaraju, V.L., Damaraju, S., Young, J.D., Baldwin, S.A., Mackey, J., Sawyer, M.B. and Cass, C.E. 2003. Nucleoside anticancer drugs: the role of nucleoside transporters in resistance to cancer chemotherapy. *Oncogene*. **22**(47), pp. 7524-7536.

Danielli, J.F. and Davson, H. 1935. A contribution to the theory of permeability of thin films. *J. Cell. Comp. Physiol.* **5**(4), pp. 495-508.

Department of Physics, The Chinese University of Hong Kong. 2016. *Basic principle of transmission electron microscope*. [Online]. [Accessed 3 April 2016]. Available from: http://www.hk-phy.org/atomic_world/tem/tem02_e.html.

Diaz, A.J., Albertorio, F., Daniel, S. and Cremer, P.S. 2008. Double cushions preserve transmembrane protein mobility in supported bilayer systems. *Langmuir*. **24**(13), pp. 6820-6826.

Dietrich, C., Bagatolli, L.A., Volovyk, Z.N., Thompson, N.L., Levi, M., Jacobson, K. and Gratton, E. 2001. Lipid rafts reconstituted in model membranes. *Biophys. J.* **80**(3), pp. 1417-1428.

Dobro, M.J., Melanson, L.A., Jensen, G.J. and McDowall, A.W. 2010. Plunge freezing for electron cryomicroscopy. *Methods Enzymol.* **481**, pp. 63-82.

Dodd, C.E., Johnson, B.R.G. and Jeuken, L.J.C. 2008. Native *E. coli* inner membrane incorporation in solid-supported lipid bilayer membranes. *Biointerphases*. **3**(2), pp. FA59-FA67.

Domingo-Calap, P., Georgel, P. and Bahram, S. 2016. Back to the future: bacteriophages as promising therapeutic tools. *HLA*. **87**(3), pp. 133-140.

Dubochet, J., Adrian, M., Chang, J.J., Homo, J.C., Lepault, J., McDowall, A.W. and Schultz, P. 1988. Cryo-electron microscopy of vitrified specimens. *Q. Rev. Biophys.* **21**(2), pp. 129-228.

Dubochet, J., Ducommun, M., Zollinger, M. and Kellenberger, E. 1971. A new preparation method for dark-field electron microscopy of biomacromolecules. *J. Ultrastruct. Res.* **35**(1), pp. 147-167.

Dynarowicz-Łątka, P., Dhanabalan, A. and Oliveira Jr., O.N. 2001. Modern physicochemical research on Langmuir monolayers. *Adv. Colloid Interface Sci.* **91**(2), pp. 221-293.

Elie-Caille, C., Fliniaux, O., Pantigny, J., Mazière, J.C. and Bourdillon, C. 2005. Self-assembly of solid-supported membranes using a triggered fusion of phospholipid-enriched proteoliposomes prepared from the inner mitochondrial membrane. *Langmuir.* **21**(10), pp. 4661-4668.

Elliot, A.J., Malek, G.A., Lu, R., Han, S., Yiu, H., Zhao, S. and Wu, J.Z. 2014. Integrating atomic layer deposition and ultra-high vacuum physical vapor deposition for *in situ* fabrication of tunnel junctions. *Rev. Sci. Instrum.* **85**(7), article no: 073904 [no pagination].

Erni, R., Rossell, M.D., Kisielowski, C. and Dahmen, U. 2009. Atomic-resolution imaging with a sub-50-pm electron probe. *Phys. Rev. Lett.* **102**(9), article no: 096101 [no pagination].

Fang, J., Ren, C., Zhu, T., Wang, K., Jiang, Z. and Ma, Y. 2015. Comparison of the different responses of surface plasmon resonance and quartz crystal microbalance techniques at solid-liquid interfaces under various experimental conditions. *Analyst.* **140**(4), pp. 1323-1336.

FEI. 2016a. *Tecnai*. [Online]. [Accessed 14 March 2016]. Available from: https://www.fei.com/products/tem/tecnai/.

FEI. 2016b. *Vitrobot for Life Sciences*. [Online]. [Accessed 11 March 2016]. Available from: http://www.fei.com/products/vitrobot/.

Fitzpatrick, A.W.P., Lorenz, U.J., Vanacore, G.M. and Zewail, A.H. 2013. 4D cryo-electron microscopy of proteins. *J. Am. Chem. Soc.* **135**(51), pp. 19123-19126.

Fleischer, S., Brierley, G., Klouwen, H. and Slautterback, D.B. 1962. Studies of the electron transfer system: XLVII. The role of phospholipids in electron transfer. *J. Biol. Chem.* **237**(10), pp. 3264-3272.

Fulford, G.D. 1968. Pouring holy oil on troubled waters. *Isis*. **59**(2), pp. 198-199.

Gaines Jr., G.L. 1983. On the history of Langmuir-Blodgett films. *Thin Solid Films*. **99**(1-3), pp. ix-xiii.

Galush, W.J., Shelby, S.A., Mulvihill, M.J., Tao, A., Yang, P. and Groves, J.T. 2009. A nanocube plasmonic sensor for molecular binding on membrane surfaces. *Nano. Lett.* **9**(5), pp. 2077-2082.

Gamkrelidze, M. and Dąbrowska, K. 2014. T4 bacteriophage as a phage display platform. *Arch. Microbiol.* **196**(7), pp. 473-479.

Garavito, R.M. and Ferguson-Miller, S. 2001. Detergents as tools in membrane biochemistry. *J. Biol. Chem.* **276**(35), pp. 32403-32406.

Geertsma, E.R., Nik Mahmood, N.A.B., Schuurman-Wolters, G.K. and Poolman, B. 2008. Membrane reconstitution of ABC transporters and assays of translocator function. *Nat. Protoc.* **3**(2), pp. 256-266.

Ghorbanzade, T., Jafari, S.M., Akhavan, S. and Hadavi, R. 2016. Nano-encapsulation of fish oil in nano-liposomes and its application in fortification of yogurt. *Food Chem.* **216**, pp. 146-152.

Giess, F., Friedrich, M.G., Heberle, J., Naumann, R.L. and Knoll, W. 2004. The protein-tethered lipid bilayer: a novel mimic of the biological membrane. *Biophys. J.* **87**(5), pp. 3213-3220.

Gorter, E. and Grendel, F. 1925. On bimolecular layers of lipoids on the chromocytes of the blood. *J. Exp. Med.* **41**(4), pp. 439-443.

Granéli, A., Rydström, J., Kasemo, B. and Höök, F. 2003. Formation of supported lipid bilayer membranes on SiO_2 from proteoliposomes containing transmembrane proteins. *Langmuir*. **19**(3), pp. 842-850.

Green, D.E., Allmann, D.W., Bachmann, E., Baum, H., Kopaczyk, K., Korman, E.F., Lipton, S., MacLennan, D.H., McConnell, D.G., Perdue, J.F., Rieske, J.S. and Tzagoloff, A. 1967. Formation of membranes by repeating units. *Arch. Biochem. Biophys.* **119**(1), pp. 312-335.

Green, D.E. and Fleischer, S. 1963. The role of lipids in mitochondrial electron transfer and oxidative phosphorylation. *Biochim. Biophys. Acta.* **70**, pp. 554-582.

Green, D.E. and Perdue, J.F. 1966. Membranes as expressions of repeating units. *Proc. Natl. Acad. Sci. USA.* **55**(5), pp. 1295-1302.

Groves, J.T. 2002. Membrane array technology for drug discovery. *Curr. Opin. Drug Discov. Devel.* **5**(4), pp. 606-612.

Gunning, P. 2012. BioArchitecture: the organization and regulation of biological space. *Bioarchitecture.* **2**(6), pp. 200-203.

Hagn, F., Etzkorn, M., Raschle, T. and Wagner, G. 2013. Optimized phospholipid bilayer nanodiscs facilitate high-resolution structure determination of membrane proteins. *J. Am. Chem. Soc.* **135**(5), pp. 1919-1925.

Hammill, J.A., VanSeggelen, H., Helsen, C.W., Denisova, G.F., Evelegh, C., Tantalo, D.G.M., Bassett, J.D. and Bramson, J.L. 2015. Designed ankyrin repeat proteins are effective targeting elements for chimeric antigen receptors. *J. Immunother. Cancer.* **3**, article no: 55 [no pagination].

Hanahan, D. 1983. Studies on transformation of *Escherichia coli* with plasmids. *J. Mol. Biol.* **166**(4), pp. 557-580.

Hanenberg, M., McAfoose, J., Kulic, L., Welt, T., Wirth, F., Parizek, P., Strobel, L., Cattepoel, S., Späni, C., Derungs, R., Maier, M., Plückthun, A. and Nitsch, R.M. 2014. Amyloid-*β* peptide-specific DARPins as a novel class of potential therapeutics for Alzheimer disease. *J. Biol. Chem.* **289**(39), pp. 27080-27089.

Hanes, J. and Plückthun, A. 1997. *In vitro* selection and evolution of functional proteins by using ribosome display. *Proc. Natl. Acad. Sci. USA.* **94**(10), pp. 4937-4942.

Hanes, J., Schaffitzel, C., Knappik, A. and Plückthun, A. 2000. Picomolar affinity antibodies from a fully synthetic naive library selected and evolved by ribosome display. *Nat. Biotechnol.* **18**(12), pp. 1287-1292.

Hantke, K. 1976. Phage T6 – colicin K receptor and nucleoside transport in *Escherichia coli*. *FEBS Lett.* **70**(1), pp. 109-112.

Hao, Z., Thomsen, M. Postis, V.L.G., Lesiuk, A., Sharples, D., Wang, Y., Bartlam, M. and Goldman, A. 2016. A novel and fast purification method for nucleoside transporters. *Front. Mol. Biosci.* **3**, article no: 23 [no pagination].

Hausammann, S., Vogel, M., Kremer Hovinga, J.A., Lacroix-Desmazes, S., Stadler, B.M. and Horn, M.P. 2013. Designed ankyrin repeat proteins: a new approach to mimic complex antigens for diagnostic purposes?. *PLoS One*. **8**(4), article no: e60688 [no pagination].

Heller, G.T., Mercer-Smith, A.R. and Johal, M.S. 2015. Quartz microbalance technology for probing biomolecular interactions. *Methods Mol. Biol.* **1278**, pp. 153-164.

Hengerer, A., Decker, J., Prohaska, E., Hauck, S., Kößlinger, C. and Wolf, H. 1999. Quartz crystal microbalance (QCM) as a device for the screening of phage libraries. *Biosens. Bioelectron.* **14**(2), pp. 139-144.

Hoogenboom, H.R. 2002. Overview of antibody phage-display technology and its applications. *Methods Mol. Biol.* **178**, pp. 1-37.

Hopkins, A.L. and Groom, C.R. 2002. The druggable genome. *Nat. Rev. Drug Discov.* **1**(9), pp. 727-730.

Hübner, C.A. and Jentsch, T.J. 2002. Ion channel diseases. *Hum. Mol. Gen.* **11**(20), pp. 2435-2445.

Imai, K and Takaoka, A. 2006. Comparing antibody and small-molecule therapies for cancer. *Nat. Rev. Cancer*. **6**(9), pp. 714-727.

International Human Genome Sequencing Consortium. 2001. Initial sequencing and analysis of the human genome. *Nature*. **409**(6822), pp. 860-921.

Israelachvili, J.N. 1977. Refinement of the fluid mosaic model of membrane structure. *Biochim. Biophys. Acta*. **469**(2), pp. 221-225.

Janshoff, A., Galla, H.J. and Steinem, C. 2000. Piezoelectric mass-sensing devices as biosensors – an alternative to optical biosensors?. *Angew. Chem. Int. Ed. Engl.* **39**(22), pp. 4004-4032.

Jaruwongrungsee, K., Waiwijit, U., Wisitsoraat, A., Sangworasil, M., Pintavirooj, C. and Tuantranont, A. 2015. Real-time multianalyte biosensors based on interference-free multichannel monolithic quartz crystal microbalance. *Biosens. Bioelectron.* **67**, pp. 576-581.

Jass, J., Tjärnhage, T. and Puu, G. 2000. From liposomes to supported, planar bilayer structures on hydrophilic and hydrophobic surfaces: an atomic force microscopy study. *Biophys. J.* **79**(6), pp. 3153-3163.

Jensen, E.C. 2012. Types of imaging, part 1: electron microscopy. *Anat. Rec.* **295**(5), pp. 716-721.

Jensen, M.H., Morris, E.J. and Simonsen, A.C. 2007. Domain shapes, coarsening, and random patterns in ternary membranes. *Langmuir.* **23**(15), pp. 8135-8141.

Jin, X., Huang, Y., Mason, A. and Zeng, X. 2009. Multichannel monolithic quartz crystal microbalance gas sensor array. *Anal. Chem.* **81**(2), pp. 595-603.

John Innes Centre. 2016. *What is electron microscopy?*. [Online]. [Accessed 2 April 2016]. Available from: https://www.jic.ac.uk/microscopy/intro_EM.html.

Johnson, J.E. and Cornell, R.B. 1999. Amphitropic proteins: regulation by reversible membrane interactions (review). *Mol. Membr. Biol.* **16**(3), pp. 217-235.

Jost, C. and Plückthun, A. 2014. Engineered proteins with desired specificity: DARPins, other alternative scaffolds and bispecific IgGs. *Curr. Opin. Struct. Biol.* **27**, pp. 102-112.

Kajander, T., Cortajarena, A.L. and Regan, L. 2006. Consensus design as a tool for engineering repeat proteins. *Methods Mol. Biol.* **340**, pp. 151-170.

Keller, D., Larsen, N.B., Møller, I.M and Mouritsen, O.G. 2005. Decoupled phase transitions and grain-boundary melting in supported phospholipid bilayers. *Phys. Rev. Lett.* **94**(2), article no: 025701 [no pagination].

Kikhney, A.G. and Svergun, D.I. 2015. A practical guide to small angle X-ray scattering (SAXS) of flexible and intrinsically disordered proteins. *FEBS Lett.* **589**(19 Pt A), pp. 2570-2577.

Knol, J., Sjollema, K. and Poolman, B. 1998. Detergent-mediated reconstitution of membrane proteins. *Biochemistry.* **37**(46), pp. 16410-16415.

Knoll, W., Frank, C.W., Heibel, C., Naumann, R., Offenhäusser, A., Rühe, J., Schmidt, E.K., Shen, W.W. and Sinner, A. 2000. Functional tethered lipid bilayers. *J. Biotechnol.* **74**(3), pp. 137-158.

Korlach, J., Schwille, P., Webb, W.W. and Feigenson, G.W. 1999. Characterization of lipid bilayer phases by confocal microscopy and fluorescence correlation spectroscopy. *Proc. Natl. Acad. Sci. USA.* **96**(15), pp. 8461-8466.

Köhler, G. and Milstein, C. 1975. Continuous cultures of fused cells secreting antibody of predefined specificity. *Nature.* **256**(5517), pp. 495-497.

Krause, R., Watzke, N. Kelety, B., Dörner, W. and Fendler, K. 2009. An automatic electrophysiological assay for the neuronal glutamate transporter mEAAC1. *J. Neurosci. Methods.* **177**(1), pp. 131-141.

Kučerka, N., Nieh, M.P. and Katsaras, J. 2011. Fluid phase lipid areas and bilayer thicknesses of commonly used phosphatidylcholines as a function of temperature. *Biochim. Biophys. Acta.* **1808**(11), pp. 2761-2771.

Kunji, E.R.S., Harding, M., Butler, P.J.G. and Akamine, P. 2008. Determination of the molecular mass and dimensions of membrane proteins by size exclusion chromatography. *Methods.* **46**(2), pp. 62-72.

Kutter, E., Gachechiladze, K., Poglazov, A., Marusich, E., Shneider, M., Aronsson, P., Napuli, A., Porter, D. and Mesyanzhinov, V. 1995. Evolution of T4-related phages. *Virus Genes.* **11**(2-3), pp. 285-297.

le Maire, M., Champeil, P. and Møller, J.V. 2000. Interaction of membrane proteins and lipids with solubilizing detergents. *Biochim. Biophys. Acta.* **1508**(1-2), pp. 86-111.

Lee, C.M.Y., Iorno, N., Sierro, F. and Christ, D. 2007. Selection of human antibody fragments by phage display. *Nat. Protoc.* **2**(11), pp. 3001-3008.

Lee, S.C., Knowles, T.J., Postis, V.L.G., Jamshad, M., Parslow, R.A., Lin, Y., Goldman, A., Sridhar, P., Overduin, M., Muench, S.P. and Dafforn, T.R. 2016. A method for detergent-free isolation of membrane proteins in their local lipid environment. *Nat. Protoc.* **11**(7), pp. 1149-1162.

Lepper, S., Merkel, M., Sartori, A., Cyrklaff, M. and Frischknecht, F. 2010. Rapid quantification of the effects of blotting for correlation of light and cryo-light microscopy images. *J. Microsc.* **238**(1), pp. 21-26.

Li, H., Xiao, S., Yao, D., Lam, M.H. and Liang, H. 2015. A smart DNA-gold nanoparticle probe for detecting single-base changes on the platform of a quartz crystal microbalance. *Chem. Commun. (Camb).* **51**(22), pp. 4670-4673.

Li, Q., Jogini, V., Wanderling, S., Cortes, D.M and Perozo, E. 2012. Expression, purification, and reconstitution of the voltage-sensing domain from Ci-VSP. *Biochemistry.* **51**(41), pp. 8132-8142.

Litman, G.W., Rast, J.P., Shamblott, M.J., Haire, R.N., Hulst, M., Roess, W., Litman, R.T., Hinds-Frey, K.R., Zilch, A. and Amemiya, C.T. 1993. Phylogenetic diversification of immunoglobulin genes and the antibody repertoire. *Mol. Biol. Evol.* **10**(1), pp. 60-72.

Liu, C., Monson, C.F., Yang, T., Pace, H. and Cremer, P.S. 2011. Protein separation by electrophoretic-electroosmotic focusing on supported lipid bilayers. *Anal. Chem.* **83**(20), pp. 7876-7880.

Lockhart, J.N., Beezer, D.B., Stevens, D.M., Spears, B.R. and Harth, E. 2016. One-pot polyglycidol nanogels via liposome master templates for dual drug delivery. *J. Control. Release.* **244**(Pt B), pp. 366-374.

Loewen, S.K., Yao, S.Y.M., Slugoski, M.D., Mohabir, N.N., Turner, R.J., Mackey, J.R., Weiner, J.H., Gallagher, M.P., Henderson, P.J.F., Baldwin, S.A., Cass, C.E. and Young, J.D. 2004. Transport of physiological nucleosides and anti-viral and anti-neoplastic nucleoside drugs by recombinant *Escherichia coli* nucleoside-H^+ cotransporter (NupC) produced in *Xenopus laevis* oocytes. *Mol. Membr. Biol.* **21**(1), pp. 1-10.

Luckey, M. 2008. *Membrane structural biology: with biochemical and biophysical foundations*. Cambridge: Cambridge University Press, p. 7.

Lundqvist, M.L., Middleton, D.L., Radford, C., Warr, G.W. and Magor, K.E. 2006. Immunoglobulins of the non-galliform birds: antibody expression and repertoire in the duck. *Dev. Comp. Immunol.* **30**(1-2), pp. 93-100.

Mager, T., Rimon, A., Padan, E. and Fendler, K. 2011. Transport mechanism and pH regulation of the Na^+/H^+ antiporter NhaA from *Escherichia coli*: an electrophysiological study. *J. Biol. Chem.* **286**(26), pp. 23570-23581.

Mancia, F. and Love, J. 2010. High-throughput expression and purification of membrane proteins. *J. Struct. Biol.* **172**(1), pp. 85-93.

Marčelja, S. 1976. Lipid-mediated protein interaction in membranes. *Biochim. Biophys. Acta.* **455**(1), pp. 1-7.

Marx, K.A. 2003. Quartz crystal microbalance: a useful tool for studying thin polymer films and complex biomolecular systems at the solution-surface interface. *Biomacromolecules.* **4**(5), pp. 1099-1120.

Mathew-Fenn, R.S., Das, R., Silverman, J.A., Walker, P.A. and Harbury, P.A.B. 2008. A molecular ruler for measuring quantitative distance distributions. *PLoS One.* **3**(10), article no: e3229 [no pagination].

McMillan, D.G.G., Marritt, S.J., Firer-Sherwood, M.A., Shi, L., Richardson, D.J., Evans, S.D., Elliott, S.J., Butt, J.N. and Jeuken, L.J.C. 2013. Protein-protein interaction regulates the direction of catalysis and electron transfer in a redox enzyme complex. *J. Am. Chem. Soc.* **135**(28), pp. 10550-10556.

Miller, E.F., Vaish, S. and Maier, R.J. 2012. Efficiency of purine utilization by *Helicobacter pylori*: roles for adenosine deaminase and a NupC homolog. *PLoS One.* **7**(6), article no: e38727 [no pagination].

Miller, E.S., Kutter, E., Mosig, G., Arisaka, F., Kunisawa, T. and Rüger, W. 2003. Bacteriophage T4 genome. *Microbiol. Mol. Biol. Rev.* **67**(1), pp. 86-156.

Milne, J.L.S., Borgnia, M.J., Bartesaghi, A., Tran, E.E.H., Earl, L.A., Schauder, D.M., Lengyel, J., Pierson, J., Patwardhan, A. and Subramaniam, S. 2013. Cryo-electron microscopy: a primer for the non-microscopist. *FEBS J.* **280**(1), pp. 28-45.

Milstein, C. 1999. The hybridoma revolution: an offshoot of basic research. *Bioessays.* **21**(11), pp. 966-973.

Miranda, K., Girard-Dias, W., Attias, M., de Souza, W. and Ramos, I. 2015. Three dimensional reconstruction by electron microscopy in the life sciences: an introduction for cell and tissue biologists. *Mol. Reprod. Dev.* **82**(7-8), pp. 530-547.

Mohanty, A.K. and Wiener, M.C. 2004. Membrane protein expression and production: effects of polyhistidine tag length and position. *Protein Expr. Purif.* **33**(2), pp. 311-325.

Molecular Partners. 2016a. *DARPin® Technology*. [Online]. [Accessed 1 March 2016]. Available from: http://www.molecularpartners.com/aboutdarpins/.

Molecular Partners. 2016b. *Pipeline*. [Online]. [Accessed 14 March 2016]. Available from: http://www.molecularpartners.com/our-products/.

Moody, P., Chudasama, V., Nathani, R.I., Maruani, A., Martin, S., Smith, M.E.B. and Caddick, S. 2014. A rapid, site-selective and efficient route to the dual modification of DARPins. *Chem. Commun. (Camb).* **50**(38), pp. 4898-4900.

Moore, T.L., Rodriguez-Lorenzo, L., Hirsch, V., Balog, S., Urban, D., Jud, C., Rothen-Rutishauser, B., Lattuada, M. and Petri-Fink, A. 2015. Nanoparticle colloidal stability in cell culture media and impact on cellular interactions. *Chem. Soc. Rev.* **44**(17), pp. 6287-6305.

Morandat, S., Azouzi, S., Beauvais, E., Mastouri, A. and El Kirat, K. 2013. Atomic force microscopy of model lipid membranes. *Anal. Bioanal. Chem.* **405**(5), pp. 1445-1461.

Mornet, S., Grasset, F., Portier, J., Duguet, E. 2002. Maghemite@silica nanoparticles for biological applications. *Eur. Cell. Mater.* **3**(2), pp. 110-113.

Mornet, S., Lambert, O., Duguet, E. and Brisson, A. 2005. The formation of supported lipid bilayers on silica nanoparticles revealed by cryoelectron microscopy. *Nano Lett.* **5**(2), pp. 281-285.

Mouritsen, O.G. 2011a. Lipidology and lipidomics – *quo vadis*? A new era for the physical chemistry of lipids. *Phys. Chem. Chem. Phys.* **13**(43), pp. 19195-19205.

Mouritsen, O.G. 2011b. Model answers to lipid membrane questions. *Cold Spring Harb. Perspect. Biol.* **3**(9), article no: a004622 [no pagination].

Mouritsen, O.G. and Bloom, M. 1984. Mattress model of lipid-protein interactions in membranes. *Biophys. J.* **46**(2), pp. 141-153.

Muench, S.P., Huss, M., Song, C.F., Phillips, C., Wieczorek, H., Trinick, J. and Harrison, M.A. 2009. Cryo-electron microscopy of the vacuolar ATPase motor reveals its mechanical and regulatory complexity. *J. Mol. Biol.* **386**(4), pp. 989-999.

Münch, R.C., Muth, A., Muik, A., Friedel, T., Schmatz, J., Dreier, B., Trkola, A., Plückthun, A., Büning, H. and Buchholz, C.J. 2015. Off-target-free gene delivery by affinity-purified receptor-targeted viral vectors. *Nat. Commun.* **6**, article no: 6246 [no pagination].

Nanion Technologies GmbH. 2016a. *N1 Single Sensor Chips*. [Online]. [Accessed 7 March 2016]. Available from: http://www.nanion.de/products/surfe2r.html.

Nanion Technologies GmbH. 2016b. *SURFE2R N1 & N96 Product Sheet*. [Online]. [Accessed 8 March 2016]. Available from: http://www.nanion.de/images/stories/pdf/Nanion_Surfer_PS_Online.pdf.

Newstead, S. 2011. Towards a structural understanding of drug and peptide transport within the proton-dependent oligopeptide transporter (POT) family. *Biochem. Soc. Trans.* **39**(5), pp. 1353-1358.

Newstead, S., Drew, D., Cameron, A.D., Postis, V.L.G., Xia, X., Fowler, P.W., Ingram, J.C., Carpenter, E.P., Sansom, M.S.P., McPherson, M.J., Baldwin, S.A. and Iwata, S. 2011. Crystal structure of a prokaryotic homologue of the mammalian oligopeptide-proton symporters, PepT1 and PepT2. *EMBO J.* **30**(2), pp. 417-426.

Nicholes, N., Date, A., Beaujean, P., Hauk, P., Kanwar, M. and Ostermeier, M. 2016. Modular protein switches derived from antibody mimetic proteins. *Protein Eng. Des. Sel.* **29**(2), pp. 77-85.

Nguyen, H.T., Pabit, S.A., Meisburger, S.P., Pollack, L. and Case, D.A. 2014. Accurate small and wide angle x-ray scattering profiles from atomic models of proteins and nucleic acids. *J. Chem. Phys.* **141**(22), article no: 22D508 [no pagination].

Nordlund, G., Sing Ng, J.B., Bergström, L. and Brzezinski, P. 2009. A membrane-reconstituted multisubunit functional proton pump on mesoporous silica particles. *ACS Nano.* **3**(9), pp. 2639-2646.

O'Sullivan, C.K. and Guilbault, G.G. 1999. Commercial quartz crystal microbalances – theory and applications. *Biosens. Bioelectron.* **14**(8-9), pp. 663-670.

Overington, J.P., Al-Lazikani, B. and Hopkins, A.L. 2006. How many drug targets are there?. *Nat. Rev. Drug Discov.* **5**(12), pp. 993-996.

Pace, H., Simonsson Nyström, L., Gunnarsson, A., Eck, E., Monson, C., Geschwindner, S., Snijder, A. and Höök, F. 2015. Preserved transmembrane protein mobility in polymer-supported lipid bilayers derived from cell membranes. *Anal. Chem.* **87**(18), pp. 9194-9203.

Palade, G.E. 1953. An electron microscope study of the mitochondrial structure. *J. Histochem. Cytochem.* **1**(4), pp. 188-211.

Patching, S.G., Baldwin, S.A., Baldwin, A.D., Young, J.D., Gallagher, M.P., Henderson, P.J.F. and Herbert, R.B. 2005. The nucleoside transport proteins, NupC and NupG, from *Escherichia coli*: specific structural motifs necessary for the binding of ligands. *Org. Biomol. Chem.* **3**(3), pp. 462-470.

Patel, A.R., Kanazawa, K.K. and Frank, C.W. 2009. Antibody binding to a tethered vesicle assembly using QCM-D. *Anal. Chem.* **81**(15), pp. 6021-6029.

Pauw, B.R. 2013. Everything SAXS: small-angle scattering pattern collection and correction. *J. Phys. Condens. Matter.* **25**(38), article no: 383201 [no pagination].

Pérez, J. and Nishino, Y. 2012. Advances in X-ray scattering: from solution SAXS to achievements with coherent beams. *Curr. Opin. Struct. Biol.* **22**(5), pp. 670-678.

Pintschovius, J. and Fendler, K. 1999. Charge translocation by the Na^+/K^+-ATPase investigated on solid supported membranes: rapid solution exchange with a new technique. *Biophys. J.* **76**(2), pp. 814-826.

Plant, A.L. 1993. Self-assembled phospholipid/alkanethiol biomimetic bilayers on gold. *Langmuir.* **9**(11), pp. 2764-2767.

Pockels, A. 1891. Surface tension. *Nature.* **43**, pp. 437-439.

Q-Sense. 2006. *Introduction and QCM-D theory.* [Online]. [Accessed 28 March 2016]. Available from: http://www.bu.edu/becf/downloads/BioInterface%20Technologies/QCMD/QCM-D%20Theory.pdf.

Quantifoil. 2016. *Products.* [Online]. [Accessed 5 April 2016]. Available from: http://www.quantifoil.com/index.php?name=products.

Quinn, P.J. and Wolf, C. 2010. An X-ray diffraction study of model membrane raft structures. *FEBS J*. **277**(22), pp. 4685-4698.

Quispe, J., Damiano, J., Mick, S.E., Nackashi, D.P., Fellmann, D., Ajero, T.G., Carragher, B. and Potter, C.S. 2007. An improved holey carbon film for cryo-electron microscopy. *Microsc*. *Microanal*. **13**(5), pp. 365-371.

Rahman, M., Ismat, F., McPherson, M.J. and Baldwin, S.A. 2007. Topology-informed strategies for the overexpression and purification of membrane proteins. *Mol*. *Membr*. *Biol*. **24**(5-6), pp. 407-418.

Rang, H.P., Dale, M.M., Ritter, J.M. and Flower, R.J. 2007. *Rang and Dale's Pharmacology*. 6th ed. London: Elsevier Limited, pp. 772-773.

Reichert, J.M., Rosensweig, C.J., Faden, L.B. and Dewitz, M.C. 2005. Monoclonal antibody successes in the clinic. *Nat*. *Biotechnol*. **23**(9), pp. 1073-1078.

Richards, M.J., Hsia, C.Y., Singh, R.R., Haider, H., Kumpf, J., Kawate, T. and Daniel, S. 2016. Membrane protein mobility and orientation preserved in supported bilayers created directly from cell plasma membrane blebs. *Langmuir*. **32**(12), pp. 2963-2974.

Richter, R.P., Bérat, R. and Brisson, A.R. 2006. Formation of solid-supported lipid bilayers: an integrated view. *Langmuir*. **22**(8), pp. 3497-3505.

Richter, R.P. and Brisson, A. 2004. QCM-D on mica for parallel QCM-D-AFM studies. *Langmuir*. **20**(11), pp. 4609-4613.

Robertson, J.D. 1957. New observations on the ultrastructure of the membranes of frog peripheral nerve fibers. *J*. *Biophys*. *Biochem*. *Cytol*. **3**(6), pp. 1043-1048.

Roder, F., Waichman, S., Paterok, D., Schubert, R., Richter, C., Liedberg, B. and Piehler, J. 2011. Reconstitution of membrane proteins into polymer-supported membranes for probing diffusion and interactions by single molecule techniques. *Anal*. *Chem*. **83**(17), pp. 6792-6799.

Rubinger, C.P.L., Moreira, R.L., Cury, L.A., Fontes, G.N., Neves, B.R.A., Meneguzzi, A. and Ferreira, C.A. 2006. Langmuir-Blodgett and Langmuir-Schaefer films of poly(5-amino-1-naphthol) conjugated polymer. *Appl*. *Surf*. *Sci*. **253**(2), pp. 543-548.

Rycovska, A., Hatahet, L., Fendler, K. and Michel, H. 2012. The nitrite transport protein NirC from *Salmonella typhimurium* is a nitrite/proton antiporter. *Biochim. Biophys. Acta.* **1818**(5), pp. 1342-1350.

Sackmann, E. 1995a. Biological Membranes Architecture and Function. In: Lipowski, R. and Sackmann, E. eds. *Handbook of Biological Physics – Structure and Dynamics of Membranes: From Cells to Vesicles*. London: Elsevier Ltd, pp. 1-63.

Sackmann, E. 1995b. Physical Basis of Self-Organization and Function of Membranes: Physics of Vesicles. In: Lipowski, R. and Sackmann, E. eds. *Handbook of Biological Physics – Structure and Dynamics of Membranes: From Cells to Vesicles*. London: Elsevier Ltd, pp. 213-304.

Salamon, Z., Wang, Y., Soulages, J.L., Brown, M.F. and Tollin, G. 1996. Surface plasmon resonance spectroscopy studies of membrane proteins: transducin binding and activation by rhodopsin monitored in thin membrane films. *Biophys. J.* **71**(1), pp. 283-294.

Samsonov, A.V., Mihalyov, I. and Cohen, F.S. 2001. Characterization of cholesterol-sphingomyelin domains and their dynamics in bilayer membranes. *Biophys. J.* **81**(3), pp. 1486-1500.

Sauerbrey, G. 1959. Verwendung von Schwingquarzen zur Wägung dünner Schichten und zur Mikrowägung. *Zeitschrift für Physik.* **155**(2), pp. 206-222.

Scalise, M., Galluccio, M., Pochini, L. and Indiveri, C. 2012. Over-expression in *Escherichia coli*, purification and reconstitution in liposomes of the third member of the OCTN sub-family: the mouse carnitine transporter OCTN3. *Biochem. Biophys. Res. Commun.* **422**(1), pp. 59-63.

Schadauer, F., Geiss, A.F., Srajer, J., Siebenhofer, B., Frank, P., Reiner-Rozman, C., Ludwig, B., Richter, O.M.H., Nowak, C. and Naumann, R.L.C. 2015. Silica nanoparticles for the oriented encapsulation of membrane proteins into artificial bilayer lipid membranes. *Langmuir.* **31**(8), pp. 2511-2516.

Schertler, G.F.X. 2015. Rhodopsin on tracks: new ways to go in signaling. *Structure.* **23**(4), pp. 606-608.

Schilling, J., Schöppe, J. and Plückthun, A. 2014. From DARPins to LoopDARPins: novel LoopDARPin design allows the selection of low picomolar binders in a single round of ribosome display. *J. Mol. Biol.* **426**(3), pp. 691-721.

Schulz, P., Dueck, B., Mourot, A., Hatahet, L. and Fendler, K. 2009. Measuring ion channels on solid supported membranes. *Biophys. J.* **97**(1), pp. 388-396.

Schulz, P., Garcia-Celma, J.J. and Fendler, K. 2008. SSM-based electrophysiology. *Methods*. **46**(2), pp. 97-103.

Seddon, A.M., Curnow, P. and Booth, P.J. 2004. Membrane proteins, lipids and detergents: not just a soap opera. *Biochim. Biophys. Acta*. **1666**(1-2), pp. 105-117.

Seifert, K., Fendler, K. and Bamberg, E. 1993. Charge transport by ion translocating membrane proteins on solid supported membranes. *Biophys. J.* **64**(2), pp. 384-391.

Serebryany, E., Zhu, G.A. and Yan, E.C.Y. 2012. Artificial membrane-like environments for *in vitro* studies of purified G-protein coupled receptors. *Biochim. Biophys. Acta*. **1818**(2), pp. 225-233.

Sévin-Landais, A., Rigler, P., Tzartos, S., Hucho, F., Hovius, R. and Vogel, H. 2000. Functional immobilisation of the nicotinic acetylcholine receptor in tethered lipid membranes. *Biophys. Chem.* **85**(2-3), pp. 141-152.

Shi, D., Nannenga, B.L., Iadanza, M.G. and Gonen, T. 2013. Three-dimensional electron crystallography of protein microcrystals. *eLife*. **2**, article no: e01345 [no pagination].

Shimshick, E.J. and McConnell, H.M. 1973. Lateral phase separation in phospholipid membranes. *Biochemistry*. **12**(12), pp. 2351-2360.

Shpigel, N., Levi, M.D., Sigalov, S., Girshevitz, O., Aurbach, D., Daikhin, L., Jäckel, N. and Presser, V. 2015. Non-invasive in situ dynamic monitoring of elastic properties of composite battery electrodes by EQCM-D. *Angew. Chem. Int. Ed. Engl.* **54**(42), pp. 12353-12356.

Simon, M., Frey, R., Zangemeister-Wittke, U. and Plückthun, A. 2013. Orthogonal assembly of a designed ankyrin repeat protein-cytotoxin conjugate with a clickable serum albumin module for half-life extension. *Bioconjug. Chem.* **24**(11), pp. 1955-1966.

Simons, K. and Ikonen, E. 1997. Functional rafts in cell membranes. *Nature*. **387**(6633), pp. 569-572.

Simons, K. and van Meer, G. 1988. Lipid sorting in epithelial cells. *Biochemistry*. **27**(17), pp. 6197-6202.

Simonsen, A.C. and Bagatolli, L.A. 2004. Structure of spin-coated lipid films and domain formation in supported membranes formed by hydration. *Langmuir*. **20**(22), pp. 9720-9728.

Singer, S.J. and Nicolson, G.L. 1972. The fluid mosaic model of the structure of cell membranes. *Science*. **175**(4023), pp. 720-731.

Smith, G.P. 1985. Filamentous fusion phage: novel expression vectors that display cloned antigens on the virion surface. *Science*. **228**(4705), pp. 1315-1317.

Smith, K.M., Slugoski, M.D., Loewen, S.K., Ng, A.M.L., Yao, S.Y.M., Chen, X.Z., Karpinski, E., Cass, C.E., Baldwin, S.A. and Young, J.D. 2005. The broadly selective human Na^+/nucleoside cotransporter (hCNT3) exhibits novel cation-coupled nucleoside transport characteristics. *J. Biol. Chem.* **280**(27), pp. 25436-25449.

Stoeckenius, W. 1962. Structure of the plasma membrane: an electron-microscope study. *Circulation*. **26**, pp. 1066-1069.

Stoeckenius, W. and Engelman, D.M. 1969. Current models for the structure of biological membranes. *J. Cell. Biol.* **42**(3), pp. 613-646.

Stumpp, M.T., Binz, H.K. and Amstutz, P. 2008. DARPins: a new generation of protein therapeutics. *Drug Discov. Today*. **13**(15-16), pp. 695-701.

Syndercombe Court, D., Domizio, N. and Yeatman, N. 2009. Pathology and immunology. In: Naish, J., Revest, P. and Syndercombe Court, D. eds. 2009. *Medical Sciences*. London: Elsevier Limited, pp. 237-301.

Tabor, D. 1980. Babylonian lecanomancy: an ancient text on the spreading of oil on water. *J. Colloid Interface Sci.* **75**(1), pp. 240-245.

Tadini-Buoninsegni, F., Bartolommei, G., Moncelli, M.R. and Fendler, K. 2008. Charge transfer in P-type ATPases investigated on planar membranes. *Arch. Biochem. Biophys.* **476**(1), pp. 75-86.

Tamaskovic, R., Simon, M., Stefan, N., Schwill, M. and Plückthun, A. 2012. Designed ankyrin repeat proteins (DARPins): from research to therapy. *Methods Enzymol*. **503**, pp. 101-134.

Tanaka, M. and Sackmann, E. 2005. Polymer-supported membranes as models of the cell surface. *Nature*. **437**(7059), pp. 656-663.

Tate, C.G. 2001. Overexpression of mammalian integral membrane proteins for structural studies. *FEBS Lett*. **504**(3), pp. 94-98.

Tate, C.G. 2010. Practical considerations of membrane protein instability during purification and crystallisation. *Methods Mol. Biol*. **601**, pp. 187-203.

Tatsuma, T., Watanabe, Y., Oyama, N., Kitakizaki, K. and Haba, M. 1999. Multichannel quartz crystal microbalance. *Anal. Chem*. **71**(17), pp. 3632-3636.

Terrettaz, S., Stora, T., Duschl, C. and Vogel, H. 1993. Protein binding to supported lipid membranes: investigation of the cholera toxin-ganglioside interaction by simultaneous impedance spectroscopy and surface plasmon resonance. *Langmuir*. **9**(5), pp. 1361-1369.

Thorn, J.A. and Jarvis, S.M. 1996. Adenosine transporters. *Gen. Pharmacol*. **27**(4), pp. 613-620.

Toporkiewicz, M., Meissner, J., Matusewicz, L., Czogalla, A. and Sikorski, A.F. 2015. Toward a magic or imaginary bullet? Ligands for drug targeting to cancer cells: principles, hopes and challenges. *Int. J. Nanomedicine*. **10**, pp. 1399-1414.

Trépout, S., Mornet, S., Benabdelhak, H, Ducruix, A., Brisson, A.R. and Lambert, O. 2007. Membrane protein selectively oriented on solid support and reconstituted into a lipid membrane. *Langmuir*. **23**(5), pp. 2647-2654.

Tuantranont, A., Wisitsora-at, A., Sritongkham, P. and Jaruwongrungsee, K. 2011. A review of monolithic multichannel quartz crystal microbalance: a review. *Anal. Chim. Acta*. **687**(2), pp. 114-128.

Wagner, M.L. and Tamm, L.K. 2000. Tethered polymer-supported planar lipid bilayers for reconstitution of integral membrane proteins: silane-polyethyleneglycol-lipid as a cushion and covalent linker. *Biophys. J*. **79**(3), pp. 1400-1414.

Wallin, E. and von Heijne, G. 1998. Genome-wide analysis of integral membrane proteins from eubacterial, archaean and eukaryotic organisms. *Protein Sci*. **7**(4), pp. 1029-1038.

Wallmann, J., Pali-Schöll, I. and Jensen-Jarolim, E. 2010. Anti-ids in allergy: timeliness of a classic concept. *World Allergy Organ. J*. **3**(6), pp. 195-201.

Watts, T.H., Gaub, H.E. and McConnell, H.M. 1986. T-cell-mediated association of peptide antigen and major histocompatibility complex protein detected by energy transfer in an evanescent wave-field. *Nature*. **320**(6058), pp. 179-181.

Weidle, U.H., Auer, J., Brinkmann, U., Georges, G. and Tiefenthaler, G. 2013. The emerging role of new protein scaffold-based agents for treatment of cancer. *Cancer Genomics Proteomics*. **10**(4), pp. 155-168.

Wesołowska, O., Michalak, K., Maniewska, J. and Hendrich, A.B. 2009. Giant unilamellar vesicles – a perfect tool to visualize phase separation and lipid rafts in model systems. *Acta Biochim. Pol*. **56**(1), pp. 33-39.

Williams, D.B. and Carter, C.B. 2009. *Transmission electron microscopy: a textbook for Materials Science*. [Online]. 2nd ed. New York: Springer Science and Business Media. [Accessed 3 April 2016]. Available from: https://books.google.co.uk/books?id=2dVHAAAAQBAJ.

Wittenberg, N.J., Im, H., Johnson, T.W., Xu, X., Warrington, A.E., Rodriguez, M. and Oh, S.H. 2011. Facile assembly of micro- and nanoarrays for sensing with natural cell membranes. *ACS Nano*. **5**(9), pp. 7555-7564.

Woof, J.M. and Burton, D.R. 2004. Human antibody-Fc receptor interactions illuminated by crystal structures. *Nat. Rev. Immunol*. **4**(2), pp. 89-99.

Yang, Z., Wang, C., Zhou, Q., An, J., Hildebrandt, E., Aleksandrov, L.A., Kappes, J.C., DeLucas, L.J., Riordan, J.R., Urbatsch, I.L., Hunt, J.F. and Brouillette, C.G. 2014. Membrane protein stability can be compromised by detergent interactions with the extramembranous soluble domains. *Protein Sci*. **23**(6), pp. 769-789.

Yu, C. and Groves, J.T. 2010. Engineering supported membranes for cell biology. *Med. Biol. Eng. Comput*. **48**(10), pp. 955-963.

Zahnd, C., Kawe, M., Stumpp, M.T., de Pasquale, C., Tamaskovic, R., Nagy-Davidescu, G., Dreier, B., Schibli, R., Binz, H.K., Waibel, R. and Plückthun, A. 2010. Efficient tumor targeting with high-affinity designed ankyrin repeat proteins: effects of affinity and molecular size. *Cancer Res*. **70**(4), pp. 1595-1605.

Zeuthen, T., Alsterfjord, M., Beitz, E. and MacAulay, N. 2013. Osmotic water transport in aquaporins: evidence for a stochastic mechanism. *J. Physiol*. **591**(20), pp. 5017-5029.

APPENDIX

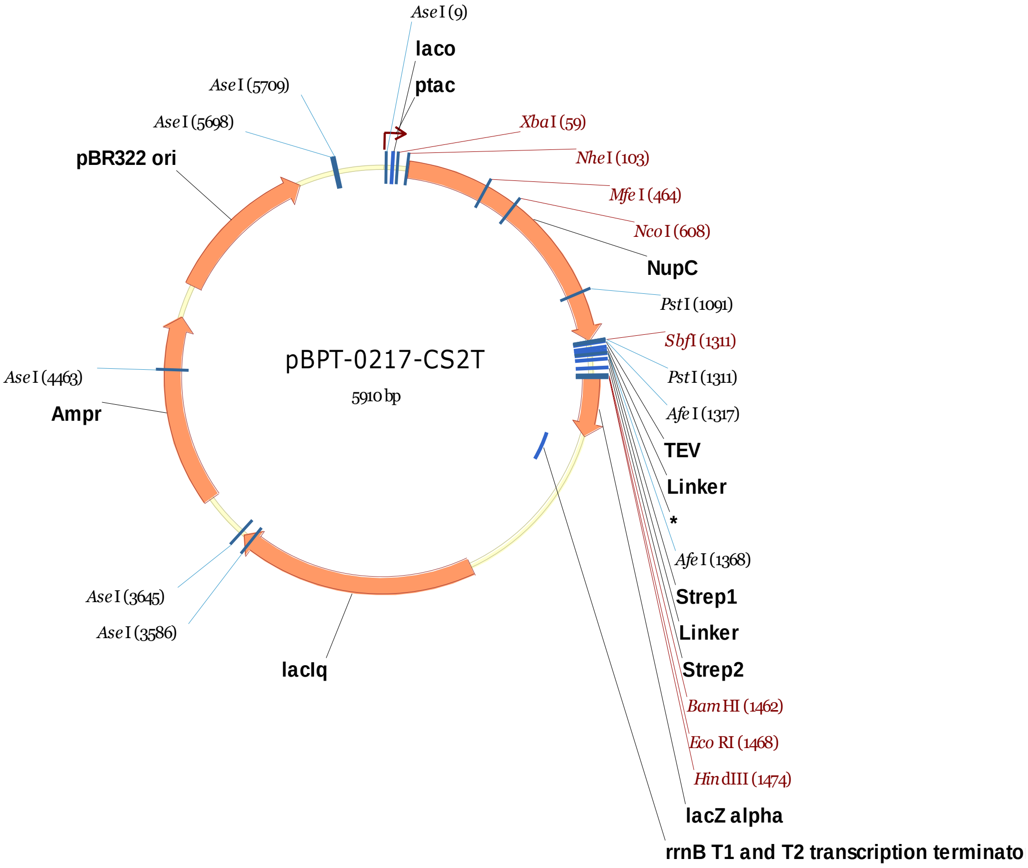

Figure A1. Map of the pBPT-0217-CS2T plasmid encoding double Strep-tagged NupC (courtesy of Dr. Vincent Postis, The School of Biomedical Sciences, University of Leeds).

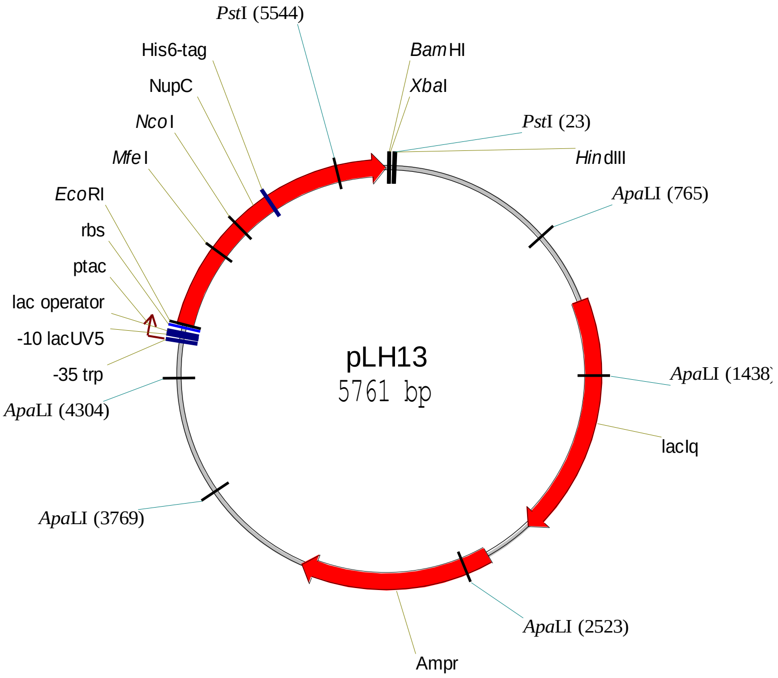

Figure A2. Map of the pLH13 plasmid encoding His$_6$-tagged NupC (courtesy of Dr. Vincent Postis, The School of Biomedical Sciences, University of Leeds).

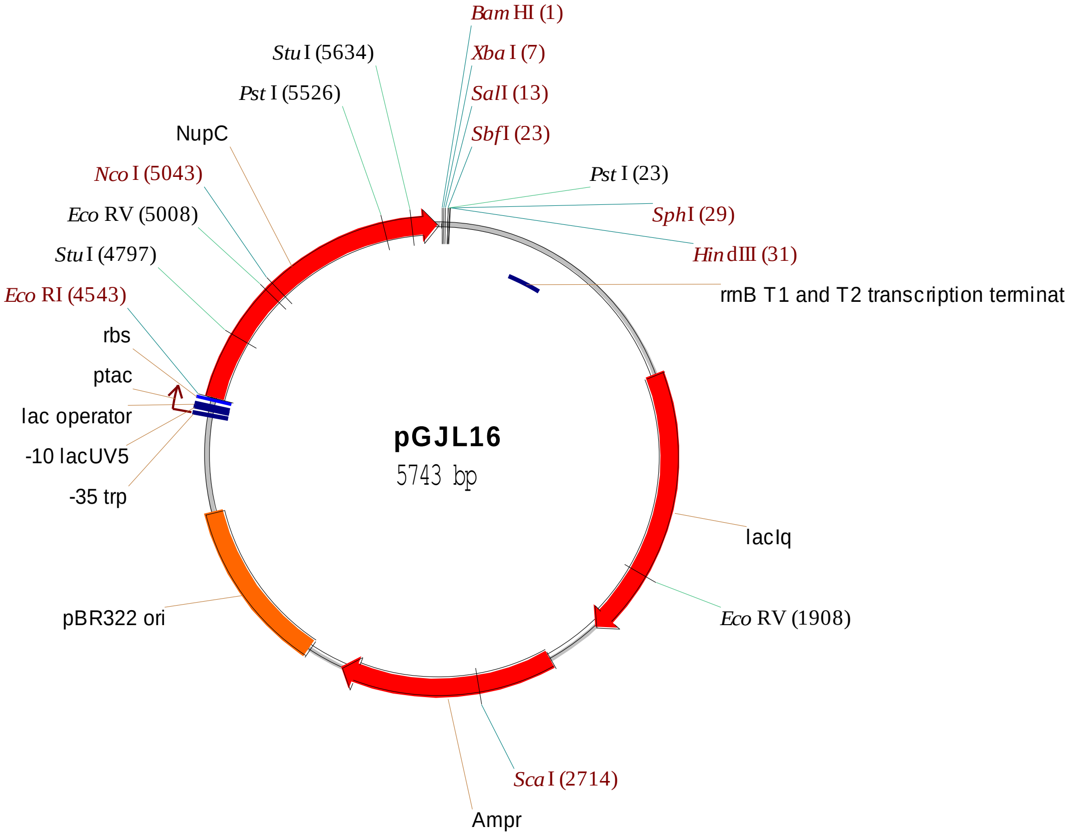

Figure A3. Map of the pGJL16 plasmid encoding untagged/wild-type NupC (courtesy of Dr. Vincent Postis, The School of Biomedical Sciences, University of Leeds).

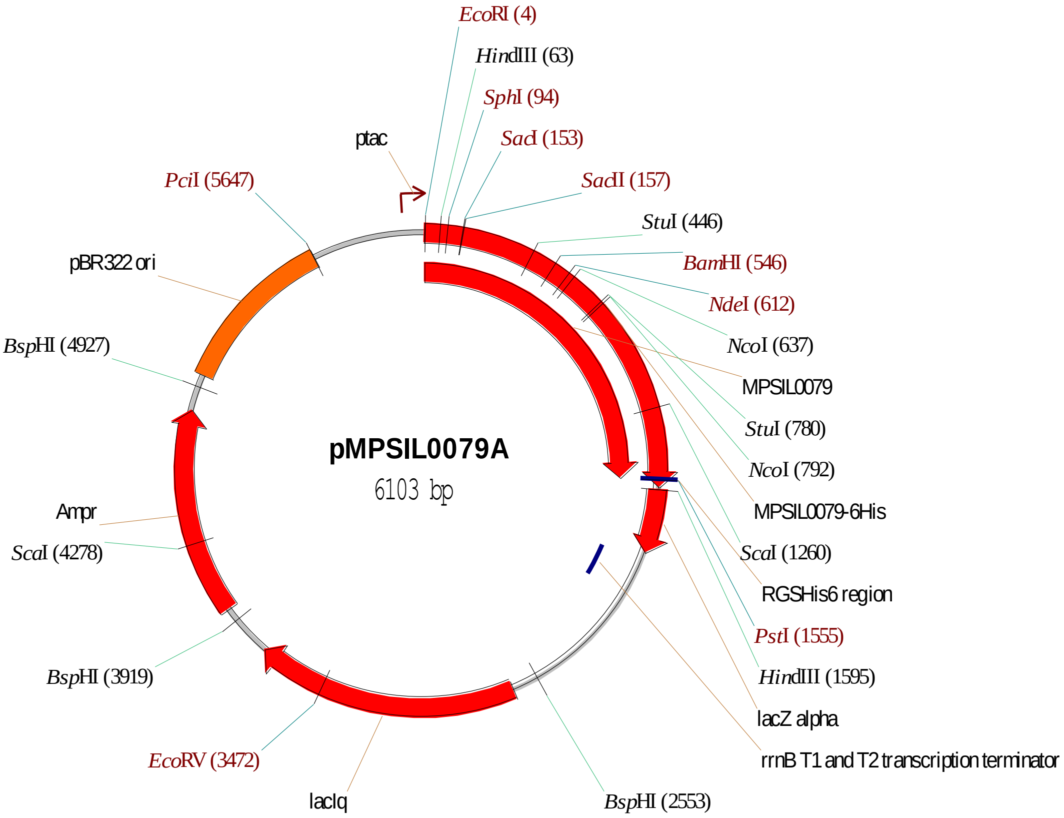

Figure A4. Map of the pMPSIL0079A plasmid encoding His$_6$-tagged PepTSo (courtesy of Dr. Vincent Postis, The School of Biomedical Sciences, University of Leeds).